

A11104 637778

NIST  
PUBLICATIONS

**NISTIR 5594**

# **NIST Reactor: Summary of Activities, October 1993 through September 1994**

**Reactor Radiation Division**

U.S. DEPARTMENT OF COMMERCE  
Technology Administration  
National Institute of Standards  
and Technology  
Gaithersburg, MD 20899

QC  
100  
.U56  
NO. 5594  
1995

**NIST**



# **NIST Reactor: Summary of Activities, October 1993 through September 1994**

## **Reactor Radiation Division**

U.S. DEPARTMENT OF COMMERCE  
Technology Administration  
National Institute of Standards  
and Technology  
Gaithersburg, MD 20899



U.S. DEPARTMENT OF COMMERCE  
Ronald H. Brown, Secretary  
TECHNOLOGY ADMINISTRATION  
Mary L. Good, Under Secretary for Technology  
NATIONAL INSTITUTE OF STANDARDS  
AND TECHNOLOGY  
Arati Prabhakar, Director



## FOREWORD

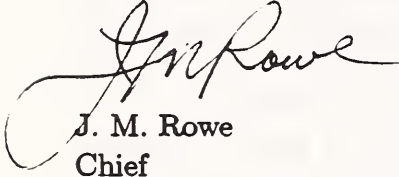
This has been a year of great excitement in neutron scattering — the 1994 Nobel Prize for Physics was awarded to C. G. Shull and B. N. Brockhouse for their pioneering research in neutron diffraction and inelastic scattering. Also, as this is written early in 1995, the ILL reactor has been restarted after installation of a new vessel, and we extend our congratulations to them. At NIST, the Research Reactor and Cold Neutron Research Facility have had another successful year, including the successful beginning of the maintenance and upgrade shutdown (started at the end of May, 1994) which will provide substantially enhanced performance for all experiments.

The reactor operated well prior to the beginning of the shutdown, and most activity centered around preparation for the extensive work to be performed. The initial stages of the shutdown went extremely well, showing the beneficial results of the extensive planning done. The old heat exchangers were removed and shipped for disposal without incident, and a great deal of preparation work by Health Physics and Operations in the process room reduced personnel exposures to a minimum. The new heat exchangers were pressure and helium leak tested at the factory prior to acceptance and delivery to NIST and installation. The very extensive primary and secondary piping changes are now almost complete, and testing is under way. In the course of inspection of the reactor vessel, a problem in the refuelling plug was identified and is being repaired. Throughout all of the shutdown activities, the emphasis has been on designing and installing for a thirty year life. There are no outstanding problems connected with the shutdown, and the path to completion of all work is now well established.

Prior to the shutdown in May, the science program had an extremely productive period of data collection. The use of the new powder diffractometer continued to grow at a rapid pace, with some 500 individual patterns recorded. A similar expansion of applications resulted from the extended use of the new horizontal reflectometer and the time-of-flight spectrometer in the CNRF. A design effort to replace all of the thermal neutron instruments over the next several years was initiated, while construction of the new BT-8 residual stress/single crystal diffraction instrument is well under way. Since the beginning of the shutdown, the scientific staff have made good use of the free time to analyse existing data, with occasional forays to our sister laboratories. A new direction for the future was established through the successful development of an initiative to use reflectometry to study biological systems in collaboration with the Biotechnology Division.

In spite of delays in cold source fabrication, the Cold Neutron Project advanced on a number of fronts during the year. The old cold source and bismuth tip were successfully removed, new beam shutters were installed, and the hydrogen cold source cryostat was inserted into the cryogenic port. Much of the hydrogen plumbing external to the biological shield is now installed and tested, while work continues on the balance of the plumbing. The in-pile part of guides 5-7 is installed, the new casings are installed, and the glass is being installed in the casings. Work on the back reflection, spin echo, and high resolution time-of-flight spectrometers continues, and the improved SPINS spectrometer has been installed at NG-5. Testing of various components is under way for each of these instruments, with generally good results.

Finally, as a result of the delays in fabrication of the new source, it now appears that reactor restart will be delayed by at least a month beyond the original longest estimate of nine months. While we will continue to try to make up some of the lost time, the best current estimate is that restart will not occur before the end of March, 1995. While we are of course disappointed that we cannot meet the original schedule, we are looking forward to a greatly improved facility.



J. M. Rowe

Chief

Reactor Radiation Division

## Abstract

This report summarizes all the programs which use the NIST reactor. It covers the period for October 1993 through September 1994. The programs range from the use of neutron beams to study the structure and dynamics of materials through nuclear physics and neutron standards to sample irradiations for activation analysis, isotope production, neutron radiography, and nondestructive evaluation.

**KEY WORDS:** activation analysis; cold neutrons; crystal structure; diffraction; isotopes; molecular dynamics; neutron; neutron radiography; nondestructive evaluation; nuclear reactor; radiation.

## DISCLAIMER

Certain trade names and company products are identified in order to adequately specify the experimental procedure. In no case does such identification imply recommendation or endorsement by the National Institute of Standards and Technology, nor does it imply that the products are necessarily the best for the purpose.





## CONTENTS

Foreword .....	iii
Abstract .....	v
<b>Chemical Physics of Materials .....</b>	<b>1</b>
Dynamics of Molecules in Porous Systems .....	1
Dynamics of Boron Nitride .....	6
Dynamics of $C_{61}H_2$ .....	8
Lattice and Molecular Dynamics of Poly (p-phenylene vinylene) .....	10
Isotope-Dilution Studies of H-H Interactions in Rare-Earth Hydrides .....	12
Research Topics .....	14
Affiliations .....	15
<b>Magnetism and Superconductivity .....</b>	<b>16</b>
Heavy Fermion-Type Systems .....	16
Non-Fermi Liquids .....	17
Spin Dynamics of Finite-Size Chains .....	18
Magnetic Order in Superconductors .....	20
Anomalous Exchange in $MnCl_2$ .....	22
Magnetic Ordering in Nd/Y Superlattices .....	23
Research Topics .....	25
Affiliations .....	28
<b>Crystallography .....</b>	<b>30</b>
Phase Analysis .....	30
Crystal Structures .....	30
Database Activities .....	36
Research Topics .....	37
Affiliations .....	40
<b>Surface and Interfacial Studies .....</b>	<b>41</b>
Depositional Interdiffusion in Ba Stearate LB Films .....	41
Neutron Reflectivity Studies of Single Lipid Bilayers .....	42
Magnetic Systems .....	43
Anomalous Critical Scattering in Tb .....	47
Polymer Systems .....	48
New Methods and Capabilities .....	53
Research Topics .....	59
Affiliations .....	60
<b>Macromolecular and Microstructure Studies .....</b>	<b>62</b>
Polymers .....	62
Structural Biology .....	65
Microporous Materials .....	66
Structured Fluids .....	68

Research Topics .....	69
Affiliations .....	73
<b>Neutron Beam Applications .....</b>	<b>74</b>
Neutron Diffraction Measurement of Residual Stress .....	74
Neutron Diffraction Measurement of Texture .....	80
Neutron Autoradiography of Paintings .....	82
Research Topics .....	83
Affiliations .....	84
<b>Analytical Chemistry .....</b>	<b>85</b>
Nuclear Methods Group .....	85
Smithsonian Institution .....	92
Food and Drug Administration .....	93
Federal Bureau of Investigation .....	94
University of Maryland .....	95
Research Topics .....	96
Affiliations .....	99
<b>Neutron Interactions and Dosimetry .....</b>	<b>100</b>
Fundamental Neutron Physics .....	100
Neutron Fields and Standards .....	101
Research Topics .....	103
Affiliations .....	103
<b>Polymers Division Programs .....</b>	<b>105</b>
Block Copolymers, Blends and Networks in Bulk .....	105
Polymer Blend Films .....	108
Research Topics .....	111
Affiliations .....	112
<b>Exxon Research at the CNRF .....</b>	<b>113</b>
Research Topics .....	119
Affiliations .....	120
<b>University of Minnesota Programs .....</b>	<b>121</b>
SANS .....	121
Reflectometry .....	122
Research Topics .....	124
Affiliations .....	124
<b>CNRF Instrumentation Development .....</b>	<b>125</b>
New Instruments .....	125
Other Instrumentation .....	129
The Hydrogen Cold Source .....	130
Research Topics .....	132
Affiliations .....	133

<b>Guest Researchers and Collaborations</b> .....	134
<b>Reactor Operations and Engineering</b> .....	138
<b>Personnel Roster</b> .....	139
NBSR and CNRF Resident Staff .....	140
Research and Engineering Staff .....	143
Technical Staff .....	147
Reactor Operations .....	147
Reactor Engineering .....	147
Neutron Condensed Matter Research .....	147
<b>Publications</b> .....	148



# Chemical Physics of Materials

NBSR research that falls into this category typically involves inelastic neutron scattering measurements of the dynamics of molecular solids, various inclusion compounds, and structurally disordered materials. These studies yield detailed information on the atomic and molecular interactions responsible for many properties of these systems. For cases involving either rotational excitations or hydrogen motions or both, this information is difficult, if not impossible, to obtain by other means. Furthermore, since thermal neutron wavelengths are comparable to interatomic spacings, one is able to ascertain the geometry of the various motions in a way unmatched by other spectroscopic probes. Each of these attributes is featured in one or more of the examples that are highlighted here.

## Dynamics of Molecules in Porous Systems

- **Molecular Dynamics of Replacement Refrigerants Encaged in Zeolites**

There is an impetus to develop replacement refrigerants for chlorofluorocarbons (CFCs) due to increasing concerns for the damage that the ozone-depleting CFCs present to the environment. The urgency is underscored by the looming international ban on CFC production after 1995. While significant advances have already been made in identifying new refrigerants, economically viable synthesis and separation routes remain a critical issue on the pathway to commercialization of some of the most promising ones. Key to the development of advanced production methods is the role of surface chemistry in both the synthesis and separation steps. Although an enormous effort has been given to the development of environmentally benign refrigerants such as hydrofluorocarbons (HFCs), there is still much to be learned about their properties, chemistry, and interactions with surfaces of solids.

With this in mind, a recent collaborative research effort has been initiated between scientists of the Reactor Radiation Division, Surface and Microanalysis Science Division, and DuPont to investigate by neutron scattering techniques, the prototypical alternative refrigerant HFC 134a ( $F_3C-CF_2H$ ) and its isomer 134 ( $HF_2C-CF_2H$ ) encaged in the cavities of dehydrated Na-X zeolite ( $Na_{86}Al_{86}Si_{106}O_{384}$ ). Our goal is to characterize the guest-host interactions that influence the bonding geometry and dynamics of these HFC molecules in this well-characterized molecular sieve. The purification of HFCs is one potential application [1] of the size-selective molecular-adsorption properties of zeolites. This collaborative research effort is directed toward the development of improved methods for the separation and storage of 134 and 134a, both of which are formed during industrial production of the latter.

All incoherent-inelastic-neutron-scattering (IINS) measurements were performed at the NBSR. The Na-X zeolite samples were dehydrated at 673 K in vacuum. Adsorptions of the HFCs by the dehydrated Na-X were carried out at room temperature. Saturation uptakes corresponded to  $\sim 4$  molecules per supercage. This is equal to the number of Na ions located at the  $S_{III}$  positions (see Fig. 1) in the supercages of the Na-X-zeolite structure [2]. This fact and the observed lack of significant HFC adsorption in the related zeolite, Na-Y, which possesses no Na ions at the  $S_{III}$  positions [2] strongly suggest that the Na-X-adsorbed HFCs are associated with the Na ions at these sites. The IINS measurements below energy transfers of 240 meV revealed markedly different spectral signatures for 134 and 134a bound in Na-X (see Figs. 2 and 3). Measurements at lower loading indicated that the HFC vibrational spectra were largely independent of concentration.

Initial efforts to develop force fields to account for the data for 134a are encouraging.

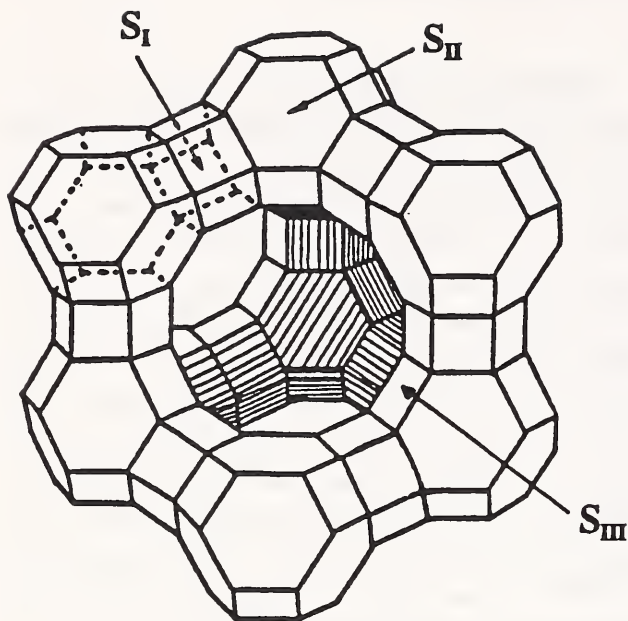


Figure 1. The Na-X zeolite structure indicating the location of the  $S_{III}$  position inside the supercage.

Simple Wilson FG matrix analysis of the 134a molecule without the inclusion of off-diagonal matrix elements or guest-host interactions was used to produce the model spectrum in figure 2. Although no attempt was made to include multiphonon scattering contributions, this model is still fairly successful in reproducing the main vibrational bands. From analysis of the potential energy distributions, the model suggests, among other things, the association of the normal-mode feature at 17 meV with the molecular torsions, the features at 45 and 52 meV with the C-C-F and F-C-F deformations, and the higher-energy features above  $\sim 120$  meV with the C-C-H, F-C-H, and H-C-H deformations. There are indications from the literature [3] that the extra, unexplained scattering intensity between  $\sim 60$  and 100 meV may be associated with adsorbate-coupled zeolite-framework vibrations, which are a direct manifestation of significant guest-host interactions.

Unlike its isomer, the 134 molecule presents a more complex situation. For this molecule, the existence of two conformations is well-known

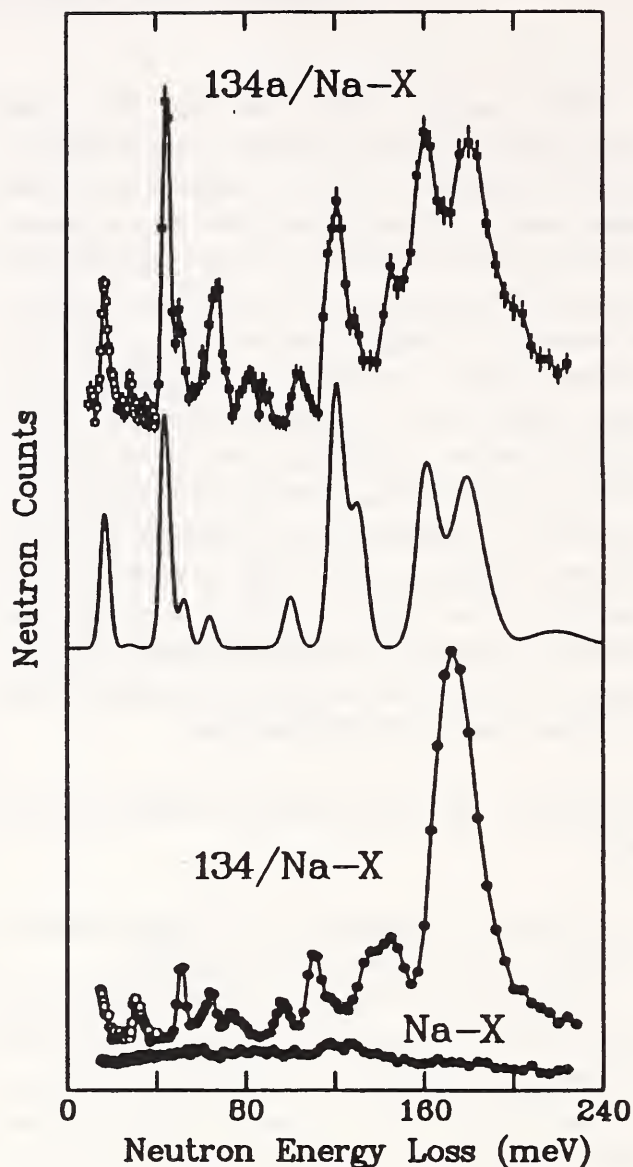


Figure 2. The IINS spectra of 134 and 134a in Na-X zeolite at saturation loading ( $\sim 4$  molecules per supercage) as well as unloaded Na-X, below 10 K, measured with the BT-4 spectrometer. The solid-line spectrum is a preliminary model-generated fit of the 134a spectrum using Wilson FG matrix force-field analysis.

from gas-phase measurements [4] with the trans conformer being 5 kJ/mole more stable than the gauche conformer. (See Fig. 4.) For 134 in Na-X at 4 K, the presence of vibrational contributions from either two conformers, or possibly a single conformer in multiple binding sites cannot be

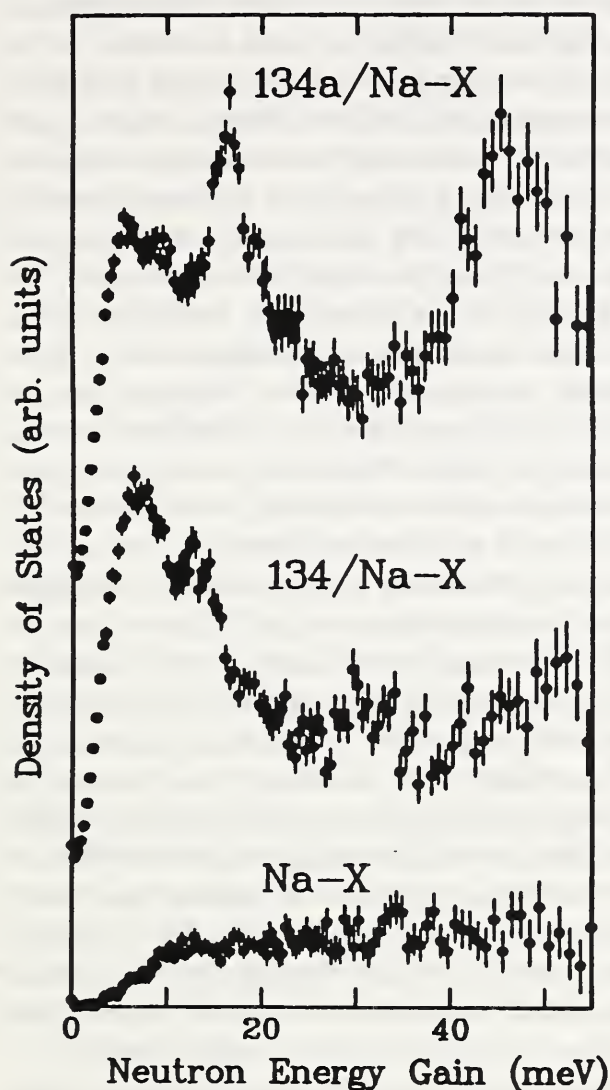


Figure 3. The low-energy IINS spectra at 200 K of 134 and 134a in Na-X zeolite at saturation loading ( $\sim 4$  molecules per supercage) as well as unloaded Na-X, measured in energy gain using the Fermi-chopper time-of flight spectrometer.

ruled out from a consideration of the IINS spectrum (Fig. 2). Indeed, recent room temperature Raman spectra obtained at DuPont support the contention that, although the *trans* conformer is favored in the gas phase, both 134 conformers do, in fact, exist in the zeolite supercages. This suggests that the energy difference between *trans* and *gauche* conformers is altered in the zeolite, the unusual stability of the *gauche* con-

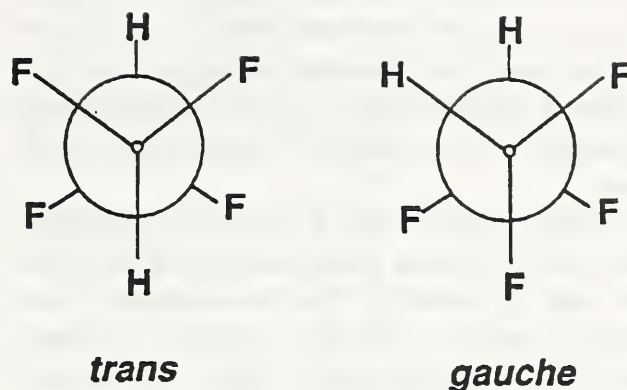


Figure 4. Schematic of the two conformations of the 134 molecule. The C-C axis is aligned perpendicular to the page.

former possibly resulting from a favorable geometric arrangement between this conformer and the Na-X adsorption site. More experiments are underway to further investigate the apparently stable coexistence of both conformers in Na-X.

Preliminary force-field models have, up until now, failed to provide a satisfactory fit to the 134 IINS data, although it is probable that the lowest-energy scattering intensity in figure 2 is due to the torsional vibrations and the highest-energy vibrations above 120 meV involve F-C-H and C-C-H deformations. Figure 3 displays the low-energy vibrational features for the HFCs in Na-X at 200 K in neutron energy gain using the Fermi-chopper time-of-flight spectrometer. The torsional vibrations are tentatively assigned to the peak at  $\sim 12$  meV (compared with 17 meV for 134a). The torsional vibrations for both HFCs appear to be shifted upwards by 2-3 meV compared with their gas-phase values [4-6]. The large scattering intensity below  $\sim 10$  meV is associated with whole-molecule vibrations inside the supercages and corroborates the existence of significant guest-host interactions.

A series of time-of-flight measurements of the quasielastic scattering in these systems was also undertaken. Results were obtained over the temperature range from 1.4 to 350 K, with both 4.1 and 5.0 Å incident neutrons. While clear dependence on temperature and momentum trans-

fer were evident, the data suggest that more than one type of reorientational process is occurring over this temperature range, thus precluding a detailed analysis of the reorientational dynamics of either caged HFC molecule at this time.

Current efforts are focused on combining data from gas-phase measurements of the structure and dynamics of the free molecule, with multiple probes (including neutron, infrared, and Raman spectroscopies, NMR, and neutron diffraction) of the properties of the molecules inside the Na-X supercages. In the final force-field analysis that results from these efforts, we hope to elucidate the important HFC-Na and/or HFC-framework interactions so as to achieve a detailed understanding of the binding forces and reorientational dynamics within this type of sieve.

## References

- [1] D. R. Corbin and C. P. Grey, (DuPont) unpublished data.
- [2] D. W. Breck, *Zeolite Molecular Sieves*, John Wiley and Sons, New York (1974).
- [3] W. P. J. H. Jacobs, J. H. M. C. van Wolput, R. A. van Santen, and H. Jobic, *Zeolites* **14**, 117 (1994).
- [4] V. F. Kalasinsky, H. V. Anjaria, and T. S. Little, *J. Phys. Chem.* **86**, 1351 (1982).
- [5] A. Danti and J. L. Wood, *J. Chem. Phys.* **30**, 582 (1959).
- [6] M. K. Crawford and D. R. Corbin, (DuPont) unpublished data.

### • Quantifying Freezable Water in Portland Cement Paste

Portland cement concrete is the most widely used material in the United States with approximately 500 million tons incorporated into the infrastructure each year. It has been estimated that it will cost over 400 billion dollars between now and the beginning of the next century simply to repair existing bridges and highways. Although the failure of concrete can be caused by a number of factors including heavy traffic loading, fatigue, and corrosion of the reinforcing

steel, a significant portion of the necessary repairs is due to damage resulting from repeated freezing and thawing of water contained in the pores of the material. Thus attaining a detailed understanding of the freeze-thaw process in concrete could have a significant economic impact.

It is widely accepted that the freeze-thaw resistance of concrete and other porous materials depends primarily on their microstructure. To date, most of the information available on the pore size distribution in concrete comes from mercury intrusion porosimetry. However the intrusion of mercury is only a surrogate for the freezing of water within the pore system, and the details of the relationship between the microstructure and the formation of ice are not understood. Therefore a nondestructive measurement technique which couples directly to water within the concrete pores is required. Quasielastic neutron scattering is such a technique because of its sensitivity to molecular motions and the unusually large scattering cross section of hydrogen. During the past year, engineers from the University of New Hampshire and Worcester Polytechnic Institute in collaboration with scientists from the Federal Highways Administration and the Reactor Radiation Division have used quasielastic neutron scattering to probe the freezing of water in portland cement paste.

Experience has shown that the freeze-thaw resistance of concrete increases as the water/cement ratio of the initial mix is decreased. Therefore three cement paste samples were prepared by mixing distilled water and type I portland cement with water/cement ratios of 0.3, 0.4, and 0.5. When the samples were 14 days old,  $\sim 0.5$  mm thick wafers were cut from each mix. These wafers were then stored under a saturated lime solution and were never allowed to dry. Shortly before the neutron scattering measurements were to occur, half of each sample was dried in an oven overnight for use as a blank. The neutron scattering measurements were performed on the Fermi chopper time-of-flight spectrometer located in the Cold Neutron Research Facility. Spectra were collected as a function of



decreasing temperature only. Data were typically collected for  $\sim 3$  h for the wet samples and  $\sim 1$  h for the dry blank. Since the presence of lime water in the pore system was the only difference in the sample and the blank, the spectra which resulted from subtracting the blank's spectrum from that of the sample should reflect the pore water and not the hydrogen incorporated into the cement paste during curing.

Figure 5 shows representative spectra for the sample having an initial water/cement ratio of 0.5. At  $3^\circ\text{C}$  and  $-13^\circ\text{C}$  the spectra consist of two components: a resolution limited peak that reflects the presence of immobile water and a broadened peak due to the mobile molecules. Clearly, the integrated area of the Lorentzian component decreases as the temperature is lowered and by  $-40^\circ\text{C}$  this component has almost completely disappeared. Since this area is a direct measure of the amount of mobile water in the system, the observed decrease reflects the freezing of the pore water. In addition, the width of the Lorentzian component decreases as the temperature decreases indicating that the time scale of the motion slows as the temperature is lowered. In fact, the width follows the expected Arrhenius law with an activation energy of  $11.6$  kJ/mol, independent of the initial water/cement ratio.

In order to separate and quantify the scattering due to bound and mobile water, the spectra were fit with a delta function elastic component and a Lorentzian quasielastic component, each convoluted with the experimental resolution function. The lines in figure 5 are the result of this procedure. The bound water index (BWI) was obtained from these fits by dividing the integrated intensity of the elastic component by the total integrated intensity. The temperature dependence of the BWI is shown in figure 6. Below  $\sim 250$  K the BWI is indistinguishable for the three samples. This suggests that the relatively small gel pores (i.e. those with a radius  $\leq 20$  nm) play a relatively minor role in the freeze-thaw durability of concrete.

Above  $250$  K the BWI's of the three samples

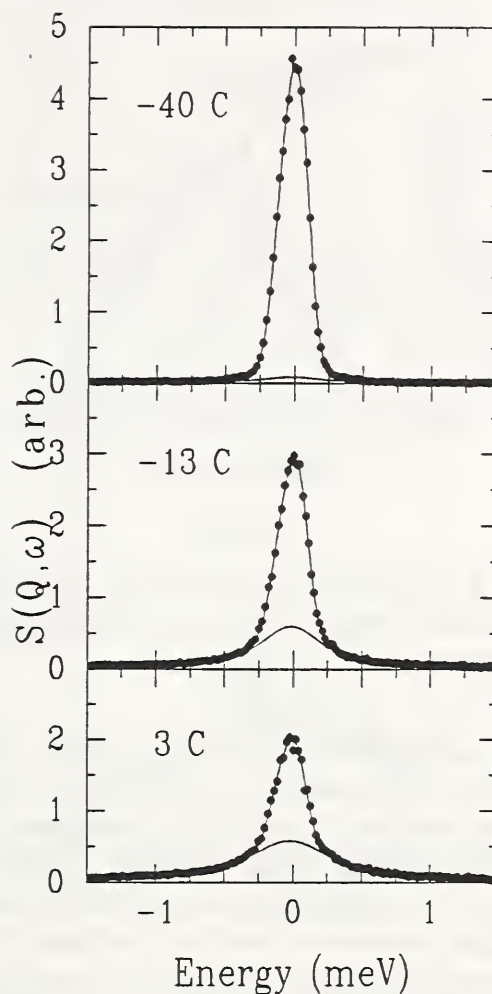


**Figure 5.** Representative quasielastic spectra for water in the pores of the cement paste sample which had an initial water/cement ratio of 0.5. The Lorentzian component due to the mobile water is indicated. The intensity of this component decreases with decreasing temperature due to freezing of water in the pores.

begin to deviate from each other and reach a maximum difference above the freezing point of bulk water. In fact at  $276$  K, the BWI for the 0.3 sample, the most resistant to freeze-thaw, is roughly 50% higher than that for the 0.5 sample. Because water in the larger capillary pores would be expected to freeze first, this suggests that the difference in the freeze-thaw durabil-

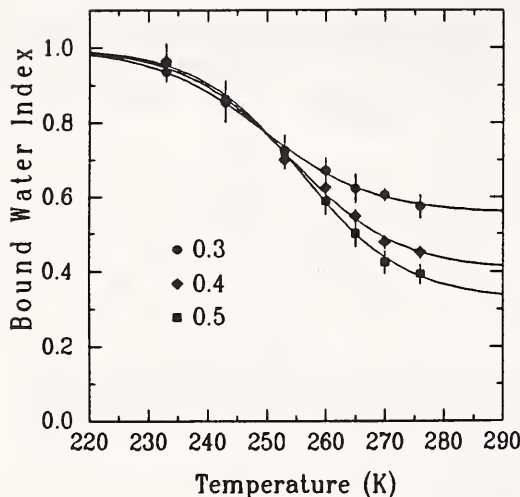


**Figure 6.** The bound water index as a function of temperature for water in the pores of three different cement pastes.

ity is due to the water in these larger pores (i.e. those with radius  $\geq 100$  nm). It's interesting to note that the BWI is never zero even above the freezing point of water. There are at least two possible reasons for this. Perhaps the drying procedure used for the blank drove off some of the hydrogen that had been bound into the structure whereas this bound hydrogen would have remained in the wet sample. Thus extra elastic scattering not due to the pore water might remain in the spectra shown in figure 5. The more likely and more interesting possibility is that the elastic scattering is due to water which, on the neutron time scale, has been immobilized by being on or near the surface of the pores. The only evidence for this explanation is that above 273 K, the BWI tends to decrease slowly with increasing temperature. This may be due to water in the top-most "surface layers" becoming mobile.

While there are still several open questions concerning the interpretation of these results, quasielastic neutron scattering is apparently capable of discerning differences in cement pastes with different resistance to freeze-thaw. From

these preliminary findings, it seems that in order to improve the freeze-thaw durability of concrete, one should try to increase the surface/volume ratio of the large capillary pores. This finding is consistent with common sense and with the vast amount of empirical knowledge about concrete. In the future, quasielastic neutron scattering will also be applied to the new high performance concretes to attempt to quantify the as of yet unknown freeze-thaw durability of these materials.

### Dynamics of Boron Nitride

The utility of the carbon solids graphite and diamond is primarily due to their exceptional thermal properties. For example, the very high melting temperature of graphite (3820 K) makes it the material of choice for many high-temperature applications, while the large thermal conductivity of diamond, which exceeds that of good metals, offers great promise for its use as a substrate for electronic devices. Unfortunately, these materials are sometimes unsuitable for these purposes for reasons unrelated to their thermal properties. For instance, despite a great deal of effort, it has proven difficult to fabricate diamond films that could be used in electronic devices or for wear-resistant coatings. Therefore the intense interest in carbon solids has been echoed in research on various materials which could substitute for diamond and graphite, most notably cubic and hexagonal boron nitride (c-BN and h-BN respectively). Neutron spectroscopy is uniquely sensitive to the vibrational states which, on a microscopic scale, underly the important thermal properties of these materials. Thus NIST scientists, in collaboration with scientists from General Motors, General Electric, and Advanced Ceramics Corporation, have initiated a program designed to understand the vibrational properties of BN.

The spectra obtained for c-BN and h-BN reflect the similarities and differences from their carbon analogues, diamond and graphite. Figure 7 shows the vibrational densities of states obtained for c-BN and diamond. The spectra are

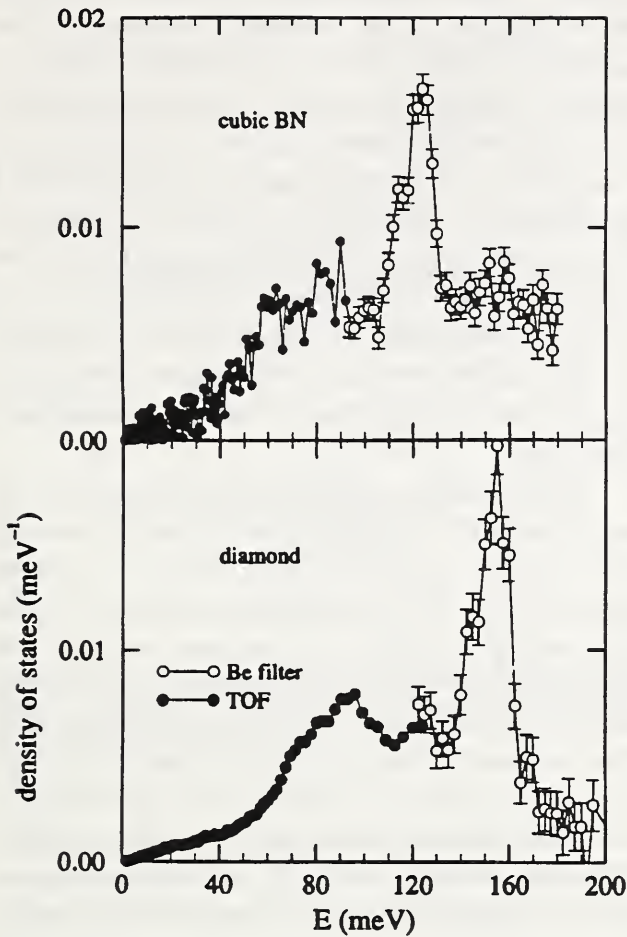


**Figure 7.** Vibrational densities of states for c-BN and diamond. The high-energy shoulder above 130 meV for BN may be an experimental artifact. Data obtained by the time-of-flight method and the Be-filter-analyzer method are shown as filled and open circles respectively.

rather similar, but the BN features are lower in energy, because the B-N covalent bond is somewhat weaker than the C-C bond. The 155 meV bond-stretching peak of diamond is lowered to 120 meV in c-BN. These spectra may be used to calculate intrinsic thermal properties, such as specific heat and thermal conductivity, for diamond and c-BN.

Inelastic neutron scattering measurements have also been made on hexagonal boron nitride (h-BN) and on graphite powder, with the results shown in figure 8. These vibrational densities of states extend to higher energies than

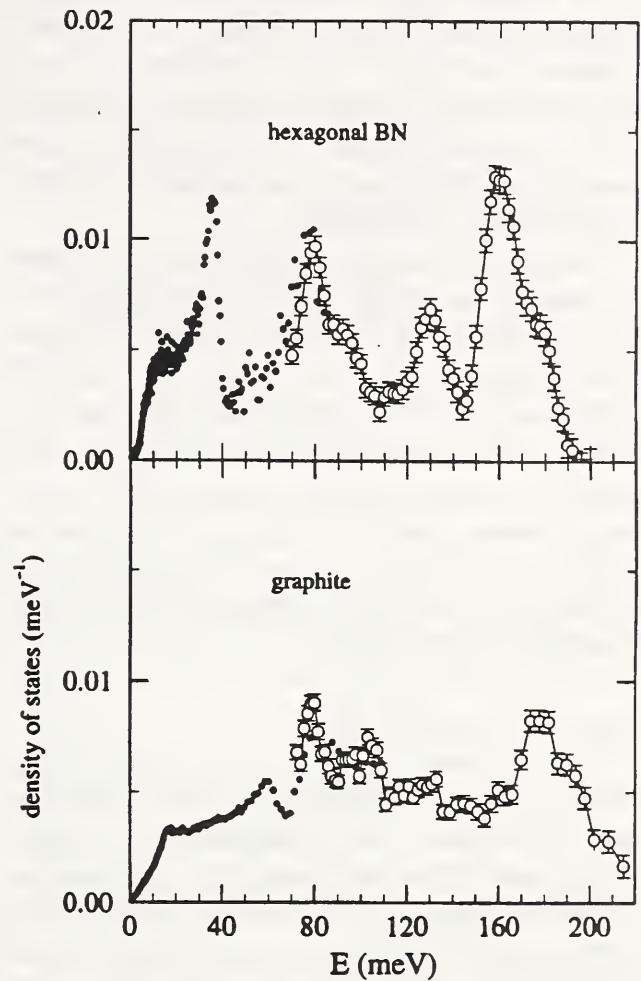


**Figure 8.** Vibrational densities of states for h-BN and graphite. Filled and open circles have the same meanings as in figure 7.

those of figure 7, reflecting the fact that the in-plane bonds in these layered solids are somewhat stronger than those of c-BN and diamond. Examination of various features in the densities of states, together with previous measurements of low-energy phonon dispersion curves, leads us to the following conclusions about the intralayer and interlayer bonding in h-BN. All characteristic energies are somewhat lower in h-BN than in graphite, but not all in the same proportion. In-layer modulation of atomic positions, characterized by the highest energies in the spectra, imply energies in h-BN which are only slightly smaller than in graphite. In contrast, the feature at 36 meV in h-BN, corresponding to modes in

which neighboring B and N atoms in the same layer are displaced perpendicular to the layers in opposite directions, is very much lower in energy than the 60 meV feature in graphite. Interlayer force constants in h-BN are about 30% weaker than in graphite, despite the presence of an ionic contribution in the former.

The data of figures 7 and 8 were made possible through the preparation of isotopically purified samples of  $^{11}\text{BN}$ . Samples of BN with natural isotopic composition, which contains 20% of the isotope  $^{10}\text{B}$ , would have an unacceptably high neutron absorption cross section. This research is continuing with more neutron scattering measurements and computer simulations in progress. The latter are being carried out by groups at Ohio University and the Technical University of Chemnitz.

### Dynamics of $\text{C}_{61}\text{H}_2$

The discovery of a method to make significant quantities of the fullerenes, such as  $\text{C}_{60}$ , has opened the door to research into a completely new class of molecular architectures. These materials offer great promise for future applications, but it has proven difficult to control their chemistry at a molecular level. A notable exception is the methanofullerenes, in which an additional carbon atom is attached across a bond joining two of the carbons in the fullerene backbone. Two chemical groups can then be attached to this extra carbon. The simplest "group" is a single hydrogen atom so that the basic molecular derivative in this class is the compound  $\text{C}_{61}\text{H}_2$ . Since previous neutron scattering measurements on powder samples of  $\text{C}_{60}$  revealed considerable information, particularly regarding the rotational potential sensed by molecules as they change their orientations, a series of measurements has been undertaken on  $\text{C}_{61}\text{H}_2$ , specifically the "6:5" isomer which is obtained by breaking one of the bonds that joins a pentagon to a hexagon in the  $\text{C}_{60}$  molecule.

$\text{C}_{60}$  undergoes a first order transition, at  $\sim 260\text{ K}$ , from a low temperature orientationally ordered phase to a high temperature disordered

phase.  $\text{C}_{61}\text{H}_2$  undergoes a similar transition at  $\sim 290\text{ K}$  [1]. The increased resistance to rotational motion, due to the added methylene group, explains the higher transition temperature. Neutron diffraction patterns have been obtained for a deuterated sample using the BT-1 spectrometer. Above the transition temperature the pattern indexes to a face centered cubic lattice in analogy with the high temperature phase of  $\text{C}_{60}$  (space group  $\text{Fm}\bar{3}\text{m}$ ). There is also substantial diffuse scattering which is well described by a model that assumes complete orientational disorder.

At low temperatures the powder pattern can be indexed to a simple cubic lattice in analogy with the low temperature phase of  $\text{C}_{60}$  (space group  $\text{Pa}\bar{3}$ ). If the orientation adopted by the  $\text{C}_{60}$  moiety in  $\text{C}_{61}\text{D}_2$  is the same as the more populated molecular orientation in pristine  $\text{C}_{60}$ , the methylene group can be accommodated in the "octahedral" site, in which case there is little change in the C-C interactions responsible for the orientational ordering of molecules in  $\text{C}_{60}$ . Note that since the  $\text{C}_{61}\text{D}_2$  molecule does not have a threefold axis, there must either be residual orientational disorder to produce a threefold axis, or else the symmetry of the lattice must actually be lower than cubic. In fact, at low temperatures, diffuse scattering, which has the shape expected for orientational disorder, is observed.

The orientational order-disorder transition in  $\text{C}_{61}\text{H}_2$  also manifests itself in the low energy transfer scattering. Measurements of this scattering have been made using the BT-4 triple-axis spectrometer and the Fermi chopper time-of-flight spectrometer (Fig. 9). At 200 K an inelastic peak is observed, centered at  $\sim 2.5\text{ meV}$  and attributed to molecular librations in the orientational potential responsible for securing the low-temperature structure. The observed peak positions in  $\text{C}_{61}\text{H}_2$  are slightly higher than those in  $\text{C}_{60}$ , reflecting the higher orientational ordering temperature of the compound. The peaks are also much broader in  $\text{C}_{61}\text{H}_2$ , possibly reflecting a more anisotropic potential. Above the

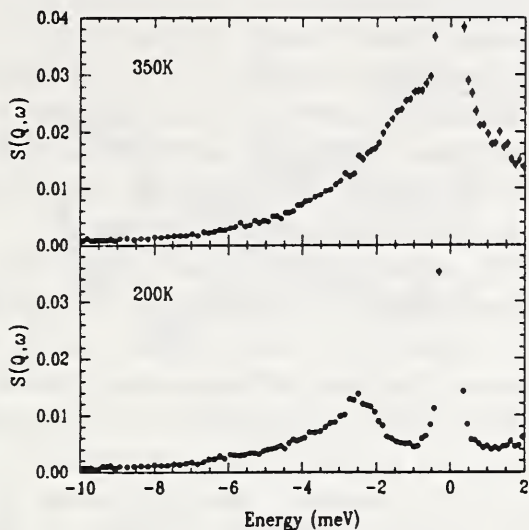


**Figure 9.** Q-integrated plots of  $S(Q, \omega)$  for  $C_{61}H_2$  at 200 K and 350 K, obtained using the Fermi chopper time-of-flight spectrometer.

transition temperature, a broad feature is observed, centered at zero energy, and associated with diffusive rotational motion. The  $Q$  dependence of the integrated intensity of the low energy scattering, both below and above the transition temperature, confirms that the scattering is primarily associated with rotational motion of the molecules.

The measured vibrational density of states for  $C_{61}H_2$  is shown in figure 10. Because the scattering cross section of H is more than an order of magnitude larger than that of C, modes involving significant motion of H atoms are emphasized. Comparing the  $C_{61}H_2$  spectrum with spectra for  $C_{61}D_2$  and  $C_{60}$ , we have determined that the modes at 37.8, 130, 152, and 180 meV include substantial contributions from hydrogen atoms. We assign these peaks to a rocking mode of the entire methylene group in the mirror plane of the molecule, a twisting mode of the methylene group in which the C is essentially stationary and the H's are displaced perpendicular to the mirror plane, a wagging mode in which all atoms are displaced perpendicular to the mir-

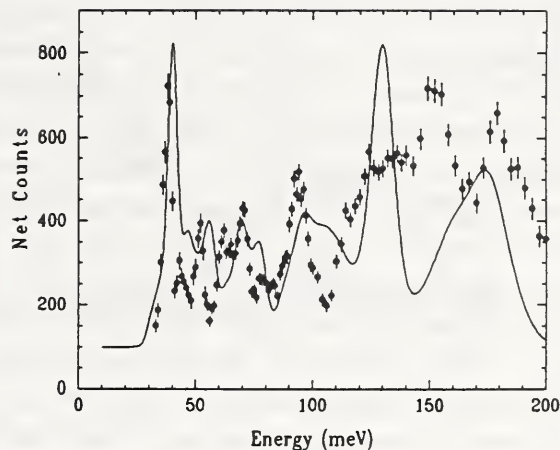


**Figure 10.** The spectrum of internal modes in  $C_{61}H_2$  at 10 K, measured with the BT-4 spectrometer operated as a filter analyzer spectrometer. The solid line is the result of a calculation described in the text.

ror plane with the motion of the C out of phase with the motion of the H's, and a H-C-H bending mode in which the H displacements are in the mirror plane and out-of-phase with each other, respectively. In a recent infrared study, Cardini *et al.* [2] assigned peaks at 37.7, 112.7, 152.5, and 178.3 meV respectively to the modes of the methylene group. The energies of 3 of these 4 peaks are in excellent agreement with the energies of the peaks we identify as being due to modes involving relatively large displacements of H atoms. The most probable explanation for the lone discrepancy is that the mode observed at 112.7 meV in the infrared spectrum is actually a shoulder on the very broad peak due to the methylene twisting mode which is centered at  $\sim 130$  meV (Fig. 10). The peaks observed between 40 and 100 meV are largely unchanged from those seen in  $C_{60}$ . Detailed assignments are difficult because each of these peaks is due to multiple modes of the  $C_{60}$  framework.

Since the inelastic neutron scattering cross section only depends on the known scattering cross sections of the atoms, and on the energies and eigenvectors of the modes, we can gain fur-

ther confidence in these assignments by directly comparing the results of dynamical calculations with the measured spectrum. The solid line in figure 10 represents a spectrum calculated with the program MOPAC using the AM1 Hamiltonian [3], convoluted with the known instrumental resolution function. The only adjustable parameters are an overall intensity scale and an average displacement of the atoms due to the lattice modes, assumed to be 0.1 Å in our calculations. Below ~100 meV there appears to be a one to one correspondence between peaks in the calculated and measured spectra. The principal problem is that the calculation somewhat overestimates the energies. The sharp peak at 40.1 meV in the calculation is the methylene rocking mode, confirming the assignment of the peak observed at 37.8 meV. Above 100 meV the situation is less satisfactory. In this region, the strongest peaks in the calculation are at 129.1, 130.3 (the methylene twisting mode), 160.6 (the methylene wag mode), and 175.7 meV (the H-C-H bending mode). The main problem is that the peaks at 129.1 and 130.3 meV are too close together and have too much intensity as compared with the peak at 160.6 meV. Work to resolve these discrepancies is in progress.

## References

- [1] A. N. Lommen, P. A. Heiney, G.B.M. Vaughan, P. W. Stephens, D. Liu, D. Li, A. L. Smith, A. R. McGhie, R. M. Strongin, L. Brard, and A. B. Smith III, *Phys. Rev. B* **49**, 12572 (1994).
- [2] G. Cardini, R. Bini, P. R. Salvi, V. Schettino, M. L. Klein, R. M. Strongin, L. Brard, and A. B. Smith III, *J. Phys. Chem.* **98**, 9966 (1994).
- [3] M.J.S. Dewar, E. G. Zoebisch, E. F. Healy, and J. P. Stewart, *J. Am. Chem. Soc.* **107**, 3902 (1985).

## Lattice and Molecular Dynamics of Poly (p-phenylene vinylene)

The discovery that conjugated organic polymers become highly conductive upon doping with various electron-donating or electron-accepting species initiated intensive research

in this field. Recently, increased attention has been focused on ring-containing non-degenerate ground state polymers, such as poly(*p*-phenylene vinylene) (PPV), because of their interesting electronic and nonlinear optical properties. Potential applications of PPV derivatives include light-emitting diodes and other polymer-based electronic devices.

PPV chains are composed of alternating phenylene rings ( $-\text{C}_6\text{H}_4-$ ) and vinylene segments ( $-\text{CH}=\text{CH}-$ ). The polymer can be synthesized in the form of free-standing air-stable films which exhibit a high degree of crystallinity. Whereas the simplest models envision a fully planar PPV molecule, the refinements of x-ray and neutron diffraction profiles of high-quality PPV films suggest a nonplanar thermal-average chain conformation as well as large amplitude phenylene-ring librations. Furthermore, the value of the average dihedral angle formed by the plane of the ring and the plane of the vinylene segment increases with temperature. This is particularly important, since the changes of the dihedral angle are closely related to the electronic properties of the polymer.

Inelastic neutron scattering (INS) experiments provide complementary information on the dynamic properties of PPV. Indeed, the measured INS spectra confirm significant phenylene-ring motions and librations, and also reveal low-frequency lattice vibrational modes that are not readily accessible by optical spectroscopic methods. The stretch-oriented PPV films used in the experiments were prepared by thermal conversion of stretched precursors. Two samples were employed: one was the all-hydrogen polymer, and the other was a partially deuterated PPV ( $\text{C}_6\text{H}_4\text{C}_2\text{D}_2$ )<sub>x</sub> in which ~70% of the vinylene hydrogens were replaced by deuterium. The c-axis mosaic of both films was determined to be about 10° (full width at half maximum).

The inelastic scattering data were obtained using the BT-4 filter-analyzer spectrometer with the low-pass Be/graphite filter. Two different scattering geometries were designed so that the

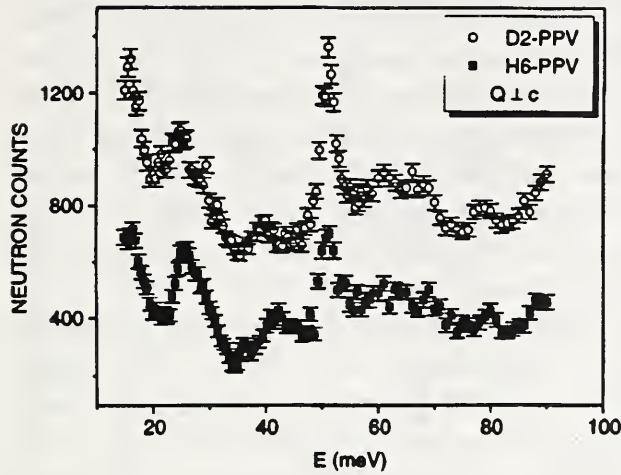


**Figure 11.** Spectra obtained in the  $Q \perp c$  configuration at 150 K. Solid squares correspond to the 720 mg all-hydrogen PPV sample; open circles to the 1050 mg vinylene-deuterated sample. The upper spectrum is offset by 300 counts for clarity.

wave-vector transfer  $Q$  was either perpendicular or parallel to the chain axis (the  $c$  axis) of the stretch-oriented polymer. Here we recall that the scattering function  $S_{\text{inc}}(\mathbf{Q}, \omega)$  depends on the product  $Q \cdot e_j^d(\mathbf{q})$ , where  $e_j^d(\mathbf{q})$  is the displacement vector of the  $d$ th hydrogen atom for the  $j$ th normal mode and phonon wave-vector  $\mathbf{q}$ . Thus, the FAS spectra measured in the  $Q \perp c$  ( $Q \parallel c$ ) configuration reflect the contribution of vibrational modes with displacements normal (parallel) to the chain axis.

Figure 11 shows the neutron scattering spectra of the fully-protonated “H6” and the vinylene-deuterated “D2” samples recorded in the  $Q \perp c$  configuration at 150 K. The two spectra are very similar and demonstrate that all of the strong vibrational features involve phenylene motions. Only the second peak at 25 meV has a higher relative intensity in H6 than in D2, suggesting non-negligible contributions of vinylene motions to this mode. In figure 12, the same 150 K spectrum for D2-PPV is compared with its  $Q \perp c$  analog. Mainly parallel features are observed near 40 and 80 meV, and the strong peaks found at 15, 25, and 51 meV correspond clearly to modes with perpendicular polarization.

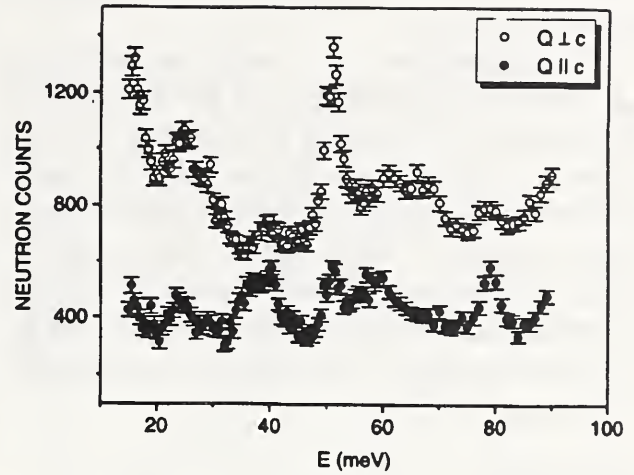


**Figure 12.** A comparison of the D2-PPV spectra obtained in the parallel (solid circles) and perpendicular (open circles) configuration at 150 K. The upper spectrum is offset by 300 counts for clarity.

The assignment of modes was based on polarization analysis, isotope substitution results, analogies to the dynamics of another ring containing polymer – polyaniline [6], and on the vibrational analysis of a single PPV chain with the force field derived by a semi-empirical Hartree-Fock calculation. The sharp peak at 51 meV is produced by the out-of-plane ring-bending vibration (a mode with  $A_u$  symmetry in para-disubstituted benzenes corresponding to the  $\nu_{16a}$  vibration of benzene). The broader structure between 60 and 70 meV is assigned to out-of-plane ring deformations (a “butterfly” mode) at 68 meV and in-plane circular motions of phenylene rings at 60 meV. The parallel mode near 80 meV involves longitudinal stretching and in-plane deformations of rings ( $q = 0$  optical phonon mode) and is also observed as a Raman line at 82.0 meV. The second parallel peak near 40 meV is attributed to the maximum of the density of longitudinal acoustic modes at the edge of the Brillouin zone. Finally, the two perpendicular features at 15 and 25 meV can be assigned to chain-torsional motions and whole-chain librations (possibly coupled with ring librations), respectively. The 25 meV peak also shows a pronounced anharmonic character and shifts to

lower frequency by  $\sim 2$  meV as the temperature increases by 150 K.

The inelastic neutron scattering technique can also be an interesting tool for determining the nature of PPV chains after doping. For instance,  $n$  doping (as in Na doped PPV) adds electrons to the chain and thus changes its electronic structure. This should affect the frequency of phenylene librations and out-of-plane ring deformations, which are readily observed by INS. Investigation in this direction is currently in progress.

## References

- [1] J. H. Burroughes, D. D. C. Bradley, A. R. Brown, R. N. Marks, K. Mackay, R. H. Friend, P. L. Burn, and A. B. Holmes, *Nature* **347**, 539 (1990).
- [2] C. Zhang, D. Braun, and A. J. Heeger, *J. Appl. Phys.* **73**, 5177 (1993).
- [3] G. Mao, J. E. Fischer, F. E. Karasz, and M. J. Winokur, *J. Chem. Phys.* **98**, 712 (1993).
- [4] H. S. Woo, O. Lhost, S. C. Graham, D. D. C. Bradley, R. H. Friend, C. Quattrocchi, J. L. Bredas, R. Schenk, and K. Mullen, *Synth. Met.* **59**, 13 (1993).
- [5] P. Papanek, J. E. Fischer, J. L. Sauvajol, A. J. Dianoux, G. Mao, M. J. Winokur, and F. E. Karasz, *Phys. Rev. B* **50**, 15668, (1994).
- [6] J. L. Sauvajol, D. Djurado, A. J. Dianoux, J. E. Fischer, E. M. Scherr, and A. G. MacDiarmid, *Phys. Rev. B* **47**, 4959 (1993).

## Isotope-Dilution Studies of H-H Interactions in Rare-Earth Hydrides

Over the past year, isotope-dilution neutron spectroscopy (IDNS) has been used to explore the subtleties of the different H-H interactions present in the rare-earth hydrides. For example, the broad, complex hydrogen density of states (DOS) resulting from the presence of significant dynamic H-H interactions in the tetrahedral ( $t$ ) sublattice of the stoichiometric rare-earth dihydrides is shown for  $YH_2$  and  $YD_2$  in figure 13. These bimodal spectra are typical of the fluorite-type dihydrides. Early lattice

dynamical modelling by Slaggie [1] attributed the width (*i.e.*, splitting) of these optical distributions to nearest-neighbor  $H_t$ - $H_t$  interactions. Figure 13 illustrates what happens to the DOS when one destroys the dynamical coupling interactions between neighboring  $H_t$  and  $D_t$  atoms by isotopically diluting these atoms in the  $t$  sublattice with their companion isotopes. For  $Y(H_{0.02}D_{0.98})_2$ , the majority of diluted  $H_t$  defect atoms are isotopically isolated, possessing only  $D_t$  host neighbors. Although  $H_t$ - $D_t$  interactions are still present, the dynamical manifestation of the interactions is prevented by the differences in isotopic mass, because the lighter  $H_t$  atoms cannot dynamically couple with the heavier vicinal  $D_t$  atoms. The same reasoning applies for  $Y(H_{0.9}D_{0.1})_2$ , where now the heavier  $D_t$  defect atoms are diluted in a predominantly  $H_t$  host sublattice. The spectroscopic result of an isotopically isolated atom is a collapse of the broad, complex DOS to a sharp, triply-degenerate, local-mode feature. The  $H_t$  and  $D_t$  defect mode energies found at 126.2 and 88.1 meV, respectively, are in general agreement with the predictions of simple mass defect theory [2].

The relatively high resolution of the  $D_t$  defect spectrum and the significant isotope fraction of  $D_t$  defect atoms (0.1) permitted us to measure the DOS contribution of those  $D_t$  defect atoms that reside as members of isolated  $D_t$ - $D_t$  pairs. Indeed, an expansion of the energy scale for the DOS of the  $D_t$  defects in  $Y(H_{0.9}D_{0.1})_2$  shown in figure 14 allows one to discern more clearly both higher- and lower-energy shoulders that roughly coincide with the major split features of the  $YD_2$  spectrum in figure 13. These shoulders are tentatively attributed to the local, axially-polarized, "acoustic" and "optic" vibrational modes of dynamically-coupled, nearest-neighbor  $D_t$ - $D_t$  defect pairs. This is reminiscent of the similar bimodal lineshapes observed previously [3,4] for the dynamically coupled  $D_t$ - $D_t$  and  $H_t$ - $H_t$   $c$ -axis-directed pairs present in  $\alpha$ - $YD_x$  and  $\alpha$ - $YH_x$ . A multicomponent gaussian fit of the  $D_t$ -defect spectrum locates the acoustic and optic modes at 85.7 and 90.8 meV, respectively,



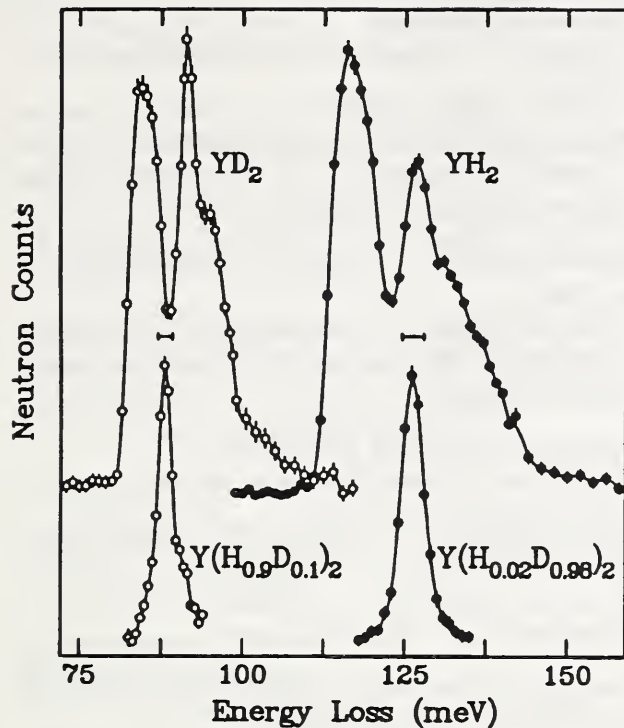


**Figure 13.** High-resolution vibrational spectra of  $\text{YD}_2$ ,  $\text{YH}_2$ ,  $\text{Y}(\text{H}_{0.9}\text{D}_{0.1})_2$ , and  $\text{Y}(\text{H}_{0.02}\text{D}_{0.98})_2$  below 10 K.

split by  $\approx 5$  meV. The vibrations of the  $\text{D}_t$  pair members in the other normal-mode directions perpendicular to the  $\text{D}_t$ - $\text{D}_t$  axis (assuming that there are no nearest-neighbor  $\text{D}_t$  atoms in these directions) are considered to be identical to the vibrations of isolated  $\text{D}_t$  defects and contribute to the central feature at 88.1 meV. Applying a simple, one-dimensional, coupled-harmonic oscillator model similar to that used previously to analyze the spectroscopic splitting of  $c$ -polarized  $\text{H}_t$  vibrations in  $\alpha\text{-YH}_x$ , [3] one obtains a calculated  $\text{D}_t$ - $\text{D}_t$  coupling constant that is  $\sim 6\%$  as large as the Y-D force constant, which is consistent with the value determined from analysis of the phonon-dispersion-curve data for single-crystal  $\text{CeD}_{2.12}$  [5].

This study, in particular, illustrates the capability of IDNS to investigate the behavior of heavy mass defects in an otherwise purely hydrided material, which to our knowledge has not previously been attempted due to much larger

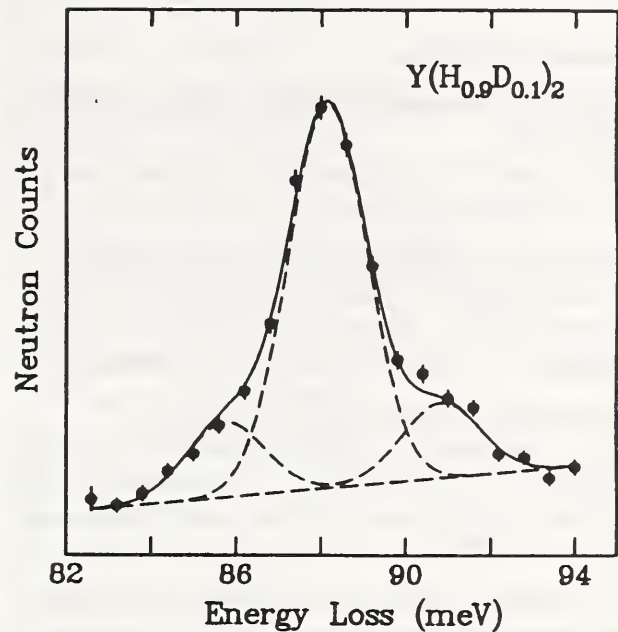


**Figure 14.** Multicomponent gaussian fit (solid curve) of the high-resolution,  $\text{D}_t$ -defect-mode, vibrational spectrum for  $\text{Y}(\text{H}_{0.9}\text{D}_{0.1})_2$ . All peaks were constrained to have the same widths and the components of the doublet were constrained to have the same intensity. Individual features are indicated by the dashed curves. The central peak represents isolated  $\text{D}_t$  atom vibrations; the doublet represents the acoustic and optic components of  $\text{D}_t$ - $\text{D}_t$  pair vibrations.

neutron-scattering cross section for H compared to D. This capability should have many applications in future studies of metal hydride and hydrogenous molecular systems.

## References

- [1] E. L. Slaggie, *J. Phys. Chem. Solids* **29**, 923 (1968).
- [2] T. J. Udovic, J. J. Rush, and I. S. Anderson, *Phys. Rev.* **B50**, 15739 (1994).
- [3] I. S. Anderson, N. F. Berk, J. J. Rush, and T. J. Udovic, *Phys. Rev.* **B37**, 4358 (1988).
- [4] I. S. Anderson, J. J. Rush, T. Udovic, and J. M. Rowe, *Phys. Rev. Lett.* **57**, 2822 (1986).
- [5] C. J. Glinka, J. M. Rowe, J. J. Rush, G. G. Libowitz, and A. Maeland, *Solid State Commun.* **22**, 541 (1977).

## Research Topics

### Quantifying Freezable Water In Portland Cement Paste

D. L. Gress<sup>22</sup>, T. El-Korchi<sup>23</sup>, D. A. Neumann<sup>16</sup>, R. A. Livingston<sup>24</sup>, and J. J. Rush<sup>16</sup>

### Rotational Dynamics of C<sub>61</sub>H<sub>2</sub> and C<sub>61</sub>D<sub>2</sub>

J. E. Fischer<sup>15,16</sup>, D. A. Neumann<sup>16</sup>, J.R.D. Copley<sup>16</sup>, P. A. Heiney<sup>15</sup>, J. J. Rush<sup>16</sup>, R. M. Strongin<sup>15</sup>, L. Brard<sup>15</sup>, and Amos B. Smith III<sup>15</sup>

### Intramolecular Dynamics of C<sub>61</sub>H<sub>2</sub>

D. A. Neumann<sup>16</sup>, J. E. Fischer<sup>15,16</sup>, J. R. D. Copley<sup>16</sup>, P. A. Heiney<sup>15</sup>, J. J. Rush<sup>16</sup>, J. E. Fischer<sup>15</sup>, R. M. Strongin<sup>15</sup>, L. Brard<sup>15</sup>, and Amos B. Smith III<sup>15</sup>

### Low Energy Dynamics of Doped Poly(p-phenylene vinylene)

P. Papanek<sup>15</sup>, J. E. Fischer<sup>15,16</sup>, J. L. Sauvajol<sup>18</sup>, A. J. Dianoux<sup>19</sup>, G. Mao<sup>19</sup>, M. J. Winokur<sup>19</sup>, and F. A. Karasz<sup>21</sup>

### Intramolecular Dynamics of Doped Poly(p-phenylene vinylene)

P. Papanek<sup>15</sup>, J. E. Fischer<sup>15,16</sup>, J. L. Sauvajol<sup>18</sup>, A. J. Dianoux<sup>19</sup>, G. Mao<sup>19</sup>, M. J. Winokur<sup>19</sup>, and F. A. Karasz<sup>21</sup>

### Neutron Scattering Study of the Lattice Modes of Solid Cubane C<sub>8</sub>H<sub>8</sub>

P. M. Gehring<sup>16</sup>, D. A. Neumann<sup>16</sup>, W. A. Kamitakahara<sup>16</sup>, J. J. Rush<sup>16</sup>, P. E. Eaton<sup>6</sup>, and D. P. VanMeurs<sup>6</sup>

### Intramolecular Dynamics of C<sub>60</sub>-piperazine

A. K. Qasba<sup>14</sup>, D. A. Neumann<sup>16</sup>, J. E. Fischer<sup>15,16</sup>, A. Smith<sup>2</sup>, and P. Klosowski<sup>8</sup>

### Rotational Dynamics of Na<sub>x</sub>C<sub>60</sub>

D. Reznik<sup>8</sup>, D. A. Neumann<sup>16</sup>, J. E. Fischer<sup>15,16</sup>, T. Yildirim<sup>15,16</sup>, and J. R. D. Copley<sup>16</sup>

### Intramolecular Vibrations in C<sub>60</sub>

W. A. Kamitakahara<sup>16</sup>, J. R. D. Copley<sup>16</sup>, D. A. Neumann<sup>16</sup>, R. L. Cappelletti<sup>17</sup>, and J. J. Rush<sup>16</sup>

### Dynamics and Molecular Spectroscopy of 134 and 134a Hydrofluorocarbons Encaged in Na-X Zeolite

T. J. Udovic<sup>16</sup>, J. M. Nicol<sup>16</sup>, R. R. Cavanagh<sup>11</sup>, J. J. Rush<sup>16</sup>, M. K. Crawford<sup>10</sup>, C. Grey<sup>10</sup>, and D. R. Corbin<sup>10</sup>

### Tunnelling Spectroscopy of Dihydrogen in IrIh<sub>2</sub>(μ-H<sub>2</sub>)(PiPr<sub>3</sub>)<sub>2</sub>

J. Eckert<sup>12</sup>, C. Jenson<sup>13</sup>, J. M. Nicol<sup>16</sup>, and T. J. Udovic<sup>16</sup>

### Dynamics of Benzene in Si-Y Zeolite

L. Bull<sup>25</sup>, R. Morris<sup>25</sup>, A. K. Cheetham<sup>25</sup>, D. A. Neumann<sup>16</sup>, and J. M. Nicol<sup>16</sup>

### High-Frequency Phonon Dispersion in La<sub>1.85</sub>Sr<sub>0.15</sub>

A. H. Moudden<sup>1</sup>, P. M. Gehring<sup>16</sup>, B. Hennion<sup>1</sup>, M. Matsuda<sup>3</sup>, G. Shirane<sup>3</sup>, Y. Endoh<sup>4</sup>, I. Tanaka<sup>5</sup>, and H. Kojima<sup>5</sup>

### Hydrogen Dynamics in NaNH<sub>2</sub>

F. Altorfer<sup>8</sup>, J. Senker<sup>9</sup>, and H. Jacobs<sup>9</sup>

### Anharmonicity of the Soft Ferroelectric Modes in PbTiO<sub>3</sub>

P. M. Gehring<sup>16</sup>, D. A. Neumann<sup>16</sup>, and C. M. Foster<sup>7</sup>

### Polarized Vibrational Density of States of Alkali-Doped Polyacetylene

P. Papanek<sup>15</sup>, J. E. Fischer<sup>15</sup>, J. L. Sauvajol<sup>18</sup>, P. MacNellis<sup>44</sup>, and Claude Mathis<sup>44</sup>

### Inelastic Neutron Scattering Study of β-Tb(H<sub>y</sub>D<sub>1-y</sub>)<sub>2+x</sub> (0 ≤ x ≤ 0.25)

T. J. Udovic<sup>16</sup>, J. J. Rush<sup>16</sup>, and I. S. Anderson<sup>19</sup>

### Inelastic Neutron Scattering Study of La(H<sub>y</sub>D<sub>1-y</sub>)<sub>2+x</sub> (0 ≤ x ≤ 1)

T. J. Udovic<sup>16</sup>, J. J. Rush<sup>16</sup>, I. S. Anderson<sup>19</sup>

### Local-Mode Dynamics in YH<sub>2</sub> and YD<sub>2</sub> by Isotope Dilution Neutron Spectroscopy

T. J. Udovic<sup>16</sup>, J. J. Rush<sup>16</sup>, and I. S. Anderson<sup>19</sup>

### Inelastic Neutron Scattering Study of YH<sub>3</sub> and YD<sub>3</sub>

T. J. Udovic<sup>16</sup> and J. J. Rush<sup>16</sup>

### Dynamics of Hydrogen in Nanocrystalline Palladium

U. Stuhr<sup>26,27</sup>, H. Wipf<sup>26</sup>, T. J. Udovic<sup>16</sup>, J. Weißmüller<sup>28</sup>, and H. Gleiter<sup>28</sup>

### Inelastic Neutron Scattering Study of the Nb-H(D) Phase Diagram

B. Hauer<sup>27</sup>, R. Hempelmann<sup>28</sup>, D. Richter<sup>29</sup>, T. J. Udovic<sup>16</sup>, and J. J. Rush<sup>16</sup>

### Excited-State Tunnel Splitting in Nb(TiH)<sub>x</sub>

B. Hauer<sup>29</sup>, R. Hempelmann<sup>28</sup>, D. Richter<sup>29</sup>, T. J. Udovic<sup>16</sup>, and J. J. Rush<sup>16</sup>

**Dynamics of Partially-Deuterated  $\text{H}_5\text{O}_2^+$  Ions in  $(\text{H}_5\text{O}_2)_3\text{PW}_{12}\text{O}_{40}$**

T. J. Udovic<sup>16</sup> and J. M. Nicol<sup>16</sup>

**Inelastic Neutron Scattering Study of the Interaction of Hydrogen with Ir Clusters in Zeolites**

J. M. Nicol<sup>16</sup>, T. J. Udovic<sup>16</sup>, R. R. Cavanagh<sup>11</sup>, Z. Xu<sup>30,31</sup>, S. Kawi<sup>30,31</sup>, T. Mure<sup>30,31</sup>, and B. C. Gates<sup>30,31</sup>

**Dynamics of Hydrogen in  $\alpha$ - $\text{LaNi}_5$  Hydride**

C. Schönfeld<sup>29</sup>, R. Hempelmann<sup>28</sup>, D. Richter<sup>29</sup>, T. Springer<sup>29</sup>, A. J. Dianoux<sup>19</sup>, J. J. Rush<sup>16</sup>, T. J. Udovic<sup>16</sup>, and S. M. Bennington<sup>32</sup>

**Dynamics of  $\mu^+$  in Sc and  $\alpha$ - $\text{ScH}_x$**

F. N. Gygax<sup>33</sup>, A. Amato<sup>33</sup>, R. Feyerherm<sup>33</sup>, A. Schenck<sup>33</sup>, I. S. Anderson<sup>19</sup>, T. J. Udovic<sup>16</sup>, J. J. Rush<sup>16</sup>, and G. Solt<sup>34</sup>

**Orientalional Dynamics of  $\text{P}_4$  molecules in White Phosphorus**

W. A. Kamitakahara<sup>16</sup>, D. A. Neumann<sup>16</sup>, F. Gompf<sup>35</sup>, and Q. Huang<sup>8</sup>

**Vibrational Densities of States for Chalcogenide Glasses**

R. L. Cappelletti<sup>17</sup>, D. Islam<sup>36</sup>, and W. A. Kamitakahara<sup>16</sup>

**Vibrational Densities of States for Cubic and Hexagonal Boron Nitride**

W. A. Kamitakahara<sup>16</sup>, D. A. Neumann<sup>16</sup>, G. Doll<sup>37</sup>, B. Sweeting<sup>38</sup>, and A. W. Moore<sup>39</sup>

**Dynamics of Polymer Glasses**

J. Colmenero<sup>40</sup>, A. Arbe<sup>40</sup>, B. Frick<sup>19</sup>, and S. F. Trevino<sup>41</sup>

**Conformational Diffusion in Liquid Crystalline Copolymer Melts**

C. K. Loong<sup>7</sup>, C. K. Saw<sup>42</sup>, G. L. Collins<sup>42</sup>, and T. J. Udovic<sup>16</sup>

**Shear Elastic Constants for Li-Graphite Compounds**

J. E. Fischer<sup>15</sup> and W. A. Kamitakahara<sup>16</sup>

**Measurement of the Phonon Density of States in Various Energetic Materials**

S. F. Trevino<sup>41</sup> and L. Fried<sup>43</sup>

<sup>4</sup>Tohoku University

<sup>5</sup>Yamanashi University

<sup>6</sup>University of Chicago

<sup>7</sup>Argonne National Laboratory

<sup>8</sup>University of Maryland

<sup>9</sup>University of Dortmund

<sup>10</sup>E. I. DuPont

<sup>11</sup>Surface & Microanalysis Division

<sup>12</sup>Los Alamos National Laboratory

<sup>13</sup>University of Hawaii

<sup>14</sup>Montgomery Blair High School

<sup>15</sup>University of Pennsylvania

<sup>16</sup>Reactor Radiation Division

<sup>17</sup>Ohio University

<sup>18</sup>Université Montpellier II

<sup>19</sup>Institute Laue-Langevin

<sup>20</sup>University of Wisconsin

<sup>21</sup>University of Massachusetts

<sup>22</sup>University of New Hampshire

<sup>23</sup>Worcester Polytechnic Institute

<sup>24</sup>Office of Advanced Research, FHWA

<sup>25</sup>University of California, Santa Barbara

<sup>26</sup>Technische Hochschule Darmstadt

<sup>27</sup>Hahn-Meitner Institut Berlin

<sup>28</sup>Universität des Saarlandes

<sup>29</sup>Institut für Festkörperforschung

<sup>30</sup>University of Delaware

<sup>31</sup>University of California, Davis

<sup>32</sup>Rutherford Appleton Laboratory

<sup>33</sup>Eidg. Technische Hochschule Zürich

<sup>34</sup>Paul Scherrer Institut

<sup>35</sup>Karlsruhe Nuclear Research Center

<sup>36</sup>Central Michigan University

<sup>37</sup>General Motors NAO R&D Center

<sup>38</sup>General Electric Corp. Res. and Dev.

<sup>39</sup>Advanced Ceramics Corp.

<sup>40</sup>Universidad del Pais Vasco

<sup>41</sup>U.S. Army Res., Dev., and Eng. Ctr.

<sup>42</sup>Hoechst Celanese Corp.

<sup>43</sup>Lawrence Livermore National Laboratory

<sup>44</sup>Laboratoire Ch. Sadron

**Affiliations**

<sup>1</sup>Laboratoire Léon Brillouin

<sup>2</sup>Drexel University

<sup>3</sup>Brookhaven National Laboratory

# Magnetism and Superconductivity

Research in these general areas covers a wide range of topics this year, although it is interesting to note that a considerable amount of effort has been devoted to systems that are both magnetic *and* superconducting. Following are some highlights; the research topics section provides an idea of the breadth of the ongoing work.

## Heavy Fermion-Type Systems

One of the areas of particular interest this year concerns the spin dynamics of materials that belong to the heavy-fermion class of systems. The first material we discuss is YbBiPt, which is a newly discovered heavy fermion system that has an enormous linear specific-heat coefficient,  $\gamma = 8\text{J/mol-K}^2$ , an order of magnitude more than that of typical heavy fermion compounds and three orders of magnitude more than that of conventional metals. YbBiPt was reported to form the MgAgAs structure type (space group  $F\bar{4}3m$ ), which is a common Heusler-alloy structure. Powder diffraction data by Robinson *et al.* [1] obtained both at NIST and elsewhere resolved the ambiguities in the crystal structure, showing that none of the sites are chemically disordered in this material. In addition, there is a phase transition at 400 mK that is thought to be magnetic in origin. We therefore carried out powder diffraction experiments in a dilution refrigerator with a low temperature capability of  $\sim 50$  mK. We did not observe the development on any long range magnetic order, and our data place an upper limit of  $0.25 \mu_B$  on any ordered moment that develops below 400 mK. We have also searched at low temperatures for displacements or splittings of crystallographic peaks that might indicate a distortion from the cubic structure, and have found no such evidence. Thus the nature of this 400 mK transition remains a mystery.

The enormous specific heat is of course directly related to the excitations in the system, and the nature of these excitations can

be probed with inelastic neutron scattering. YbBiPt has previously been characterized by means of electrical resistivity, magnetoresistance, *ac* and *dc* magnetic susceptibility and specific heat measurements. In order to explain these data, it was suggested that the cubic crystal field splits the  $4f_{7/2}$  Yb<sup>3+</sup> Hund's rule state into two doublets ( $\Gamma_7$  and  $\Gamma_6$ , split by  $\sim 1$  meV), and a  $\Gamma_8$  quartet, in that order. Earlier inelastic work at higher temperatures (above 1.5 K) showed that there is a crystal-field degeneracy at low energies and that the ground state may best be thought of as comprising both the  $\Gamma_7$  doublet and the  $\Gamma_8$  quartet. Both levels are intrinsically broadened, and the inelastic response can be fit fairly well by a two-component Gaussian quasielastic response, the narrow Gaussian ( $\Gamma_7$ ) having a width of  $\sim 0.4$  meV and the broad Gaussian ( $\Gamma_8$ ) a width of  $\sim 1.4$  meV. The purpose of the present inelastic experiments was to study this response to lower temperatures, down to 350 mK using a <sup>3</sup>He cryostat on the cold-neutron time-of-flight diffractometer in the guide hall.

We took data utilizing incident energies of  $E_i = 4.5$  meV and 2.7 meV. The measured elastic resolution after summing over all detectors was  $280 \mu\text{eV}$  FWHM at  $E_i = 4.5$  meV and  $110 \mu\text{eV}$  FWHM at 2.7 meV. Data were collected at 10 K, as well as above (450 mK) and below (350 mK) the 400 mK transition. However, there was no detectable difference between these latter sets of data and they were simply summed in the following discussion; the sum is denoted by T = 400 mK. The data are shown in figure 1. The 10 K data in figure 1(a) show the two component response observed previously, but at 400 mK some structure appears in the broad magnetic response, as shown in figure 1(b). There are clearly two discrete inelastic levels at approximately 1 and 2 meV. Within a conventional crystal-field description, this must correspond to some external field splitting of the  $\Gamma_8$  quartet,

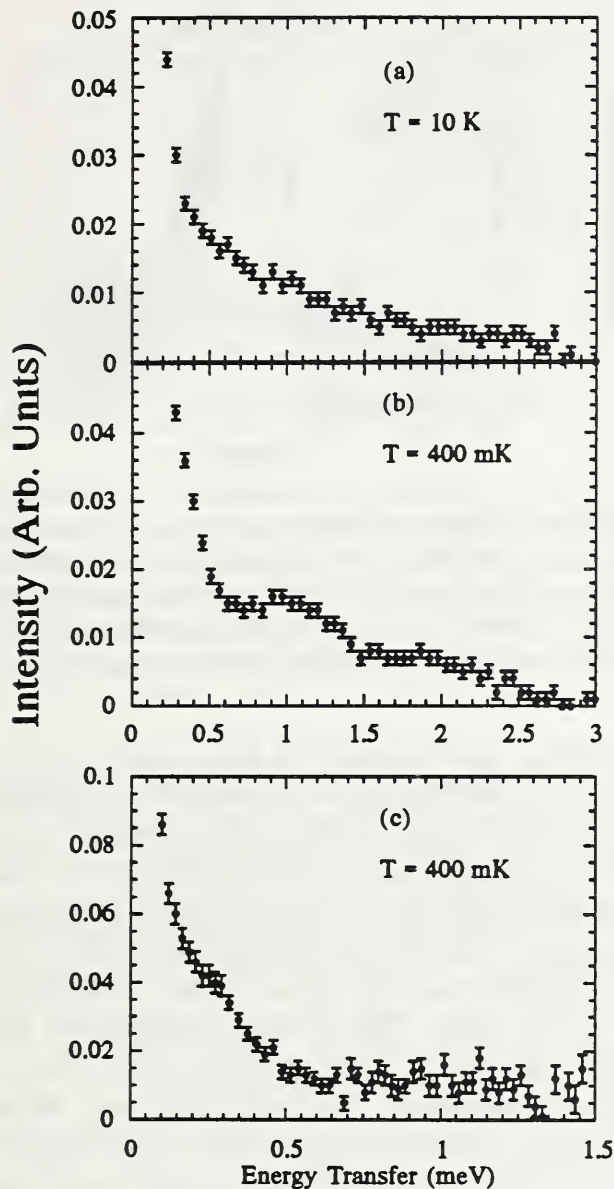


**Figure 1.** Observed time-of-flight spectra from Yb-BiPt, taken on the cold-neutron time-of-flight spectrometer, (a) at 10 K using  $E_i = 4.5$  meV, (b) the sum of data at 350 mK and 450 mK using  $E_i = 4.5$  meV and (c) the sum of data at 350 mK and 450 mK using  $E_i = 2.7$  meV.

as this is the only unresolved degeneracy in the problem. In order to study the “true” quasielastic response, measurements were also made with higher resolution, as shown in figure 1(c). In this case, the quasielastic response below 0.5

meV is better fit using a Gaussian rather than a Lorentzian lineshape, indicating that a conventional single-site Kondo picture is inappropriate and that the magnetic fluctuations involve intersite correlations. However, there are still significant deviations from the assumed Gaussian response, and there is some evidence for a more divergent response at still lower energies. Experiments with even higher resolution would clearly be desirable to pursue this low energy dynamic response.

The electronic specific heat can be calculated from the measured inelastic response using a generalized Schottky-model approach and the broadened levels that we observe. This gives agreement with the bulk specific heat  $\gamma$  to within 25% or so. If we assume the two inelastic levels shown in figure 1(b) together with the observed temperature-dependent line broadening, all the qualitative features in the specific heat are reproduced. Thus it seems that roughly half of the electronic specific heat is due to broadening of the  $\Gamma_7$  doublet level (with a Kondo temperature of roughly 2.2 K), and the other half is due to the presence of the low-lying  $\Gamma_8$  levels.

## Non-Fermi Liquids

Fermi liquid theory (FLT) is fundamental to our understanding of the nature of electronic excitations in metals, as it establishes a one-to-one correspondence between the excitations of a free electron gas and those of real interacting conduction electrons in metals. One of the central premises of FLT is the existence of a single energy scale, the Fermi energy  $E_F$ , whereby for energies  $E \ll E_F$  and temperatures  $kT \ll E_F$  the electronic properties exhibit universal behavior. In heavy fermion systems such as the material just discussed, the low temperature properties do indeed exhibit a dependence on a single energy scale as expected for a Fermi liquid, but with enormous enhancements of the effective mass of the electrons. However, recently a new class of compounds has been discovered that exhibits low temperature properties inconsistent with con-

ventional Fermi liquid theory. The  $\text{UCu}_{5-x}\text{Pd}_x$  alloy belongs to this new class of materials, and has the attractive property that all  $x$  share the common  $\text{AuBe}_5$  crystal structure. The parent  $\text{UCu}_5$  compound is a prototypical Kondo lattice antiferromagnet with a Néel temperature of 15 K and a Kondo temperature of  $\sim 80$  K as inferred from the observed quasielastic linewidth. With Pd doping the antiferromagnetic order is quickly suppressed, and the low temperature thermal and transport measurements exhibit remarkable temperature and magnetic field scaling properties that are manifestly non-Fermi liquid like. The nature of the magnetic excitations has been investigated for samples with  $x = 1$  and  $x = 1.5$  by Aronson *et al.*, [2] where no magnetic long range order of any kind is found.

The inelastic neutron scattering measurements were carried out in a  $\text{He}^3$  cryostat on the time-of-flight spectrometer to elucidate the underlying frequency and temperature dependence of the excitation spectrum associated with these unique scaling properties. The low energy portion of the magnetic fluctuation spectrum is shown in figure 2. The scattering on the energy loss side ( $E > 0$ ) exhibits a unique insensitivity to the temperature, while the scattering on the energy gain side ( $E < 0$ ) increases with increasing temperature in accordance with detailed balance. This lack of temperature dependence on the energy loss side suggests that the electrons in this material form a novel non-Fermi-liquid electronic ground state. Inelastic measurements [2] extending to much higher energies reveal that there does not appear to be a unique energy scale, also in contradiction to the FLT hypothesis. This scale-invariant magnetic excitation spectrum is suggestive of the absence of a well defined Fermi energy in this class of materials.

### Spin Dynamics of Finite-Size Chains

Quasi-one-dimensional  $S = 1$  antiferromagnets that do not exhibit long range order at low temperatures are unique in the world of magnets. In such systems strong fluctuations pre-

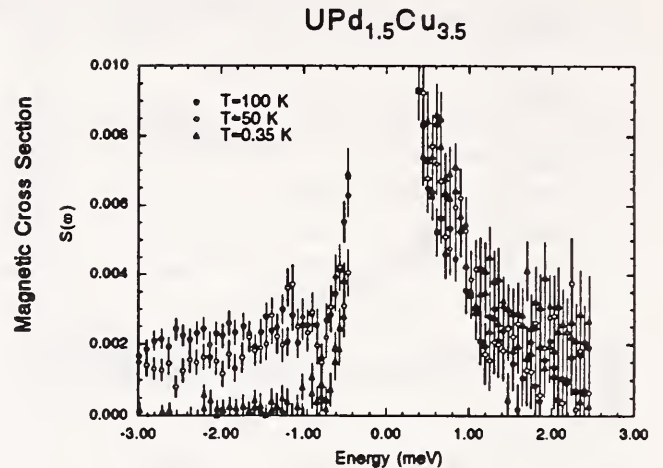


**Figure 2.** High resolution measurement of the magnetic excitations in  $\text{UPd}_{1.5}\text{Cu}_{3.5}$ . The intensity on the energy-loss side ( $E > 0$ ) is temperature independent, while the scattering on the energy gain side ( $E < 0$ ) follows the detailed balance factor.

vent the establishment of long range order as  $T \rightarrow 0$ , and induce a quantum liquid ground state with a Haldane gap in the excitation spectrum. In the past the only examples of such magnets were found among organic insulators. Recently, however, a transition metal oxide with this special low temperature phase,  $\text{Y}_2\text{BaNiO}_5$ , was discovered. The crucial importance of this new material is that, in contrast to the organic insulators, it can be appropriately doped to introduce free charge carriers in the material. Such doping creates a simple yet truly novel condensed matter system—charge carriers interacting with a quantum spin liquid—that is not only unique and interesting in its own right but also has many similarities to the cuprate superconductors.

$\text{Y}_2\text{BaNiO}_5$  is orthorhombic, with the  $\text{Ni}^{2+}$  ( $S = 1$ ) ions residing in the interstices of corner-sharing oxygen octahedra. The chains are magnetically isolated from each other by  $\text{Y}^{3+}$  and  $\text{Ba}^{2+}$  ions, and form chains where nearest-neighbor spins are coupled antiferromagnetically. Two types of doping are then possible. One type is to dope directly on the chains, substituting  $\text{Zn}^{2+}$  for  $\text{Ni}^{2+}$  to form the alloy

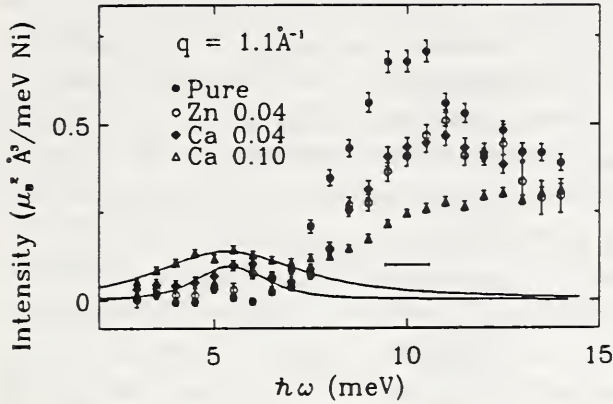


**Figure 3.** Background subtracted and normalized inelastic magnetic neutron scattering from  $\text{Y}_2\text{BaNiO}_5$ ,  $\text{Y}_2\text{BaNi}_{0.96}\text{Zn}_{0.04}\text{O}_5$ ,  $\text{Y}_{1.96}\text{Ca}_{0.04}\text{BaNiO}_5$  and  $\text{Y}_{1.9}\text{Ca}_{0.1}\text{BaNiO}_5$  at a wave-vector transfer  $Q=1.1\text{\AA}^{-1}=1.3\pi/a$ . The energy resolution is indicated by the horizontal bar at  $\hbar\omega=10$  meV.

$\text{Y}_2\text{BaNi}_{1-y}\text{Zn}_y\text{O}_5$ . The superexchange interaction that operates through the non-magnetic  $\text{Zn}^{2+}$  is negligible, and thus the spin chains separate into segments with an average length  $1/y$ . The second type of doping occurs when  $\text{Y}^{3+}$  is substituted by  $\text{Ca}^{2+}$  to form  $\text{Y}_{2-x}\text{Ca}_x\text{BaNiO}_5$ . In this case  $S = 1/2$  holes are placed on the  $(\text{NiO}_5)^{8-}$  chains, with an average separation  $1/x$ . Polarized soft x-ray absorption spectroscopy has shown that the holes reside primarily on the corner-shared oxygen, which likely causes a modification of the superexchange interaction mediated through that oxygen atom. Resistivity data also indicate that the holes are mobile along the spin chain.

A comparative study of how the quantum spin liquid of the parent compound is affected by each of these perturbations has been undertaken by DiTusa *et al.* [3]. The results are summarized in figure 3, which shows the intensity of inelastic magnetic neutron scattering as a function of energy transfer for four different powder specimens. These scans probe the spherically-averaged dynamic spin correlation function  $\tilde{S}(Q,\omega)$ . In order to be sensitive to modifications in the low energy response,

the wave-vector transfer  $Q=1.3\pi/a$  was chosen so that  $\tilde{S}(Q,\omega)=(1/4)\int_0^1 du\sqrt{1-u^2}S(u,Q,\omega)$  is dominated by antiferromagnetic fluctuations, with wave-vector transfer  $\pi/a$  along the chain.

In the pure compound (filled circles in Fig. 3)  $\tilde{S}(Q,\omega)$  vanishes below 9 meV. This Haldane gap in the excitation spectrum is the defining feature of the one-dimensional  $S = 1$  quantum spin-liquid. For  $\hbar\omega \approx 10$  meV,  $\tilde{S}(Q,\omega)$  has a pronounced peak associated with the creation of weakly interacting massive bosons.

In the Zn-doped compound (open circles in Fig. 3) we see that spectral weight is shifted to higher energies, while the low energy range remains free of magnetic excitations. This is a simple consequence of reducing the average chain length to  $1/y = 25$ . That this trend is correct may be appreciated by considering the case of a “chain” of just two spins; the gap in this case just equals the exchange constant and thus the scattering occurs at high energies. The spin degrees of freedom associated with the ends of the finite spin chains, on the other hand, are not apparent in the data. These end effects give rise to a “Curie tail” in the low temperature susceptibility, but we expect that the corresponding magnetic scattering directly associated with the impurities resides below the range of energies that could be resolved in this experiment.

For the hole-doped compound (filled diamonds and triangles in Fig. 3), where a modulation in superexchange is caused by the holes, the same finite size effects as for the Zn doping are observed at higher energies. Below the Haldane gap, on the other hand, the behavior is quite different; there is a resonance that develops at approximately half of the Haldane gap energy. Constant-energy cuts through  $\tilde{S}(Q,\omega)$  reveal that the structure factor of the resonant mode resembles that of the quantum spin liquid itself. Reducing the average hole spacing to  $1/x = 10$  (triangles in Fig. 3) does not shift this resonance nor does it change the relative spectral weights, but it does lead to broadening both in  $Q$  and  $\omega$ , indicating that impurity interactions become significant at this level of

doping. It is interesting to note that this occurs as the average impurity separation approaches the equal time correlation length ( $\xi \approx 6$ ) in the parent quantum spin-liquid.

The simplest model for the hole-doped compound would treat the holes as static perturbations in the superexchange. In the analogous phonon problem a localized perturbation of interactions leads to a bound state or localized "optical" mode. It is presently not clear whether a static impurity model would provide an adequate description of the system, or whether the hole mobility is instrumental in creating the sub-gap resonance. It also remains to be seen whether hole transport is affected by the unusual nature of the magnetic excitations in the parent compound. It is fortunate that in one dimension detailed analysis of realistic models is possible. Such calculations as well as further experiments on single crystal samples will be required to understand the origin of the sub-gap resonance in a hole-doped quantum spin liquid.

### Magnetic Order in Superconductors

The interplay between the competing effects of superconductivity and magnetism remains at the forefront of research into the microscopic mechanisms underlying these ordered states of matter. In the well-known ferromagnetic systems  $\text{ErRh}_4\text{B}_4$  and  $\text{HoMo}_6(\text{S,Se})_8$  such coupling manifests itself in the appearance of an oscillatory magnetic state ( $T \sim 1$  K), often as a precursor to ferromagnetism, which then extinguishes the superconductivity at low temperatures. More common for these ternary systems is the coexistence of antiferromagnetism and superconductivity, where anomalies in  $H_{c2}$  are often observed near  $T_N$ . The newly discovered rare-earth quaternary nickel boron carbide systems are ideal candidates for study as they represent a new class of non-cuprate high- $T_c$  superconductors which exhibit coupling of the rare-earth moments with the superconducting order parameter. The relatively high temperature scale of the magnetism necessitates that exchange interactions dominate the energetics.

The most interesting material appears to be  $\text{HoNi}_2\text{B}_2\text{C}$ , which becomes superconducting at  $\sim 7.5$  K, reenters the normal conducting state at 5 K, and quickly recovers superconductivity at lower temperature. The diffraction measurements carried out by Grigereit *et al.* [4] show that the magnetic order that first forms on cooling is oscillatory in nature, and is directly coupled to the superconducting order parameter. In contrast to previously known systems, however, this oscillatory state is detrimental to superconductivity, and the superconducting state only survives at low temperatures because of a first-order transition to a compensated antiferromagnetic state.

We start our description of the magnetism by considering the magnetic ground state. The Ho magnetic structure consists of ferromagnetic sheets of spins in the  $a$ - $b$  plane, with the sheets coupled antiferromagnetically along the tetragonal  $c$ -axis. The ordered moment is  $8.7 \pm 0.2 \mu_B$ , substantially below the free-ion value of  $10 \mu_B$ , indicating that crystal field effects are important, and inelastic measurements reveal that the first two excited crystal field states are at 11.3 meV and 16.0 meV. Thus in the ordered magnetic state the Ho ions are predominantly in the crystal field ground state, which is a doublet. In addition, field-dependent diffraction measurements show that the moments strongly prefer to lie in the  $a$ - $b$  plane and indeed it is quite easy to produce a sample with the  $c$ -axis aligned perpendicular to the field direction by the application of modest fields at low temperatures. Thus an  $xy$  model with four-fold anisotropy would be suitable to describe the moments at low  $T$ . For the exchange interactions an anisotropic three-dimensional exchange model is likely appropriate, with ferromagnetic exchange in the  $a$ - $b$  plane and a weaker antiferromagnetic exchange being mediated through the Ni layers.

Upon cooling from the paramagnetic state, on the other hand, the magnetic state which first forms is oscillatory in nature. In particular, satellite peaks are observed on either side of the fundamental antiferromagnetic Bragg reflec-



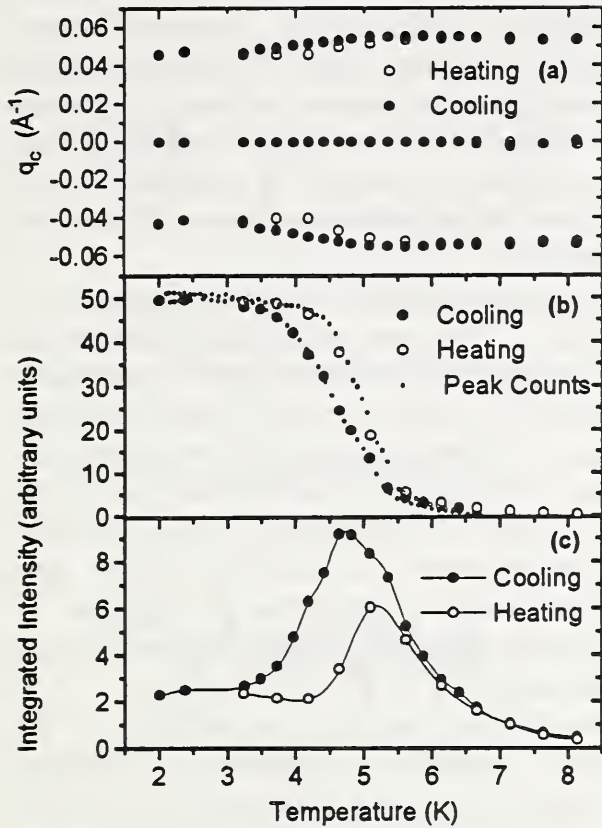


**Figure 4.** Magnetic Ordering in  $\text{HoNi}_2\text{B}_2\text{C}$ . (a) Spiral satellite positions as a function of temperature, (b) antiferromagnetic Bragg intensity vs.  $T$ , and (c) oscillatory intensity vs.  $T$ .

tions. Based on a detailed comparison of  $\sim 30$  satellites the modulation wave vector is found to be along the  $c$ -axis, with the moments being transversely polarized with respect to the oscillatory wave vector  $(0,0,q_c)$ . This wave vector is essentially temperature independent above  $\sim 5$  K as shown in figure 4(a), with  $q_c = 0.0543 \text{ \AA}^{-1}$  which corresponds to a wavelength  $\lambda = 2\pi/q_c = 115.7 \text{ \AA}$ , or about eleven unit cells along the  $c$ -axis.  $q_c$  is only weakly temperature dependent below 5 K and is also field independent. In view of the propensity of the moments to lie in the  $a$ - $b$  plane and the net ferromagnetic interactions within these planes, the most likely model to describe the oscillation is a spiral in which the ferromagnetic planes rotate from layer to layer

along the  $c$ -axis, with a turn angle of  $16.4^\circ$  away from the antiparallel direction for each holmium layer. We also observe a commensurate antiferromagnetic peak in addition to the satellites. If these two types of peaks are coming from the same regions of the sample then the full magnetic structure would be the coherent superposition of these two structures; above  $\sim 5$  K the spiral amplitude would be twice as large as the antiferromagnetic component of the moment.

The temperature dependence is shown in figure 4(b) for the commensurate antiferromagnetic peak, and in figure 4(c) for the oscillatory peak. On cooling, these peaks first become observable just above 8 K, and initially they increase in intensity at the same rate. This is the same temperature regime where the superconducting state is forming, with  $T_c \approx 7.5$  K. The intensities of both types of peaks continue to grow down to 5 K, where the intensity at  $q_c$  suddenly begins to drop. This is just in the narrow temperature range where the normal conducting state is reentered, and demonstrates that the oscillatory component is directly coupled to the superconductivity. With further decrease of temperature the oscillatory amplitude rapidly drops, and superconductivity is quickly restored again in the system. The intensity belonging to the commensurate antiferromagnetic state, on the other hand, continues to grow as  $T \rightarrow 0$ , and this antiferromagnetic state readily coexists with superconductivity at low temperature. However, the intensity at  $q_c$  does not go completely to zero, but comprises  $\sim 4\%$  of the total intensity at low temperatures, with a somewhat longer and temperature-dependent wavelength. This residual intensity could be from non-superconducting domain boundaries, and indeed the highest-resolution data reveal a small temperature independent, intrinsic width to the magnetic Bragg peaks, which we attribute to domain size effects ( $\sim 2000 \text{ \AA}$ ). Upon warming, strong hysteresis occurs in all the intensities, and to a lesser extent in  $q_c$ .

The overall behavior for  $\text{HoNi}_2\text{B}_2\text{C}$  appears at first glance to be similar in some respects

to the "ferromagnetic" superconductors such as  $\text{HoMo}_6\text{S}_8$  and  $\text{ErRh}_4\text{B}_4$ . In those materials superconductivity is well established before the magnetic system tries to order ferromagnetically at low  $T$ . Initially a compromise oscillatory state is formed, but the ferromagnetism quickly dominates the energetics and they lose their superconductivity and are ferromagnetic and normal at low temperature. The behavior in  $\text{HoNi}_2\text{B}_2\text{C}$  is similar in that an oscillatory state is also realized at high temperatures and is suppressed at low temperature, but the nature of the magnetism is quite different. In this new system the oscillatory state forms at, or slightly above, the superconducting state. Initially the amplitudes of both states are feeble, and the superconductivity is not able to force such an oscillatory state to form. More importantly, as the oscillatory state is suppressed superconductivity returns, and quite readily coexists with the commensurate antiferromagnetic state at low temperature. We conclude that the oscillatory state itself is the preferred magnetic order. For the superconductivity, however, the misalignment of adjacent ferromagnetic planes destroys the antiferromagnetic compensation on the Ni planes and produces a net ferromagnetic component on the Ni layers which destroys superconductivity; just the opposite behavior as for the ferromagnetic superconductors.

Finally we note that the  $\text{ErNi}_2\text{B}_2\text{C}$  system has been investigated by Sinha *et al.*, [5] and in this case a transversely polarized incommensurate spin density wave state is also observed, but the modulation wave vector is along the  $a$  axis. This state happily coexists with superconductivity for the full temperature range, and no hysteresis in the physical properties is observed. Hence there is no obvious competition between the superconductivity and magnetic order in the case of an  $a$ -axis modulated state.

### Anomalous Exchange in $\text{MnCl}_2$

$\text{MnCl}_2$  is a  $\text{CdCl}_2$ -type layered material in which  $\text{Mn}^{2+}$  ions lie in close-packed triangular layers, separated by two layers of  $\text{Cl}^-$  ions.

The hexagonal unit cell contains three molecular units with lattice constant  $a = 3.7 \text{ \AA}$  (representing the near-neighbor distance between magnetic ions) and  $c = 17.5 \text{ \AA}$  (corresponding to three times the distance between consecutive  $\text{Mn}^{2+}$  layers). Despite the fact that  $\text{MnCl}_2$  has been studied by a variety of methods for over fifty years, its magnetic structure is still not well understood.

There are two features that have escaped explanation: First, the ordering temperature of  $\approx 2 \text{ K}$  is quite low considering the large magnetic moment ( $S = 5/2$ ) of the  $\text{Mn}^{2+}$  ions, especially compared to the much higher ordering temperatures of isomorphous transition metal chlorides ( $T_N \approx 25 \text{ K}$  for  $\text{FeCl}_2$  and  $\text{CoCl}_2$ ). In addition, the magnetic unit cell is extremely large (60 spins when it first order and 90 spins at low temperature) indicating a complicated spin Hamiltonian.

One way to simplify interpretation of the magnetic structure is by reducing the interplanar interaction through intercalation of  $\text{MnCl}_2$  into graphite, forming  $\text{MnCl}_2$  graphite intercalation compound (GIC), where the intercalated  $\text{MnCl}_2$  forms a triangular lattice, nearly identical to that in pristine material.

The reciprocal lattice of the  $\text{MnCl}_2$ -GIC (Fig. 5a) shows the reciprocal lattice vectors of the graphene layer and those of the  $\text{Mn}^{2+}$  lattice. The lattice constant for the  $\text{Mn}^{2+}$  layer is essentially the same as for the bulk material, indicating that intercalation preserves the in-plane structure of the  $\text{MnCl}_2$ . At lower temperatures, magnetic scattering has been observed by Wiesler *et al.* [6] (Fig. 5b), with peaks appearing at incommensurate positions such as (0.153, 0.153) referred to the  $\text{Mn}^{2+}$  sublattice. The magnitude of this ordering vector is greater than that for the bulk material (1/10,1/10) but is in the same direction, suggesting a similarity between the magnetic structures of the two materials.

ESR measurements indicate an easy-plane anisotropy for the  $\text{Mn}^{2+}$  moments and, with the observation of an incommensurate structure,

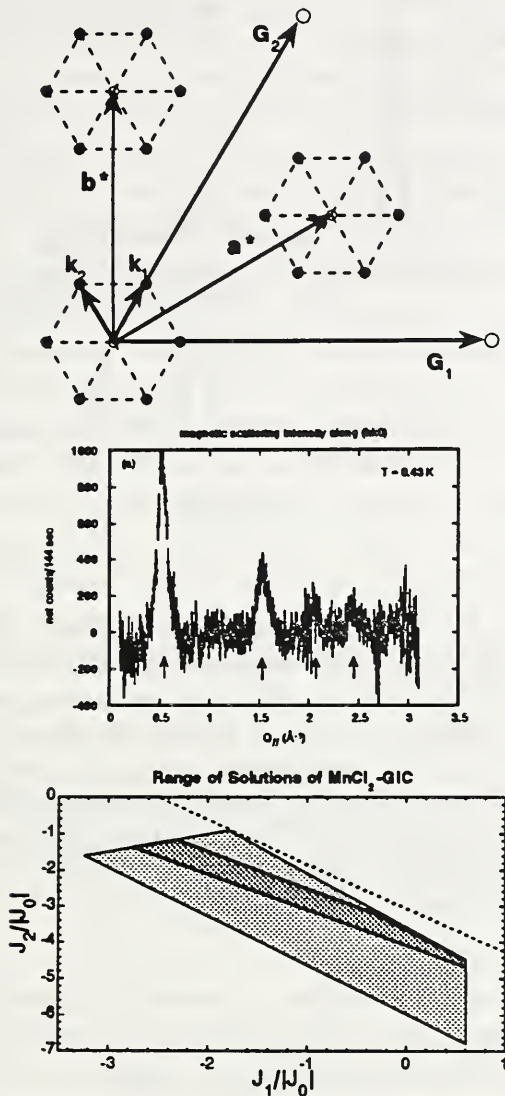


**Figure 5.** Schematic reciprocal lattice plane for MnCl<sub>2</sub>-GIC. Large open circles are nuclear reflections from the graphite, small open circles are nuclear reflections for the MnCl<sub>2</sub> layer, and closed circles are magnetic reflections. (b) Magnetic scattering along  $(hk0)$  at  $T = 0.43$  K. (c) Hamiltonian phase diagram projected onto the  $J_1 - J_2$  plane for  $J_0 > 0$ . The large quadrilateral denotes the range of solutions consistent with the high-temperature susceptibility data and the observed modulation wave vector. The smaller shaded region denotes the subset of these solutions for which the energy minimum would occur at the pristine wave vector with the addition of a suitable interplanar exchange.

imply a helimagnetic configuration in the  $a$ - $b$  plane, which we use to calculate the ground-state energy for various interaction configurations. The observed incommensurate ordering can only be reproduced with *three* interactions: a weak ferromagnetic nearest-neighbor interaction  $J_0$ , a next-nearest-neighbor interaction of undetermined sign  $J_1$ , and an antiferromagnetic third-nearest-neighbor interaction  $J_2$ . Applying a similar model to the ordering for pristine MnCl<sub>2</sub>, and assuming that the in-plane coupling is not changed by intercalation, allows the further restriction of allowed values for the coupling constants (Fig. 5c).

The dominance of  $J_2$  is surprising, as is the ferromagnetic character of the nearest-neighbor superexchange. Although second-neighbor exchange interactions are sometimes larger than those for first neighbors, we are unaware of *any* other insulating magnetic system for which three in-plane exchange coupling are required, let alone for which the third-neighbor exchange is the strongest. In this case, however, the antiferromagnetic quasi-direct exchange between the Mn<sup>2+</sup> appears to be balanced out by the “90° superexchange” via the Cl<sup>-</sup>. The preponderant influence of  $J_2$  over  $J_1$  is explained by the fact that the former interaction is mediated only via  $\sigma$  bonds and not by  $\pi$  bonds as in the case of  $J_1$ . Inelastic neutron scattering studies of the spin-wave dispersion are planned in order to determine the exact solutions for the exchange.

## Magnetic Ordering in Nd/Y Superlattices

For over a decade advances in the controlled deposition of materials using molecular beam epitaxy (MBE) have accelerated progress in the fabrication of crystalline magnetic films and superlattices with 3- $d$  transition metal, transition-metal oxide, and rare-earth components. In particular, systematic studies of heavy rare-earth superlattices with nanometer-scale interlayers led to the first observation of coupling of magnetic interlayers across nonmagnetic spacers, a phenomenon recently observed in 3- $d$  transition-

metal superlattices. Long-range magnetic order, which has been observed in systems including Gd/Y, Dy/Y and Er/Y, originates from an RKKY-like exchange interaction mediated by the conduction electrons in the nonmagnetic material. In the bulk rare-earths, however, magnetostrictive terms in the energy also become important at low temperatures. The magnetic phase diagram of rare-earth superlattices thus is highly sensitive to the epitaxial strain that arises from the lattice mismatch between the bilayer components in the growth plane.

Until now there has been no study of epitaxial superlattices incorporating light rare-earth components because they exhibit more complex magnetic ordering than the heavy rare earths. Their spin structures, however, should exhibit comparable sensitivity to epitaxial strain and artificial periodicity. To test these predictions, a series of seven *c*-axis Nd/Y superlattices were grown at the University of Illinois using MBE methods. Neutron diffraction measurements by Everitt *et al.* [7] have shown that the magnetic structure of the Nd in these systems is highly perturbed from the structure in bulk, possibly due to changes in the magnetic interactions induced by grown-in strains.

Bulk Nd has the dhcp crystal structure with a repeated four layer stacking sequence along the *c*-axis direction of ABAC. The B and C layer magnetic sites have hexagonal symmetry and order at  $T_N=19.9$  K. Their magnetic moment vectors lie in the basal plane along one of three equivalent *b*-axes. The magnitude of these moments is sinusoidally modulated with an incommensurate ordering wave vector of  $0.14a^*$  just below  $T_N$  ( $a^*$  is parallel to the *b*-axis). The moments are aligned antiferromagnetically in going from B to C layers. The cubic sites (A layers) order below 8.2 K in the same type of structure as the hexagonal sites but with a modulation wave vector of  $0.18a^*$  just below 8.2 K.

The features of the magnetic structure in the superlattices are exhibited by neutron diffraction scans along  $a^*$  through the (003) dhcp reciprocal lattice point, as shown in the figure 6 for

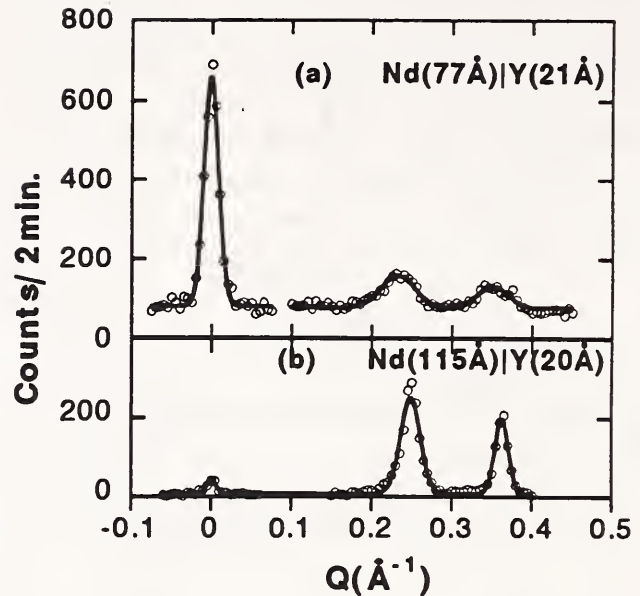


Figure 6. (a) Neutron diffraction scan along  $a^*$  through the (003) reciprocal lattice point for  $[Nd(77\text{\AA})|Y(21\text{\AA})]$  at 5K. The antiferromagnetic peak at (003) is not present in bulk Nd. The peaks centered at  $0.12a^*$  and  $0.18a^*$  are due to bulk-like hexagonal and cubic site magnetic ordering. (b) Similar scan for  $[Nd(115\text{\AA})|Y(20\text{\AA})]$  at 1.5K. In this sample with a greater relative amount of Nd there is only a weak magnetic peak at (003).

two of the superlattices. As shown in figure 6(a) the superlattice  $[Nd(77\text{\AA})|Y(21\text{\AA})]$  exhibits a strong (003) antiferromagnetic reflection at 1.5K that is not found in bulk Nd. The incommensurate ordering of the hexagonal and cubic sites is also observed, with split peaks as in bulk Nd. Data for the superlattice  $[Nd(115\text{\AA})|Y(20\text{\AA})]$ , which has a larger fraction of Nd, are shown in 6(b). Now the antiferromagnetic type ordering is almost completely suppressed, and the magnetic ordering is very nearly bulk-like, except that the incommensurate peaks are not split. Peak widths have been used to extract the coherence lengths of the magnetic ordering, giving 300 Å in the basal plane for the (003) antiferromagnetic ordering, and more than 100 Å in the basal plane for the incommensurate ordering. The magnetic coherence along the growth axis is

generally confined to individual Nd blocks, with only the two superlattices with the thinnest Y layers exhibiting any signs of interlayer coupling. We note that the absence of long-range magnetic order along the c-axis contrasts sharply with the behavior of heavy rare earth superlattices.

Finally, the ordering temperatures for the hexagonal sites have been shown to be enhanced by > 40% relative to the bulk value. Previous studies of Nd/Y alloys have reported shifts of the signature magnetization temperatures as the alloy structure progresses from dhcp for small relative amounts of Y to the hcp structure for large amounts of Y. Off-axis ( $10\ell$ ) x-ray diffraction scans for the superlattices indicate that they are primarily dhcp, suggesting that the substantial changes observed in the magnetic structure as the relative amount of Nd to Y is changed are likely caused by epitaxial strain and not a modified close-packed structure within the Nd layers.

## References

- [1] R. A. Robinson, A. Purwanto, M. Kohgi, P. C. Canfield, T. Kamiyama, T. Ishigaki, J. W. Lynn, R. Erwin, E. Peterson and R. Movshovich, *Phys. Rev. B* 50 (in press, 1994); R. A. Robinson, M. Kohgi, T. Osakabe, F. Trouw, J. W. Lynn, P. C. Canfield, J. D. Thompson, and Z. Fisk (preprint).
- [2] M. C. Aronson, R. Osborn, R. A. Robinson, J. W. Lynn, R. Chau, C. L. Seaman, and M. B. Maple (preprint).
- [3] J. F. DiTusa, S-W. Cheong, J.-H. Park, G. Aeppli, C. Broholm and C. T. Chen, *Phys. Rev. Lett.* **73**, 1857 (1994). J. F. DiTusa, S-W. Cheong, C. Broholm, G. Aeppli, L. W. Rupp, and B. Batlogg, *Physica, B* **194-196**, 181 (1994).
- [4] T. E. Grigereit, J. W. Lynn, Q. Huang, A. Santoro, R. J. Cava, J. J. Krajewski, and W. F. Peck, Jr., *Phys. Rev. Lett.* (to be published). Q. Huang, A. Santoro, T. E. Grigereit, J. W. Lynn, R. J. Cava, J. J. Krajewski, and W. F. Peck, Jr. (preprint).
- [5] S. K. Sinha, J. W. Lynn, T. E. Grigereit, Z. Hosain, L. C. Gupta, R. Nagarajan, and C. Godart, *Phys. Rev. B* (*Rapid Communications*, in press).
- [6] D. G. Wiesler, M. Suzuki, I. Suzuki, and N. Rosov (preprint).
- [7] B. A. Everitt, J. A. Borchers, M. B. Salamon, J. J. Rhyne, R. W. Erwin, B. J. Park and C. P. Flynn, *Magn. Mater.* (in press).

## Research Topics

### Polarization Analysis of the Magnetic Excitations in Invar

J. W. Lynn<sup>27</sup>, N. Rosov<sup>27</sup>, M. Acet<sup>38</sup>, and H. Bach<sup>28</sup>.

### Vortex Lattice and Melting in Nb

J. W. Lynn<sup>27</sup>, N. Rosov<sup>27</sup>, T. E. Grigereit<sup>43</sup>, H. Zhang<sup>43,27</sup>, and T. W. Clinton<sup>43</sup>.

### Structure of the Vortex Lattice in $\text{YBa}_2\text{Cu}_3\text{O}_7$

B. Keimer<sup>25</sup>, I. Aksay<sup>25</sup>, F. Dogan<sup>25</sup>, R. W. Erwin<sup>27</sup>, J. W. Lynn<sup>27</sup>, and M. Sarikaya<sup>25</sup>.

### Magnetic Structure of the Heavy Fermion Compound $\text{CeCu}_{5.5}\text{Au}_{0.5}$

A. Schröder<sup>18</sup>, J. W. Lynn<sup>27</sup>, M. Loewenhaupt<sup>14</sup>, and H. V. Löhneysen<sup>39</sup>.

### Temperature Dependence of the Magnetic Excitations in Ordered and Disordered $\text{Fe}_3\text{Pt}$

N. Rosov<sup>27</sup>, J. W. Lynn<sup>27</sup>, J. Kästner<sup>33</sup>, E. F. Wassermann<sup>33</sup>, and H. Bach<sup>28</sup>.

### Magnetic Structure and Spin Dynamics of the Pr and Cu ions in $\text{Pr}_2\text{CuO}_4$

I. W. Sumarlin<sup>43</sup>, J. W. Lynn<sup>27</sup>, T. Chattopadhyay<sup>12</sup>, S. N. Barilo<sup>6</sup>, D. I. Zhigunov<sup>6</sup> and J. L. Peng<sup>43</sup>

### Crystal Structure and Magnetic Ordering of the Rare Earth and Cu Moments in $\text{RBa}_2\text{Cu}_2\text{NbO}_{10}$ ( $\text{R}=\text{Nd}, \text{Pr}$ )

N. Rosov<sup>27</sup>, J. W. Lynn<sup>27</sup>, H. B. Radousky<sup>15</sup>, M. Bennahmias<sup>38</sup>, T. J. Goodwin<sup>38</sup>, P. Klavins<sup>38</sup>, and R. N. Shelton<sup>38</sup>.

### Magnetic Ordering of Pr and Cu in $\text{TlBa}_2\text{PrCu}_2\text{O}_{7-y}$

K. J. Chang<sup>20</sup>, W. T. Hsieh<sup>20</sup>, W.-H. Li<sup>20</sup>, K. C. Lee<sup>20</sup>, J. W. Lynn<sup>27</sup>, C. C. Lai<sup>20</sup>, and H. C. Ku<sup>20</sup>.

### Two-dimensional Magnetic Order in $\text{Pb}_2\text{Sr}_2\text{TbCu}_3\text{O}_8$

S. Y. Wu<sup>20</sup>, W. T. Hsieh<sup>20</sup>, W.-H. Li<sup>20</sup>, K. C. Lee<sup>20</sup>, J. W. Lynn<sup>27</sup>, and H. D. Yang<sup>21</sup>.

**Effects of Ga Doping on the Pr Magnetism in PrBa<sub>2</sub>Cu<sub>3</sub>O<sub>7</sub>**

W. T. Hsieh<sup>20</sup>, K. J. Chang<sup>20</sup>, W.-H. Li<sup>20</sup>, and J. W. Lynn<sup>27</sup>.

**Magnetic Properties of Single-crystal UCu<sub>3</sub>Al<sub>2</sub>**

H. Nakotte<sup>41</sup>, E. Bruck<sup>41</sup>, J. H.V.J. Brabers<sup>41</sup>, K. Prokes<sup>41</sup>, F. R. de Boer<sup>41</sup>, V. Sechovsky<sup>8</sup>, K. H. J. Buschow<sup>24</sup>, A. V. Andreev<sup>49</sup>, R. A. Robinson<sup>17</sup>, A. Purwanto<sup>27</sup>, and J. W. Lynn<sup>27</sup>.

**Nuclear and Magnetic Structures of the Substitutional Compounds (Y-Ca)Ba<sub>2</sub>Fe<sub>3</sub>O<sub>8</sub>**

I. Natali-Sora<sup>31</sup>, Q. Huang<sup>43,27</sup>, J. W. Lynn<sup>27</sup>, N. Rosov<sup>27</sup>, P. Karen<sup>47</sup>, A. Kjekshus<sup>47</sup>, V. L. Karen<sup>27</sup>, A. D. Mighell<sup>27</sup>, and A. Santoro<sup>27</sup>.

**Non-collinear Magnetic Structure of the Cu Spins in R<sub>2</sub>CuO<sub>4</sub> (R=Nd, Sm, Pr)**

S. Skanthakumar<sup>43,3</sup>, J. W. Lynn<sup>27</sup>, and I. W. Sumarlin<sup>43</sup>.

**Magnetic Ordering in Eu<sub>2</sub>CuO<sub>4</sub>**

T. Chattopadhyay<sup>12</sup>, J. W. Lynn<sup>27</sup>, N. Rosov<sup>27</sup>, T. E. Grigereit<sup>43</sup>, S. N. Barilo<sup>6</sup>, and D. I. Zhigurov<sup>6</sup>.

**Magnetic Field Penetration Depth in Superconductors by Polarized Neutron Reflectometry**

H. Zhang<sup>43,27</sup>, J. W. Lynn<sup>27</sup>, C. F. Majkrzak<sup>27</sup>, S. K. Satija<sup>27</sup>, and J. H. Kang<sup>50</sup>.

**Non-Fermi Liquid Scaling in UCu<sub>5-x</sub>Pd<sub>x</sub> Alloys**

M. Aronson<sup>44</sup>, R. Osborn<sup>3</sup>, R. A. Robinson<sup>17</sup>, J. W. Lynn<sup>27</sup>, R. Chau<sup>39</sup>, C. L. Seaman<sup>39</sup>, and M. B. Maple<sup>39</sup>.

**Crystal and Magnetic Structures of NiF<sub>3</sub>**

L. Chacon<sup>37</sup>, N. Rosov<sup>27</sup>, and J. W. Lynn<sup>27</sup>.

**Magnetic Small Angle Scattering in the Nanocrystalline Amorphous System Fe<sub>73.5</sub>B<sub>9</sub>Si<sub>13.5</sub>Cu<sub>1</sub>Nb<sub>3</sub>**

N. Rosov<sup>27</sup>, J. W. Lynn<sup>27</sup>, and G. Fish<sup>1</sup>.

**Magnetic Order in the Superconductor ErNi<sub>2</sub>B<sub>2</sub>C**

S. K. Sinha<sup>10</sup>, J. W. Lynn<sup>27</sup>, T. E. Grigereit<sup>43</sup>, Z. Hossain<sup>30</sup>, L. C. Gupta<sup>30</sup>, R. Nagarajan<sup>30</sup>, and C. Godart<sup>63</sup>.

**Magnetic Ordering in Dy<sub>5</sub>Os<sub>4</sub>Ge<sub>10</sub>**

T. E. Grigereit<sup>43</sup>, J. W. Lynn<sup>27</sup>, L. C. Gupta<sup>30</sup>, M. Lin<sup>10</sup>, and S. K. Sinha<sup>10</sup>.

**Magnetic Order in the Reentrant Superconductor HoNi<sub>2</sub>B<sub>2</sub>C**

T. E. Grigereit<sup>43</sup>, J. W. Lynn<sup>27</sup>, Q. Huang<sup>27,43</sup>, A. Santoro<sup>27</sup>, R. J. Cava<sup>5</sup>, J. J. Krajewski<sup>5</sup>, and W. F. Peck, Jr<sup>5</sup>.

**Magnetic Ordering in RPO<sub>4</sub> and RVO<sub>4</sub> Systems**

S. Skanthakumar<sup>43,3</sup>, C.-K. Loong<sup>3</sup>, L. Soderholm<sup>3</sup>, and J. W. Lynn<sup>27</sup>.

**Spin Dynamics of the Super-heavy Fermion System YbBiPt**

R. A. Robinson<sup>17</sup>, J. W. Lynn<sup>27</sup>, and P. Canfield<sup>62</sup>.

**Magnetic Ordering in UAuCu<sub>4</sub> and UAgCu<sub>4</sub>**

M. Aronson<sup>44</sup>, J. W. Lynn<sup>27</sup>, Y. Dalichaouch<sup>39</sup>, and M. B. Maple<sup>39</sup>.

**Magnetic Structure Determination in Fe<sub>3</sub>O<sub>4</sub>/NiO Superlattices**

J. A. Borchers<sup>27</sup>, R. W. Erwin<sup>27</sup>, S. D. Berry<sup>11</sup>, and D. M. Lind<sup>11</sup>.

**Spatially Modulated Antiferromagnetic Order in NiO/CoO Superlattices**

J. A. Borchers<sup>27</sup>, R. W. Erwin<sup>27</sup>, M. J. Carey<sup>39</sup>, A. E. Berkowitz<sup>39</sup>, and C. F. Majkrzak<sup>27</sup>.

**Characterization of the Magnetic Structures in Nd Films and Nd/Y Superlattices**

B. A. Everitt<sup>42</sup>, J. A. Borchers<sup>27</sup>, R. W. Erwin<sup>27</sup>, M. B. Salamon<sup>42</sup>, B. J. Park<sup>42</sup>, C. P. Flynn<sup>42</sup>, and J. J. Rhyne<sup>45</sup>.

**Incommensurate Magnetic Order in MnCl<sub>2</sub> Graphite Intercalate**

D. G. Wiesler<sup>27</sup>, N. Rosov<sup>27</sup>, M. Suzuki<sup>29</sup>, and I. Suzuki<sup>29</sup>.

**Magnetism on an Isosceles Triangular Lattice: CuCl<sub>2</sub>-intercalated Graphite**

D. G. Wiesler<sup>27</sup>, I. Suzuki<sup>29</sup>, M. Suzuki<sup>29</sup>, and N. Rosov<sup>27</sup>.

**Crystal Structure of Annealed and As-Prepared HgBa<sub>2</sub>CaCu<sub>2</sub>O<sub>6+δ</sub>**

Q. Huang<sup>43,27</sup>, J. W. Lynn<sup>27</sup>, R. L. Meng<sup>41</sup>, and C. W. Chu<sup>41</sup>.

**Two- and Three-Dimensional Magnetic Order of Er in Superconducting ErBa<sub>2</sub>Cu<sub>3</sub>O<sub>7</sub>**

T. W. Clinton<sup>43</sup>, J. W. Lynn<sup>27</sup>, J. Z. Liu<sup>38</sup>, Y. X. Jia<sup>38</sup>, and R. N. Shelton<sup>38</sup>.

**Neutron Powder Diffraction Study of the Nuclear and Magnetic Structures of the Oxygen-Deficient Perovskite YBCuCoO<sub>5</sub>**

- Q. Huang<sup>43,27</sup>, P. Karen<sup>47</sup>, V. L. Karen<sup>27</sup>, A. Kjekshus<sup>47</sup>, J. W. Lynn<sup>27</sup>, A. D. Mighell<sup>27</sup>, I. Nantali Sora<sup>31</sup>, N. Rosov<sup>27</sup>, and A. Santoro<sup>27</sup>.
- Effects of the Chain Layer Oxygen on the Magnetic Order of Nd in NdBa<sub>2</sub>Cu<sub>3</sub>O<sub>6+x</sub>**  
T. W. Clinton<sup>43</sup>, J. W. Lynn<sup>27</sup>, B. W. Lee<sup>39</sup>, M. Buchgeister<sup>39</sup>, and M. B. Maple<sup>39</sup>.
- Magnetic Ordering of Pr and Cu in TlBa<sub>2</sub>PrCu<sub>2</sub>O<sub>7-y</sub>**  
W.-H. Li<sup>20</sup>, K. C. Lee<sup>20</sup>, J. W. Lynn<sup>27</sup>, C. C. Lai<sup>20a</sup>, and H. C. Ku<sup>20a</sup>.
- Temperature Dependence of Magnetic Order in Single-crystalline UPdSn**  
R. A. Robinson<sup>17</sup>, J. W. Lynn<sup>27</sup>, A. C. Lawson<sup>17</sup>, and H. Nakotte<sup>41</sup>.
- Magnetic Order of Dy in DyBa<sub>2</sub>Cu<sub>3</sub>O<sub>6+x</sub>**  
T. W. Clinton<sup>43</sup>, J. W. Lynn<sup>27</sup>, J. Z. Liu<sup>38</sup>, Y. X. Jia<sup>38</sup>, T. J. Goodwin<sup>38</sup>, and R. N. Shelton<sup>38</sup>.
- Influence of Chain-Site Oxygen on the Magnetic Order of Er in ErBa<sub>2</sub>U<sub>3</sub>O<sub>6+x</sub>**  
T. W. Clinton<sup>43</sup>, J. W. Lynn<sup>27</sup>, and J. L. Peng<sup>43</sup>.
- Crystallography and Magnetism of the Heavy-Fermion Compound YbBiPt**  
R. A. Robinson<sup>17</sup>, A. Purwanto<sup>17</sup>, M. Kohgi<sup>53</sup>, P. C. Canfield<sup>62</sup>, T. Kamiyama<sup>64</sup>, Y. Ishigaki<sup>64</sup>, J. W. Lynn<sup>27</sup>, R. W. Erwin<sup>27</sup>, and E. Peterson<sup>17</sup>.
- Effects of Ga-Doping on the Magnetic Ordering of Pr in PrBa<sub>2</sub>Cu<sub>3</sub>O<sub>7</sub>**  
W.-H. Li<sup>20</sup>, C. J. Jou<sup>20</sup>, S. T. Shyr<sup>20</sup>, K. C. Lee<sup>20</sup>, J. W. Lynn<sup>27</sup>, H. L. Tsay<sup>21</sup>, and H. D. Yang<sup>21</sup>.
- Magnetic Ordering of Pr in Pb<sub>2</sub>Sr<sub>2</sub>PrCu<sub>3</sub>O<sub>8</sub>**  
W. T. Hsieh<sup>20</sup>, W.-H. Li<sup>20</sup>, K. C. Lee<sup>20</sup>, J. W. Lynn<sup>27</sup>, J. H. Shieh<sup>20a</sup>, and H. C. Ku<sup>20a</sup>.
- Zero-Field Magnetic Structure of EuNi<sub>5</sub>P<sub>3</sub>**  
J. L. Luce<sup>37</sup>, J. V. Badding<sup>66</sup>, A. M. Stacy<sup>37</sup>, J. W. Lynn<sup>27</sup>, R. W. Erwin<sup>27</sup>, and D. E. Cox<sup>7</sup>.
- Neutron Scattering Study of the Magnetism in a Nanocrystalline/Amorphous Material**  
N. Rosov<sup>27</sup>, J. W. Lynn<sup>27</sup>, and G. Fish<sup>1</sup>.
- Neutron Scattering from a Phase-Separated Ferrofluid**  
M. Y. Lin<sup>10</sup>, W. Luo<sup>65</sup>, and J. W. Lynn<sup>27</sup>.
- Structural and Magnetic Phase Transitions in Pure and Ca-doped KMnF<sub>3</sub>**  
P. M. Gehring<sup>27</sup>, S. M. Shapiro<sup>7</sup>, B. J. Sternlieb<sup>7</sup>, A. Gibaud<sup>35</sup>, J. Nouet<sup>35</sup>, and H. You<sup>3</sup>.
- Effects of Random Magnetic Anisotropy on the Magnetism of Dy<sub>x</sub>Y<sub>1-x</sub>Al<sub>2</sub> Single Crystals.**  
P. M. Gehring<sup>27</sup> and A. del Moral<sup>48</sup>.
- Anomalous Critical Scattering in Tb.**  
P. M. Gehring<sup>27</sup>, C. F. Majkrzak<sup>27</sup>, K. Hirota<sup>7</sup>, and G. Shirane<sup>7</sup>.
- Anomalous Critical Scattering in Ho Thin Films.**  
P. M. Gehring<sup>7</sup>, C. F. Majkrzak<sup>7</sup>, D. F. McMorrow<sup>57</sup>, R. A. Cowley<sup>58</sup>, L. D. Gibbs<sup>7</sup>, T. R. Thurston<sup>7</sup>, J. P. Hill<sup>7</sup>, and G. Helgesen<sup>7</sup>.
- Anomalous Critical Scattering in Diblock Copolymer Thin Films.**  
P. M. Gehring<sup>27</sup>, C. F. Majkrzak<sup>27</sup>, S. K. Satija<sup>27</sup>, and T. P. Russell<sup>55</sup>.
- Low-Field Giant Magnetoresistance in (Fe-Ni)/Ag Multilayers.**  
J. A. Borchers<sup>27</sup>, P. M. Gehring<sup>27</sup>, C. F. Majkrzak<sup>27</sup>, J. F. Ankner<sup>45</sup>, T. L. Hylton<sup>54</sup>, K. R. Coffey<sup>54</sup>, M. A. Parker<sup>54</sup>, and J. K. Howard<sup>54</sup>.
- High-Frequency Phonon Dispersion in La<sub>1.85</sub>Sr<sub>0.15</sub>CuO<sub>4</sub>.**  
A. H. Moudden<sup>56</sup>, B. Hennion<sup>56</sup>, P. M. Gehring<sup>27</sup>, M. Matsuda<sup>7</sup>, G. Shirane<sup>7</sup>, Y. Endoh<sup>53</sup>, I. Tanaka<sup>52</sup>, and H. Kojima<sup>52</sup>.
- The Neel Temperature of Nanocrystalline Chromium**  
J. A. Eastman<sup>3</sup>, M. R. Fitzsimmons<sup>17</sup>, R. A. Robinson<sup>17</sup>, and J. W. Lynn<sup>27</sup>.
- On the Roles of Classical Nonlocality and Acceleration in the Analogs of the Aharonov-Bohm and Related Phases for Neutrons**  
R. C. Casella<sup>27</sup>.
- Spin Correlations in Metallic and Insulating V<sub>2-y</sub>O<sub>3</sub> and (V<sub>1-x</sub>Cr<sub>x</sub>)<sub>2</sub>O<sub>3</sub>**  
W. Bao<sup>13</sup>, C. Broholm<sup>13</sup>, G. Aeppli<sup>5</sup>, J. M. Honig<sup>26</sup>, and P. Metcalf<sup>26</sup>.
- Magnetic And Charge Dynamics in a Doped One-Dimensional Transition Metal Oxide**  
J. F. Ditusa<sup>5</sup>, S.-W. Cheong<sup>5</sup>, J.-H. Park<sup>5</sup>, G. Aeppli<sup>5</sup>, C. T. Chen<sup>5</sup>, and C. Broholm<sup>13</sup>.
- Suppression of the Antiferromagnetic Moment in the Superconducting Phase of UPt<sub>3</sub>**  
C. Broholm<sup>13</sup>, R. W. Erwin<sup>27</sup>, E. D. Isaacs<sup>5</sup>, G. Aeppli<sup>5</sup>, A. P. Ramirez<sup>5</sup>, C. S. Oglesby<sup>5</sup>, E. Bucher<sup>5</sup>, P. Zschack<sup>61</sup>, and C. Burns<sup>60</sup>.

**Neutron Scattering Study of the  $S=1/2$  1D Heisenberg Antiferromagnet Copper Benzoate**

D. Dender<sup>13</sup>, D. Reich<sup>13</sup>, C. Broholm<sup>13</sup>, G. Aeppli<sup>5</sup>, and K. Lefmann<sup>57</sup>.

**Investigation of a One Dimensional  $S=1/2$  Magnet with a Potential for Frustration:  $\text{CuN}_2\text{D}_5\text{Cl}_3$**

Shaolong Ma<sup>13</sup>, C. Broholm<sup>13</sup>, D. Davidovic<sup>13</sup>, D. H. Reich<sup>13</sup>, and R. W. Erwin<sup>27</sup>

**Crystal Field in  $\text{Pr}_{1.85}\text{Ce}_{0.15}\text{CuO}_4$**

F. Altorfer<sup>43</sup>, W. Hengeler<sup>59</sup>, and A. Furrer<sup>59</sup>

**Field Dependence of the Magnetic Structure in  $\text{Fe}_3\text{O}_4/\text{NiO}$  Superlattices**

R. W. Erwin<sup>27</sup>, J. A. Borchers<sup>27</sup>, D. M. Lind<sup>11</sup>, and S. D. Berry<sup>11</sup>

**Observation of the Verwey Transition in  $\text{Fe}_3\text{O}_4/\text{NiO}$  Superlattices and an  $\text{Fe}_3\text{O}_4$  Film**

J. A. Borchers<sup>27</sup>, R. W. Erwin<sup>27</sup>, S. D. Berry<sup>11</sup>, and D. M. Lind<sup>11</sup>

**Characterization of the Magnetic Structure and Interlayer Coupling in Nd/Y Superlattices**

B. A. Everitt<sup>42</sup>, J. A. Borchers<sup>27</sup>, R. W. Erwin<sup>27</sup>, M. B. Salamon<sup>42</sup>, B. J. Park<sup>42</sup>, C. P. Flynn<sup>42</sup>, and J. J. Rhyne<sup>45</sup>

**Incommensurate Magnetic Structures in  $\text{Nd}_x\text{Y}_{1-x}$  Alloy Films**

B. A. Everitt<sup>42</sup>, R. W. Erwin<sup>27</sup>, J. A. Borchers<sup>27</sup>, D. McMorrow<sup>67</sup>, M. B. Salamon<sup>42</sup>, B. J. Park<sup>42</sup>, C. P. Flynn<sup>42</sup>, and J. J. Rhyne<sup>45</sup>

**Temperature Dependence of the Magnetic Phase Angle in Ho/Y Superlattices**

J. A. Borchers<sup>27</sup>, R. W. Erwin<sup>27</sup>, M. J. Conover<sup>3</sup>, S. D. Bader<sup>3</sup>, and J. J. Rhyne<sup>45</sup>

**Magnetic Structure Determination for  $\text{FeF}_2$  Thin Films**

J. A. Borchers<sup>27</sup>, R. W. Erwin<sup>27</sup>, D. Lederman<sup>39</sup>, I. K. Schuller<sup>39</sup>, and J. F. Ankner<sup>45</sup>

**Lattice Dynamics of  $\text{Ba}_{1-x}\text{K}_x\text{BiO}_3$  Studied by Inelastic Neutron Scattering**

M. A. Green<sup>68</sup>, K. Prassides<sup>69</sup>, D. A. Neuman<sup>27</sup>, and P. Day<sup>68</sup>

**Affiliations**

<sup>1</sup>Allied Signal Corp.

<sup>2</sup>Army Armament RD&E Center

<sup>3</sup>Argonne National Lab

<sup>4</sup>Arizona State University

<sup>5</sup>AT&T Bell Laboratories

<sup>6</sup>Belarus Academy of Sciences

<sup>7</sup>Brookhaven National Lab

<sup>8</sup>Charles University

<sup>9</sup>Columbia University

<sup>10</sup>Exxon Research & Engineering

<sup>11</sup>Florida State University

<sup>12</sup>Institut Laue-Langevin

<sup>13</sup>Johns Hopkins University

<sup>14</sup>KFA Jülich

<sup>15</sup>Lawrence Livermore Laboratory

<sup>16</sup>Lehigh University

<sup>17</sup>Los Alamos National Laboratory

<sup>18</sup>McMaster University

<sup>19</sup>Morris Research, Berkeley

<sup>20</sup>National Central University

<sup>20a</sup>National Tsing Hua University

<sup>21</sup>National Sun Yat-Sen University

<sup>22</sup>Niffon Electric Co.

<sup>23</sup>Oak Ridge National Lab

<sup>24</sup>Philips Research Labs

<sup>25</sup>Princeton University

<sup>26</sup>Purdue University

<sup>27</sup>Reactor Radiation Division

<sup>28</sup>Ruhr Universität, Bochum

<sup>29</sup>SUNY at Binghamton

<sup>30</sup>Tata Inst. of Fundamental Res.

<sup>31</sup>Università di Brescia

<sup>33</sup>Universität Duisberg

<sup>34</sup>Universität Karlsruhe

<sup>35</sup>Université du Maine

<sup>36</sup>University of Amsterdam

<sup>37</sup>University of California, Berkeley

<sup>38</sup>University of California, Davis

<sup>39</sup>University of California, San Diego

<sup>40</sup>University of Chicago

<sup>41</sup>University of Houston

<sup>42</sup>University of Illinois

<sup>43</sup>University of Maryland

<sup>44</sup>University of Michigan

<sup>45</sup>MURR, University of Missouri

<sup>46</sup>University of Nancy I

<sup>47</sup>University of Oslo

<sup>48</sup>University of Zaragoza



- <sup>49</sup>Ural State University
- <sup>50</sup>Westinghouse
- <sup>51</sup>University of Missouri
- <sup>52</sup>Yamanashi University
- <sup>53</sup>Tohoku University
- <sup>54</sup>IBM Storage Systems Division
- <sup>55</sup>IBM Almaden Research
- <sup>56</sup>Laboratoire Léon Brillouin
- <sup>57</sup>Risø National Laboratory
- <sup>58</sup>Oxford University
- <sup>59</sup>Lab. for Neutron Scattering
- <sup>60</sup>Western Michigan University
- <sup>61</sup>Oak Ridge Inst. for Science and Education
- <sup>62</sup>Ames Laboratory
- <sup>63</sup>CNRS, Meudon
- <sup>64</sup>University of Tsukuba
- <sup>65</sup>University of Central Florida
- <sup>66</sup>Penn State University
- <sup>67</sup>Risø National Laboratory
- <sup>68</sup>Royal Institution of Great Britain
- <sup>69</sup>Sussex University

# Crystallography

Routine operation of the 32 detector powder diffractometer at BT-1 continued through the period during which the reactor was in operation. In eight months 500 data sets were collected on more than 200 different materials, even while the instrument was under occasional testing. In addition to the determination and refinement of crystal structures, the power of the instrument as a tool for phase analysis was further demonstrated. In this section we present some of the highlights of these extensive efforts.

## Phase Analysis

### • ZrO<sub>2</sub> Powders

Yttria-stabilized ZrO<sub>2</sub> powders are of technological importance as ceramic thermal barrier coatings. ZrO<sub>2</sub> occurs in nature as the monoclinic mineral baddeleyite; additions of small amounts of yttria (Y<sub>2</sub>O<sub>3</sub>) stabilize both a tetragonal and a cubic phase. Since feedstock powders containing greater than 5% of the monoclinic phase are not desirable due to cracking of the coatings, it is important that an accurate method of determining phase fractions be available.

Samples of feedstock powders were analyzed using the program GSAS for multiphase Rietveld refinement on neutron data collected using the Cu311 monochromator. Neutrons provide a significant advantage over x-rays in this case, owing to the greater range of available data, the relatively increased sensitivity to oxygen scattering, and the symmetric line shape. It is necessary to refine the complete crystal structures in all cases, as varying amounts of yttria substitution result in changes in atomic positions and lattice parameters in the three phases. Additionally, the line shapes of the three phases also change depending upon composition and processing parameters. A portion of the diffraction pattern of sample P is given in figure 1, showing the three individual contribu-

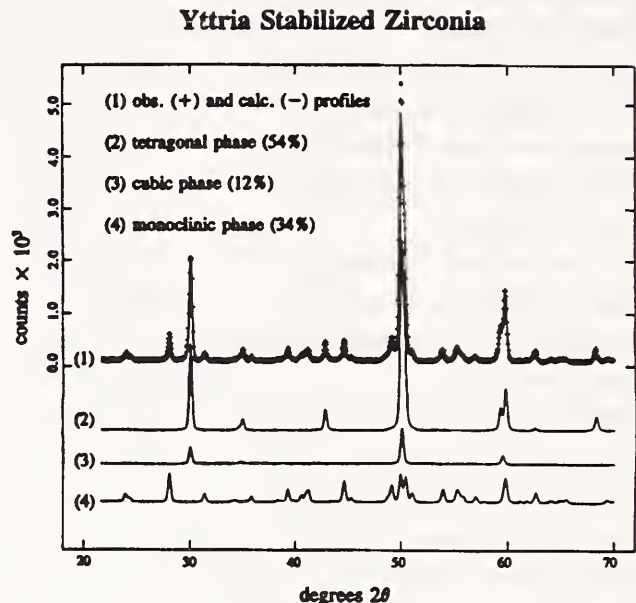


Figure 1. A portion of the neutron powder diffraction pattern of sample P, showing contributions from the three constituent ZrO<sub>2</sub> phases.

tions to the overall pattern. Table 1 gives the results of the phase analyses, along with those reported from traditional x-ray techniques. It can be seen that the monoclinic and tetragonal fractions have been systematically underestimated using x-ray methods, while the cubic fraction is overestimated. Encouraging fast results were also obtained on actual ceramic coatings deposited under different chemical and temperature conditions.

## Crystal Structures

### • Intermetallic Compounds ZrIr and ZrRh

The compounds ZrIr and ZrRh possess ordered B2-type structures (CsCl-type, space group *Pm3m*) at high temperature, and both compounds transform martensitically. A shape memory effect was reported to occur in ZrRh in the approximate temperature range 570 — 680 °C, and was predicted but not observed for

**Table 1.** Phase Composition of Yttria Stabilized ZrO<sub>2</sub> Powders

Sample	% cubic		% tetragonal		% monoclinic	
	Neutron	X-ray	Neutron	X-ray	Neutron	X-ray
P	12	37-40	54	40-37	34	22
M	59	85	20	0	21	15
A	20	45-50	80	55-50	0	0
F	26	50	74	50	0	0
H	52	78-79	12	0	36	21-22
J	12	53-54	77	41-42	11	4-5

ZrIr. The x-ray powder diffraction patterns produced by the low-temperature martensitic forms of these two compounds are virtually identical, with very broad diffraction lines, but the structure itself has not previously been carefully studied. A NiTi-type structure has been proposed, but this lattice does not adequately index the observed powder patterns.

High-resolution neutron powder diffraction data were obtained at room temperature on cast, annealed rods of both materials using the Cu220 monochromator ( $\lambda = 1.5567 \text{ \AA}$ ). Both patterns again exhibited very broad diffraction lines, but using limited transmission electron microscopy (TEM) data, cell volume restrictions, and the program TREOR it was possible to index the pattern for ZrIr based upon a doubled NiTi-type cell (monoclinic,  $a = 3.370$ ,  $b = 4.398$ ,  $c = 9.943 \text{ \AA}$ ;  $\beta = 99.7^\circ$ ). Rietveld refinement starting with a model based upon this doubled NiTi-type structure (space group  $P2_1/m$ ) converged to a solution with orthorhombic symmetry, and refinement of the ZrIr structure was completed in the orthorhombic space group  $Cmcm$  ( $a = 3.369$ ,  $b = 19.60$ ,  $c = 4.397 \text{ \AA}$ ). The resulting atomic positions also gave good agreement with the observed x-ray data, and similar results were obtained for the neutron and x-ray patterns of ZrRh.

This new structure type can be described as a derivative of the B2 type structure (figure 2), in which strain built up by the large size of the Zr atoms is relieved after four layers by a translation parallel to the  $a$  axis. For ZrIr, the TEM

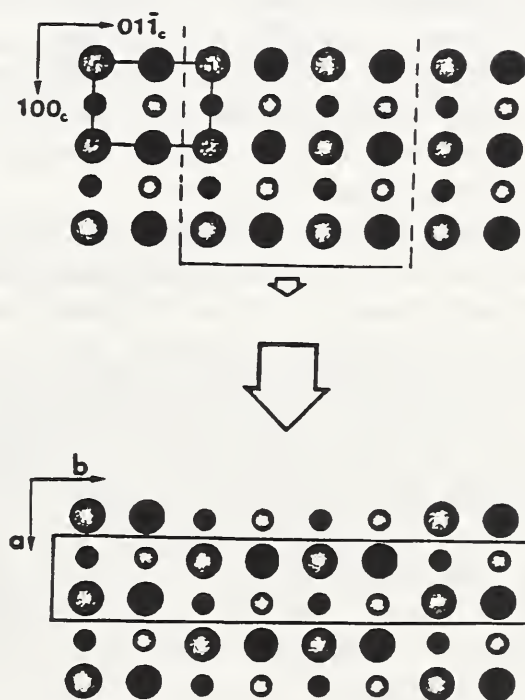


**Figure 2.** Derivation of the ZrIr-type structure from the B2 type. The large circles represent Zr atoms and the small circles represent Ir atoms; black circles are displaced  $1/2$  unit cell in the  $c$  direction. The block of four layers perpendicular to the  $b$  axis shifts one layer along the direction of the  $a$  axis.

results agree well with the structure proposed from the neutron data. One sample of ZrRh, however, exhibited a modulation in the structure parallel to the orthorhombic  $b$  axis with a period of approximately  $60 \text{ \AA}$ . It is conceiv-

able that the structure determined from powder data provides only an average structure for these materials, with large local variations possible. This hypothesis is somewhat supported by the extremely broad powder diffraction lines, which are not sharpened by annealing. Further TEM studies on ZrRh are in progress.

#### • Cation Siting Determination in CaLSX

Low silica X (LSX) zeolite is the Al-rich end-member of the faujasite zeolite family with a Si:Al ratio of 1.0 and thus has the highest possible density of cation sites. The faujasite family of molecular sieves are used for a variety of industrial processes, including catalysis and separation technologies. Understanding these processes requires detailed knowledge of the zeolite framework topology and, particularly, the siting of the charge-compensating cations.

Diffraction data for dehydrated CaLSX were collected at room temperature using synchrotron x-ray radiation at the X7a beamline at the NSLS and using CW neutrons using the 32-detector BT-1 diffractometer at NIST. The crystal structure was refined using the Rietveld method in cubic space group  $Fd\bar{3}$  in a combined x-ray/neutron refinement using the GSAS software package. The majority of the Ca is found in site I, a six-coordinate site at the center of the hexagonal prism and at site II, a three-coordinate site in the plane of the six-ring on the wall of the supercage. If these two sites were fully occupied, this would account for the stoichiometric amount of Ca. However, the occupancy of each site is below unity. About 10% of the Ca is found in site I', a three-coordinate site in the face of the hexagonal prism.

It is useful to contrast the information provided by each dataset to the CaLSX structure. As expected, a refinement using the x-ray dataset alone provided significant detail of the Ca siting, to the extent of demonstrating significant anisotropic thermal parameters for Ca in site II. However, the x-ray only refinement was insensitive to the zeolite framework and bond-length constraints were needed to prevent diver-

gence or oscillation. In contrast, the neutron-only refinement was more sensitive to the framework structure, but was less conclusive with respect to Ca siting. In both cases, significant correlation was noted between background parameters, thermal parameters and cation occupancies. In both refinements, extensive restraints on background or thermal parameters were required to obtain a model that refined in a stable manner. In the combined refinement, it was possible to refine background, thermal parameters and occupancies without any constraints. A single constraint was added in the final stages of refinement on the total amount of Ca present to ensure that the model was consistent with its chemical composition. This work demonstrates the significant advantages that can be obtained from a joint x-ray and neutron refinement.

#### • LaD<sub>2.25</sub> and TbD<sub>2.25</sub>

Typically, the superstoichiometric rare-earth metal dihydrides RH<sub>2+x</sub> possess a nominal fcc metal-lattice structure. At  $x = 0$ , the two tetrahedral (*t*) interstitial sites per metal atom are occupied by hydrogen to form a CaF<sub>2</sub>-like structure; for  $x > 0$ , the additional hydrogen partially occupies the octahedral (*o*) interstitial sites. There is some evidence that the octahedrally coordinated hydrogen (H<sub>o</sub>) atoms of both light- and heavy-rare-earth metal hydrides have similar ordering tendencies near  $x = 0.25$ . For example, neutron powder diffraction studies of both CeD<sub>2.26</sub> and the superstoichiometric heavy-rare-earth dideuteride  $\beta$ -TbD<sub>2+x</sub> ( $0.095 \leq x \leq 0.18$ ) have reported  $I4/mmm$  symmetries, indicating identically ordered D<sub>o</sub>-sublattice structures characterized by  $[0, 0, 1]_C$  and  $[1, 0, \frac{1}{2}]_C$  wavevectors. (Cubic indices are designated by either the subscript *C* or no subscript; tetragonal indices are designated by the subscript *T*.) Moreover, recent first-principles calculations of hydrogen ordering in  $\beta$ -YH<sub>2+x</sub> yielded results that indicated that the  $I4/mmm$  structure is the stable configuration near  $x = 0.25$ . A detailed neutron powder diffraction study was undertaken to help clarify whether or not  $I4/mmm$

ordering in the octahedral sublattice is indeed a general phenomenon for superstoichiometric rare-earth dihydrides having  $D(H)/\text{metal}$  ratios near 2.25.

Neutron diffraction measurements were performed between 15 and 400 K. The high-temperature patterns above 345 K could be completely indexed using a cubic cell ( $Fm\bar{3}m$  symmetry) with  $a_C \approx 5.65 \text{ \AA}$ , in accordance with previous  $\text{LaH}_{2+x}$  structural studies. The La atoms were located at  $2a$  (0,0,0),  $D_t$  atoms at  $8c$  ( $\frac{1}{4}, \frac{1}{4}, \frac{1}{4}$ ), and  $D_o$  atoms disordered over the sites  $2b$  ( $\frac{1}{2}, 0, 0$ ). At 365 K, the refinement with this model gave good agreement parameters  $R_p = 6.60\%$ ,  $R_{wp} = 8.11\%$ , and  $\chi^2 = 1.45$ . Below 345 K, some peaks showed splitting, and additional weak superlattice peaks appeared. All lines readily indexed using an enlarged tetragonal unit cell with  $a_T = a_C$  and  $c_T \approx 2a_C$ . This low-temperature tetragonal phase possessed  $I4/mmm$  symmetry and  $D_o$  ordering similar to that observed for  $\text{CeD}_{2.26}$  and  $\text{TbD}_{2+x}$ . The La atoms, located at (0,0,0) in the cubic unit cell, were split into the positions La(1) at  $4e$  (0,0, $z$ ) and La(2) at  $4c$  ( $\frac{1}{2}, 0, 0$ ); the  $D_o$  atoms, located at ( $\frac{1}{2}, 0, 0$ ) in the cubic cell, were split into D(o1) at  $2a$  (0,0,0), D(o2) at  $2b$  ( $\frac{1}{2}, \frac{1}{2}, 0$ ), and D(o3) at  $4d$  ( $\frac{1}{2}, 0, \frac{1}{4}$ ); and finally, the  $D_t$  atoms were located at the D( $t$ ) position  $16n$  ( $x, x, z$ ). Refinement of the 15 K data yielded lattice constants  $a_T = 5.6174(1)$  and  $c_T = 11.3054(3)$  with  $0.5c_T/a_T = 1.00628(5)$ ; atomic coordinates  $z = 0.2459(2)$  for La(1), and  $x = 0.2593(2)$  and  $z = 0.1267(2)$  for D( $t$ ); and occupancy parameters  $n_{D(o1)} \approx 1$ ,  $n_{D(o2)} \approx 0.06$ ,  $n_{D(o3)} \approx 0$ , and  $n_{D(t)} \approx 1$ . The resulting agreement parameters were  $R_p = 5.97\%$ ,  $R_{wp} = 7.79\%$ , and  $\chi^2 = 1.40$ . This refinement model also gave reasonable structural parameters, except for somewhat large temperature factors for the  $D_o$  atoms.

The  $\text{LaD}_{2.25}$  structures at high and low temperatures are illustrated in Figures 3 and 4. Figure 3 shows the unit cell representing the high-temperature cubic structure with randomly occupied  $o$  sites. Figure 4 shows the doubled unit

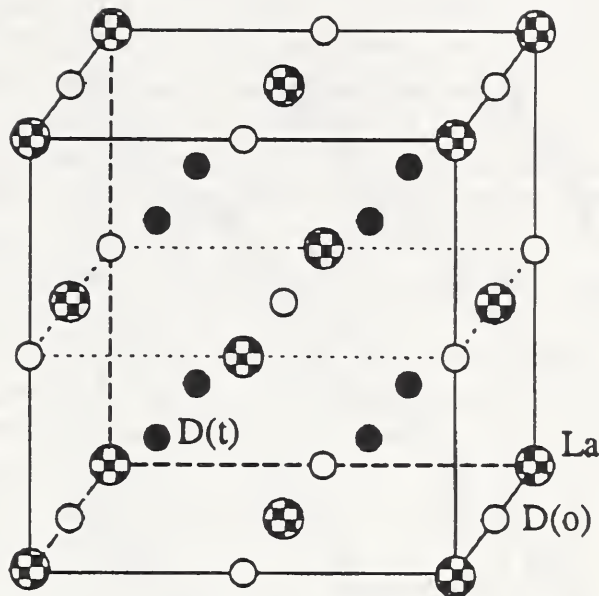


Figure 3. The  $\text{LaD}_{2.25}$  structure at high temperature (space group  $Fm\bar{3}m$ ).

cell of the low-temperature ordered structure. In the ideally ordered  $D_o$  sublattice, all D(o1) sites are occupied, while all D(o2) and D(o3) sites are vacant, suggesting that the  $D_o$  ordering is driven by a repulsive interaction between  $D_o$  atoms. The La atoms in the La(1) sites are shifted in the  $c$  direction toward the occupied D(o1) sites. The tetrahedrally coordinated deuterium ( $D_t$ ) atoms are shifted away from the center of the  $t$  sites. The net effect is an expansion of the cubes of eight  $D_t$  atoms surrounding the occupied D(o1) sites.

The La(1) and D( $t$ ) site displacements and tetragonal distortion are similar to those reported for  $\text{CeD}_{2.26}$ . Yet the  $\text{TbD}_{2+x}$  structure refinement indicated that it was not necessary to introduce an additional distortion of either the  $D_t$  or Tb sublattices to attain good agreement with the ordering model. Moreover, the upper limit for a possible tetragonal distortion was found to be  $c_C/a_C < 1.001$ . To investigate these discrepancies, the neutron powder diffraction pattern was measured for  $\text{TbD}_{2.25}$  at 70 K and the structure was refined using the

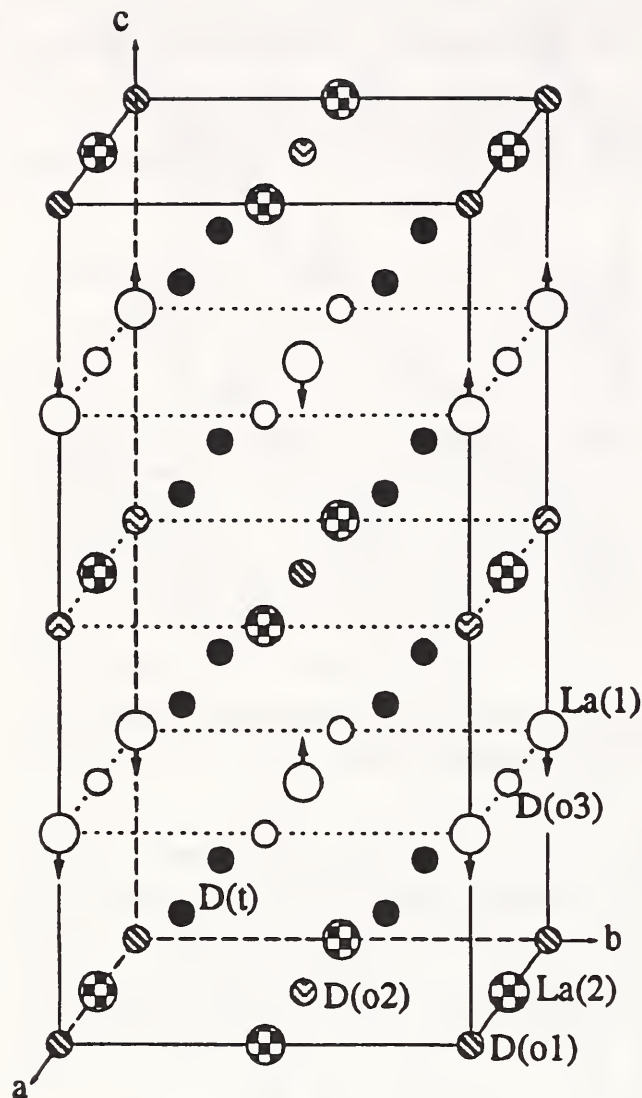


Figure 4. The  $\text{LaD}_{2.25}$  structure at low temperature (space group  $I4/mmm$ ).

same procedures as for  $\text{LaD}_{2.25}$ . Preliminary results confirm a slight tetragonal distortion ( $0.5c_T/a_T = 1.00067(8)$ , with  $a_T = 5.2196(1)$  and  $c_T = 10.4462(5)$ ), as well as significant distortions of the  $\text{D}_t$  and Tb sublattices. For Tb(1) at  $4e (0, 0, z)$  and  $\text{D}(t)$  at  $16n (x, x, z)$ , model refinement indicated  $z = 0.2465(2)$  for Tb(1), and  $x = 0.2581(2)$  and  $z = 0.1266(2)$  for  $\text{D}(t)$ . This is in excellent agreement with the  $\text{LaD}_{2.25}$  80K values,  $z = 0.2463(2)$  for La(1), and  $x = 0.2591(2)$  and  $z = 0.1269(2)$  for  $\text{D}(t)$ . Thus,

the present data indicate that there is indeed total agreement among the structural details of the La, Ce, and Tb deuterides with a D/metal stoichiometric ratio near 2.25. The tetragonal distortion observed for all of these compounds appears to accommodate better the long-range-ordered arrangement of  $\text{D}_o$  atoms.

#### • Iron Analogues of the 123-type Structure

The substitution of copper by other metal species in the structure of the 123 superconductor,  $\text{YBa}_2\text{Cu}_3\text{O}_{6+x}$ , has been used extensively to investigate the correlation between the modifications induced in the structure by the substituting cations, and the changes in the superconducting properties of the resulting materials.

In this line of research, the nuclear and magnetic structures of the compound  $\text{YBa}_2\text{Fe}_3\text{O}_{8+\delta}$ , with  $\delta \approx 0$ , were investigated a few years ago in this laboratory, and subsequently other related materials were synthesized and characterized by neutron powder diffraction techniques. The substitution compound of formula  $(\text{Y}_{1-x}\text{Ca}_x)\text{Ba}_2\text{Cu}_3\text{O}_{8+\delta}$  (with  $x=0.05, 0.10$ , and  $0.20$ ), in which yttrium is partly replaced by calcium, was used mainly to influence the saturated oxygen content in a controlled manner ( $\delta=0.09, 0.07$ , and  $0.03$  for the three samples) and to determine the location of the oxygen atoms in excess of the  $\text{O}_8$  stoichiometry. The results of this analysis can be summarized in the following way: (i) the extra oxygen atoms corresponding to  $\delta > 0$  are located on the Y/Ca layer; (ii) the presence of these atoms produces some disorder in the structure, revealed by unusually high thermal factors of the neighboring oxygen atoms of the  $(\text{FeO}_2)$  layers located below and above the Y/Ca layer; (iii) the charge compensation required by the substitution of  $\text{Y}^{3+}$  by  $\text{Ca}^{2+}$  is achieved by elimination of some of the extra oxygen, rather than oxidation of the iron atoms; (iv) the magnetic structure of these Ca-substituted compounds is similar to that of  $\text{YBa}_2\text{Fe}_3\text{O}_{8+\delta}$ ; the iron moments are coupled antiferromagnetically within each  $(\text{FeO}_2)$  layer, as well as in

the direction perpendicular to these planes and have values ranging from  $\langle \mu \rangle = 3.50(3)\mu_\beta$  to  $3.62(2)\mu_\beta$  at room temperature.

It is well known that the structure of the 123-type is generated from that of perovskite by the ordering of the cations  $Y^{3+}$  and  $Ba^{2+}$ , which results in the tripling of the c-axis of the unit cell, and by the forming of oxygen vacancies in the yttrium layer and, in the case of  $YBa_2Cu_3O_{6+x}$ , in the basal plane of the copper atoms. This process is driven by many factors, including the relative size of the cations involved in the formation of the structure. In order to throw some light on this problem, we have prepared and analyzed by neutron powder diffraction the compounds  $RBa_2Fe_3O_{8+\delta}$  with  $R=La, Nd, Dy, Er$  and  $Y$  again, in which the ionic radii of the  $R$  cations range from 1.004 Å for  $Er^{3+}$  (VIII) to 1.36 Å for  $La^{3+}$  (XII). The results of these studies show that the compounds  $RBa_2Fe_3O_{8+\delta}$  with  $R = La$  and  $Nd$  retain the structure of cubic perovskite and crystallize with the symmetry of space group  $Pm\bar{3}m$ , while the compounds with  $R=Dy, Er$  and, of course  $Y$ , form the 123-type structure with tripled c-axis and space group symmetry  $P4/mmm$ . The analysis of these results, and in particular of the relationship between ionic size and structural type, is still going on at this time. In addition, the  $La$  and  $Nd$  cubic compounds are oxygen-deficient perovskites, while the  $Dy, Er,$  and  $Y$  phases have an oxygen stoichiometry slightly higher than  $O_8$ . These features introduce some disordering into the corresponding structures which further complicates the analysis of the results.

#### • Mercury Compounds

The mercury compounds belonging to the homologous series  $HgBa_2Ca_{n-1}Cu_nO_{2n+2+\delta}$  show transition temperatures as high as 140 K at ambient pressure and over 150 K under high pressure. These compounds are isomorphous with those of the thallium series  $TlBa_2Ca_{n-1}Cu_nO_{2+3-\delta}$  and their structures consist of blocks of layers  $(BaO)(HgO_\delta)(BaO)$ , having the rock-salt configuration, interleaved

with perovskite-type blocks of variable thickness, such as  $(CuO_2), (CuO_2)(Ca)(CuO_2), (CuO_2)(Ca)(CuO_2)(Ca)(CuO_2)$ , etc. for the first, second, third, etc. member of the series, respectively. The compounds with  $n = 1, 2, 3$  have been described in a previous annual report. The structural analysis of the series has now been completed with a Rietveld study of the compounds Hg-1234 and Hg-1245, both based on neutron powder diffraction data. The results of these studies, combined with those obtained previously, can be summarized in the following way: (i) the oxygen stoichiometry of each compound depends on the method of preparation and the heat treatment of the sample; (ii) in each compound, the value of  $T_c$  is a function of oxygen stoichiometry. More specifically, as  $\delta$  increases,  $T_c$  at first increases, reaches a maximum value and then decreases; (iii) the oxygen content corresponding to the maximum value of  $T_c$  increases with  $n$ , i.e. with the thickness of the perovskite block, for example, the maximum value of  $T_c$  is obtained for  $\delta = 0.06$  in Hg-1201 and for  $\delta = 0.22$  in Hg-1212; (iv) the maximum value of  $T_c$  increases with  $n$ , but less and less rapidly as  $n$  increases; (v) the presence of doping mechanisms other than that provided by the oxygen atoms located at the center of the mercury layers is possible. So far, however, none of these extra defects has been identified and characterized with certainty.

Structural studies have also been carried out on the compound  $Hg_2Ba_2YCu_2O_{8-\delta}$ , belonging to the homologous series  $Hg_2Ba_2R_{n-1}Cu_nO_{2n+2+\delta}$ . The crystal structure of the prototype yttrium compound is schematically illustrated in figure 5. From a structural point of view, the main difference between the atomic configuration of the members of this series and that of the series  $HgBa_2Ca_{n-1}Cu_nO_{2n+2+\delta}$  is in the thickness of the rock-salt type block, which is now made of four layers of sequence  $(BaO)(HgO_\delta)(HgO_\delta)(BaO)$  rather than by the three layer block  $(BaO)(HgO_\delta)(BaO)$ . If the oxygen sites of the layers  $(HgO_\delta)$  were fully

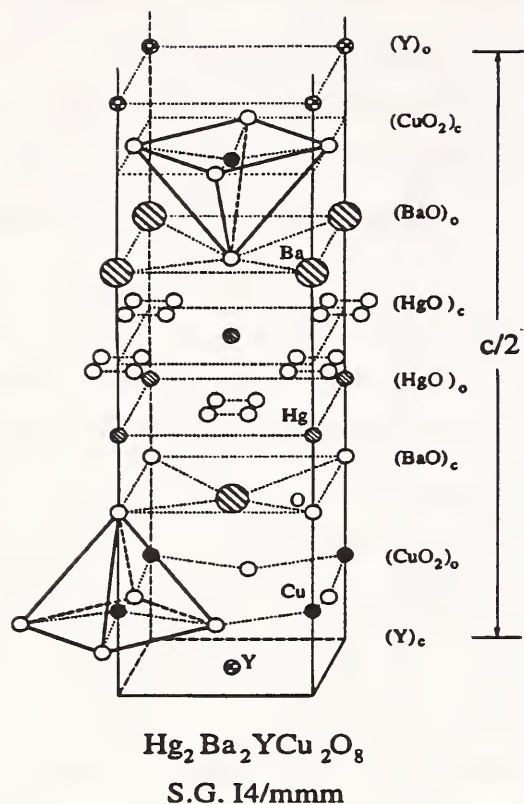


**Figure 5.** Schematic representation of the structure of  $\text{Hg}_2\text{Ba}_2\text{YCu}_2\text{O}_{8-\delta}$ . For clarity, only half of the *c*-axis is shown. The oxygen atoms of the  $(\text{HgO}_\delta)$  layers are disordered over the four position indicated in the figure.

occupied ( $\delta=1$ ) the mercury atoms would have sixfold octahedral coordination, as in  $\text{HgO}$ , with the octahedra in each block sharing edges. In fact, however, 20%–25% of the oxygen sites are vacant in  $\text{Hg}_2\text{Ba}_2\text{YCu}_2\text{O}_{8-\delta}$ , as well as in the Ca-doped material  $\text{Hg}_2\text{Ba}_2\text{Y}_{0.6}\text{Ca}_{0.4}\text{Cu}_2\text{O}_{8-\delta}$ , and thus some of the mercury atoms may acquire a fivefold pyramidal coordination. The pure yttrium compound is an insulator. Superconductivity, however, with a maximum critical temperature of 45 K can be induced by partially replacing yttrium with calcium. The question of course is whether structurally similar compounds with even higher values of the critical temperature can be prepared, and our present emphasis in this field of research is on trying to synthesize such materials.

## Database Activities

### • The NIST Crystal and Electron Diffraction Data Center

The NIST Crystal and Electron Diffraction Data Center is concerned with the collection, evaluation and dissemination of data on solid-state materials. The data center maintains a comprehensive database with chemical, physical, and crystallographic information on all types of well-characterized substances. These materials fall into the following categories: inorganic, organic, organometallic, metals, intermetallics, and minerals. During this year, the master database has been significantly augmented with respect to all categories of materials and now contains approximately 215,000 entries. From this central database, two distribution databases are produced: (1) NIST CRYSTAL DATA and (2) the NIST/Sandia/ICDDD Electron Diffraction Database.

During the year, the 1994 update to NIST Crystal Data and a new version of the Electron Diffraction Database have been completed. These databases are made available to the scientific community through computer oriented modes of dissemination including: CD-ROM, scientific instruments, and on-line searching.

In addition to the Database products, a cross-index for the Electron Diffraction Database (EDD) has been prepared. With the index, users of the EDD can immediately link an EDD entry to relevant entries in the Powder Diffraction File. This new index will be made available to manufacturers of automated Analytical Electron Microscopes as well as independent users of the EDD. Fortunately, the theory and software developed to generate this cross-index have many other applications. Especially important, from the materials science point of view, is that entries on crystalline materials in diverse databases can be uniquely cross-indexed on the basis of their lattices. Thus thermodynamic, phase diagram, and crystallographic data on the same substance can be reliably extracted from different scientific databases. In poten-



tial projects under consideration, NIST Crystal Data would serve as a hub as it links together entries in all relevant materials databases.

## Research Topics

### Structure and Phase Transition in ZrPd

L. A. Bendersky<sup>18</sup>, J. K. Stalick<sup>25</sup>, R. Portier<sup>10</sup>, and R. M. Waterstrat<sup>1</sup>.

### Martensitic Structure and Transformations in ZrIr and ZrRh.

R. M. Waterstrat<sup>1</sup>, X. Meng-Burany<sup>28</sup>, A. E. Curzon<sup>28</sup>, M. A. Estermann<sup>11</sup>, and J. K. Stalick<sup>25</sup>.

### Phase Analysis of ZrO<sub>2</sub> Coatings and Precursors

J. K. Stalick<sup>25</sup>

### Phase Analysis of SiC Powders

B. J. Wuensch<sup>17</sup> and J. K. Stalick<sup>25</sup>.

### Structural Studies of Sr<sub>3</sub>M(1)M(2)O<sub>6</sub> (M(1) = Co, Ni; M(2) = Ir, Pt) and Bi<sub>2</sub>Sr<sub>2</sub>Nb<sub>2</sub>MO<sub>11.5</sub> (M = Al, Ga)

H. zur Loye<sup>17</sup>, B. J. Wuensch<sup>17</sup>, J. Thomas<sup>17</sup> and T. Nguyen<sup>17</sup>.

### Study of the Crystal Structure of X-Form Metal-Free Phthalocyanine by Rietveld Analysis

T. L. Bluhm<sup>50</sup>, W. J. Orts<sup>25</sup>, and J. K. Stalick<sup>25</sup>.

### Crystal Structure of Annealed and As-Prepared HgBa<sub>2</sub>CaCu<sub>2</sub>O<sub>6+δ</sub>

Q. Huang<sup>25,42</sup>, J. W. Lynn<sup>25</sup>, R. L. Meng<sup>40</sup> and C. W. Chu<sup>40</sup>.

### Neutron Powder Diffraction Study of the Nuclear and Magnetic Structures of the Oxygen-Deficient Perovskite YBaCuCoO<sub>5</sub>

Q. Huang<sup>25,42</sup>, P. Karen<sup>44</sup>, V. L. Karen<sup>25</sup>, A. Kjekshus<sup>44</sup>, J. W. Lynn<sup>25</sup>, A. D. Mighell<sup>25</sup>, I. Natali Sora<sup>33</sup>, N. Rosov<sup>25</sup>, and A. Santoro<sup>25</sup>.

### Local Structure, Vacancy Ordering, and Oxide-ion Motion in Defective Perovskites

S. Adler<sup>34</sup>, S. Russek<sup>34</sup>, J. Reimer<sup>34</sup>, M. Fendorf<sup>34</sup>, A. Stacy<sup>34</sup>, Q. Huang<sup>25,42</sup>, A. Santoro<sup>25</sup>, J. W. Lynn<sup>25</sup>, J. Baltisberger<sup>34</sup>, and U. Werner<sup>34</sup>.

### Neutron Powder Diffraction Study of the Nuclear and Magnetic Structures of the Substitutional Compounds (Y<sub>1-x</sub>Ca<sub>x</sub>)Ba<sub>2</sub>Fe<sub>3</sub>O<sub>8+δ</sub>

I. Natali Sora<sup>33</sup>, Q. Huang<sup>25,42</sup>, J. W. Lynn<sup>25</sup>, N. Rosov<sup>25</sup>, P. Karen<sup>44</sup>, A. Kjekshus<sup>44</sup>, V. L. Karen<sup>25</sup>, A. D. Mighell<sup>25</sup>, and A. Santoro<sup>25</sup>.

### On the Crystallography and Magnetism of the Heavy-Fermion Compound YbBiPt

R. A. Robinson<sup>16</sup>, A. Purwanto<sup>47</sup>, M. Kohgi<sup>47</sup>, P. C. Canfield<sup>3,16</sup>, T. Kamiyama<sup>47</sup>, Y. Ishigaki<sup>47</sup>, J. W. Lynn<sup>25</sup>, R. W. Erwin<sup>25</sup>, and E. Peterson<sup>16</sup>.

### Corrections for High-absorbing Samples on Multi-detector Diffractometers

N. Rosov<sup>25</sup> and J. W. Lynn<sup>25</sup>.

### Synthesis and Properties of a Cuprate Superconductor Containing Double Mercury-Oxygen Layers

P. G. Radaelli<sup>7</sup>, M. Marezio<sup>7,5</sup>, M. Perroux<sup>7</sup>, S. de Brion<sup>7</sup>, J. L. Tholence<sup>7</sup>, Q. Huang<sup>25,42</sup>, and A. Santoro<sup>25</sup>.

### Neutron Powder Diffraction Study of the Crystal Structure of HgBa<sub>2</sub>Ca<sub>4</sub>Cu<sub>5</sub>O<sub>12+δ</sub> at Room Temperature and at 10K

Q. Huang<sup>25,42</sup>, O. Chmaissem<sup>25</sup>, J. J. Capponi<sup>7</sup>, C. Chailout<sup>7</sup>, M. Marezio<sup>7,5</sup>, J. T. Tholence<sup>7</sup>, and A. Santoro<sup>25</sup>.

### Crystal Structure of Oxygen Overdoped HgBa<sub>2</sub>CuO<sub>4+δ</sub> (T<sub>c</sub> = 0K)

A. Santoro<sup>25</sup>, Q. Huang<sup>25,42</sup>, and M. Marezio<sup>7</sup>.

### Neutron Diffraction Study of the Nuclear and Magnetic Structures of LaVO<sub>3</sub> under Magnetic Field

Q. Huang<sup>25,42</sup>, A. Santoro<sup>25</sup>, R.J.Cava<sup>5</sup>, and M. Marezio<sup>7,5</sup>.

### Neutron Powder Diffraction Study of the Nuclear and Magnetic Structure of the Antiferromagnetic Superconductor HoNi<sub>2</sub>B<sub>2</sub>C

Q. Huang<sup>25,42</sup>, A. Santoro<sup>25</sup>, T. D. Grigereit<sup>25</sup>, J. W. Lynn<sup>25</sup>, R. J. Cava<sup>5</sup>, J. J. Krajewski<sup>5</sup>, and W. F. Peck, Jr<sup>5</sup>.

### Phase Structure and Phase Transition in the BaPbO<sub>3</sub>-BaBiO<sub>3</sub> System

Q. Huang<sup>25,42</sup>, A. Santoro<sup>25</sup>, and R. J. Cava<sup>5</sup>.

### Neutron Diffraction Study of the Nuclear and Magnetic Structures of REBa<sub>2</sub>Fe<sub>3</sub>O<sub>8+δ</sub>

A. Santoro<sup>25</sup>, Q. Huang<sup>25,42</sup>, P. Karen<sup>44</sup>, V. L. Karen<sup>25</sup>, J. W. Lynn<sup>25</sup>, A. D. Mighell<sup>25</sup>, and T. D. Grigereit<sup>25</sup>.

### The Nuclear and Magnetic Structures of YBa<sub>2</sub>Fe<sub>3-x</sub>Co<sub>x</sub>O<sub>8+δ</sub>

A. Santoro<sup>25</sup>, Q. Huang<sup>25,42</sup>, P. Karen<sup>44</sup>, V. L. Karen<sup>25</sup>, J. W. Lynn<sup>25</sup>, A. D. Mighell<sup>25</sup>, and T. D. Grigereit<sup>25</sup>.

- Oxygen Content Dependence of the Crystal Structure of  $\text{YBa}_2\text{Fe}_3\text{O}_{8+6}$**   
Q. Huang<sup>25,42</sup>, A. Santoro<sup>25</sup>, P. Karen<sup>44</sup>, V. L. Karen<sup>25</sup>, J. W. Lynn<sup>25</sup>, A. D. Mighell<sup>25</sup>, and T. E. Grigereit<sup>25</sup>.
- Neutron Diffraction Study of Structure of the Solid Solution in the  $\text{LaFeO}_3\text{-YFeO}_3$  System**  
A. Santoro<sup>25</sup>, Q. Huang<sup>25,42</sup>, P. Karen<sup>44</sup>, V. L. Karen<sup>25</sup>, J. W. Lynn<sup>25</sup>, A. D. Mighell<sup>25</sup>, T. D. Grigereit<sup>25</sup>, and O. Chmaissem<sup>25</sup>.
- Magnetic Susceptibility and Low Temperature Structure of the Linear Chain Cuprate  $\text{Sr}_2\text{CuO}_3$**   
T. Ami<sup>9</sup>, M. K. Crawford<sup>9</sup>, R. L. Harlow<sup>9</sup>, Z. R. Wang<sup>13</sup>, D. C. Johnston<sup>13</sup>, Q. Huang<sup>25,42</sup>, and R. W. Erwin<sup>25</sup>.
- Structural Phase Transition in  $\text{La}_{2-x}\text{Ba}_x\text{CuO}_4$**   
M. Crawford<sup>9</sup> and Q. Huang<sup>25,42</sup>.
- Neutron Powder Diffraction Study of the Crystal Structure of Na-doped Y-123 High  $T_c$  Superconductor**  
Q. Huang<sup>25,42</sup>, C. H. Chen<sup>8</sup> and B. Kumar<sup>8</sup>.
- The Crystal Structure of  $\text{YBa}_2\text{Cu}_{3-x}\text{M}_x\text{O}_{7-6}$  ( $\text{M} = \text{Fe}, \text{Zn}$ )**  
Q. Huang<sup>25,42</sup> and T. Clinton<sup>42</sup>.
- Oxygen Content Dependence of the Crystal Structure and Its Relation to Superconductivity in  $\text{HgBa}_2\text{CuO}_{4+6}$**   
Q. Huang<sup>25,42</sup>, J. W. Lynn<sup>25</sup>, Q. Xiong<sup>40</sup>, and C. W. Chu<sup>40</sup>.
- Neutron Powder Diffraction Studies of  $\text{Sr}_4\text{N}_2\text{ND}$**   
F. Altorfer<sup>25,42</sup>, T. Sichla<sup>38</sup>, and H. Jacobs<sup>38</sup>.
- Strain Partitioning Feasibility Studies for Titanium Matrix Composites**  
H. J. Prask<sup>25</sup>, P. C. Brand<sup>25</sup>, B. Maruyama<sup>25,49</sup>, D. B. Miracle<sup>49</sup>, and P. Smith<sup>49</sup>.
- Neutron Diffraction Study of Austempered Cast Irons**  
C. S. Choi<sup>24,25</sup>, W. Sharpe<sup>24</sup>, J. Barker<sup>25</sup>, and C. J. Glinka<sup>25</sup>.
- Study of Carbon Nanotubes**  
D. Reznik<sup>25</sup>, D. A. Neumann<sup>25</sup>, J. R. D. Copley<sup>25</sup>, M. G. Mitch<sup>23</sup>, and J. S. Lannin<sup>23</sup>.
- Neutron Powder Diffraction Studies of  $\text{LaD}_{2+x}$  ( $x=0.25, 0.50, 0.625, 0.75$ )**  
T. J. Udovic<sup>25</sup>, Q. Huang<sup>25,42</sup>, J. J. Rush<sup>25</sup>, J. Schefer<sup>11,22</sup>, and I. S. Anderson<sup>12</sup>.
- Neutron Powder Diffraction Study of  $\text{YD}_3$**   
T. J. Udovic<sup>25</sup>, Q. Huang<sup>25,42</sup>, and J. J. Rush<sup>25</sup>.
- Neutron Powder Diffraction Study of  $\beta\text{-TbD}_{2.25}$**   
T. J. Udovic<sup>25</sup>, Q. Huang<sup>25,42</sup>, J. J. Rush<sup>25</sup>, J. Schefer<sup>11,22</sup>, and I. S. Anderson<sup>12</sup>.
- Neutron Powder Diffraction Study of  $\text{NbD}(\text{H})_x$  ( $0.72 \leq x \leq 0.92$ )**  
B. Hauer<sup>14</sup>, R. Hempelmann<sup>46</sup>, D. Richter<sup>14</sup>, T. J. Udovic<sup>25</sup>, and J. J. Rush<sup>25</sup>.
- The Location and Geometry of the Hydrofluorocarbons 134 and 134a Encaged in Na-X Zeolite**  
M. K. Crawford<sup>9</sup>, T. J. Udovic<sup>25</sup>, J. M. Nicol<sup>25</sup>, R. R. Cavanagh<sup>30</sup>, J. J. Rush<sup>25</sup>, J. B. Parise<sup>29</sup>, C. P. Grey<sup>9</sup>, and D. R. Corbin<sup>9</sup>.
- Structural Characterization of  $\text{Ba}_2\text{MBiO}_6$  ( $\text{M} = \text{Ce}, \text{Tb}, \text{Pr}$ ) Phases**  
K. P. Reis<sup>40</sup>, A. J. Jacobson<sup>40</sup>, and J. M. Nicol<sup>25</sup>.
- Structural Characterization of  $\text{RbBiNb}_2\text{O}_7$**   
W. T. A. Harrison<sup>40</sup>, A. J. Jacobson<sup>40</sup>, and J. M. Nicol<sup>25</sup>.
- Structural Characterization of Cation Locations in Zeolite Molecular Sieves**  
B. H. Toby<sup>2</sup>, C. G. Coe<sup>2</sup>, and J. M. Nicol<sup>25</sup>.
- Structural Characterization of Oxide Phases**  
T. M. Nenoff<sup>27</sup> and J. M. Nicol<sup>25</sup>.
- Structural Characterization of  $\text{ZnV}_2\text{O}_4$**   
W. T. A. Harrison<sup>40</sup>, A. J. Jacobson<sup>40</sup>, and J. M. Nicol<sup>25</sup>.
- Structural Studies of  $\text{Bi}_2\text{O}_2\text{Mn}_{0.25}\text{V}_{0.25}\text{O}_{3.5}$  and  $\text{Bi}_2\text{Mn}_{0.2}\text{V}_{0.8}\text{O}_{5.5}$**   
W. T. A. Harrison<sup>40</sup>, A. J. Jacobson<sup>40</sup>, and J. M. Nicol<sup>25</sup>.
- Structural Refinement of  $\text{SrCo}_{0.8}\text{Fe}_{0.2}\text{O}_x$  Phases**  
W. T. A. Harrison<sup>40</sup>, A. J. Jacobson<sup>40</sup>, and J. M. Nicol<sup>25</sup>.
- Structural Refinement of Deuterated SAPO-5 Zeolite**  
D. Demuth<sup>41</sup>, J. MacLeod<sup>37</sup>, G. D. Stucky<sup>37</sup>, and J. M. Nicol<sup>25</sup>.

### Room Temperature Structural Studies of Ca-LSX Zeolite

R. Morris<sup>25,37</sup>, A. K. Cheetham<sup>37</sup>, B. H. Toby<sup>2</sup>, J. E. MacDougall<sup>2</sup>, and C. G. Coe<sup>2</sup>.

### Structural Studies of Adsorbate and Cation Locations in Zeolites

B. H. Toby<sup>2</sup>, C. G. Coe<sup>2</sup>, and J. M. Nicol<sup>25</sup>.

### Maximum Entropy Phase Determination, Extension, and Refinement for Macromolecules

E. Prince<sup>25</sup>, L. Sjölin<sup>39</sup>, J. M. Stewart<sup>42</sup>, and D. M. Collins<sup>20</sup>.

### Crystal Structure and Magnetism in Layered Cuprates

W.-H. Li<sup>19</sup>, W. T. Hsieh<sup>19</sup>, J. W. Lynn<sup>25</sup>, K. C. Lee<sup>19</sup>, J. H. Shieh<sup>19</sup>, and H. C. Ku<sup>19</sup>.

### Crystallography and Sample Characterization of UPd<sub>x</sub>Cu<sub>5-x</sub>

M. Aronson<sup>43</sup>, R. Osborn<sup>4</sup>, R. A. Robinson<sup>16</sup>, J. W. Lynn<sup>25</sup>, R. Chau<sup>36</sup>, C. L. Seaman<sup>36</sup>, and M. B. Maple<sup>36</sup>.

### Search for a Structural Phase Transition in Elemental Tb

M. Melamud<sup>18</sup>, Q. Huang<sup>25,42</sup>, J. W. Lynn<sup>25</sup>, and J. Cullen<sup>21</sup>.

### Structure of BaCuO<sub>2</sub>

M. Melamud<sup>18</sup>, L. H. Bennett<sup>18</sup>, and J. K. Stalick<sup>25</sup>.

### The Structure of White Phosphorus in the Orientationally Ordered and Disordered Phases

W. A. Kamitakahara<sup>25</sup>, Q. Huang<sup>25,42</sup>, F. Gompf<sup>15</sup>, and D. A. Neumann<sup>25</sup>.

### Crystal Structure and Magnetism of the Spin-Peierls Compound GeCuO<sub>3</sub>

M. A. Green<sup>26</sup>, M. Kurmoo<sup>26</sup>, J. K. Stalick<sup>25</sup>, and P. Day<sup>26</sup>.

### Structure and Conductivity of the Layered Oxides (Ba,Sr)<sub>n+1</sub>(Sn,Sb)<sub>n</sub>O<sub>3n+1</sub>

M. A. Green<sup>26</sup>, K. Prassides<sup>31</sup>, P. Day<sup>26</sup>, and J. K. Stalick<sup>25</sup>.

### Synchrotron X-ray Diffraction, Neutron Diffraction, NMR, and Computational Study of the Siliceous Form of Zeolite Ferrierite

R. E. Morris<sup>37</sup>, S. J. Weigel<sup>37</sup>, N. J. Henson<sup>37</sup>, L. M. Bull<sup>37</sup>, and A. K. Cheetham<sup>37</sup>.

### La<sub>2+x</sub>Ti<sub>5+0.75y</sub>Al<sub>17-y</sub>O<sub>38-x</sub>, Related Structures and Their Relationship to Ca- and Al-Rich Inclusions in Meteorites

R. E. Morris<sup>37</sup>, J. J. Owen<sup>37</sup>, and A. K. Cheetham<sup>37</sup>.

### Determination of D<sub>2</sub>O Locations in D-SAPO34 by Neutron Diffraction

L. J. Smith<sup>37</sup>, R. E. Morris<sup>37</sup>, A. K. Cheetham<sup>37</sup>, L. Marchese<sup>26</sup>, and J. M. Thomas<sup>26</sup>.

### Neutron Powder Diffraction Studies of Na Zeolite Y

L. M. Bull<sup>37</sup>, R. E. Morris<sup>37</sup>, and A. K. Cheetham<sup>37</sup>.

### Structural Studies of Li<sub>1-5x</sub>Ta<sub>1+x</sub>O<sub>3</sub> Glasses

J. A. Alleman<sup>37</sup>, Y. Xia<sup>37</sup>, R. E. Morris<sup>37</sup>, H. Eckert<sup>37</sup>, J. S. Speck<sup>37</sup>, C. G. Levi<sup>37</sup>, F. F. Lange<sup>37</sup>, and S. Anderson<sup>48</sup>.

### Neutron Powder Diffraction Study of the Gallosilicate Analogue of Zeolite Ferrierite

S. Weigel<sup>37</sup>, R. E. Morris<sup>37</sup>, and A. K. Cheetham<sup>37</sup>.

### Neutron and Synchrotron Powder Diffraction Studies of Cu-Ferrierite and Cu-Mordenite Zeolites

M. P. Attfield<sup>37</sup>, R. E. Morris<sup>37</sup>, S. Weigel<sup>37</sup>, and A. K. Cheetham<sup>37</sup>.

### Crystal and Magnetic Structure of Pr<sub>1.5</sub>Ce<sub>0.5</sub>Sr<sub>2</sub>Ba<sub>2</sub>TaO<sub>10</sub>

N. Rosov<sup>25</sup>, J. W. Lynn<sup>25</sup>, T. Goodwin<sup>35</sup>, and R. N. Shelton<sup>35</sup>.

### Crystal Structure of Orthorhombic and Rhombohedral NiF<sub>3</sub>

L. Chacon<sup>34</sup>, N. Bartlett<sup>34</sup>, N. Rosov<sup>25</sup>, and J. W. Lynn<sup>25</sup>.

### Crystal Structure of the Molecular Ferromagnet Ni(oxamide)

N. Rosov<sup>25</sup>, J. W. Lynn<sup>25</sup>, and C. Landee<sup>6</sup>.

### Structural Studies of CuMP<sub>2</sub>(S,Se)<sub>6</sub> (M=Cr, In)

V. Cajipe<sup>45</sup> and J. E. Fischer<sup>45</sup>.

### NIST Lattice Theory and Software

V. L. Karen<sup>25</sup> and A. D. Mighell<sup>25</sup>.

### Applications of NIST's Crystallographic Data Bases

V. L. Karen<sup>25</sup> and A. D. Mighell<sup>25</sup>.

**Structural Phase Transitions in  $\text{KMnF}_3$** P. M. Gehring<sup>25</sup>, S. M. Shapiro<sup>51</sup>, and A. Giband<sup>52</sup>**Orientational Order in  $\text{C}_{61}\text{H}_2$** J. E. Fischer<sup>25,45</sup>, D. A. Neumann<sup>25</sup>, J. R. D. Copley<sup>25</sup>, P. A. Heiney<sup>45</sup>, R. M. Strongin<sup>45</sup>, M. Cichy<sup>45</sup>, and A. B. Smith III<sup>45</sup>.**Orientational Order and Disorder in  $\text{Na}_x\text{C}_{60}$** T. Yildirim<sup>42,45</sup>, D. A. Neumann<sup>25</sup>, J. E. Fischer<sup>25,45</sup>, D. Reznik<sup>25</sup>, and J. R. D. Copley<sup>25</sup>**Affiliations**

- <sup>1</sup>ADA Paffenbarger Research Center  
<sup>2</sup>Air Products and Chemicals  
<sup>3</sup>Ames Laboratory  
<sup>4</sup>Argonne National Lab  
<sup>5</sup>AT & T Bell Laboratories  
<sup>6</sup>Clark University  
<sup>7</sup>C.N.R.S., France  
<sup>8</sup>Dayton University  
<sup>9</sup>E. I. Du Pont de Nemours and Company  
<sup>10</sup>E. N. S. C. P., France  
<sup>11</sup>ETH Zürich  
<sup>12</sup>Institut Laue-Langevin, France  
<sup>13</sup>Iowa State University  
<sup>14</sup>KFA Jülich, Germany  
<sup>15</sup>KFZ Karlsruhe, Germany  
<sup>16</sup>Los Alamos National Laboratory  
<sup>17</sup>Massachusetts Institute of Technology  
<sup>18</sup>Metallurgy Division  
<sup>19</sup>National Central Univeristy, Taiwan  
<sup>20</sup>Naval Research Laboratory  
<sup>21</sup>Naval Surface Warfare Center  
<sup>22</sup>Paul Scherrer Institut, Switzerland  
<sup>23</sup>Pennsylvania State University  
<sup>24</sup>Army Armament RD&E Ctr.  
<sup>25</sup>Reactor Radiation Division  
<sup>26</sup>Royal Institution of Great Britain  
<sup>27</sup>Sandia National Laboratory  
<sup>28</sup>Simon Fraser University, Canada  
<sup>29</sup>SUNY Stonybrook  
<sup>30</sup>Surface and Microanalysis Science Division  
<sup>31</sup>Sussex University, UK  
<sup>32</sup>Tohoku University, Japan  
<sup>33</sup>University of Brescia, Italy  
<sup>34</sup>University of California, Berkeley  
<sup>35</sup>University of California, Davis

- <sup>36</sup>University of California, San Diego  
<sup>37</sup>Univeristy of California, Santa Barbara  
<sup>38</sup>University of Dortmund, Germany  
<sup>39</sup>University of Göteborg, Sweden  
<sup>40</sup>University of Houston  
<sup>41</sup>University of Mainz, Germany  
<sup>42</sup>University of Maryland  
<sup>43</sup>University of Michigan  
<sup>44</sup>University of Oslo, Norway  
<sup>45</sup>University of Pennsylvania  
<sup>46</sup>Universität des Saarlandes, Germany  
<sup>47</sup>University of Tsukuba, Japan  
<sup>48</sup>Westmont College  
<sup>49</sup>Wright Laboratory  
<sup>50</sup>Xerox Corp  
<sup>51</sup>Brookhaven National Laboratory  
<sup>52</sup>Université du Maine, France

# Surface and Interfacial Studies

Many interesting studies have been performed on the NG-7 and BT-7 reflectometers since the last report and prior to the reactor shutdown at the end of May 1994. Both instruments were, in fact, oversubscribed by approximately a factor of two. What follows are some of the highlights in thin film, multilayer, and related surface and interface research, carried out here at NIST in the Reactor Radiation Division.

## Depositional Interdiffusion in Ba Stearate LB Films

Langmuir-Blodgett (LB) films have been the subject of a considerable research effort for the last decade because of their potential use as sensors, microelectronic devices, dielectric films, and structural templates. Technological development has been slower than anticipated, due largely to the observation that films undergo rearrangement and interdiffusion both during deposition and at elevated temperatures, where devices based on LB technology might be used [1].

In order to understand these rearrangement processes better, we have employed both neutron and x-ray reflectivity measurements to characterize Langmuir-Blodgett films deposited on a hydrophobic substrate. Contrast between neighboring bilayers was obtained in the neutron measurements by various schemes of selective deuteration during film fabrication. Measurements have been conducted for both as-deposited films and films annealed just below the melting temperature. We report here our results for one of the as-deposited films. A more detailed publication is forthcoming [2].

Figures 1 and 2 show the neutron and x-ray reflectivity data of an LB film composed of twenty bilayers of barium stearate, with the aliphatic tails of every odd bilayer deuterated. The dashed curves are the simulated reflectivity from a "perfect" film, where there is no interdiffusion between monolayers, where each hydrophilic head group consists entirely of bar-

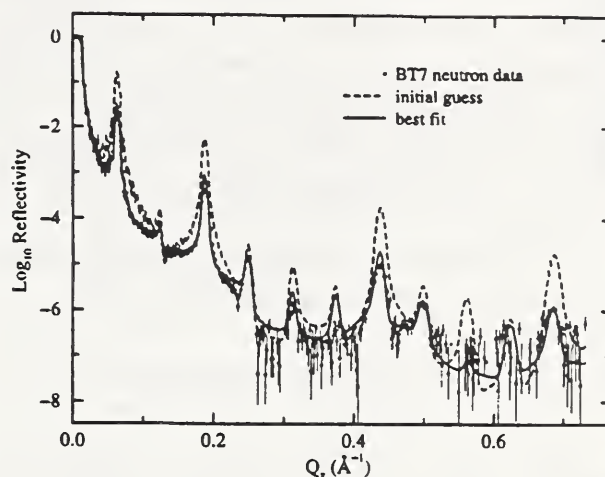


Figure 1. Neutron reflectivity and fits for as-deposited film.

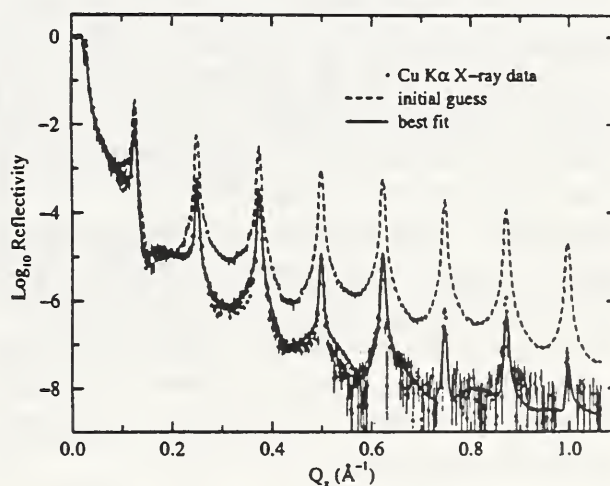


Figure 2. X-ray reflectivity and fits for as-deposited film.

ium salts, and where the interfaces are perfectly smooth. The deviation of this curve from the data indicates some molecular rearrangement upon deposition. We have fit the data to a model which assumes the following: (1) some degree of interdiffusion between H and D molecules, assumed constant over the film; (2) some amount of  $\text{Ba}^{2+}$  replaced with two protons in the hy-

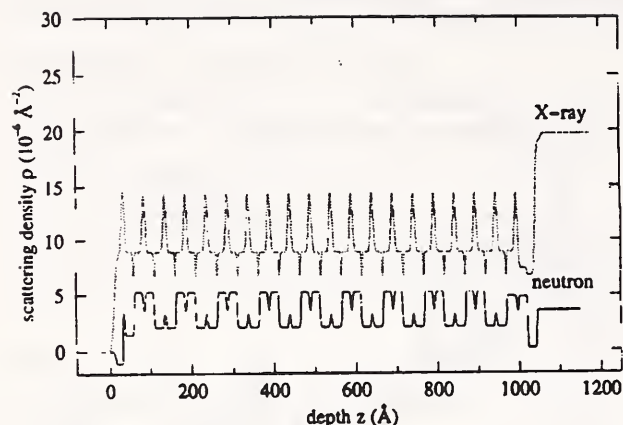


Figure 3. Reflectivity profiles: final fit.

drophilic layers; and (3) roughness between the layers. In addition, the overall density and thicknesses of the  $-\text{CH}_2-$  and head group units were allowed to vary. The best fits are shown in the solid lines of figure 1.

Model fitting of these data sets shows the following: (1) The bilayer thickness is  $50.41 \pm 0.02$  Å, consistent with an untilted aliphatic tail. (2) The area per molecule is  $20.2 \pm 0.1$  Å<sup>2</sup>, consistent with the area derived from pressure-area isotherms for the Langmuir layer. (3) The hydrophilic layer consists of a mixture of Ba salts and undissociated carboxylic acid groups. Its stoichiometry is given as  $\text{Ba}_{1-y}\text{H}_{2y}(\text{COO})_2$ , where  $y = 0.45 \pm 0.04$ . (4) Neighboring bilayers are 30% intermixed, an amount too large to be explained solely by incomplete transfer coefficients during growth.

Real space scattering density profiles corresponding to the best fit neutron and x-ray reflectivity data are shown in figure 3.

Several interdiffusion mechanisms may be responsible for the observed rearrangements, including bilayer or monolayer folding while under water or single-molecule self-diffusion, either at the meniscus or while immersed [2,3]. Further measurements are in progress to help distinguish these mechanisms, as well as to investigate the diffusion at elevated temperatures.

## References

- [1] M. R. Buhaenko, M. J. Grundy, R. M. Richardson, and S. J. Roser, *Thin Solid Films* **159**, 253 (1988).
- [2] D. G. Wiesler, C. F. Majkrzak, J. F. Ankner, L. A. Feigin, T. S. Berzina, and V. I. Troitsky, To be submitted to *J. Phys. Chem.*
- [3] D. K. Schwartz, J. Garnæs, R. Viswanathan, and J. A. N. Zasadzinski, *Science* **257**, 508 (1992); D. K. Schwartz, R. Viswanathan, and J. A. N. Zasadzinski, *J. Phys. Chem.* **96**, 10444 (1992).

## Neutron Reflectivity Studies of Single Lipid Bilayers Supported on Planar Substrates

The neutron reflectivity technique is well-suited to the study of structural changes in lamellar systems such as lipid monolayers, bilayers or multilayers and biological membranes. It is important to be able to measure a single lipid bilayer in aqueous solution since it represents a working model for a biological membrane. Parameters of interest include the thickness of bilayer and its individual components, penetration of water into bilayer, asymmetry of the lipid distribution and changes in membrane properties due to interactions with small ions, peptides, proteins and other lipids. In addition, the depth of penetration of protein amino acid side chains and small molecules which interact with the bilayer as well as the density of incorporation of peptides and proteins within the membrane are important parameters since membrane proteins play a crucial role in biological function.

Neutron reflectivity has been used to probe the structure of single phosphatidylcholine (PC) bilayers adsorbed onto a planar silicon surface in an aqueous environment [1]. Fluctuations in the neutron density profiles perpendicular to the Si/water interface were determined for different lipids as a function of the hydrocarbon chain length. A novel experimental set-up was implemented to decrease the incoherent background scattering, thereby extending the spec-

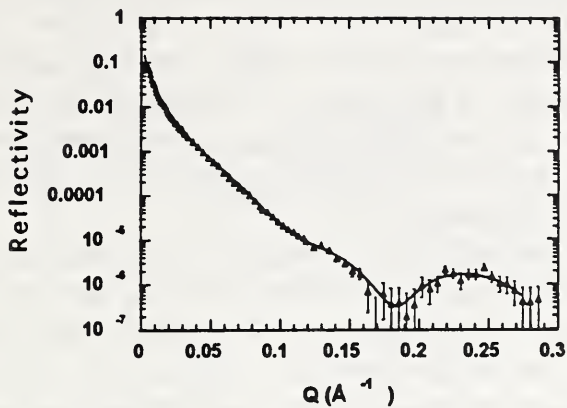


**Figure 4.** Reflected intensity versus  $Q$  for a DPPC bilayer with deuterated hydrocarbon chains in silicon-matched solvent. The solid line represents one of the model-independent fits.

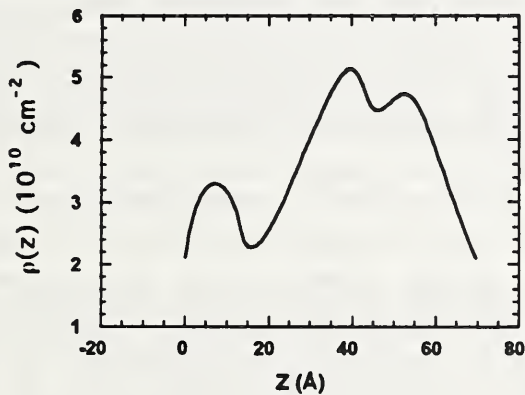


**Figure 5.** Scattering length density profile as a function of distance perpendicular to the bilayer corresponding to the fitted line in figure 4.

tral range and increasing the resolution of the measurements. For PC bilayers in  $D_2O$  and silicon-matched (38%  $D_2O/62\%H_2O$ ) solvents, reflectivity was obtained to  $Q \leq 0.3 \text{ \AA}^{-1}$ , which covered up to seven orders of magnitude in reflected intensity. The lipids were studied in both the gel and liquid crystalline phases by monitoring changes in the density profiles as a function of temperature. Contrast variation experiments were used to aid in the accurate modeling of the

scattering data and to pinpoint the presence of water around the hydrophilic head groups.

Scattering length density profiles were obtained from the data using two different fitting methods. In the model-dependent method, the density profiles were composed of histogram functions based on the theoretical lipid composition whereas, in the model-independent method, the density profiles were composed of randomly-generated smooth functions represented by parametric  $B$ -splines. Figure 4 shows the reflected intensity as a function of  $Q$  for a single dipalmitoyl-phosphatidylcholine (DPPC) bilayer in silicon-matched solvent. The hydrocarbon chains were deuterated in order to enhance their scattering density with respect to the lipid head groups and the solvent. The solid line represents one of the model-independent fits. The scattering length density profile corresponding to the fitted line is illustrated in figure 5. The first, smaller peak represents the silicon-oxide layer at the surface of the substrate and the larger peak results mainly from the deuterated hydrocarbon chains which have a much higher scattering length density than the oxide layer or the solvent.

## Reference

- [1] S. Krueger, W. J. Orts, N. F. Berk, C. F. Majkrzak, B. Koenig, and K. Gawrisch, to be published.

## Magnetic Systems

### • Field Dependence of the Magnetic Coupling Angle in a $Fe_{25}Co_{75}/Mn$ Superlattice

As demonstrated in multilayers composed of  $Fe/Cr$  [1],  $Co/Ru$  [2] and similar transition-metals [3], ferromagnetic layers tend to align parallel or antiparallel across nonmagnetic layers depending in an oscillatory manner on the interlayer thickness. Recent experimental studies of  $Fe/Cr$  [4],  $Fe/Al$  [5], and  $Fe/Cu$  [6] suggest that under particular conditions the interlayer exchange coupling may be biquadratic in

nature with the layer moments aligned at a  $90^\circ$  angle. In a formalism [4] developed to describe this phenomena, the exchange energy includes contributions from the usual bilinear coupling ( $\mathcal{J}^{\text{BL}}$ ) between the moments in adjacent layers ( $\bar{\mu}_1$  and  $\bar{\mu}_2$ ) and from a biquadratic coupling term ( $\mathcal{J}^{\text{BQ}}$ ):

$$E(\phi) = -\mathcal{J}^{\text{BL}}\bar{\mu}_1 \cdot \bar{\mu}_2 - \mathcal{J}^{\text{BQ}}(\bar{\mu}_1 \cdot \bar{\mu}_2)^2. \quad (1)$$

Minimization of this expression suggests that noncollinear spin structures with coupling angles ranging from  $0^\circ$  -  $180^\circ$  may be stable depending on the relative sign and magnitude of the exchange coefficients.

Based upon preliminary analysis of bulk magnetization and ferromagnetic resonance (FMR) data [7], our collaborators at the Naval Research Laboratory have inferred that  $\text{Fe}_{25}\text{Co}_{75}/\text{Mn}$  multilayers and trilayers exhibit a noncollinear magnetic ordering with a coupling angle near  $90^\circ$  in zero field. To corroborate their conclusions and determine the exact coupling angle, we have extracted the depth-dependent magnetization for a (100)  $[\text{Mn}(1.3 \text{ nm})|\text{Fe}_{25}\text{Co}_{75}(7.0 \text{ nm})]_5$  superlattice using polarized neutron reflectivity. We note that this superlattice structure was grown by molecular beam epitaxy techniques [7] and was characterized first by x-ray reflectivity to verify its structural integrity.

We performed the neutron reflectivity studies on the BT-7 reflectometer with the samples magnetized in fields ranging from 90 - 6500 Oe applied along the [001] in-plane axis. A typical neutron scan for the superlattice in a small field of 90 Oe is shown in figure 6. The circles and squares correspond to the (++) and (--) non-spin flip cross sections respectively, and the triangles and inverted triangles mark the (+-) and (-+) spin flip cross sections. The plus and minus subscripts designate the indices for neutrons polarized parallel and antiparallel to the applied guide field. In general, the non-spin flip cross sections are sensitive both to the sample structure and the in-plane component of the sample moment parallel to the field direction.

The spin flip cross sections measure the in-plane component of the sample moment perpendicular to the applied field. Measuring all four spin states one can obtain a spatial profile of the distribution of structural and magnetic scatterers through the sample using a model based upon the one-dimensional wave equation for a stratified medium.[8]

Several features in figure 6 provide qualitative information about the resultant spin structure. A pronounced peak is evident in the spin flip data at  $Q \approx 0.039 \text{ \AA}^{-1}$ . Clearly the perpendicular component of the moment has a periodicity of 16.5 nm, which is twice the repeat distance of the superlattice bilayer (8.3 nm). Similar features are apparent in the non-spin flip cross sections. A simultaneous fit of all four data sets (solid lines) reveals that the spins in alternating  $\text{Fe}_{25}\text{Co}_{75}$  layers are separated by an angle of  $70^\circ \pm 5^\circ$  (shown schematically in Fig. 6), rather than the expected  $90^\circ$  coupling angle. The moments in the layers tend to align parallel to easy-axes directions because of the competing effects of anisotropy and interlayer exchange coupling.

In a field of 850 Oe, neutron reflectivity data suggest that the spins retain their  $70^\circ$  coupling angle between adjacent layers, but they reorient symmetrically about the applied field direction. Upon increasing the field to 6500 Oe, the coupling angle slowly collapses to  $40^\circ \pm 5^\circ$ . In agreement with bulk magnetization results, we observe that the saturation field exceeds 10,000 Oe.

While the evolution of the spin structure with field can be understood in terms of the competing contributions from anisotropy, exchange and Zeeman energies, the origin of the  $70^\circ$  coupling angle at low field values is still unclear. While the addition of a biquadratic term in the exchange term (equation 1) may give rise to noncollinear structures, the magnetization and FMR data are better described by a model [9] which includes the effects of interfacial roughness on the ferromagnetic  $\text{Fe}_{25}\text{Co}_{75}$  and antiferromagnetic Mn layers. Further polarized neu-



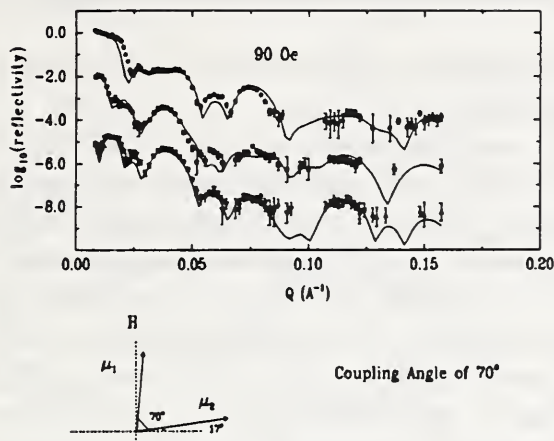


**Figure 6.** Polarized neutron reflectivity of a (100)  $[\text{Mn}(1.3 \text{ nm})|\text{Fe}_{25}\text{Co}_{75}(7.0 \text{ nm})]_5$  superlattice as a function of wavevector  $Q$  at room temperature in a field of 90 Oe. The  $(++)$  and  $(--)$  non-spin flip cross sections are designated by circles and squares respectively and the latter is vertically offset for clarity. The  $(+-)$  and  $(-+)$  spin flip cross sections are marked by upright and inverted triangles, and these data are offset from the non-spin flip data. The solid lines represent a fit to the data. The schematic shows the coupling angle between adjacent layer moments determined from the fit.

neutron reflectivity studies will be performed on similar trilayer structures to probe the dependence of the coupling angle on Mn interlayer thickness, interfacial roughness and other structural parameters.

## References

- [1] M.N. Baibich, J.M. Broto, A. Fert, F. Nguyen van Dau, F. Petroff, P. Eitenne, G. Creuzet, A. Friederich and J. Chazelas, *Phys. Rev. Lett.* **61**, 2472 (1988).
- [2] S.S.P. Parkin, N. More and K.P. Roche, *Phys. Rev. Lett.* **64**, 2304 (1990).
- [3] S.S.P. Parkin, *Phys. Rev. Lett.* **67**, 3598 (1991).
- [4] M. Ruhrig, R. Schafer, A. Hubert, R. Mosler, J.A. Wolf, S. Demokritov and P. Grunberg, *Phys. Stat. Sol. (a)* **125**, 635 (1991); J. Unguris, R.J. Celotta and D.T. Pierce, *Phys. Rev. Lett.* **67**, 140 (1991).
- [5] A. Fuss, S. Demokritov, P. Grunberg and W. Zinn, *J. Magn. Magn. Mater.* **103**, L221 (1992); C.J. Gutierrez, J.J. Krebs, M.E. Filipkowski and G.A. Prinz, *J. Magn. Magn. Mater.* **116**, L305 (1992).
- [6] B. Heinrich, Z. Celinski, J.F. Cochran, A.S. Arrott, K. Myrtle and S.T. Purcell, *Phys. Rev.* **B47**, 5077 (1993).
- [7] M.E. Filipkowski, 1994 (unpublished).
- [8] J. F. Ankner and C.F. Majkrzak *Neutron Optical Devices and Applications*, edited by C.F. Majkrzak and J.L. Wood, SPIE Conferenc Proc. **1738**, 260 (1992).
- [9] J. Slonczewski, 1993 (unpublished). (1994).

## • Long range correlations in MnTe/CdTe systems

The system of MnTe/CdTe superlattices belongs to the family of artificial multilayered structures composed from zinc-blende (ZB) II-VI semiconducting compounds and Mn chalcogenides. The MnTe/CdTe specimens were prepared using ALE for the growth of CdTe layers, allowing the preparation of good quality superlattices with extremely thin (2-3 monolayers) CdTe spacers, and much thicker MnTe layers. Therefore, the non-magnetic layer thickness becomes sufficiently thin to allow observable magnetic interlayer coupling effects which had not been seen previously in Mn-VI/Zn-VI systems [1-3] made solely by MBE.

Neutron studies were performed on BT-2, BT-9 and SPINS. Different families of magnetic reflections were observed for samples with the following CdTe:MnTe thickness proportions (in monolayers); 2:10, 3:11, 4:9, 5:13, 6:10, 8:10 and 10:10. The number of bilayers in each sample was 100.

Scanning  $Q$ -space near the magnetic peaks, parallel to the growth direction, gave two very interesting results: (i) very narrow peaks of the same width as in the growth plane - essentially the instrumental resolution - implying magnetic correlation across the non-magnetic spacers and (ii) satellite peaks at positions corresponding to

the superlattice periodicity. These verify the coherence of spin ordering in consecutive magnetic layers. From the widths of the peaks, the coherence range is of the order of 5-10 bilayer thicknesses. However, the range of these correlations appears to be surprisingly long: the first sign of their deterioration is observed only when the CdTe thickness becomes as large as 10 monolayers ( $> 30 \text{ \AA}$ ), i.e., several times thicker than the expected range of superexchange coupling.

The origin of the magnetic interlayer coupling through the non-magnetic barriers is unknown. Superexchange is an unlikely cause, since it decreases too rapidly with distance:  $J(R) \sim R^{-6,8}$ . CdTe is a wide bandgap semiconductor, so there are too few carriers for some RKKY-like interaction to be responsible for the correlations. There could be a weak long-range component in the spin-spin interactions in the II-VI-based magnetic semiconductors that has not been detected in experiments on bulk alloys because of the overwhelming contribution from pairs with shorter spin-spin distances. Alternatively, impurities are an interesting possibility: magnetic interactions could percolate through a chain of magnetic impurities in the CdTe layers. (We have measured 3% CdTe in the MnTe layers but minimal Mn in the CdTe layers.) However, at the low temperatures of these measurements (12 K) the situation would be of two magnetic layers separated by a spin glass. If this were the cause of the coupling, it would in itself be an interesting scenario.

Attempts to model the samples and quantitative analyses of the data are underway. Both strain and layer thickness are important and the thicknesses of the magnetic layers are not the same in all the samples, therefore, these should be taken into account in a quantitative analysis of the data. Finite size effects should also be considered. Experiments are planned with samples in which the CdTe layers are even thicker, in order to see the satellites disappear to provide information on the interlayer coupling. These studies of interlayer coupling effects may give us new insight into the nature of weak long-range

magnetic exchange interactions in diluted magnetic semiconductors based on II-VI compounds.

#### • Temperature dependence of interlayer coupling

As mentioned above, previous Mn-VI/Zn-VI systems had not shown evidence of interlayer coupling. However, the studies had been on samples with Zn-VI thicknesses ranging from 17 to 28 monolayers [2]. In this study the interlayer correlations in  $[(\text{ZnTe})_5(\text{MnTe})_{10}]_{400}$  have been investigated by neutron diffraction. The 5 monolayers of ZnTe correspond to a layer thickness of  $15 \text{ \AA}$ , comparable to the non-magnetic layer thicknesses detailed in the CdTe/MnTe work above.

Diffraction scans along the z-axis (growth axis) revealed satellite peaks indicating interlayer correlations. More importantly, scans made at different temperatures indicated a *temperature dependence* of these correlations. The relative intensities at different temperatures are shown in figure 7. At low temperature, a zero-order peak ( $S_0$ ) is seen with satellites ( $S_1$  and  $S_{-1}$ ) corresponding to the superlattice spins being in phase with the bulk AF structure (see Fig. 8(a)). In addition, there is indication of two more satellites ( $S_{1/2}$  and  $S_{-1/2}$ ) midway between the central magnetic peak position and the first order satellites. As the sample temperature is raised, the intensities of the zeroth and first order peaks decrease, until at 55 K only the two half-order peaks are seen. These peaks can be obtained using a model in which the superlattice spins are out of phase with the bulk structure (see Fig. 8(b)).

This is the first known evidence of a temperature dependent term in the interlayer coupling. Bruno [4] predicted thermally induced coupling across an insulated spacer between two ferromagnetic layers. These data may be an experimental demonstration of the same effect for antiferromagnetic layers.

#### References

- [1] T. M. Giebultowicz, N. Samarth, H. Luo, P.

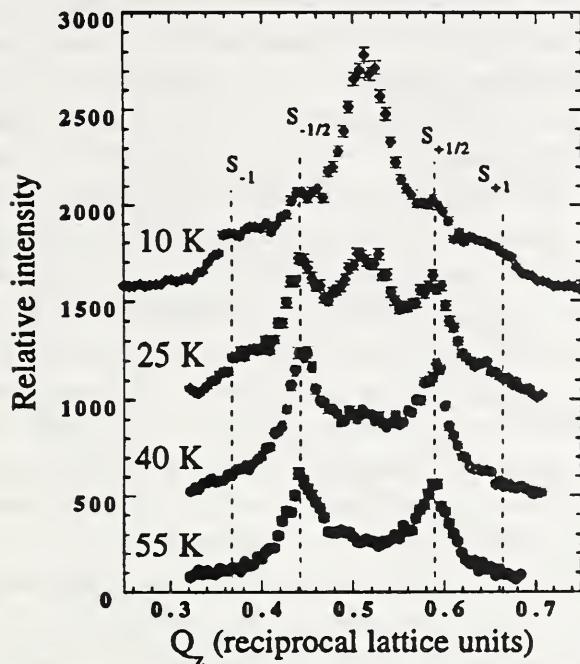


**Figure 7.** Diffraction scans along the  $z$ -direction in  $Q$ -space (the growth direction) of the  $(0\ 1\ 1/2)$  magnetic reflection for the  $[(\text{ZnTe})_5(\text{MnTe})_{10}]_{400}$  superlattice at different sample temperatures. For clarity, relative intensities are shown and the plots have been separated along the vertical scale.

Klosowski, J. K. Furdyna and J. J. Rhyne, *Phys. Rev. B* **46**, 12076 (1992).

[2] T. M. Giebultowicz, P. Klosowski, N. Samarth, H. Luo, J. K. Furdyna and J. J. Rhyne, *Phys. Rev. B* **48**, 12817 (1993).

[3] N. Samarth, P. Klosowski, H. Luo, T. M. Giebultowicz, J. K. Furdyna, B. Larson and N. Otsuka, *Phys. Rev. B* **44**, 4701 (1991).

[4] P. Bruno, *Phys. Rev. B* **49**, 13231 (1994).

### Anomalous Critical Scattering in Tb

Recent neutron studies of the two magnetic correlation lengths in Tb carried out last year on the NBSR BT-7 reflectometer showed that the scattering intensity from the anomalous second length scale is strongly enhanced over a  $200\ \mu\text{m}$  thick region, or “skin”, near the surface of the crystal. These studies therefore demonstrated

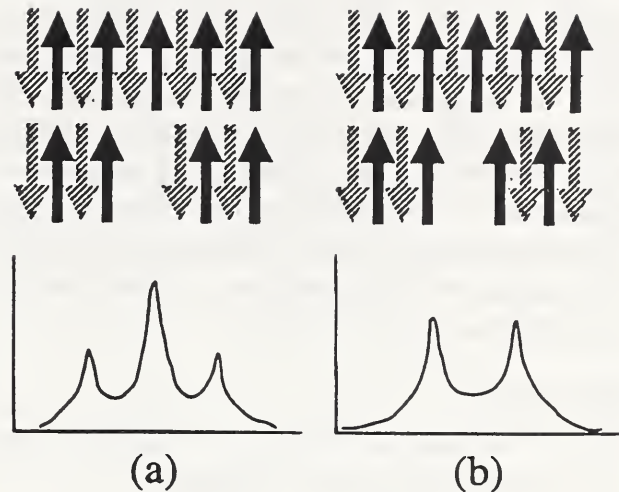


**Figure 8.** Schematic diagrams showing the superlattice spins in and out of phase with the bulk AF structure and the corresponding calculated diffraction patterns. The superlattice spins are shown under the bulk spin structure and the gap in the superlattice structure would be filled by the nonmagnetic spacer layers. In (a) the superlattice spins are in phase with the bulk structure and the corresponding diffraction pattern shows a zero-order peak and satellites at  $S_{+1}$  and  $S_{-1}$  positions. In (b) the superlattice spins are out of phase with the bulk structure leading to  $S_{+1/2}$  and  $S_{-1/2}$  satellites but no zero-order peak.

that the second length scale, which has been observed in  $\text{SrTiO}_3$ ,  $\text{RbCaF}_3$ ,  $\text{KMnF}_3$ , Ho, and NpAs and several other systems, is not a simple surface effect because the anomalous scattering is distributed over a macroscopic distance of order of  $100\ \mu\text{m}$ , and not just one or two.

A fundamental question that remains, however, is whether or not this second length scale is an intrinsic property of the bulk. Using a new, much larger cube-shaped Tb crystal, we have been able to mask the scattered neutron beam such that contributions to the total intensity arising from the skin associated with each face of the sample never reach the detector [1]. Under these conditions we find no evidence of the second length scale. Thus the anomalous

second length scale is not an intrinsic property of bulk terbium. This result is exceedingly important from a theoretical point of view inasmuch as the anomalous second length scale has been observed in such a large number of different condensed matter systems. The question of whether defects near the crystal surface produce the second length scale, or whether it is an intrinsic effect of the presence of a crystal boundary, remains open.

## Reference

- [1] P. M. Gehring, K. Hirota, C. F. Majkrzak, and G. Shirane, Phys. Rev. B, accepted.

## Polymer Systems

### • Wetting of a Polymer Brush Coated Surface

The technological motivation for studying tethered polymer systems, so-called polymer “brushes”, is their ability to modify various surface properties. One important class of surface properties is that of wetting, *i.e.* the interaction of a heterogeneous system containing two or more phases with a surface, and the resulting equilibrium configuration of the various phases near the surface. One of the more interesting cases of equilibrium wetting behavior occurs when there are two immiscible phases near their de-mixing critical point. In this type of system, the very strong temperature dependence of the thermodynamic variables which govern wetting results in a rich variety of observed wetting phenomena and surface induced phase transitions. Here, we highlight some recent neutron reflectivity measurements [1] aimed at studying the wetting behavior of a critical binary liquid mixture with a polymer brush grafted onto a Si substrate. Novel wetting behavior has been recently predicted [2] for this class of system since there are now two new length scales in the problem associated with the brush coated wall: the brush height  $h$ , and the mean separation between chain grafting sites on the surface,  $l \sim 1/\sigma^{1/3}$ , where  $\sigma$  is the grafting number density of the brush.

The system studied was a high molecular

weight polystyrene (PS) chemically end-grafted onto a polished, single-crystal Si substrate by condensation of the hydroxylated trichlorosilane polymer end groups with the hydroxyl groups on the native oxide surface of the Si wafer. This grafting procedure results in a uniform polymer film with a moderately high grafting density where the PS chains are strongly stretched normal to the substrate surface. This type of system has been previously studied using neutron reflectivity [3] in a variety of single solvents. In athermal, good solvents such as toluene, the measured brush profile is found to be well described by a parabola, while in cyclohexane (CH) which is a theta solvent in the measured temperature range, the polymer composition profile is more compact and step-like. Representative data from reference [3] are shown in figure 9 for the PS brush in CH at several temperatures in the vicinity of the theta temperature. The shift of the first minima in the reflectivity towards higher  $q$  as the temperature is decreased demonstrates the reduction in the brush height as the solvent quality is reduced.

For these measurements the polymer solvent was a perdeuterated mixture of cyclohexane and methanol (MeOH), a poor solvent for PS, prepared near its critical composition of  $\phi_c = 0.71$ . Precise temperature control of the solvent mixture in the scattering cell (better than  $\pm 20$  mK) was maintained due to the strong temperature dependence of the composition and interfacial energy between the two coexisting phases. The measured phase separation temperature for this system is  $T_c = 47.87 \pm .02$  °C. We measured the neutron reflectivity as a function of temperature both above  $T_c$ , in the one phase region, and below  $T_c$  where the CH-rich and MeOH-rich phases coexist. The two-phase measurements were repeated with the brush coated substrate located both above the solvent reservoir in contact with the less dense bulk phase, and below the solvent reservoir in contact with the denser bulk phase. We found no difference in the scattering in the two orientations suggesting that the polymer surface is completely wet by the pre-

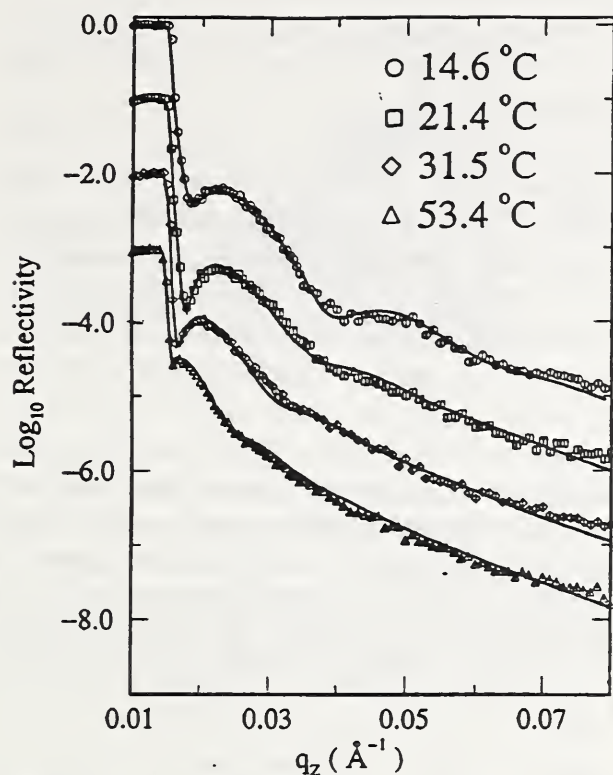


**Figure 9.** Measured reflectivity for a PS brush in d-cyclohexane at several temperatures. (From reference [3])

ferred phase and is therefore not in contact with the adjacent bulk phase. Results are shown in figure 10. Unlike the single solvent CH measurements, we found almost no temperature dependence to the brush height in either the one- or two- phase region of the solvent mixture phase diagram. This rather surprising result suggests that the solvent composition near the brush is continuously “adjusted” as a function of temperature to maintain a constant degree of swelling, disregarding the phase transition occurring in the adjacent bulk phase. Further experiments are underway to study the brush profile at different solvent compositions, and to change the isotopic labeling of the solvent mixture to monitor the fluid composition in the vicinity of the brush.

## References

[1] P. D. Gallagher, S. K. Satija, A. Karim, and L. J.

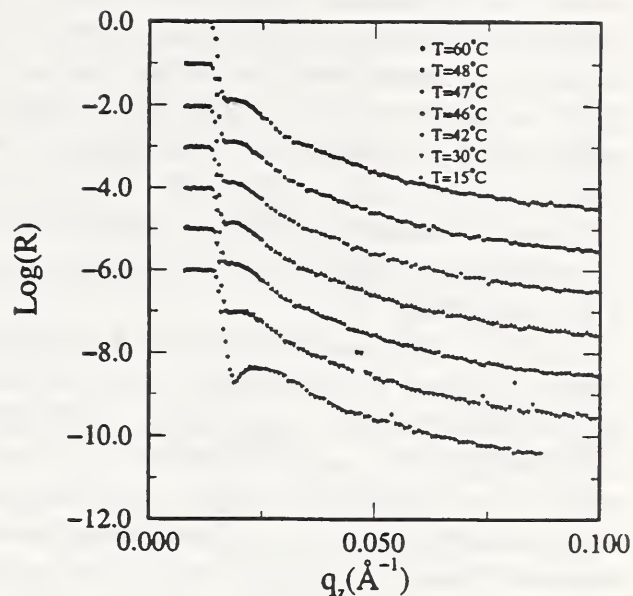


**Figure 10.** Measured reflectivity for a PS brush in a deuterated mixture of cyclohexane/methanol at several temperatures. The top two profiles were measured at temperatures in the one phase region, and the lower five profiles were measured below  $T_c$ , in the two phase region.

Fetters, in preparation.

[2] A. Johner and C. M. Marques, *Physical Review Letters* **69**, 1827 (1992).

[3] A. Karim, S. K. Satija, J. F. Douglas, J. F. Ankner, and L. J. Fetters, *Physical Review Letters*, in press.

## • Characterizing the Structure of a Bimodal Polymer Brush

The aim of this study is to characterize the structure of a tethered chain layer or “polymer brush” which is composed of two tethered chains of different molecular weight. Polymer brushes are useful to stabilize colloidal dispersions, enhance adhesion between a Polymeric matrix and a solid, and to control the domain size in incompatible polymer blends. Two primary motivations for examining bimodal brushes are i) to explore the possibility of tailoring the segmental profile in order to enhance properties beyond what can be achieved with a layer composed of a single molecular weight chain, and ii) to progress

toward understanding polydisperse brushes. In the present case the tethered chain layer is a diblock copolymer monolayer where one block (d-PS) is submerged in the subphase (ethyl benzoate) while the second block (PDMS) anchors the copolymer to the surface. We have previously reported similar reflectivity studies involving monolayers composed of a single molecular weight copolymer. [1]

In this work we have examined tethered layers composed of the following combinations of PDMS-PS diblock copolymers: 11-66/20-170, 11-66/28-330, and 4-30/20-338. In each case, the two copolymer samples were dissolved at low concentration at a 50/50 molar ratio in a common solvent (chloroform) which also served as a spreading solvent. The mixed copolymer monolayer was then spread on the surface of ethyl benzoate in a Langmuir trough using a microsyringe. Neutron reflectivity measurements were performed at low, medium, and high surface concentrations for each mixture. The surface pressure was measured simultaneous with the reflectivity. Sample reflectivity data are shown in figure 11, along with preliminary fits involving a model profile composed of the sum of two parabolas. These data will be compared to the Monte Carlo results of Chakrabarti and Toral [2] and the self-consistent field calculations of Milner et al. [3]

## References

- [1] M. S. Kent, L. T. Lee, B. Farnoux, F. Rondelez, *Macromolecules* **25**, 6240 (1992); B. J. Factor, L. T. Lee, M. S. Kent, F. Rondelez, *Phys. Rev. E., Rap. Comm.* **48**(4), 2354 (1993); M. S. Kent, L. T. Lee, B. Factor, F. Rondelez, G. Smith, *J. de Phys. IV*, 1993, 3(8), 49.
- [2] A. Chakrabarti, R. Toral, *Macromolecules*, **23**, 2016 (1990).
- [3] S. T. Milner, T. A. Witten, M. E. Cates, *Macromolecules*, **22**, 853 (1989).

## • Neutron Reflection Studies of Swelling of Chemically End-Grafted Polymer Chains

The unique properties of tethered poly-

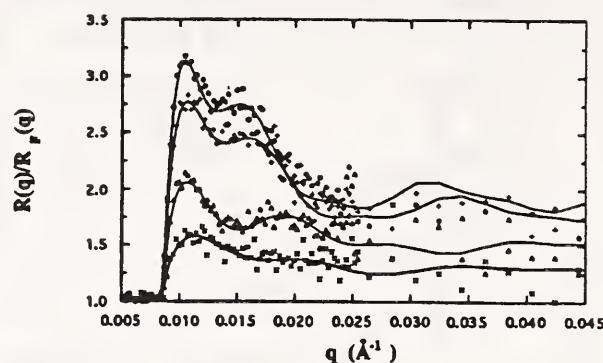


**Figure 11.** Reflectivity data for the 11-66/20-170 copolymer mixture at surface pressures of 0.4 (x), 0.7 ( ), 3.3 (+), 6.3 (o) dyne/cm. The curves through the data are best fits using a profile composed of the sum of two parabolas. For clarity, the reflectivity data are divided by the calculated Fresnel reflectivity for the pure solvent surface.

mer chains (“brushes”) are important for many applications including the modification of interfacial properties and colloid stabilization, and continues to be the subject of many theoretical, experimental and simulation studies. We have used neutron reflection to compare the swelling of two chemically end-grafted polystyrene brushes, one deuterated (dPS) and one protonated (PS), having different grafting densities exposed to a theta solvent cyclohexane and compared it to the extremes of a good solvent toluene and to the dry brush in air [1].

Neutron reflectivity measurements were performed on the NG-7 reflectometer at NIST. Figure 12 shows some of the reflectivity data that was taken at several temperatures in the vicinity of the theta-temperature ( $\theta \approx 30^\circ\text{C}$ ) of dPS in cyclohexane, and a measurement in the good solvent toluene as well. Similar results were obtained on the lower grafting density PS brush as well [2]. The brush height can be estimated from the raw data  $h \sim 2\pi/q^*$ , where  $q^*$  is the first minimum in the reflectivity oscillations corrected for refraction effects. By tracking the  $q^*$  values at different temperatures, one can in-

fer that the brush height increases with increasing temperature or solvent quality. The relative swelling can be quantified by taking the ratio of  $h$  to  $h_0$ . The stretching is then normalized by the chain length and therefore differences in chain lengths become relatively unimportant so that the difference of grafting density between the brushes becomes the most important factor. We observe [1] that the swelling range of  $h/h_0$  is considerably smaller for the higher density brush and falls within the range defined by the lower density brush. This seems to suggest that the packing effects in higher grafting density brushes give rise to very strong excluded volume interferences. For the lower grafting density the fluctuation effects are larger so changing solvent quality can have a larger effect. As mentioned in a previous paper [2] this swelling resembles the swelling of a network [3] more than a polymer in solution. In lightly cross-linked gels the extent of swelling becomes diminished and the temperature dependence of the swelling likewise becomes weaker with an increase in the cross-link density. In each case the increase of the elastic forces associated with the bound chain-end constraints increases the free-energy cost of deforming the chains. These observations suggests that brushes may be viewed as an anisotropic variety of gel and we plan to further pursue the implications of this analogy in the future.

## References

- [1] A. Karim, S. K. Satija, P. D. Gallagher, J. F. Douglas, L. J. Fetters, MRS '94, Fall proceedings.
- [2] A. Karim, S. K. Satija, J. F. Ankner, J. F. Douglas, L. J. Fetters, Phys. Rev. Lett., in press.
- [3] M. Zrinyi, F. Horkay, Macromolecules 22, 394 (1989).

### • Selective Solvent Effects on Block Copolymer Films

Ordered films of symmetric,  $f = 0.5$ , poly(styrene  $-b-$  2-vinyl pyridine) (PS-PVP) block copolymer on silicon substrates have been exposed to methanol and examined using neutron reflectivity. In the dry state, these films

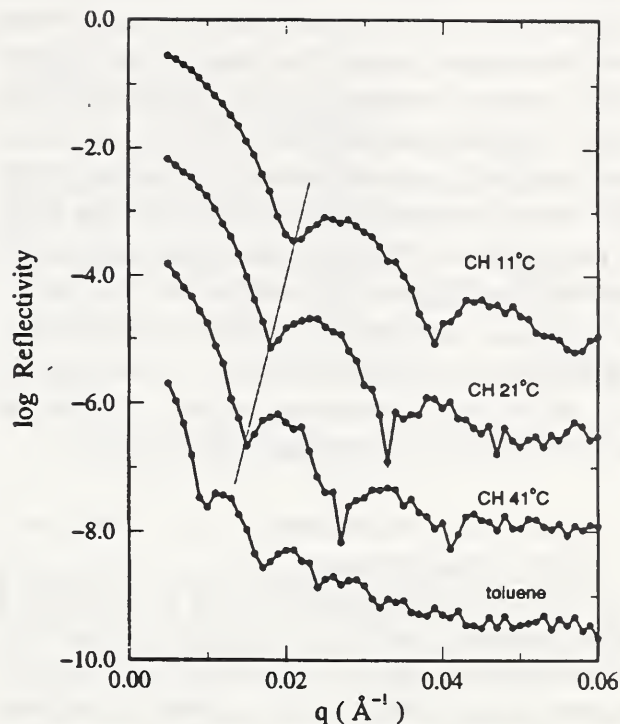


**Figure 12.** Neutron reflectivity from the dPS ( $M_w = 85k$ ) brush in cyclohexane (CH) at different temperatures and in toluene. The diagonal line tracks the  $q^*$  values at different CH temperatures thus clearly showing that the brush height increases with increasing temperature or solvent quality.

form alternating lamellar PS and PVP domains aligned parallel to the substrate surface. Methanol is a preferential solvent for PVP; consequently, it tends to segregate more to the PVP domains in the film. When the dry film is exposed to methanol, considerable swelling of the film occurs and the reflectivity curve for the swollen film shows dramatic differences from that for the dry film. Above about 40 K molecular weight of the diblock, the swelling (at ambient temperatures) is reversible in that the initial dry reflectivity profile of the film is recovered after the solvent is allowed to evaporate from the film. The films achieve equilibrium swelling relatively rapidly (on the time scale of several minutes for a film that is about 1000 Å thick), where equilibrium is defined in the sense that no further noticeable changes occur in the swollen film

reflectivity profile over a period of about 5 hrs. Furthermore, after initial exposure to solvent and subsequent drying, the films shrink slightly (a few percent) compared to the initial dry thickness. This decrease in film thickness has been attributed to a solvent-induced annealing of the film when the presence of solvent releases some of the degrees of freedom associated with chain motion. Preliminary results indicate that the local degree of swelling of the film increases with the distance from the substrate, at least for the first several microstructure periods. The overall structure remains approximately lamellar.

#### • Observed Frustration in Confined Block Copolymers

Typically, copolymer films are prepared on a solid substrate leaving the polymer surface unconstrained. At equilibrium, the total film thickness at any point has been shown to be given by  $nL_0$ , if the segments of one block segregate preferentially to both the air and substrate interfaces [1,2,3], or by  $(n+1/2)L_0$ , if one block segregates to the substrate interface and the other to the free surface [4]. Here,  $n$  is an integer. If the initial film thickness,  $t$ , does not conform to this condition, then this constraint is met by the formation of steps on the free surface with a height of  $L_0$  and a surface coverage commensurate with the relation of  $t$  to  $nL_0$  or  $(n+1/2)L_0$ , respectively. In this work the first experimental studies on thin films of diblock copolymers confined between two flat rigid surfaces are reported. Replacing the free surface with another solid surface suppresses the surface topography and eliminates this route for meeting the thickness constraint. Consequently, the copolymer is forced from its bulk equilibrium morphology into a frustrated state.

The systems under consideration are thin films of a symmetric diblock copolymer of perdeuterated polystyrene, d-PS, and poly(methyl methacrylate), PMMA, denoted P(d-S-b-MMA), with a weight average molecular weight,  $M_w$ , of  $8.0 \times 10^4$ , a polydispersity of 1.04 and a d-PS volume fraction of 0.51. In the

bulk this copolymer microphase separates into lamellar microdomains with  $L_0$  of 300 Å. Specimens were prepared by spin coating solutions of P(d-S-b-MMA) in toluene onto 5 cm diameter (5 mm thick), polished Si substrates passivated by a 15-20 Å surface oxide layer. Different film thicknesses of P(d-S-b-MMA) were attained by altering the spinning speed and/or the solution concentration. Film thicknesses were measured by both x-ray reflectivity and optical ellipsometry prior to subsequent treatment. Conservatively, the film thickness could be determined with an accuracy of  $\pm 30$  Å. An  $\sim 100$  Å layer of high molecular weight PMMA ( $M_w \simeq 1.3 \times 10^6$ ) was transferred onto the surface of the copolymer films to act as a buffer layer. A 1.2  $\mu\text{m}$  thick film of  $\text{SiO}_x$  ( $x \sim 1.4$ ) was then evaporated onto the PMMA. Care was taken to keep the temperature of the copolymer well below its glass transition temperature by evaporating the  $\text{SiO}_x$  rapidly at 200 Å/s. Prior to the neutron reflectivity experiments, the samples were heated to 175 °C under vacuum for 26 hrs and then quenched to room temperature, *i.e.*, below the glass transition temperatures of both blocks, thereby freezing in the structure at the elevated temperature. The neutron reflectivity measurements were performed on the IBM/UMINN/NIST reflectometer NG-7 in the reactor guide hall at NIST [6]. The use of the PMMA buffer layer was critical since the direct evaporation of the oxide onto the copolymer surface interfered with the ordering process. Independent neutron reflectivity measurements were made on confined films of a perdeuterated copolymer of comparable molecular weight with an overlayer of the PMMA homopolymer, prepared in the same manner as described above. The studies demonstrated that interdiffusion between the copolymer and homopolymer did not occur to any appreciable extent. In addition, the absence of off-specular scattering in these experiments showed that the formation of islands or holes on the free surface was prevented by the PMMA/ $\text{SiO}_x$  overlayer. Since PMMA preferentially interacts with both



the substrate and overlayer interfaces, this preparation leads to a copolymer being confined between two solid surfaces where one block segregates preferentially to both interfaces.

Shown in figure 13 are typical neutron reflectivity profiles for P(d-S-b-MMA) as a function of the neutron momentum normal to the surface,  $k_{z,0}$  ( $=2\pi/\lambda \sin \theta$ , where  $\lambda$  is the wavelength (4.1 Å) and  $\theta$  is the grazing angle of incidence). The film thickness are normalized as  $t/L_0$ . In all cases, multiple order odd reflections are seen regardless of the film thickness, indicating that a multilayered structure oriented parallel to the film surface is always found. This is supported by the absence of any appreciable off-specular scattering. This suggests that a loss in the orientation of the lamellar microdomains parallel to the surface does not occur to relieve the film thickness constraint. Moreover, the data clearly show that increasing  $t/L_0$  from 7.56 to 8.82 causes a clear shift in the third order reflection to smaller  $k_{z,0}$  (or larger spacing) suggesting that the fundamental repeat distance of the copolymer increases with thickness. However, for  $t/2L_0$  of 7.35, a shoulder on the third order reflection is found at higher  $k_{z,0}$ . As  $t/L_0$  increases, this shoulder becomes more pronounced and replaces the reflection at smaller  $k_{z,0}$ . In fact, the position of this shoulder is comparable to that found for the copolymer when  $t/L_0=7.8$ . The same behavior was found for samples with thicknesses between  $5.8L_0$  and  $6.8L_0$ . These results suggest that the variation in the period is cyclic with  $t/L_0$  in keeping with the theoretical predictions.

This work was partially supported by the U.S. Department of Energy, Office of Basic Energy Sciences under contract DE-FG03-88ER45375 and by the National Science Foundation under Grant No. DMR-9357602.

## References

- [1] T. P. Russell, G. Coulon, V. R. Deline, and D. C. Miller, *Macromolecule*, **22**, 4600 (1989).
- [2] M. D. Foster, M. Sikka, N. Singh, F. S. Bates, S. K. Satija, and C. F. Majkrzak, *J. Chem. Phys.*

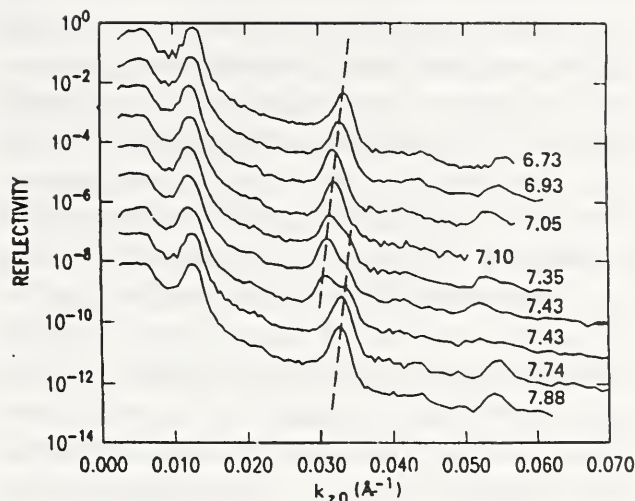


**Figure 13.** Neutron reflectivity profiles as a function of  $k_{z,0}$ , the neutron momentum transfer normal to the film surface for P(d-S-b-MMA) films confined between two solid surfaces. The film thickness,  $t$ , divided by the bulk equilibrium copolymer repeat period,  $L_0$ , are indicated in the figure. The dashed lines in the figure were drawn to emphasize the change in the position of the third order reflection and the concurrent occurrence of two reflections for some of the profiles.

96, 8605 (1992).

- [3] C. Marques, *Phys. Rev. Lett.*, **70**, 1351 (1993).
- [4] B. Collin, D. Chatenay, G. Coulon, D. Aussere, and Y. Gallot, *Macromolecule*, **25**, 1621 (1992).
- [5] G. Coulon, T. P. Russell, V. R. Deline, and P. E. Green, *Macromolecule*, **22**, 258 (1989).
- [6] P. D. Gallagher and S. K. Satija, in preparation.

## New Methods and Capabilities

### • Analyzing Specular Reflectivities with Parametric B-Splines

A novel application of parametric B-spline curves to the model-free determination of neutron and x-ray scattering length density profiles from measurements of specular reflectivity has been developed [1]. The goal is to determine a  $\rho(z)$ , representing the scattering length density of a thin film as a function of depth, from a spectrum  $|R(Q)|^2$ , representing reflectivity as a function of wavevector or, equiv-

alently, the incident or reflection angle. For given profile  $\rho(z)$ , the specular reflectance  $R(Q)$  can be computed exactly for practical purposes, but the inverse problem of determining  $\rho(z)$  from  $|R(Q)|^2$  is neither straightforward nor entirely well-defined, the loss of phase information in relating  $|R(Q)|^2$  to  $R(Q)$  being the most evident—but not the only—mathematical obstacle. Thus most approaches to analyzing reflectivities are variants of curve fitting. Model-based fitting tests parametrized formulas, often resulting from or motivated by theoretical predictions, while model-free descriptions test restricted function spaces. Both approaches involve the determination of fit variables, but a reasonably sharp distinction is that models usually are non-linear functions of their parameters, while function spaces are spanned by linear combinations of bases functions. Consequently, models tend to probe limited classes of profile shapes, especially when using a small number of fit variables, while model-free descriptions, in principle, have larger range.

Parametric B-spline curves offer a flexible and appropriate mathematical description of scattering length density profiles for reflectivity analysis. Profiles combining smooth and sharp features can be defined in low dimensional representations using control points in the density-depth plane which provide graded local influence on profile shape. These profiles exist in vector spaces defined by B-spline order and parameter knot set, which can be systematically densified during analysis. Such profiles can easily be rendered as adaptive histograms for reflectivity computation. B-spline order can be chosen to accommodate the asymptotic (large- $Q$ ) behavior indicated by reflectivity data.

In the method, scattering length density profiles  $\rho(z)$  are represented by parametric B-spline curves:

$$VCz(u, \rho(u)) = \sum_{i=0}^m (z_i, \rho_i) B_{i,k}(u), \quad (2)$$

where  $B_{i,k}(u)$  are B-splines of order  $k$  and  $u$  is

the evolution parameter of the  $(z, \rho)$  curve. For a given parameter knot sequence (a fixed set of values along the  $u$ -axis), the curve is defined by its  $m + 1$  control points,  $(z_i, \rho_i)$ , which act as fit variables. In practice  $k = 4$ , signifying cubic B-splines, is a good choice for analyzing most reflectivity data, having continuity properties consistent with spectra that fall as fast as  $Q^{-4}$ . An interactive fitting program, called PBS, uses the Nelder and Mead simplex method to search control point space.

The method has been applied to several interesting examples of neutron reflectivity data. The curves in figure 14 show the results of fitting an in-situ neutron reflectivity spectrum from titanium films which have been oxidized by contact with an aqueous electrolyte. The profile drawn with the heavy line was obtained using J. F. Ankner's MLAYER model-based fitting routine, which is a mainstay of neutron reflectivity analysis at NIST. The other curves shown were all obtained with PBS using different numbers of control points and different interactive fitting strategies. All the parametric B-spline profiles fit the spectrum to the accuracy shown in the figure. (The deviations between the MLAYER fit and the PBS fits at high  $Q$  apparently are due to the error weighting used in MLAYER; the PBS fits are not weighted.) Thus this spectrum does not uniquely determine a scattering length density profile for the film, but it does effectively isolate a family of profiles which are consistent with the data and are reasonable candidates for the physical profile. PBS is now being used to analyze recent reflectivity spectra from lipid bilayers on silicon and likely will join MLAYER as a standard component of reflectivity studies in CNRF.

## Reference

[1] N. F. Berk and C. F. Majkrzak, to be published.

## • Neutron Standing Waves and Prompt Gamma Emissions

Neutron standing waves (NSW) have been combined with neutron-capture prompt gamma

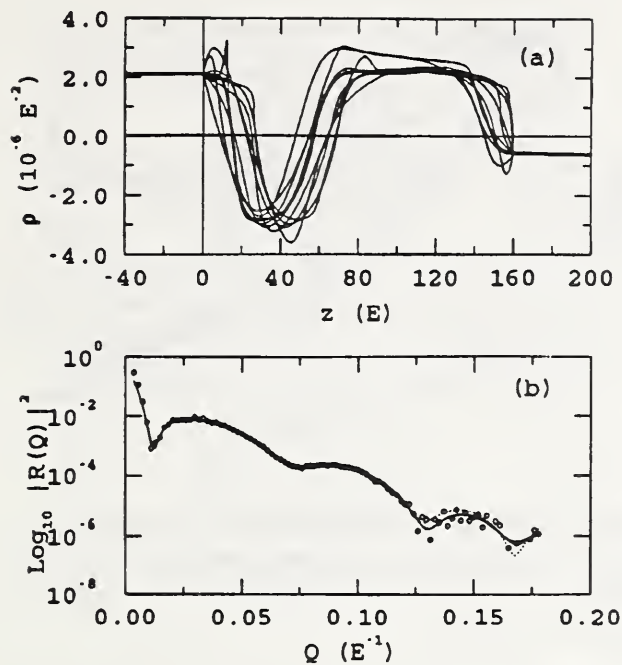


Figure 14. (a) Fitted density profiles for titanium oxide. (b) Fitted reflectivities. (See text.)

emissions (PGE) to locate buried layers in multilayer thin films [1]. This technique is not limited to low- $Z$  materials, as in the case of x-ray standing waves (XSW) and x-ray fluorescence (XF) emissions, because most materials are transparent to thermal and cold neutrons. NSW and PGE has not been reported prior to ref. 1 mainly because of low neutron beam intensities. However, observations of resonance-enhanced XSW [2-4] and NSW [5,6] in thin films suggested the feasibility of doing such experiments with neutrons. Indeed, in our experiment the neutron flux (neutron/sec.cm<sup>2</sup>) in the film has been enhanced at resonance by more than 30 times compared to the incident beam flux.

The inset of figure 8 is a schematic diagram of the sample. Approximately 0.6  $\mu\text{m}$  thick Ni was first evaporated onto a polished Si substrate of 5.1 cm in diameter. A film of polyvinylcyclohexane (PVCH) ( $\sim 720$   $\text{\AA}$  in thickness) was spin-coated onto the Ni. Subsequently, a 50  $\text{\AA}$  layer of Gd was evaporated onto the PVCH film. No precaution was taken to prevent the oxidation of the Gd to Gd<sub>2</sub>O<sub>3</sub>. A film of PVCH ( $\sim 720$   $\text{\AA}$ )

was floated onto the surface of deionized water and retrieved using the substrate, thereby entrapping the Gd between two layers of PVCH. After drying, a perdeuterated polystyrene (d-PS) film was placed on top of the PVCH in an analogous manner.

The neutron experiments were carried out at the NG-7 reflectometer. The sample was mounted horizontally and a  $\gamma$ -ray detector was installed above the sample. The active element of the detector was a high-purity Ge crystal 64 mm in diameter, placed  $\sim 10$  mm from the sample. The absolute efficiency, measured with calibrated radioactive sources, was 0.10 and 0.09 photopeak counts per photon at  $E_\gamma=181.9$  and 199.2 keV, from capture in <sup>157</sup>Gd and <sup>155</sup>Gd, respectively. The monochromated neutrons had an average wavelength of  $\lambda=4.1$   $\text{\AA}$  with  $\Delta\lambda/\lambda=0.025$ . The illuminated area of the sample was kept fixed at  $\sim 35 \times 40$  mm<sup>2</sup> by continuously opening the beam defining slits as the incident angle  $\theta$  increased. Gamma-ray intensities at  $E_\gamma=181.9$  and 199.2 keV were measured from  $k_x=0.00025$   $\text{\AA}^{-1}$  to 0.075  $\text{\AA}^{-1}$  with resolution  $\Delta k_x/k_x \cong 0.058$ . Neutron reflectivity data were taken simultaneously with the  $\gamma$ -ray data at each  $k_x$ .

Figure 15 shows the low- $k_x$  portion of the  $\gamma$ -ray data (circles) at  $E_\gamma=181.9$  keV, with the  $\gamma$ -counts normalized to the incident beam intensity. Below the critical  $k_x$  (0.0107  $\text{\AA}^{-1}$ ) of Ni, five modes of the resonance-enhanced neutron standing waves (RENSW) were expected as indicated by the arrows, and the  $\gamma$ -ray peaks for  $n=3, 4,$  and 5 modes were well resolved experimentally. The solid line is the calculated neutron-capture rate  $\tau$  for <sup>157</sup>Gd, multiplied by a constant  $C$ , with the sample structural parameters as well as  $C$  fit to the data.

A matrix method was used to calculate the neutron wavefunction  $\Psi(x)$  and the resulting neutron-capture rate  $\tau$  (neutrons/sec), as well as the neutron reflectivity. Interface roughness was modeled by smearing the abrupt change in the 1-d scattering potential at each interface with a hyperbolic tangent function, and the rough-

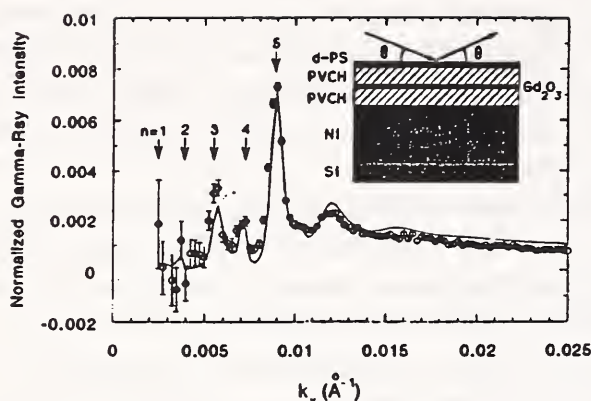


**Figure 15.** Gamma-ray data at  $E_\gamma=181.9$  keV from the neutron capture in  $^{157}\text{Gd}$ . Circles are measured  $\gamma$ -ray intensity normalized to the incident neutron beam intensity. The arrows indicate the resonance- $k_x$  positions of the RENSX for  $n=1, 2, \dots,$  and 5 modes. The solid line is the calculated neutron-capture rate multiplied by a constant representing the counting efficiency. Fitting to the data is very sensitive to the location and depth-profile of the Gd layer. The inset is a schematic diagram of the sample.

ness was parameterized by the full-width-half-maximum (FWHM) of the first derivative of the smearing function. The fitting of the calculated  $\gamma$ -ray intensity to the data was sensitive to the total thickness of the PVCH film since the  $k_x$  values of the resonance peaks were most affected by the film thickness. The relative intensities of the peaks were very sensitive to the depth and depth-profile of the Gd layer. For example, since the Gd layer is located at a trough of the RENSX for the  $n=4$  mode [see Fig. 17(a)], the  $\gamma$ -ray intensity of the  $n=4$  peak depends crucially on how the Gd layer overlaps with the neutron probability density  $|\Psi(x)|^2$ . To obtain a reasonable fit to the data the thickness of the Gd layer was increased to  $84 \text{ \AA}$  with a density only 86% that of the bulk, (which might indicate that the Gd layer was oxidized), and the roughness of both interfaces of the Gd layer were found to be  $14 \text{ \AA}$ . The PVCH film thickness was found to be  $737 \text{ \AA}$  above the Gd layer and  $741 \text{ \AA}$  below it, and the fitting to the data persistently showed

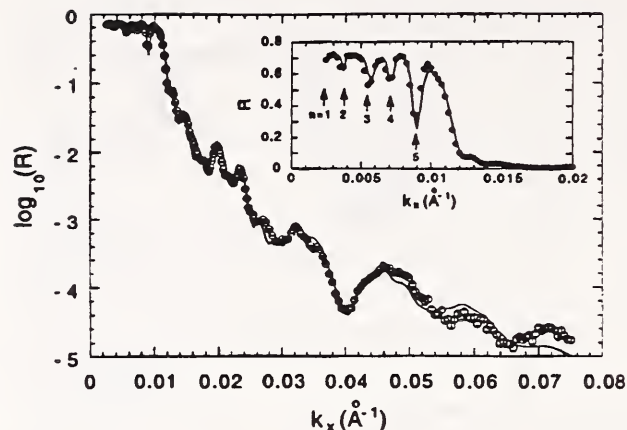


**Figure 16.** The measured neutron reflectivity on a log-scale. The inset is the low- $k_x$  portion of the data plotted on a linear scale. Solid lines are results of fitting to the data.

a thicker PVCH film at the bottom. The sensitivity of the PGE & RENSX technique to the Gd layer depth and depth-profile surpasses that of neutron reflectivity analysis alone. The d-PS film thickness was found to be  $240 \text{ \AA}$ . The real part of the resulting scattering potential  $u(x)$  is plotted as the thick solid curve in figure 17. The imaginary part  $u_{im}$  for Gd and PVCH were  $3.4 \times 10^{-5} \text{ \AA}^{-2}$  and  $9.2 \times 10^{-8} \text{ \AA}^{-2}$ , respectively.

Figure 16 shows the measured neutron reflectivity on a log-scale while the inset shows the low- $k_x$  portion on a linear scale. The solid curves were calculated with the same parameters as used in calculating the solid curve in figure 8 for the  $\gamma$ -ray intensity. Since the reflectivity analysis was sensitive to the interface roughness of the d-PS and Ni layers, we also fit the data to help determine these parameters, and fed them back when we fit the  $\gamma$ -ray data. The  $\gamma$ -ray and the neutron reflectivity results are in excellent agreement, and indeed they are complementary tools to pin down the depth-profile of the entire sample.

The thin solid lines in figure 17 show the neutron probability density  $|\Psi(x)|^2$  in the  $n=4$  (a) and 5 (b) modes, numerically calculated with the same depth-profile parameters used for the

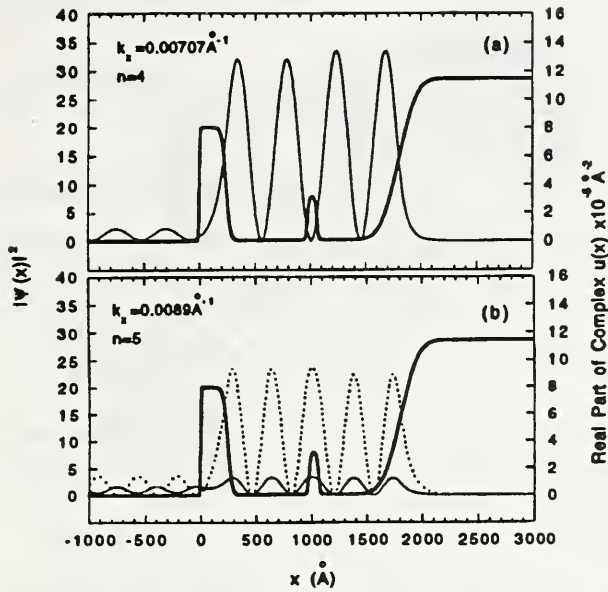


**Figure 17.** The real part of the 1-d scattering potential  $u(x)$  (thick solid lines) obtained from fitting to the  $\gamma$ -ray and neutron reflectivity data, and the neutron probability density  $|\Psi(x)|^2$  (thin solid lines) calculated accordingly with  $k_z=0.00707 \text{ \AA}^{-1}$  (a) and  $0.0089 \text{ \AA}^{-1}$  (b), respectively. For the  $n=4$  mode  $|\Psi|_{\text{max}}^2$  is resonantly amplified to  $\sim 33$  in the PVCH film. The RENS $W$  is suppressed by the absorption in the  $n=5$  mode. The dotted line in (b) is  $|\Psi(x)|^2$  calculated with the imaginary part of  $u(x)$  in the Gd layer turned off.

solid lines in figures 15 and 16. Tails of  $\Psi(x)$  extend into the potential walls on both sides, as we expect from the model calculation. For the  $n=4$  mode, even with absorption and structural imperfections included, the standing waves are still resonantly amplified to  $|\Psi|_{\text{max}}^2 \sim 33$ . For the  $n=5$  mode, however, the RENS $W$  is suppressed by the absorption. As a comparison,  $|\Psi(x)|^2$  is calculated with the imaginary part of  $u(x)$  from the Gd layer turned off, plotted as the dotted line in figure 17(b).

We have demonstrated that PGE combined with RENS $W$  is a sensitive, non-destructive technique for characterizing buried layers of neutron absorbing nuclei in thin films. The unique properties of neutrons make it particularly applicable to high- $Z$  materials such as rare-earth

thin films and multilayers where XF & XSW technique can not be utilized. Even though in this test of the technique a strong neutron absorber, Gd, is selected for the buried layer, improved sample engineering and more intense neutron beams available in future at the Advanced Neutron Source will allow us to study buried layers of various neutron-absorbing nuclei.

## References

- [1] H. Zhang, P. D. Gallagher, S. K. Satija, R. M. Lindstrom, R. L. Paul, T. P. Russell, P. Lambooy, and E. J. Kramer, Phys. Rev. Lett. 72, 3044 (1994).
- [2] D. K. G. de Boer, Phys. Rev. B 44, 498 (1991).
- [3] J. Wang, M. J. Bedzyk, and M. Caffrey, Science 256, 775 (1992).
- [4] Y. P. Feng, S. K. Sinha, H. W. Deckman, J. B. Hastings, and D. P. Siddons, Phys. Rev. Lett. 71, 537 (1993).
- [5] L. J. Norton, E. J. Kramer, R. A. L. Jones, F. S. Bates, H. R. Brown, G. P. Felcher, and R. Kleb, J. Phys. II France 4, 1 (1994).
- [6] Y. P. Feng, C. F. Majkrzak, S. K. Sinha, D. G. Wiesler, H. Zhang, and H. W. Deckman, Phys. Rev. B 49, 10814 (1994).

## • UHV Sample Chamber

With the recent advances pointed out in the preceding paragraphs, neutron reflectivity has become an established technique for high spatial resolution depth profiles of composition and magnetism. In fact, it is approaching the realm of a truly surface sensitive probe. As such, however, it is presently hampered by the surface layers of oxides and other compounds, as well as adsorbed water vapor and hydrocarbons that invariably are deposited on exposed surfaces from the atmosphere. This contamination can alter surface phenomena from the behavior that would occur on a pristine surface. In order to keep surfaces clean they must be contained in ultra high vacuum (UHV), where the rate of deposition of contaminants is reduced. For example at a pressure of  $7 \times 10^{-10}$  torr this rate is 1 mono-

layer of molecules per hour, which, assuming a sticking coefficient of 1, allows less than 1 hour to study a contamination free surface. Presently at NIST, experiments are done either in air or in the vacuum required for cryogenic isolation,  $\sim 10^{-6}$  torr. Thus the development of an ultra high vacuum (UHV) sample environment is necessary for the advent of neutron reflectivity surface science, and will open up opportunities for several new experimental investigations involving catalysis, oxidation, and hydrogenation, critical phenomena, magnetism, and diffusion at surfaces, epitaxy, and studies of hydrophilic and other contamination-sensitive materials [1].

Reflectivity measurements benefit further from the absence of a contamination layer and UHV environment even in cases in which surface phenomena are not being studied. The presence of contamination layers complicates the interpretation of the data by requiring extra fitting parameters to describe them. In addition, these layers are almost always rougher than the uncontaminated surface, which results in lower reflected intensity, decreasing the rate at which data can be taken and, to some extent, the Q-range over which data can be acquired. Furthermore, in UHV many complementary techniques of surface science and sample preparation can be employed.

In order to perform experiments on clean surfaces additional equipment is required beyond that required to maintain UHV. To create a clean surface we have chosen molecular beam epitaxy (MBE) to deposit single crystal thin films and multilayers since it is a highly versatile technique and produces state of the art sample quality and smooth surfaces. However, in-situ ion sputter etching will be provided to clean surfaces prepared elsewhere. Introduction of gas species for experiments on catalysis and hydrogen absorption will be enabled by a UHV leak valve attached to a gas manifold.

Neutron reflectivity experiments additionally require large samples and neutron windows. The latter will be provided by a cylindrical section made of Al which will also allow grazing in-

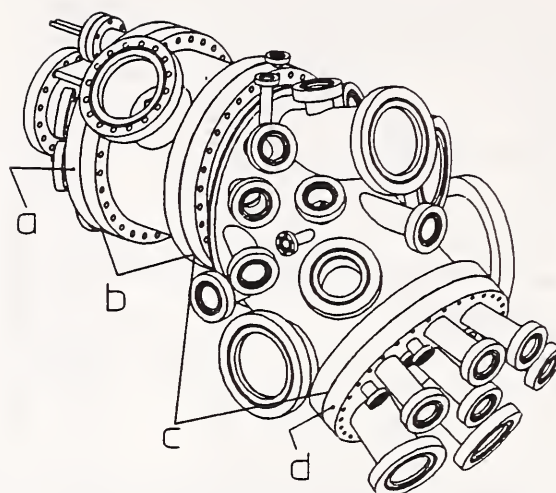


Figure 18. The MBE/Neutron Reflectivity Chamber. From left to right are the a) sample flange, b) neutron window, c) MBE section, and d) source flange.

cident diffraction. With some modifications this chamber could be used for high angle diffraction as well. The sample holder is designed for a continuous temperature range of  $\sim 8$ -1200 K, with appropriate uniformity across a 3" diameter substrate. Furthermore, means are provided for a uniform externally controlled magnetic field at the sample for polarized neutron experiments. These features call for components that are unavailable commercially, and required considerable development. (See figure 18)

While not all capabilities can be initially provided for, we will initially concentrate on studies of hydrogen in metals and the determination of the magnetic penetration depth of alkali doped  $C_{60}$ . Therefore we have adapted a lower cost UHV sample chamber from the design of the full MBE chamber at a cost that is roughly 1/3 that of the full MBE. In addition to the above experiments, this chamber is designed to be a general purpose UHV sample chamber, with its capabilities for some UHV deposition, surface reactions, and sputter cleaning of externally prepared samples. Virtually all of the parts of this chamber can be transferred to the full MBE chamber, sav-

ing most of the investment in this stage of the chamber development.

## Reference

[1] J. A. Dura, work in progress.

## Research Topics

### Field Dependence of the Magnetic Coupling Angle in a $\text{Fe}_{25}\text{Co}_{75}/\text{Mn}$ Superlattice

J. A. Borchers<sup>12</sup>, J. F. Ankner<sup>33</sup>, M. E. Filipkowski<sup>34</sup>, C. J. Gutierrez<sup>35</sup>, C. F. Majkrzak<sup>12</sup>, J. J. Krebs<sup>9</sup>, and G. A. Prinz<sup>9</sup>

### Temperature and Field Dependence of the Fe Moment Orientation in a Fe/Al/Fe Trilayer

J. F. Ankner<sup>7</sup>, J. A. Borchers<sup>12</sup>, M. E. Filipkowski<sup>34</sup>, C. J. Gutierrez<sup>35</sup>, C. F. Majkrzak<sup>12</sup>, J. J. Krebs<sup>9</sup>, and G. A. Prinz<sup>9</sup>

### Polarization of Pd Interlayers in Fe/Pd Superlattices

J. A. Borchers<sup>12</sup>, J. F. Ankner<sup>7</sup>, J. R. Childress<sup>15</sup>, C. F. Majkrzak<sup>12</sup>, and R. W. Erwin<sup>12</sup>

### Origin of Low-Field Giant Magnetoresistance in $\text{Ni}_{80}\text{Fe}_{20}/\text{Ag}$ Multilayers

J. A. Borchers<sup>12</sup>, P. M. Gehring<sup>12</sup>, J. F. Ankner<sup>7</sup>, C. F. Majkrzak<sup>12</sup>, T. L. Hylton<sup>37</sup>, K. R. Coffey<sup>37</sup>, M. A. Parker<sup>37</sup>, and J. K. Howard<sup>37</sup>

### Magnetization Profile of Co/Pt Superlattices

J. F. Ankner<sup>33</sup>, J. A. Borchers<sup>12</sup>, C. F. Majkrzak<sup>12</sup>, R.F.C. Farrow<sup>5</sup>, and R. F. Marks<sup>5</sup>

### Polarized Neutron Reflectivity Studies of Co/Cu and Co/Ag Multilayers

J. A. Dura<sup>12</sup>, T. Wantanabe<sup>38</sup>, J. A. Borchers<sup>12</sup>, C. F. Majkrzak<sup>12</sup>, and J. Bass<sup>39</sup>

### Antiferromagnetic Spin Ordering and Interlayer Magnetic Correlations In MnTe/CdTe Superlattices

T. M. Giebultowicz<sup>4</sup>, W. Faschinger<sup>18</sup>, G. Bauer<sup>18</sup>, V. Nunez<sup>19,12</sup>, P. Klosowski<sup>12</sup>, and J. K. Furdyna<sup>20</sup>

### Dynamical Scattering of Polarized Neutrons by Thin Magnetic Films

V. Nunez<sup>19,12</sup>, C. F. Majkrzak<sup>12</sup>, and N. F. Berk<sup>12</sup>

### NiC/Ti Supermirror Coating Reflectivity

J. Wood<sup>11</sup> and C. F. Majkrzak<sup>12</sup>

### In Situ Neutron Reflectivity Studies of Ti Oxidation and Dissolution

D. G. Wiesler<sup>12</sup> and C. F. Majkrzak<sup>12</sup>

### Fe/Si Supermirror Polarizer Efficiency

J. Wood<sup>11</sup> and C. F. Majkrzak<sup>12</sup>

### Co/Cu Superlattices: Polarized Neutron Reflectometry Study

A. Schreyer<sup>13</sup>, H. Zabel<sup>13</sup>, J. F. Ankner<sup>7</sup>, and C. F. Majkrzak<sup>12</sup>

### Analyzing Specular Reflectivities with Parametric *B*-Splines

N. F. Berk<sup>12</sup> and C. F. Majkrzak<sup>12</sup>

### Magnetic Critical Scattering in Single Crystal Tb: Skin Effects

P. M. Gehring<sup>12</sup>, H. Hirota<sup>1</sup>, G. Shirane<sup>1</sup>, and C. F. Majkrzak<sup>12</sup>

### Fe/Cr Superlattices: Polarized Neutron Study of Interlayer Coupling

A. Schreyer<sup>13</sup>, J. F. Ankner<sup>7</sup>, H. Zabel<sup>13</sup>, and C. F. Majkrzak<sup>12</sup>

### Neutron Channeling in Ti Films

Y. P. Feng<sup>2</sup>, S. K. Sinha<sup>2</sup>, H. Zhang<sup>12</sup>, D. G. Wiesler<sup>12</sup>, and C. F. Majkrzak<sup>12</sup>

### FeCo/Si Supermirror Efficiency

J. Wood<sup>11</sup>, H. Mook<sup>10</sup>, and C. F. Majkrzak<sup>12</sup>

### Neutron Reflectivity Studies of Biological Membrane Films

K. Gawrisch<sup>8</sup>, B. Koenig<sup>6</sup>, S. Krueger<sup>12</sup>, N. F. Berk<sup>12</sup>, C. F. Majkrzak<sup>12</sup>, S. K. Satija<sup>12</sup>, and W. J. Orts<sup>12</sup>

### Proteins in Thin Films

A. Liebmann<sup>16</sup>, H. Wu<sup>16</sup>, M. Foster<sup>16</sup>, S. K. Satija<sup>12</sup>, and C. F. Majkrzak<sup>12</sup>

### Structure and Diffusion in Langmuir-Blodgett Films

L. A. Feigin<sup>23</sup>, D. G. Wiesler<sup>12</sup>, J. F. Ankner<sup>7</sup>, C. F. Majkrzak<sup>12</sup>, S. K. Satija<sup>12</sup>, and A. Karim<sup>22</sup>

### Formation and Diffusion in Langmuir-Blodgett Films

D. G. Wiesler<sup>12</sup>, L. Feigin<sup>23</sup>, and C. F. Majkrzak<sup>12</sup>

### Structure of Adsorbed Polymers in Solution

D. G. Wiesler<sup>12</sup>, D. Perahia<sup>2</sup>, and S. K. Satija<sup>12</sup>

### Structure and Breakdown of Protective Oxides on Titanium

D. G. Wiesler<sup>12</sup> and C. F. Majkrzak<sup>12</sup>

### Structure of Passive Oxides on Iron

D. G. Wiesler<sup>12</sup>, J. Kruger<sup>6</sup>, L. A. Krebs<sup>6</sup>, C. F. Majkrzak<sup>12</sup>, and J. F. Ankner<sup>7</sup>

**Structure of Nickel Hydroxide Reversible Alkali Battery Materials**

D. G. Wiesler<sup>12</sup>, R. Hillman<sup>41</sup>, and S. Roser<sup>42</sup>

**Direct Observation of Neutron Guided Waves in a Thin-Film Waveguide**

D. G. Wiesler<sup>12</sup>, Y. P. Feng<sup>2</sup>, S. K. Sinha<sup>2</sup>, H. W. Deckman<sup>2</sup>, H. Zhang<sup>19</sup>, and C. F. Majkrzak<sup>12</sup>

**Block Copolymers in Confined Geometries**

P. Lambooy<sup>5</sup>, T. P. Russell<sup>5</sup>, G. Kellogg<sup>24</sup>, A. Mayes<sup>24</sup>, S. K. Satija<sup>12</sup>, and P. D. Gallagher<sup>12</sup>

**Interfacial Structures of Electrically Conducting Adsorbed Multilayers**

G. Kellogg<sup>24</sup>, A. Mayes<sup>24</sup>, W. Stockton<sup>5</sup>, M. Ferreira<sup>24</sup>, M. F. Rubner<sup>24</sup>, and S. K. Satija<sup>12</sup>

**Mixtures of Symmetric Diblock Copolymers**

A. M. Mayes<sup>24</sup>, T. P. Russell<sup>5</sup>, and S. K. Satija<sup>12</sup>

**Influence of Surfaces and Finite Film Thickness on Block Copolymer Morphology**

N. Singh<sup>25</sup>, M. Sikka<sup>25</sup>, F. S. Bates<sup>25</sup>, S. K. Satija<sup>12</sup>, and P. D. Gallagher<sup>12</sup>

**Structure of a Bimodal Polymer Brush**

M. S. Kent<sup>30</sup>, B. J. Factor<sup>22</sup>, G. S. Smith<sup>31</sup>, and S. K. Satija<sup>12</sup>

**Selective Salvation in Lamellar Block Copolymer Thin Films**

R. Levicki<sup>25</sup>, N. Koneripalli<sup>25</sup>, M. Tirrell<sup>25</sup>, F. S. Bates<sup>25</sup>, and S. K. Satija<sup>12</sup>

**Block Copolymer Thin Film Phase Behavior**

N. Singh<sup>25</sup>, M. Sikka<sup>25</sup>, F. S. Bates<sup>25</sup>, C. F. Majkrzak<sup>12</sup>, and A. Karim<sup>22</sup>

**Wetting on Polymer Surfaces by Critical Binary Fluids**

P. D. Gallagher<sup>12</sup>, S. K. Satija<sup>12</sup>, A. Karim<sup>22</sup>, and L. Fetters<sup>2</sup>

**Theory of Grazing Angle Neutron Diffraction on Thin Films**

H. Zhang<sup>12</sup>

**Grazing Angle Neutron Diffraction Experiments on Thin Y Films**

H. Zhang<sup>12</sup>, S. K. Satija<sup>12</sup>, P. D. Gallagher<sup>12</sup>, J. A. Dura<sup>12</sup>, C. P. Flynn<sup>32</sup>, and J. F. Ankner<sup>7</sup>

**Chemically Adsorbed Polymer Brushes**

A. Karim<sup>22</sup>, S. K. Satija<sup>12</sup>, L. J. Fetters<sup>2</sup>, and C. F. Majkrzak<sup>12</sup>

**Block Copolymer Mixtures in Thin Films**

N. Singh<sup>25</sup>, M. Sikka<sup>25</sup>, F. S. Bates<sup>25</sup>, S. K. Satija<sup>12</sup>, and C. F. Majkrzak<sup>12</sup>

**Surface Segregation in Thin Polymer Films**

N. Singh<sup>25</sup>, M. Sikka<sup>25</sup>, F. S. Bates<sup>25</sup>, S. K. Satija<sup>12</sup> and P. D. Gallagher<sup>12</sup>

**Surface and Phase Behavior of Thin Polymer Blend Films**

T. Slaweki<sup>26</sup>, S. K. Kumar<sup>26</sup>, A. Karim<sup>22</sup>, and S. K. Satija<sup>12</sup>

**Effect of Solvent on Surface Induced Diblock Copolymer Ordering**

H. Lin<sup>27</sup>, A. Steyr<sup>127</sup>, A. Karim<sup>22</sup>, T. P. Russell<sup>5</sup>, and S. K. Satija<sup>12</sup>

**Adsorption of Surfactants at a Hydrophobic Surface Near the Solid-Liquid Interface**

D. C. McDermott<sup>28</sup>, R. Thomas<sup>28</sup>, A. R. Rennie<sup>29</sup>, S. K. Satija<sup>12</sup>, and P. D. Gallagher<sup>12</sup>

**Neutron Standing Waves and Prompt Gamma Emissions**

H. Zhang<sup>19</sup>, P. D. Gallagher<sup>12</sup>, S. K. Satija<sup>12</sup>, R. M. Lindstrom<sup>40</sup>, R. Paul<sup>40</sup>, T. Russell<sup>5</sup>, P. Lambooy<sup>5</sup>, and E. Kramer<sup>5</sup>

**UHV Sample Chamber Development**

J. Dura<sup>12</sup>

**Affiliations**

<sup>1</sup>Brookhaven National Laboratory

<sup>2</sup>Exxon Research and Engineering Co.

<sup>3</sup>Florida State University

<sup>4</sup>George Mason University

<sup>5</sup>IBM Almaden

<sup>6</sup>Johns Hopkins University

<sup>7</sup>MURR, University of Missouri

<sup>8</sup>National Institute of Health

<sup>9</sup>Naval Research Laboratory

<sup>10</sup>Oak Ridge National Laboratory

<sup>11</sup>Ovonics Company

<sup>12</sup>Reactor Radiation Division

<sup>13</sup>Rürr University, Germany

<sup>14</sup>Rutgers University

<sup>15</sup>Thomson-CSF, France

<sup>16</sup>University of Akron

<sup>17</sup>University of Arizona

<sup>18</sup>University of Linz, Austria

<sup>19</sup>University of Maryland

<sup>20</sup>University of Notre Dame



- <sup>21</sup>Ceramics Division
- <sup>22</sup>Polymers Division
- <sup>23</sup>Russian Academy of Science
- <sup>24</sup>MIT
- <sup>25</sup>University of Minnesota
- <sup>26</sup>Penn State University
- <sup>27</sup>University of Rhode Island
- <sup>28</sup>University of Oxford
- <sup>29</sup>Cambridge University
- <sup>30</sup>Sandia National Laboratory
- <sup>31</sup>Los Alamos National Laboratory
- <sup>32</sup>University of Illinois
- <sup>34</sup>University of Arkansas
- <sup>35</sup>Southwest Texas State
- <sup>36</sup>University of Florida
- <sup>37</sup>IBM Storage Systems Division
- <sup>38</sup>Sandia University
- <sup>39</sup>Michigan State University
- <sup>40</sup>Inorganic Analytical Research Division
- <sup>41</sup>University of Leicester
- <sup>42</sup>University of Bath

# Macromolecular and Microstructure Studies

The macromolecular and microstructural studies highlighted in this section were carried out on the CNRF's three small angle neutron scattering (SANS) instruments. These instruments have been used to characterize nanoscale structure ( $\sim 1$  to 300 nm) in a wide range of materials including polymers, colloids and microemulsions, microporous media, biological macromolecules, nanocrystalline metals and ceramics, molecular composites, and liquid crystals among many others. From October 1993 until June 1994, when the NBSR shut down to install a new cold source and make other facility improvements,  $\sim 60$  experiments were carried out on each of the SANS instruments. Roughly one-half of the total beam time on the two, high resolution, 30 m SANS instruments ( $\sim 75\%$  on the NIST/NSF SANS and  $\sim 25\%$  on the NIST/Exxon/Univ. of Minnesota/Texaco SANS) was distributed among groups who submitted proposals that were peer reviewed and allocated beam time by the CNRF's Program Advisory Committee. In this section, the results of some of these studies, in which Reactor Division scientists have had a major role, are briefly described.

## Polymers

### • Microphase Separation in Ultrathin Copolymer Films

Neutron scattering studies of phase behavior in copolymer thin films have focused primarily on neutron reflectivity measurements since this technique is quite sensitive to structures oriented normal to the surface. This is usually the case for thin copolymer films since the strong specific interaction between the substrate and block segments orients the resulting lamellae to lie parallel to the substrate. However, several important examples where there is lateral structure in the film include non-equilibrium configurations during phase separation, and equilibrium structures

in films that are "frustrated" by confinement between two surfaces. SANS measurements in a transmission geometry, where the incident beam is normal to the surface, are a direct probe of this type of in-plane structure in thin films. In this geometry, however, the illuminated sample volume is small which makes such measurements difficult. In two recent studies carried out with scientists from IBM and MIT, the measurement of SANS from ultrathin (100 nm) polymer films has been successful for the first time, with a reduction in sample thickness by a factor of  $10^4$  compared to the typical one mm thickness used for measuring polymer blends. An acceptable signal to noise ratio was achieved because the microphase structure of the chosen system provides a strong scattering signal and because the full size of the available beam could be utilized (2.8 cm diameter sample aperture).

In one study of non-equilibrium structures present during phase separation in a thin copolymer film, symmetric diblock copolymers of polystyrene (PS) and perdeuterated poly(methyl methacrylate) (dPMMA) were spun cast from 1% toluene solutions onto silicon substrates and studied both "as-cast" and after heating to 170 °C (well above the polymer glass transition) in vacuum. Figure 1 (a-c) shows the "as-cast" (o) and post-annealed ( $\bullet$  annealed for 15 min.;  $\blacktriangle$  annealed for 23 hrs) scattering from three samples with different molecular weights ( $M_n = 29$  K, 121 K and 289 K for plots a, b, and c respectively). A peak in the scattering at a given  $Q$  corresponds to in-plane structure in the film with a characteristic length scale  $\sim 1/Q$ . Non-equilibrium, in-plane structure is seen for all except the lowest molecular weight "as-cast" films due to phase separation occurring during the spin coating process before evaporation of solvent increases the glass transition above room temperature. After annealing for 15 min, significant structure is observed for all three molecular weights, but after 23 hrs of annealing the

structure has almost disappeared except for the highest molecular weight. These changes result from two processes which occur over different time scales when the sample is heated: the fast formation of copolymer micro-domains which at first are randomly oriented with respect to the surface [1], and the slower re-orientation of the domains parallel to the surface from the specific interactions between the block segments and the substrate [2]. The slower kinetics seen for the higher molecular weight result from the strong molecular weight dependence of the chain mobility.

Equilibrium in-plane structure has also been observed in films where there is an interaction competing with the substrate preference for a specific block. This has been demonstrated using confined copolymer films where the total thickness of the film is fixed by the presence of a  $\text{SiO}_x$  cap layer. If the film thickness is incommensurate with the multilayer domain spacing the domains must either stretch or compress to compensate or reorient perpendicular to the surface to remove the constraint. In this study the strength of the specific interaction with the surface was modified by coating with a high molecular weight film of a random PS-*b*-PMMA copolymer and by varying the copolymer stoichiometry. Figure 2 shows scattered intensity difference as a function of  $Q$  between a sample with a total film thickness corresponding to 2.5 bilayer repeat distances (highly frustrated) and a film 2.8 bilayer repeat distances thick (minimal frustration). The appearance in the scattering pattern of a resolution-limited Bragg peak indicates strong in-plane correlated structure in the frustrated film. The peak position corresponds to the same bilayer spacing measured in non-confined films. Other experiments verified that increasing the wall interaction with a specific block segment by changing the random copolymer stoichiometry prevented the reorientation of the lamella normal to the surface even for highly frustrated films.

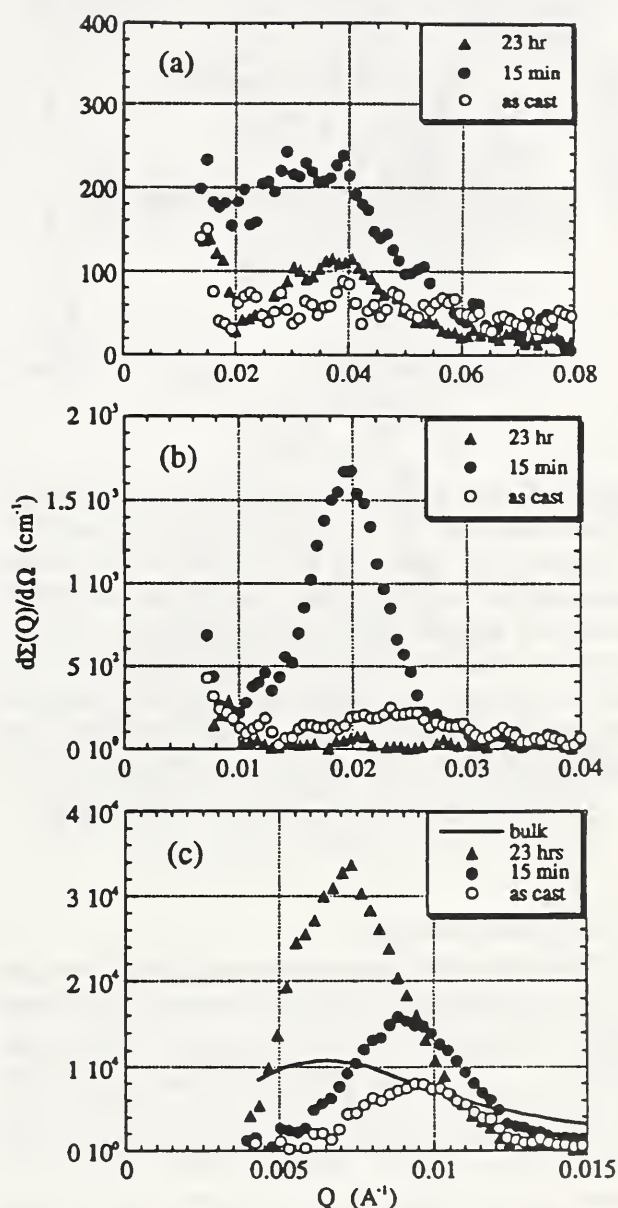


**Figure 1.** The absolute scattering cross section,  $d\Sigma/d\Omega$ , for P(S-*b*-d-MMA) copolymers on a Si substrate: (o) as-cast; (●) heated to 170 °C for 15 min; and (▲) heated to 170 °C for 23 hrs. (a) is for the 29 K copolymer; (b) is for the 121 K copolymer; and (c) is for the 289 K copolymer. The solid line in (c) is the scattering measured for the bulk copolymer.

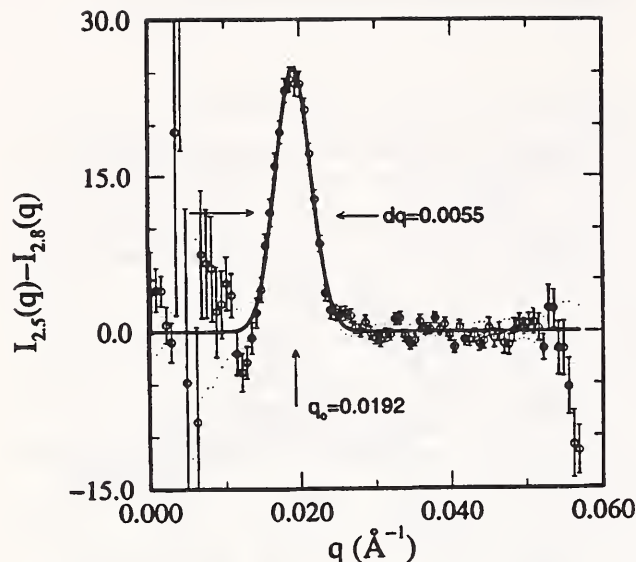


**Figure 2.** The difference in scattered neutron intensity as a function of  $Q$  between two ultrathin confined copolymer thin films, one with a total film thickness corresponding to 2.5 bilayer repeat distances (highly frustrated) and the other with a thickness of 2.8 bilayers (minimal frustration). The appearance in the scattering pattern of a resolution-limited Bragg peak indicates strong in-plane correlated structure in the frustrated film.

### • Polymer Blends

The degree of polymer miscibility affects the texture and morphology of polymeric materials which in turn affect the mechanical properties. Most polymer blends phase separate upon heating beyond the so-called lower critical spinodal temperature (LCST) although some phase separate upon cooling below an upper critical spinodal temperature (UCST). Two other characteristic temperatures play a role in determining the usefulness of a polymer mixture for specific applications: the glass-rubber transition temperature ( $T_g$ ) below which polymer melts "freeze" to form a glassy state, and the degradation temperature. The proximity of these various temperatures to ambient (or the temperature at which the material is used) determines whether the material will be rubbery, stiff, brit-

tle, etc. Detailed knowledge of phase behavior is, therefore, essential to determining processing strategies that lead to control of microstructure and resulting properties. Recent SANS measurements, in collaboration with NIST's Polymers Division and the IBM Almaden Research Center [3], have for the first time established the existence of both a LCST and a UCST in a homopolymer blend (low molecular weight polystyrene/polybutylmethacrylate). The existence of such a miscibility gap in the phase diagram opens up new possibilities for the control of polymer morphology that may lead to novel and beneficial microstructures. If successful, many other polymer blends which were thought to be purely UCST or LCST systems likely could be modified to have similar miscibility gaps.

Another approach to controlling miscibility involves the use of random or block copolymers as compatibilizers in the production of polymer blends. Although in widespread industrial use, processing methods based on this approach are generally developed by trial and error due to the lack of fundamental data that might lead to predictive capabilities. To address this situation, a program has been initiated in collaboration with scientists at Brooklyn Polytechnic University to investigate systematically the effects of adding varying amounts of symmetric diblock copolymers on the phase separation kinetics of equal mixtures (critical composition) of the corresponding homopolymers. As a first study, blends of polyethylbutylene (PEB) and polymethylbutylene (PMB) and their copolymers were quenched into the immiscible region of the phase diagram and SANS patterns were recorded every few minutes in order to follow the early stages of phase separation. At longer times, the technique of Multiple Small Angle Neutron Scattering (MSANS), which consists of monitoring the broadening of the direct beam due to multiple scattering, was used to follow the coarsening of the microstructure over a period of months. It was found that the addition of the copolymer does keep composition fluctuation length scales small (effective compatibiliza-

tion) at early stages (based on the SANS observations), but not during the late stages (based on the MSANS results) where similar kinetic behavior was observed with or without the copolymer present.

### Structural Biology

The 30 m SANS instruments continue to be used successfully for the study of a variety of biological systems. In particular, the high incident flux and wide measurement range have made it possible to reliably determine the structure of small proteins in dilute solution, even under conditions where the scattering is often very weak. As a result, several leading groups in the field are now regularly performing experiments at the CNRF and new collaborations have been developed with scientists at local institutions. The higher neutron intensity which will be available once the new cold source is installed will make the 30 m SANS instruments even better-suited for structural biology studies.

The first structural study [4,5] of skeletal muscle troponin C complexed with troponin I in the presence of calcium ( $4\text{Ca}^{2+}\cdot\text{TnC}/\text{TnI}$ ) has now been completed in collaboration with the Los Alamos National Laboratory. The TnC/TnI dimer is part of a larger troponin complex which plays an important role in calcium-regulated muscle contraction. While the crystal structure of the TnC component alone was previously known, this is the first information obtained on the structure of the  $4\text{Ca}^{2+}\cdot\text{TnC}/\text{TnI}$  complex in solution.

In an effort to better understand the specific interactions between TnC and TnI in the presence of calcium, deuterated TnC was complexed with non-deuterated TnI and a series of measurements in solvents with increasing concentrations of  $\text{D}_2\text{O}$  were made in order to separately determine the structure of each component. The results showed that TnC, with a radius of gyration of  $23.9 \pm 0.5 \text{ \AA}$ , retains its extended, dumbbell-like shape while in the  $4\text{Ca}^{2+}\cdot\text{TnC}/\text{TnI}$  complex. The TnI component, with a radius of gyration of  $41 \pm 2 \text{ \AA}$ , is

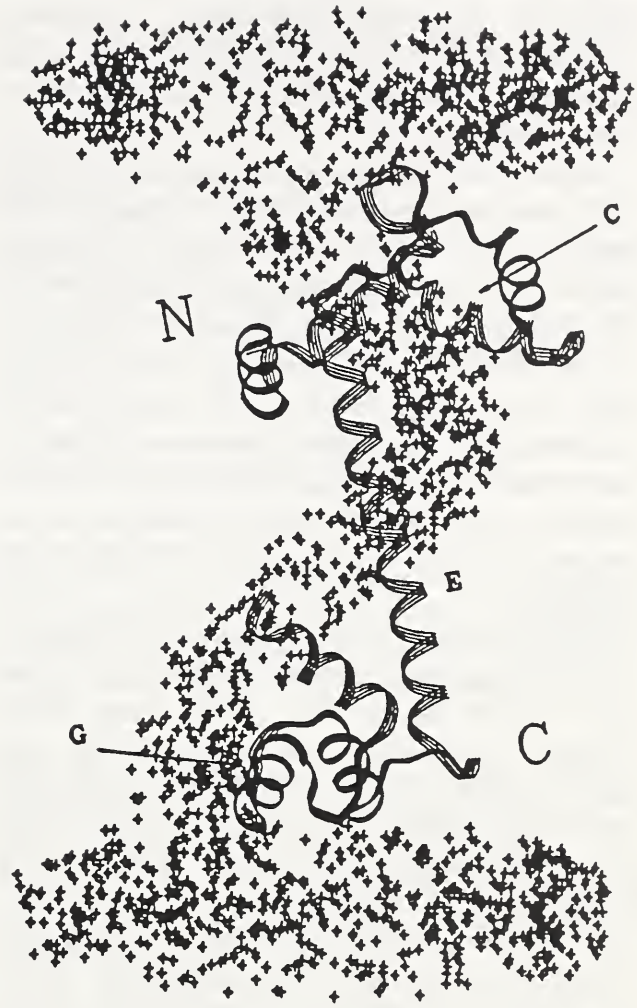


**Figure 3.** Best fit model for  $4\text{Ca}^{2+}\cdot\text{TnC}\cdot\text{TnI}$  derived from SANS and x-ray crystallography data as well as biochemical analyses. The path of TnI (plus signs) spirals around the dumbbell-shaped  $4\text{Ca}^{2+}\cdot\text{TnC}$  (ribbon). The N and C domains, as well as helices C, E, and G of TnC are labeled. [Taken from Ref. 5.]

even more extended and forms a helical structure which encompasses the TnC component. The maximum linear dimension of the complex is  $115 \pm 4 \text{ \AA}$  and the centers of mass of the two components coincide to within  $10 \text{ \AA}$ . Figure 3 illustrates the model structure for the complex which was derived from the data using a Monte Carlo modeling method [5]. The model is consistent with biochemical data which suggest that the molecular mechanism for the  $\text{Ca}^{2+}$ -sensitive switch that regulates the muscle con-

traction/relaxation cycle involves a signal transmitted via the central spiral region of troponin I. Similar SANS experiments are currently being performed on the calmodulin/myosin light chain kinase complex.

Studies of conformational changes in cyclic AMP receptor proteins (CRP) induced by the binding of the small cAMP ligand are continuing in collaboration with the NIST/Univ. of MD Center for Advanced Research in Biotechnology. CRP is a DNA-binding protein which, in its active conformation with bound cAMP, regulates gene expression in bacteria. Although the crystal structure of the CRP/cAMP complex is known, no detailed structural information on the shape of the non-liganded molecule is yet available.

Earlier small angle x-ray scattering measurements [6] suggested that the radius of gyration ( $R_g$ ) of CRP decreases by  $\sim 20\%$  when cAMP is bound. However, it was suspected that this result might be greatly influenced by aggregation of the protein. Initial measurements made on the 30m SANS instruments also showed a change in  $R_g$  of the same magnitude. However, since the scattering could be measured at smaller angles than was possible in the x-ray study, the aggregation was immediately confirmed. Once unaggregated samples could be measured, the change in radius of gyration was found to be on the order of 5%, which is more consistent with recent analytical gel chromatography [7] results. Figure 4 shows the fitted distance distribution functions obtained from a preliminary shape analysis of the data taken at higher angles. These results support the notion that CRP becomes slightly more compact upon binding of cAMP. Efforts to calculate detailed structural models based on the SANS data are currently underway. Additional experiments will explore the structure of mutant forms of CRP as well as the CRP/cAMP complex with DNA bound.

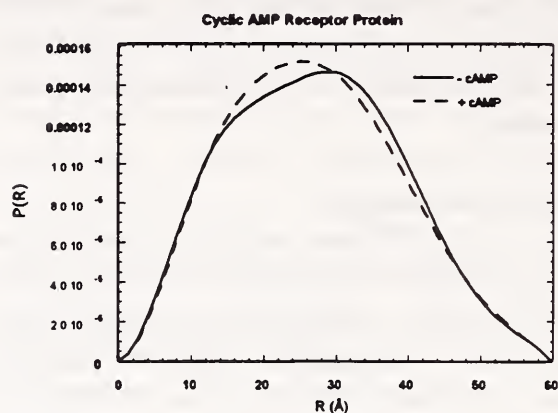


**Figure 4.** Distance distribution functions,  $P(r)$ , obtained from fits to the SANS data for non-liganded CRP and the CRP/cAMP complex. The peak in the distribution shifts to smaller distances for the CRP/cAMP complex, suggesting that CRP becomes slightly more compact upon binding of cAMP.

## Microporous Materials

### • Pore Coarsening in Selectively Dissolved Silver-Gold Alloys

When a metal is exposed to an electrolyte and an oxidizing agent, it may dissolve into the electrolyte in a corrosion process. When this occurs for an alloy or composite, the less noble constituent in the matrix will often dissolve more quickly, leaving behind a porous network formed of the more noble constituent. This selective dissolution provides fertile ground for studying surface and bulk diffusion, metal-electrolyte interactions, and the effect of local curvature on mass transport [8]. In addition, the porous networks left behind have potential commercial value as membranes or as substrates for electrochemical sensors.

In a collaboration with scientists at Johns Hopkins University to investigate dealloying of a simple binary alloy, a quartz flow cell was constructed for use in in-situ SANS measurements. Two foils of  $Ag_{70}-Au_{30}$  alloy were placed into

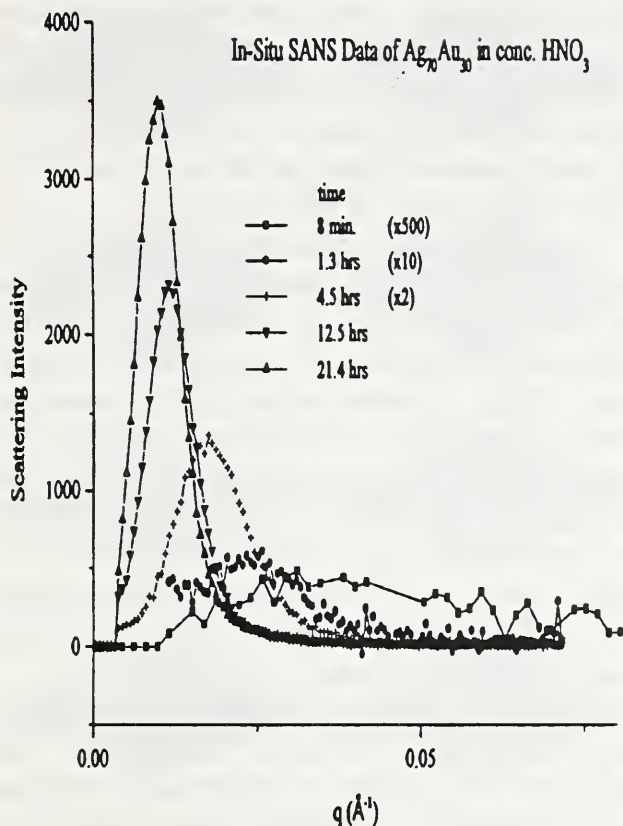


**Figure 5.** A series of circularly averaged SANS patterns collected (in about two minutes each) during the dealloying of a  $Ag_{70}Au_{30}$  sample by concentrated nitric acid. As the dealloying progresses, the intensity grows, and the maximum shifts to lower  $Q$ , consistent with a rearrangement (coarsening) of the Au atoms left behind in the porous network.

the cell, and concentrated nitric acid was flowed through. SANS data were collected in roughly two-minute intervals, as the Ag dissolved out of the alloy. Figure 5 shows a series of circularly-averaged scattering patterns for data collected over a 24-hr period. As the dealloying progresses, the intensity grows, and the maximum shifts to lower  $Q$ , consistent with a rearrangement (coarsening) of the Au atoms left behind in the porous network.

The data bear a strong resemblance to SANS profiles of porous vycor glass, which have been modeled successfully by Berk et al. [9]. Fitting our data to this model, we have determined the time evolution of the average Au ligament

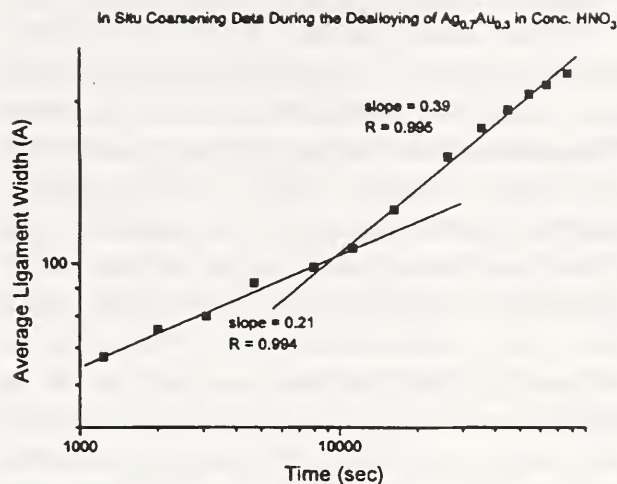


**Figure 6.** The average width of the Au ligaments versus dealloying time derived from the SANS data shown in figure 5 based on a model of a bicontinuous microstructure from Ref. [9].

size, shown in figure 6. Two scaling regimes are apparent: The scaling exponent is 0.21 at short times, but increases to 0.39 after a few hours. This change in slope may be associated with some transition from surface diffusion limited coarsening to bulk diffusion limited coarsening. Theoretical treatments of coarsening predict slopes of 0.25 and 0.33, however [10], and we do not presently understand the deviation. One possibility is that the differences are related to small changes in the dealloying rate, over which we had no control, since we used a chemical, rather than electrochemical, etchant.

The coarsening behavior of dealloyed films has also been monitored while the films were annealed at 150 °C and 200 °C. Changes in the scaling exponent are observed for some of these data as well, leading us to believe that these changes herald a real transition and are not just an artifact of a varying dissolution rate. Future in-situ dealloying measurements are planned, in which the dissolution rate will be controlled electrochemically in perchloric acid.

- **Pore Structures in Electrochemically Etched Silicon and Gallium Arsenide**

Porous silicon has been the subject of much interest because of its photoluminescent properties, which have been attributed to a variety of mechanisms, including quantum confinement and surface chemistry effects. In distinguishing between these mechanisms, it is helpful to correlate the chemical and optical properties and the growth conditions to the structure of the films. In a collaboration with Johns Hopkins University, SANS has been used to measure the porosity and morphology of a range of porous GaAs and n- and p-doped Si samples. All samples were etched electrochemically in hydrofluoric acid mixed with either ethanol or water, with varying concentrations, current densities, and growth times.

As the resistivity is increased from 0.001  $\Omega$ -cm to 1  $\Omega$ -cm, the scattering from porous n-type Si(100) evolves from a broad, diffuse pattern to a much sharper pattern with fourfold symmetry, indicating that the pores become larger and more square-sided. The p-type samples tend to produce diffuse, circularly symmetric SANS patterns, but under certain growth conditions, they too show signs of square-sided pits. Porous GaAs(100) shows four highly pronounced lobes, indicative of pore growth along the {111} directions. The results from this study have been combined with electron microscopy data to yield structure information on a broad length scale.

## Structured Fluids

- **Liquid Crystalline Ordering of Aqueous Suspensions of Cellulose Microfibrils**

Materials derived from liquid crystalline cellulose microfibrils have a huge industrial significance because of the high tensile strengths obtained by aligning these stiff crystallites under shear. Aligned cellulose microfibrils are the basic material for a wide range of products such as rayon, Viscose<sup>®</sup>, cellophane, some cotton fibers, and most recently Tencel<sup>®</sup>, which displays unique properties due to liquid crys-

talline ordering. In particular, aqueous suspensions of acid-hydrolyzed microfibrils with dimensions of approximately 50 x 50 x 2000 Å exhibit cholesteric ordering, *i.e.* the ordering of nematic layers into a chiral nematic, helicoidal structure. In the cholesteric phase microfibrils stack similarly to the steps in a spiral staircase.

SANS studies in collaboration with the Pulp and Paper Research Institute of Canada on aqueous suspensions of cellulose microfibrils have been instrumental in describing the mechanism behind cholesteric ordering. The measured inter-rod packing was significantly tighter between nematic planes than between rods within a nematic layer. Based on packing arguments, we propose that this is due to the presence of a slight helical twist in each microfibril—an asymmetry which has not been detected by any other characterization technique.

SANS was employed to determine the *in situ* shear alignment of cellulose microfibrils. Essentially, this explores the relationship between the cholesteric and nematic phases, since, under steady shear flow, cholesteric ordering is replaced by simple nematic alignment. Figure 7 highlights the increase in microfibril alignment with increasing shear rate for a 5% suspension of microfibrils (with an axial ratio of  $\sim 45$ ) in D<sub>2</sub>O. Inter-rod interference peaks, which are perpendicular to the flow direction, become sharper and more prominent with increasing shear rate. Perhaps more interesting, the highest degree of anisotropic ordering was observed after the cessation of flow. One reasonable explanation is that, the microfibrils “wobble” during shear flow because they are under constant torque due to a gradient in flow velocity perpendicular to the flow direction. Wobbles and undulations would increase the effective size of the particle and decrease the order. After shear ceases, the torque is removed and the role of undulations must change. Such considerations could have important industrial implications for optimal production of fibers spun from cellulose microfibrils.



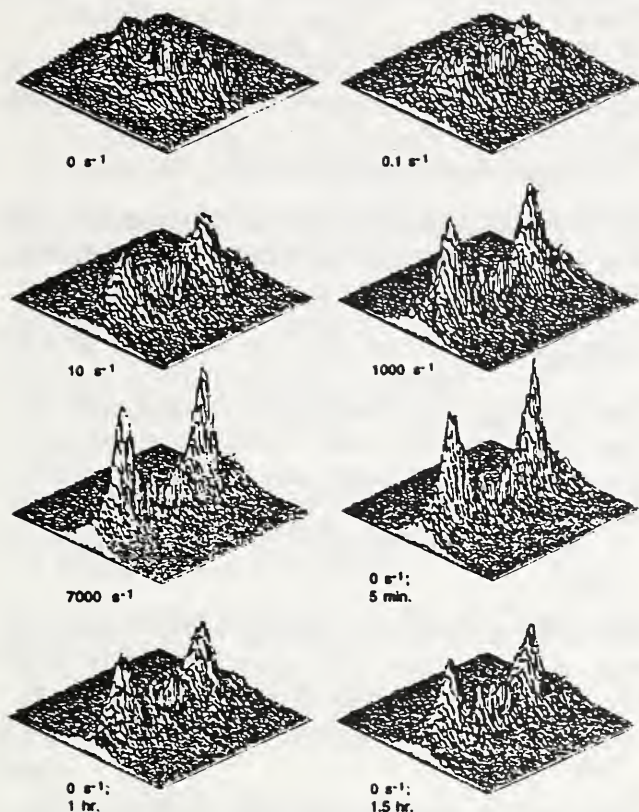


**Figure 7.** A series of isometric intensity plots of SANS data showing the alignment of cellulose microfibrils (5% in  $D_2O$ ) with increasing shear rate, as well as the relaxation of this ordering after the cessation of shear flow. The reflections, which are perpendicular to the shear flow direction, become more prominent with increasing shear rate. After the cessation of shear, peaks initially sharpen slightly, indicating an increase in anisotropic alignment, followed by relaxation of alignment with time.

## References

- [1] T. P. Russell, A. M. Mayes and M. Kunz, in *Ordering in Macromolecular Systems*, Teramoto, A., et al, eds., Springer-Verlag, Berlin, (1994), p.217-224.
- [2] G. Coulon, T. P. Russell, V. R. Deline, and P. F. Green, *Macromolecules*, **22**, 2581-2589 (1989).
- [3] B. Hammouda, B. G. Bauer, and T. P. Russell, *Macromolecules* **27**, 2357 (1994).
- [4] G. A. Olah, S. E. Rokop, L. A. Wang, S. L. Blechner, and J. Trehwella, *Biochemistry*, **33**, 8233-8239 (1994).
- [5] G. A. Olah, and J. Trehwella, *Biochemistry*, in

press (1994).

- [6] S. A. Kumar, N. S. Murthy, and J. S. Krakow, *FEBS Letters* **109**, 121-124 (1980).
- [7] E. Heyduk, T. Heyduk, and J. C. Lee, *J. Biol. Chem.* **267**, 3200-3204 (1992).
- [8] K. Sieradzki, *J. Electrochemical Soc.* **140**, 2868 (1993).
- [9] N. F. Berk, C. J. Glinka, W. Haller, and L. C. Sander, *Mat. Res. Soc. Symp. Proc. Vol. 166*, 409 (1990); N. F. Berk, *Phys. Rev. Lett.* **58**, 2718 (1987).
- [10] W. W. Mullins, in *Metal Surfaces: Structure, Energetics and Kinetics*, Am. Soc. of Metals, Metals Park, OH, p. 17 (1963).

## Research Topics

### • Polymers

#### Microphase Separation in Ultrathin Diblock Copolymer Films

T. Russell<sup>15</sup>, P. Lambooy<sup>15</sup>, J. Barker<sup>36</sup>, P. Gallagher<sup>36</sup>, S. Satija<sup>36</sup>, G. Kellogg<sup>23</sup>, and A. Mayes<sup>23</sup>

#### SANS Comparison of Polymer-Solvent Physical Gels and Microcellular Foams Derived from the Gels

R. R. Lagasse<sup>39</sup> and G. Beaucage<sup>39</sup>

#### Structure of Polymers Adsorbed in Microporous Silica

W. C. Forsman<sup>62</sup> and P. Dreux<sup>62</sup>

#### Phase Transformations and Domain Structure in Nylon

N. S. Murthy, H. Minor<sup>1</sup>, and W. J. Orts<sup>36</sup>

#### Molecular Weight Dependence of the Conformation of Dilute Polymers near their Theta Temperature

A. T. Boothroyd<sup>30</sup>, A. R. Rennie<sup>6</sup>, and L. J. Fetters<sup>13</sup>

#### Structure of Polymer Brushes Extending from Plate-like Polymer Micelles

J. S. Huang<sup>13</sup>, L. J. Fetters<sup>13</sup>, D. Richter<sup>19</sup>, and A. Gast<sup>41</sup>

#### Phase Separation Kinetics of Homopolymer/Copolymer Mixtures

B. Hammouda<sup>36</sup>, J. Lin<sup>4</sup>, and N. Balsara<sup>4</sup>

**SANS from Deuterated Polystyrene/ Polybutylmethacrylate Homopolymer Blend Mixtures**

B. Hammouda<sup>36</sup>, B. Bauer<sup>34</sup>, and T. P. Russell<sup>15</sup>

**Single Particle and Interparticle Structure of Dendrimers**

B. Bauer<sup>34</sup>, B. Hammouda<sup>36</sup>, and R. Briber<sup>58</sup>

**Star Polymers in Solution under Theta Conditions**

L. Willner<sup>19</sup>, O. Juckniskhe<sup>19</sup>, D. Richter<sup>19</sup>, L. J. Fetters<sup>13</sup>, J. Huang<sup>13</sup>, and J. Roovers<sup>25</sup>

**Scaling Behavior of the Entanglement Length in Concentrated Polyethylene Solutions**

D. Richter<sup>19</sup>, L. Willner<sup>19</sup>, S. Westermann<sup>19</sup>, L. J. Fetters<sup>13</sup>, and J. Huang<sup>13</sup>

**Butterfly Patterns from Bimodal Polymeric Networks**

R. Oeser<sup>16</sup>

**Structure and Morphology of Diblock Copolymers in a Selective Solvent**

A. P. Gast<sup>41</sup>, G. A. McConnell<sup>41</sup>, E. K. Lin<sup>41</sup>, and J. S. Huang<sup>13</sup>

**Lower ODT in Block Copolymers**

T. P. Russell<sup>15</sup>, A. M. Mayes<sup>23</sup>, and B. Hammouda<sup>36</sup>

**SANS Study of Adsorbed Copolymers**

T. Cosgrove<sup>48</sup>, P. Griffiths<sup>48</sup>, and B. Hammouda<sup>36</sup>

**Structure and Conformation of Model Telechelic Ionomers in Non-Polar Solvent under Shear**

S. Cooper<sup>54</sup>, S. Bhargava<sup>54</sup>, and E. Karayianni<sup>66</sup>

**Shear Effects on Block Copolymer Solutions**

N. P. Balsara<sup>4</sup>, C. C. Lin<sup>4</sup>, P. K. Kesani<sup>4</sup>, and B. Hammouda<sup>36</sup>

**Effects of Pressure on the Miscibility of Polymer Blends**

B. Hammouda<sup>36</sup>, B. Bauer<sup>34</sup>, and C. C. Lin<sup>4</sup>

**Phase Separation Kinetics of Homopolymer/Copolymer Mixtures**

B. Hammouda<sup>36</sup>, J. Lin<sup>4</sup>, and N. Balsara<sup>4</sup>

**SANS from Mixtures of Two Homopolymers and a Block Copolymer**

N. P. Balsara<sup>4</sup>, C. C. Lin<sup>4</sup>, P. K. Kesani<sup>4</sup>, and B. Hammouda<sup>36</sup>

**Transesterification of Polyester Sutures**

R. A. Weiss<sup>53</sup>, S. Yarmey<sup>53</sup>, and S. J. Huang<sup>53</sup>

**SANS Study of Hydrogen-Bonded Polymer Blends**

S. K. Kumar<sup>33</sup> and D. E. Bhagwagar<sup>33</sup>

**SANS from PDMS Networks in d-Toluene Solution**

B. Bauer<sup>35</sup> and B. Hammouda<sup>36</sup>

**SANS Study of Microscopic Deformation and Topological Constraints in Rubberelastic Networks**

V. Urban<sup>34</sup>, W. Pyckhout-Hintzen<sup>34</sup>, and D. Richter<sup>34</sup>

**The Scaling of the Screening Length and Radius of Gyration with Concentration in a Good Solvent: Polystyrene in Carbon Tetrachloride**

J. Barker<sup>36</sup>, A. Mayes<sup>23</sup>, R. Briber<sup>58</sup>, and W. Orts<sup>36</sup>

**The Scaling of the Screening Length and Radius of Gyration with Concentration in a Marginal Solvent: Polystyrene in cis-Decalin**

J. Barker<sup>36</sup>, A. Mayes<sup>23</sup>, R. Briber<sup>58</sup>, and W. Orts<sup>36</sup>

**Chain Conformation and Interactions in Isotopic Blends of PDMS at Cryogenic Temperatures**

G. Beaucage<sup>39</sup>, M. Kent<sup>39</sup>, and C. J. Glinka<sup>36</sup>

**Effects of Composition Fluctuations in a Critical Binary Fluid on the Conformation of Dissolved Polymer Chains**

P. Gallagher<sup>36</sup> and A. Karim<sup>34</sup>

**Compatibility of Deuterated Polystyrene/Sulfonated Polystyrene Blends**

N. C. Beck Tan<sup>58</sup>, X. Liu<sup>58</sup>, R. M. Briber<sup>58</sup>, and D. G. Peiffer<sup>13</sup>

• **Biology**

**Structural Characterization of Agarose Gels in the Presence of Pulsed and Steady-State Electric Fields**

S. Krueger<sup>36</sup>, A.P. Andrews<sup>8</sup>, and R. Nossal<sup>26</sup>

**Structure of Muscle Regulatory Proteins I: TroponinC/Troponin I Complexes**

G. Olah<sup>20</sup>, J. Trehwella<sup>20</sup>, S. Rokop<sup>20</sup>, and S. Krueger<sup>36</sup>

**Structure of Muscle Regulatory Proteins II: Calmodulin/Myosin Light Chain Kinase Complexes**

- G. Olah<sup>20</sup>, J. Trehwella<sup>20</sup>, M. Britt<sup>20</sup>, S. Rokop<sup>20</sup>, J. Stull<sup>65</sup>, and S. Krueger<sup>36</sup>
- Higher Order Structure of Plant Chromatin Fiber**  
J. G. Smith<sup>50</sup>, E. M. Bradbury<sup>50</sup>, P. M. Yau<sup>50</sup>, J. P. Baldwin<sup>68</sup>, and S. Krueger<sup>36</sup>
- The Distance Between Myosin Light Chains in Myosin and Acto-Myosin**  
R. Mendelson<sup>52</sup>, S. Fujiwara<sup>52</sup>, and D. Stone<sup>52</sup>
- Effects of Shear and pH on the Structure of Tubulin in the Presence of Taxol**  
S. Krueger<sup>36</sup>, D. Sackett<sup>26</sup>, A. Jin<sup>26</sup>, and R. Nossal<sup>26</sup>
- Ionic Strength and pH-Dependent Structure of Human Plasma Fibronectin**  
S. Krueger<sup>36</sup> and K. Ingham<sup>2</sup>
- Conformational Changes in Cyclic AMP Receptor Proteins**  
S. Krueger<sup>36</sup>, K. McKenney<sup>5</sup>, and F. Schwarz<sup>5</sup>
- Structure of the Critical Unilamellar Lipid State**  
S. Krueger<sup>36</sup>, N. Gerschfeld<sup>26</sup>, and V. I. Gordeliy<sup>18</sup>
- Structural Studies of the Phases of DNA at Intermediate and Low Concentrations**  
S. Krueger<sup>36</sup>, W. J. Orts<sup>36</sup>, H. Strey<sup>26</sup>, and R. Podgornik<sup>26</sup>
- **Structured Fluids**
- Scattering Behavior of Microemulsions near the Lifshitz Line**  
E. W. Kaler<sup>54</sup>, K.-V. Schubert<sup>54</sup>, R. Strey<sup>21</sup>, and J. G. Barker<sup>36</sup>
- The Structure and Shear Thinning Behavior of Polymeric Microgels**  
N. J. Wagner<sup>54</sup>, J. Bender<sup>54</sup>, J. Bergenholtz<sup>54</sup>, and L. Walker<sup>54</sup>
- Study of Structural Inversion of AOT/Water/Decane Microemulsions by SANS**  
S.-H. Chen<sup>23</sup>, C.-Y. Ku<sup>23</sup>, and D. Lee<sup>23</sup>
- Structure of Micelles in Viscoelastic Solutions**  
P. Butler<sup>64</sup>, L. Magid<sup>57</sup>, W. Hamilton<sup>28</sup>, and B. Hammouda<sup>36</sup>
- Micelle-Vesicle Transitions in Mixed Surfactant Colloidal Solutions**  
E. W. Kaler<sup>54</sup>, S. Kline<sup>54</sup>, K. Lusvarti<sup>54</sup>, and R. Koehler<sup>54</sup>
- Micellar Solution Phase Transition Dependence Upon Pressure**  
E. W. Kaler<sup>54</sup>, R. Zielinski<sup>54</sup>, K. Schubert<sup>54</sup>, K. Lusvarti<sup>54</sup>, and S. Kline<sup>54</sup>
- Gelation of Dense Colloidal Silica: Effects of Shear**  
H. J. M. Hanley<sup>69</sup>, G. C. Straty<sup>69</sup>, and C. D. Muzny<sup>52</sup>
- Particle Morphology in Mixed Aqueous Colloids of Monoglycerides and Bile Salts**  
R. P. Hjelm<sup>20</sup> and A. Hofmann<sup>50</sup>
- SANS Studies of Interactions in Colloid/Polymer Mixtures**  
P. Tong<sup>29</sup>, J. S. Huang<sup>13</sup>, and M. Lin<sup>13</sup>
- Microstructure of Microemulsions Formed by Siloxane Surfactants and Dimethyl Siloxane Polymers**  
R. M. Hill<sup>10</sup> and C. J. Glinka<sup>36</sup>
- SANS Study of the Structure of a Triglyceride Microemulsion**  
S. F. Trevino<sup>46</sup> and R. Joubran<sup>45</sup>
- Structure of Shearing Colloidal Gels**  
C. F. Zukoski<sup>56</sup>, K. Miller<sup>56</sup>, and M. Pertel<sup>56</sup>
- Particle Morphology and Aggregation Behavior in Asphaltene Solutions**  
E. Sheu<sup>44</sup>
- Microstructure and Processing of Liquid Crystalline Polymers**  
N. J. Wagner<sup>54</sup>, J. Bender<sup>54</sup>, M. Rivera<sup>54</sup>, L. Walker<sup>54</sup>, and R. Butera<sup>12</sup>
- Structure of Mixed MRG/Bile Salt Colloids**  
E. Y. Sheu<sup>44</sup> and M. Polikandritou-Lambros<sup>61</sup>
- Studies of Associative Polymer Molecules**  
R. H. Ottewill<sup>48</sup> and A. R. Rennie<sup>6</sup>
- Cholesteric Liquid Crystalline Phases of Cellulose Microfibrils**  
W. J. Orts<sup>36</sup>, J. F. Revol<sup>32</sup>, and M. Favier<sup>32</sup>
- Effects of Shear on Diblock Copolymers in Solution**  
B. Hammouda<sup>36</sup> and N. Balsara<sup>4</sup>
- Structure of Phospholipid Bilayers under Shear**  
B. Hammouda<sup>36</sup> and D. Worcester<sup>60</sup>
- Critical Composition Fluctuations in a Binary Fluid Confined in a Polymer Gel**

J. Maher<sup>63</sup>, J. Ganhi<sup>63</sup> and P. Gallagher<sup>36</sup>

**Morphology of Siloxane Surfactant Vesicles under Shear**

T. Lodge<sup>59</sup> and H. Doumaux<sup>59</sup>

• **Materials Science**

**Defect Structures in Nanocrystalline Palladium**

P. G. Sanders<sup>27</sup>, J. R. Weertman<sup>27</sup>, R. W. Siegel<sup>3</sup>, and J. G. Barker<sup>36</sup>

**SANS Studies of Irradiation Induced Microstructural Evolution in Pressure Vessel Steels**

G. R. Odette<sup>49</sup>, B. Wirth<sup>49</sup>, D. Klingensmith<sup>49</sup>, and J. Barker<sup>36</sup>

**Pore Structure and Formation Mechanisms of Mesoporous Molecular Sieves Prepared with Liquid Crystal Templates**

G. D. Stucky<sup>49</sup>, D. Margolese<sup>49</sup>, Q. Huo<sup>49</sup>, C. J. Glinka<sup>36</sup>, and J. Nicol<sup>36</sup>

**Microstructure Evolution of Commercial Grade Nanostructured Ceramics**

J. Parker<sup>24</sup>, S. Krueger<sup>36</sup>, G. Long<sup>7</sup>, and A. Allen<sup>58</sup>

**In-Situ Growth of Porous Silicon Structures by Electrochemical Attack**

P. Searson<sup>17</sup>, A. Natarajan<sup>17</sup>, D. Wiesler<sup>36</sup>, and J. Barker<sup>36</sup>

**In-Situ SANS Measurements of the Coarsening of the Pore Microstructure in dealloyed Ag/Au Substitutional Alloys**

K. Sieradzki<sup>17</sup>, S. Corcoran<sup>17</sup>, D. Wiesler<sup>36</sup>, and J. Barker<sup>36</sup>

**Pore Structure in Vanadium Oxide/Lithium Battery Materials**

D. Wiesler<sup>36</sup>, B. D. Lee<sup>59</sup>, and W. H. Smyrl<sup>59</sup>

**SANS as a Probe of Molecular Composites**

R. P. Hjelm<sup>20</sup>, B. Benicewicz<sup>20</sup>, and E. Douglas<sup>20</sup>

**SANS Characterization of Pore Evolution During Sintering of Dense Ceramic Compacts**

R. A. Page<sup>40</sup>, Y. Pan<sup>40</sup>, S. Krueger<sup>36</sup>, and G. G. Long<sup>7</sup>

**Dependence of Mean Pore Size upon Spraying Conditions in Alumina and Ytria Stabilized Zirconia Plasma Sprayed Coatings**

J. Ilavsky<sup>42</sup>, A. Allen<sup>58</sup>, G. G. Long<sup>7</sup>, and J. Barker<sup>36</sup>

**Microstructure Evolution of Microwave Assisted Reaction Bonded Silicon Nitride as a Function of Nitridation**

A. Allen<sup>58</sup> and G. G. Long<sup>7</sup>, S. Krueger<sup>36</sup>, J. Thomas<sup>27</sup>, and D. L. Johnson<sup>27</sup>

**Final Stage Sintering Studies of Magnesia-Doped Silicon Nitride**

S. Krueger<sup>36</sup>, A. Allen<sup>58</sup>, G. G. Long<sup>7</sup>, and J. Hwang<sup>11</sup>

**Real-Time Studies of the Thermodynamics of Sintering of Colloidal Silica Gels**

H. Kerch<sup>9</sup>, A. Allen<sup>58</sup>, G. G. Long<sup>7</sup>, H. Burdette<sup>7</sup>, and S. Krueger<sup>36</sup>

**Effects of Fabrication and Sintering Processes on the Microstructure Evolution of Nanostructured Zirconia**

G. Skandan<sup>38</sup>, S. Krueger<sup>36</sup>, G. G. Long<sup>7</sup>, A. Allen<sup>58</sup>, H. Hahn<sup>43</sup>, and H. Kerch<sup>9</sup>

**Sintering Studies of Nanostructured Alumina Produced by the Sol-Gel Process**

A. Allen<sup>58</sup>, W. Chen<sup>7</sup>, S. Malghan<sup>7</sup>, G. G. Long<sup>7</sup>, and S. Krueger<sup>36</sup>

**Assessment of Different Silica Fumes in Cement Microstructure Development**

A. Allen<sup>58</sup>, R. A. Livingston<sup>14</sup>, D. L. Gress<sup>14</sup>, and T. El-korchi<sup>67</sup>

**Microstructure of Natural Geological Candidates for Reactive Admixtures in Cements**

A. Allen<sup>58</sup>, R. A. Livingston<sup>14</sup>, and P. Heaney<sup>35</sup>

**Pore Characterization of Slip Cast Ceramic Compacts**

P. Smith<sup>31</sup>, J. Keller<sup>38</sup>, and H. Kerch<sup>9</sup>

**Correlation Hole Scattering from High Dielectric Foams**

T. Russell<sup>15</sup> and J. Barker<sup>36</sup>

**Grain Size and Interfacial Surface Area of Solid Propellants**

S. Trevino<sup>46</sup> and R. Lieb<sup>47</sup>

• **Magnetism**

**Fluxoid Lattice Morphology and Pinning in Microtwinned YBa<sub>2</sub>Cu<sub>3</sub>O<sub>7</sub>(S4-03)**

B. Keimer<sup>35</sup>, F. Dogan<sup>35</sup>, I. A. Aksay<sup>35</sup>, M. Sarikaya<sup>35</sup>, R. W. Erwin<sup>36</sup>, and J. W. Lynn<sup>36</sup>

**High Field Study of the Vortex Lattice in YBa<sub>2</sub>Cu<sub>3</sub>O<sub>7</sub>**

B. Keimer<sup>35</sup>, R. Erwin<sup>36</sup>, and J. W. Lynn<sup>36</sup>

**Fluxoid Lattice Dynamics and Melting in Niobium**J. W. Lynn<sup>36</sup>, N. Rosov<sup>36</sup>, and T. E. Grigereit<sup>58</sup>**Magnetic Critical Scattering from Invar Alloys**J. W. Lynn<sup>36</sup>, N. Rosov<sup>36</sup>, and M. Acet<sup>55</sup>**SANS Study of Superparamagnetic Correlations in Magnetic Refrigerant Nanocomposite Materials**R. D. Shull<sup>22</sup>, R. D. McMichael<sup>22</sup>, and C. J. Glinka<sup>36</sup>• **Other****Development of Analytical Smearing Corrections to SANS Data**J. Barker<sup>36</sup> and J. Pederson<sup>37</sup>**The Absolute Cross-Section of Water as a Function of Neutron Wavelength**J. Barker<sup>36</sup>**Affiliations**<sup>1</sup>Allied-Signal, Inc.<sup>2</sup>American Red Cross<sup>3</sup>Argonne National Laboratory<sup>4</sup>Brooklyn Polytechnic University<sup>5</sup>CARB<sup>6</sup>Cavendish Laboratory, UK<sup>7</sup>Ceramics Division<sup>8</sup>College of Wooster<sup>9</sup>DOE<sup>10</sup>Dow Corning Corp.<sup>11</sup>Dow Chemical Co.<sup>12</sup>DuPont Polymers<sup>13</sup>Exxon R&E Co.<sup>14</sup>Federal Highway Administration<sup>15</sup>IBM<sup>16</sup>Institut Laue Langevin<sup>17</sup>Johns Hopkins University<sup>18</sup>Joint Inst. for Nuclear Research, Moscow<sup>19</sup>KFA Julich, Germany<sup>20</sup>Los Alamos National Laboratory<sup>21</sup>Max Planck Institute<sup>22</sup>Metallurgy Division<sup>23</sup>MIT<sup>24</sup>Nanophase Technologies Corp.<sup>25</sup>National Research Council, Canada<sup>26</sup>NIH<sup>27</sup>Northwestern University<sup>28</sup>Oak Ridge National Laboratory<sup>29</sup>Oklahoma State University<sup>30</sup>Oxford University, UK<sup>31</sup>Pacific Northwest Labs<sup>32</sup>PAPRICAN<sup>33</sup>Pennsylvania State University<sup>34</sup>Polymers Division<sup>35</sup>Princeton University<sup>36</sup>Reactor Radiation Division<sup>37</sup>Riso National Laboratory, Denmark<sup>38</sup>Rutgers University<sup>39</sup>Sandia National Laboratory<sup>40</sup>Southwest Research Institute<sup>41</sup>Stanford University<sup>42</sup>SUNY<sup>43</sup>Technische Hochschule Darmstadt<sup>44</sup>Texaco R&D<sup>45</sup>U.S. Dept. of Agriculture<sup>46</sup>U.S. Army Armament RD&E Center<sup>47</sup>U.S. Army Research Laboratory<sup>48</sup>University of Bristol, UK<sup>49</sup>University of California, Santa Barbara<sup>50</sup>University of California, San Diego<sup>51</sup>University of California, San Francisco<sup>52</sup>University of Colorado<sup>53</sup>University of Connecticut<sup>54</sup>University of Delaware<sup>55</sup>University of Duisberg<sup>56</sup>University of Illinois<sup>57</sup>University of Kentucky<sup>58</sup>University of Maryland<sup>59</sup>University of Minnesota<sup>60</sup>University of Missouri<sup>61</sup>University of Oklahoma<sup>62</sup>University of Pennsylvania<sup>63</sup>University of Pittsburgh<sup>64</sup>University of Tennessee<sup>65</sup>University of Texas-Dallas<sup>66</sup>University of Wisconsin<sup>67</sup>Worcester Polytechnic<sup>68</sup>Liverpool Polytechnics<sup>69</sup>NIST, Boulder

# Neutron Beam Applications

## Neutron Diffraction Measurement of Residual Stress

Considerable progress has been made in the last three years at NIST in a number of areas relating to the neutron diffraction measurement of residual stress. This includes the development of new methods of sample alignment ("ALIGN"), the development of a comprehensive data reduction program ("STRESS"), and the design and construction of a new multipurpose double-axis diffractometer with a number of state-of-the-art features specifically for improved residual stress measurement. The first two were discussed in some detail in previous reports; an update of the third will be presented later in this section. The main focus of this section will be on recent applications of the neutron diffraction technique to real problems, the solution of which has been greatly facilitated by our recent advances in methodology.

### • Weldments

The fracture safety of welds may be compromised by the residual stress state which is usually unknown, the microstructure which may contain crack nuclei, and compositional gradients, especially that of hydrogen. Neutron techniques can, in principle, provide critical measurements of the above three phenomena and thus guide the development of rational solutions to the associated welding problems. A major portion of our experimental effort in this past year has been devoted to the study of the first of these elements, and has ranged in scope from studies of prototypical geometry weldments (to test finite element models), to specimens relating directly to real-world problems such as leaks in railroad tank cars and bridge failures.

*The variation of  $d_0$  around welds.* A critical element in the determination of the residual stresses in weldments is the value of the stress-free lattice parameter,  $d_0$ , at each measurement point in the material. As demonstrated re-

cently by Krawitz and Winholz [1], and confirmed here at NIST [2] for HSLA steel, the high temperatures associated with conventional welding methods can significantly alter alloy composition and  $d_0$ s even at centimeter distances. This is an area which is actively being investigated; results for specific specimens are discussed in the sections which follow.

*Testing models.* A very active area in welding science/technology is that of modeling weldments by means of finite element methods (FEM). One output of such modeling is the prediction of the residual stress distribution produced by the welding process. In a coordinated ORNL-NIST, ONR-supported program we have attempted to determine the residual stress distribution for a geometry amenable to modeling: a spot-welded disk.

Initial results for the specimen (assuming a uniform  $d_0$ ) were presented in last year's report. It is an HSLA-100 steel disk containing a large spot weld in the center of the top flat face. The diameter of the disk is 76.2 mm; the thickness 18.6 mm. At the center position of the disk a welding pool was created approximately 20 mm in diameter and 7 mm depth. The materials properties of this specimen (especially the stress free lattice parameter) are expected to be position dependent, because of the temperature gradients imposed by the welding. Therefore, after the stress measurements, the specimen was destroyed to verify its properties as follows. At the stress measurement positions  $2 \times 2 \times 2$  mm<sup>3</sup> cubes were extracted from the specimen by electric discharge machining (EDM). The d-spacing of these cubes was measured in 8 pseudo-random orientations, the average value of which was intended to provide  $d_0(r, \theta, z)$ . The results show a strong trend towards higher values closer to the weld. However, at positions far away from the weld, there is considerable variation in the  $d_0$ s. We believe that this is caused by small misalignments of the cubes on the specimen table of the

spectrometer, because when  $d_0$  was measured in the intact piece prior to welding, there was little variation.

At this time an estimate of the variation of  $d_0$  has been made. However, a quantitative  $d_0$  vs position, and a final determination of the complete stress distribution, will require a re-measurement of the  $d_0$ s of the extracted cubes. This will be done as soon as neutrons are again available. On the other hand, the shear stresses—which are not sensitive to the  $d_0$  value—can be compared with initial FEM calculations recently completed at ORNL [3]. The results agree in the magnitude of stresses and in the overall trend with distance away from the weld. However, the details are not in good agreement with our measured values. Refinement of the FEM model is in progress at ORNL.

*Evolution of stresses around a weld.* Utilizing the nondestructive character of neutron diffraction, an ONR-supported study of the evolution of residual stress patterns on a pass-by-pass basis was begun in FY93 on a test specimen of high-strength low-alloy steel (HSLA) in a v-notch weld channel geometry (Fig. 1). Measurements have been made in the central plane around the notch before welding and after each of four weld passes.

At each of 25 sampling points in the base metal ( $3 \times 3 \times 3 \text{ mm}^3$  gauge volume), one or two Bragg peak scans were made in the reflection geometry, and at least four scans were made in transmission. Given  $d_0$  as a function of position, this would provide sufficient information to extract, without any assumptions or approximations, three normal stress components and one shear stress component. Several points in the weld metal, which require separate analysis, were examined but are not yet analyzed. An initial “stress-free”  $d_0$  was obtained from the unwelded plate, which was confirmed to be essentially stress free by neutron diffraction. However, as described above, we find that in weldments  $d_0$  can vary with thermal history (and distance from the weld).

Based on the preliminary correlation of

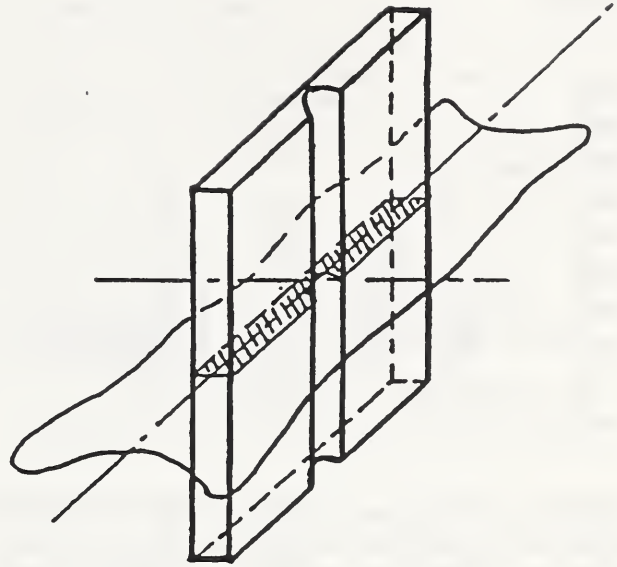
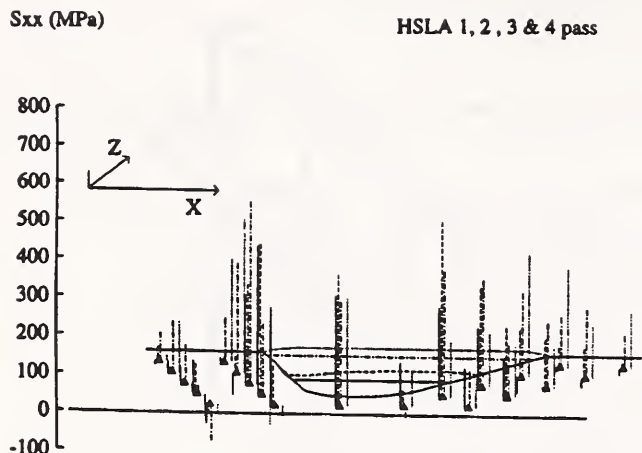


Figure 1. HSLA-100 plate for weldment residual stress studies. The plate is  $15.2 \times 15.2 \times 1.9 \text{ cm}^3$  with a rounded v-notch, 2.2 cm maximum width and 1.3 cm deep.

FWHM with  $d_0$  for the spot weld specimen described above, we estimate from the measured FWHMs in the v-notch sample that in the base metal—even at the points closest to the weld metal—the variation in  $d_0$  with position should change the residual stress values by no more than  $\approx 100 \text{ MPa}$  toward more compressive stresses. In view of this, we present in figure 2 the longitudinal ( $\sigma_{xx}$ ) residual stress distributions after each of four weld passes as an indicator of how the stress distributions evolve with weld pass.

Certain features are noteworthy:

1. A clear, highly-tensile stress field is produced in the base metal in the measurement region nearest the channel (gauge volume centers 3 mm from channel). The tensile stress maximum ( $\approx 700 \text{ MPa}$ ) occurs in the longitudinal (*i.e.*  $y$ ) direction and is approximately 50% more than the maxima in the transverse directions.
2. At gauge volume centers 8 mm away from the channel, measured stresses are near zero



**Figure 2.** The  $\sigma_{xx}$  residual stress distribution around the v-notch in the plate of figure 1. At each point four vertical lines indicate the measured residual stress after each of the four passes (1st pass  $\leftrightarrow$  the left-most line, etc.). The counting statistics lead to uncertainties of about  $\pm 25$  MPa on each stress value. It should be mentioned that "passes" 3 and 4 each required two weldments to level the weld metal in the channel.

or somewhat compressive.

3. For the gauge volumes closest to the channel, the change in tensile stress levels can be seen at each point as the weld passes fill the v-notch.

The after-four-pass neutron results for the axial and transverse directions in the central plane of the plate are in good qualitative agreement with results obtained by x-ray diffraction for surface stresses around a bead weld on a steel plate. To our knowledge, this is the first study of residual stresses after successive weld passes ever performed.

*Tank-car weldments.* The Federal Railroad Administration of the Department of Transportation (DOT) has a direct responsibility for the safe transport of hazardous materials via tank cars. One aspect of this responsibility has to do with the effectiveness and durability of axial stiffeners welded to older tank cars to increase tank shell buckling strength. Analytical calculations performed some years ago indicated that

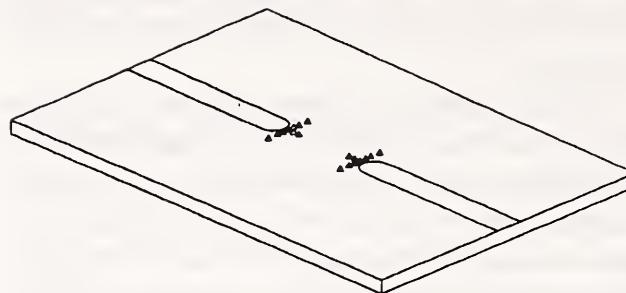


**Figure 3.** Measurement points and weldment geometry for the DOT skip-weld study.

high tensile stresses, which would promote structural failure, may occur at the start- and end-points of the skip welds used to attach the stiffeners to the tank cars [4]. In a DOT-supported collaborative project with the Metallurgy Division, we began, in FY93, the first determination of residual stress distributions in skip-weld specimens of the type used for railroad tank car stiffeners.

A total of four specimens produced under different welding conditions, an example of which is shown schematically in figure 3, and one unwelded specimen, were characterized. In this case, no systematic change in FWHMs was observed as a function of distance from the weld. We interpret this as evidence for constant  $d_0$  throughout the region of interest. This is supported by the results of surface x-ray diffraction measurements [5] on the same specimens which were in good agreement with our near-surface results.

The neutron measurements were made using a nominal  $3 \times 3 \times 3$  mm<sup>3</sup> gauge volume in identical patterns around the start and end of  $\approx 12.7$  mm wide, surface skip welds with  $\approx 40$  mm spacing between weld-start and -end on 12.7 mm thick plates. The measurements were made at three depths: 3.18, 6.36, and 9.54 mm below the welded surface. The pattern of gauge volume centers at each depth, as shown in figure 3, was identical: 7 points on a line perpendicular to the weld direction,  $\approx 2$  mm from the projection of the weld tip at its closest approach. One



point was on the weld centerline, the remaining six were at 3, 6, and 11 mm away from the centerline on either side. Two additional points were measured on the centerline at 5 and 8 mm from the weld tip. The x-ray measurements were made along line perpendicular to the weld direction at the center line and 6 mm on either side.

Partial results for one specimen—essentially typical of all four—are shown in figure 4. Also shown are surface residual stresses from x-ray measurements [5]. Overall, the measured residual stress distributions through the thickness around the start and end points of the weldments are not in very good agreement with the analytical-model predictions. We find that only the normal stresses parallel to the bead-on-plate weldment direction are tensile. In addition, although the maximum tensile stress measured is comparable to the predicted value, the measured change in stress with distance from the weld tip is much less than the model calculations.

#### • Standard Stress Sample

Although confidence in the neutron technique has increased within the materials science and engineering communities, no demonstration of standardization or consistency between laboratories has been made. One of the steps in the direction of such standardization is the development of standard specimens that have well-characterized residual stress states and which could be examined worldwide. To this end we have fabricated and characterized a steel ring-plug specimen with very well defined diametrical interference [2].

In the present measurements all six components of the stress tensor as a function of position have been determined. No prior assumptions about orientation of the principal axis system and/or multi-axiality of the residual stress pattern have been made. The specimen is a ring/plug specimen made of an 1100 type carbon steel. Its overall diameter is 50.8 mm. The thickness and plug diameter both measure 25.4 mm. Both the plug and the ring are slightly tapered (approximately 0.0175 mm/mm on the

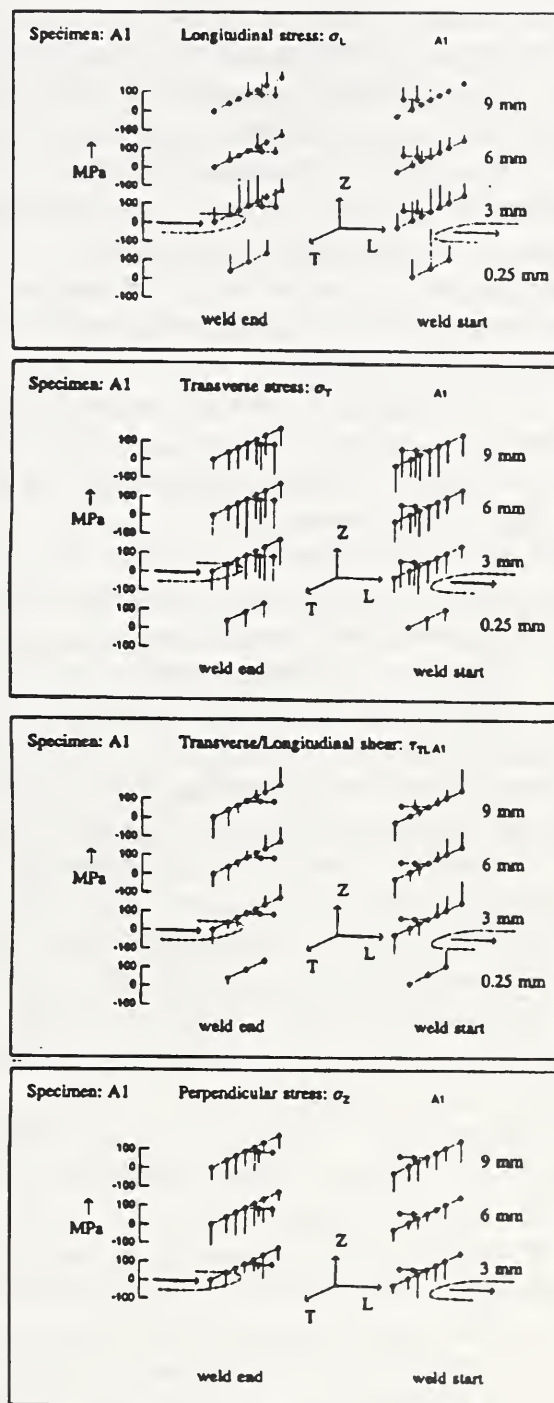


Figure 4. Measured stress distributions at three depths for one of the four DOT plates. X-ray determined stresses at six points on the surface are also shown.

diameter), so the parts could be pressed together instead of thermally shrink fitted. After press fitting and measuring the increase in overall diameter, the diametrical interference between ring and plug was inferred [6] to be 0.114 mm. The specimen possesses an analytically predictable bi-axial residual stress field, based on the equations for a thermal shrink fit. While pressing the plug in the hole no metallurgical changes take place within the specimen, so the stress free lattice parameter can be assumed to be constant and equal to its pre-assembly value throughout both parts.

In the steel disk we define a cylindrical axis system:  $r$ ,  $\theta$ , and  $z$  corresponding to the radial, hoop and axial directions respectively (see Fig. 5). The residual stress state at a position in a specimen is represented by a tensor that contains six components: three normal stresses ( $\sigma_r$ ,  $\sigma_\theta$ , and  $\sigma_z$ ) and three shear stresses ( $\tau_{r\theta}$ ,  $\tau_{rz}$ , and  $\tau_{\theta z}$ ). These components are determined from strain values that are in turn determined from the Fe-(110) lattice spacings that are measured by means of neutron diffraction. The strain at 7 different specimen orientations, equally divided over all possible orientations, is determined for various values of  $r$  and  $z$  in a plane of constant  $\theta$ . The neutron beam apertures were chosen such that the sampling volume within the specimen was about  $3 \times 3 \times 3$  mm<sup>3</sup>. Thus all six components of the residual stress tensor are determined as a function of position.

Measurements were made at three different depths (4.0, 12.7, and 21.4 mm below the surface at which the tapered pin cross section is largest). The stress free lattice parameter  $d_0$  was determined prior to assembly. The six components of the residual stress tensor are plotted as a function of their position in specimens in figure 6. To arrive at these results the following values for the diffraction elastic constants [5] are used:  $S_1 = -1.187$  TPa<sup>-1</sup> and  $S_2/2 = 5.42$  TPa<sup>-1</sup>. Also drawn in figure 6 are the stresses calculated according to the ring plug shrink fit model, which describes the experimental data very well. The results are mechanically self consistent in that all

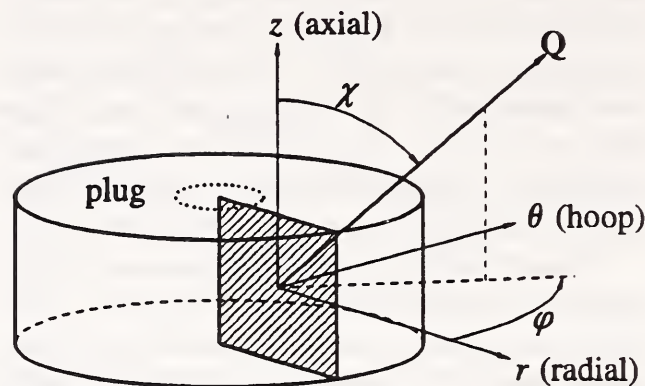


Figure 5. Schematic of ring/plug reference stress specimen.

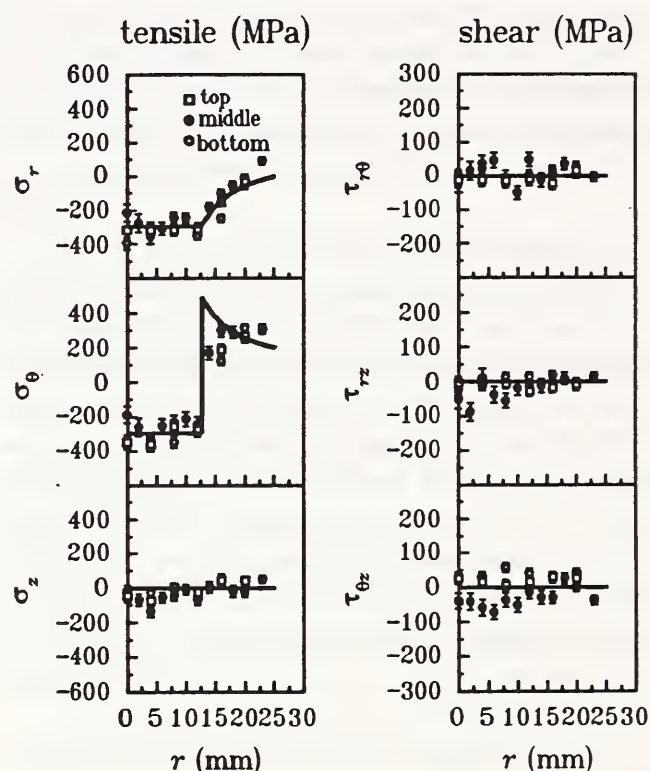


Figure 6. Measured stresses in ring/plug specimen.

applicable force balance laws are satisfied within the accuracy of the measurements.

We conclude that the ring/plug specimen appears to be an excellent candidate as a standard to intercompare neutron facilities and subsequently as a reference standard for other NDE

techniques.

- **Other Applications**

*Powder metallurgy.* Collaborative studies with researchers from M.I.T. have continued on a compacted iron powder, important for understanding new powder metallurgy techniques. Although the measurements are straightforward, in principle, the predicted strains are on the order of  $100 \mu$  strain, which is at about the limit of sensitivity of the BT-6 instrument. This work will be resumed when the new higher resolution, higher intensity instrument is operational in FY95.

*Squeeze-cast metal-ceramic composites.* Ceramic-fiber reinforced metal-matrix composites (MCCs) are beginning to be used in applications requiring good strength at high temperatures, good structural rigidity and dimensional stability, light weight, and good fabricability. One place that automotive engineers see enormous potential value for MCCs is as piston head reinforcements in automobile engines. At present, questions relating to residual stresses in the piston body, the squeeze cast reinforced top of the piston, and the effect of residual stresses on the performance of the squeeze-cast component must be answered.

We have performed a preliminary study of GM-provided aluminum-alloy matrix metal and the alumina/silicate reinforcement fiber preform to determine if neutron diffraction could characterize residual stresses in these materials. The results suggest that it should be possible in the aluminum matrix, but unlikely in the ceramic fibers (because of relatively low intensity and the complexity of the overlapping alumina and silicate diffraction patterns). Complimentary measurements were also begun on a similar composite in collaboration with Materials Reliability Division scientists.

- **A New Double-Axis Spectrometer for Residual Stress, Texture, and Single-Crystal Analysis (DARTS)**

The new DARTS is a multipurpose neutron

diffraction instrument that will be installed in 1995 on BT-8. The current status is as follows.

A basic US-1 (BNL-design: Universal Spectrometer 1) drum has been modified to safely allow monochromator take-off-angles ( $2\theta_M$ ) up to  $120^\circ$  for residual stress measurements. Texture and single-crystal diffraction will utilize a take-off angle of  $\sim 25^\circ$ . A variable beam size limiter has been built, which reduces the size of the reactor beam before it enters into the monochromator drum. This is expected to significantly reduce instrument background level. Furthermore, an extensive primary and secondary beam handling system has been designed and is now under construction. It allows a choice of potential sampling volumes from  $25 \times 25 \times 25 \text{ mm}^3$  to  $1 \times 1 \times 1 \text{ mm}^3$ . The primary beam handling system slides in and out of a plug that is secured in the monochromator drum. The diffracted beam system slides between the counter and the sample table. The sliding action is meant to allow for objects on the sample table to freely move in space while going from one scan to another, or even while performing some classes of scans. When required the slides can accommodate a set of Soller slit blades.

The sample table has been completed and tested. It consists of an  $[x, y, z]$  translation table with 17 cm travel in all three directions. The automated monochromator system with remote controlled rocking, translation, etc., and four different monochromators (on an elevator system) has been completed. Also an elevator device to shift a pyrolytic graphite filter in and out of the beam will be incorporated. Its purpose is to suppress the higher order wavelengths in the monochromatized beam for single crystal and texture measurements. A position sensitive detector system has been received from Ordella Inc. (Oak Ridge, TN) and is ready to be tested. A radial collimator option, between the specimen and the detector, continues to be evaluated.

On completion, DARTS will be a state-of-the-art facility. The expected increase in throughput for particularly residual stress measurements will be at least a factor of five.

## Neutron Diffraction Measurement of Texture

### • Studies of Shaped-Charge Liners

It is well known that the textures of polycrystalline metals play a significant role in plasticity and other important physical properties of materials. However, the utilization of texture information for the improvement of specific materials properties or to the tailoring of fabrication processes is not a common practice yet, partly because of the difficulty of obtaining quantitative three-dimensional orientation distribution functions (ODF). Very recently, a comprehensive ODF analysis program package, called popLA, has been developed by Kallend, et al. [7], which is now incorporated for routine use in our analysis software.

As part of a continuing project for DOD, complete three-dimensional ODFs of two molybdenum shaped-charge liners, FM for as-forged and RM for recrystallized (1100 °C for one hour), were determined to test for correlations between the measured textures and the macroscopic properties. Coupons labeled FM1 and RM1 were cut from the periphery, FM2 and RM2 from the mid-latitude, and FM3 and RM3 from near apex of the hemispherical liners. The three pole figures, (110) (200) and (211), were measured over the entire orientation hemisphere.

For FM1, the three pole figures showed orthorhombic sample symmetry. The orientation distribution function (ODF) was analyzed from the three pole figures with orthorhombic sample symmetry, using the WIMV method of the program popLA. For FM2, the experimental pole figures showed a slight deviation from orthorhombic symmetry. Therefore, the ODF was analysed with the triclinic sample symmetry. For FM3, the raw experimental pole figures showed features quite different from the other two samples. In the case of the uniaxial compression including the hemispherical forging, the texture of the sample near the apex is expected to have a mirror-symmetric profile about the mean ra-

dial direction, but not about the transverse direction. The pole figures were rotated by 33 degrees to satisfy the radial flow symmetry. Using the rotated pole figures, the ODF was obtained with triclinic sample symmetry. The major textures found in the FM3 were (111)-fiber and  $\{013\} \langle 031 \rangle$ .

The pole figures of RM1 were clearly different from those of FM1, with high-density localized peaks and with a slight deviation from the orthorhombic symmetry. The ODF was obtained by using the the triclinic sample symmetry. For RM2, the pole figures were similar to those of the FM2 sample. The ODF were obtained by using the triclinic sample symmetry. For RM3, the pole figures were very similar to those of the FM3 sample. The ODF were obtained by using the triclinic sample symmetry option because of the observed monoclinic-type sample symmetry.

This study indicates that the textures developed in the as-forged hemispheric liner are highly dependent on the radial distance from the apex. A relatively mild degree of texture formation, consisting of the (111) fiber and (013)  $\langle 031 \rangle$  sheet-type, was found in the near-apex position. In the mid-latitude, the texture strength was slightly increased, retaining the (111) fiber and adding (100)  $\langle 010 \rangle$  cube texture and (118)  $\langle 801 \rangle$ . The texture was developed to the highest strength at the periphery of the liner, where the (111) fiber persist with moderate strength and the (001) fiber gained strength. Two strong sheet-type textures, (001)  $\langle 110 \rangle$  and (118)  $\langle 110 \rangle$ , were found in the periphery of the liner. When the forged liner was heat-treated at 1100 C for one hour, the textures at the apex and mid-latitude region remained almost the same, but those at the periphery changed, with disappearance of the fiber-type and new formation of several strong sheet-type textures, such as (118)  $\langle 110 \rangle$  (001)  $\langle 110 \rangle$  and (111)  $\langle 257 \rangle$ . The texture strength at the periphery was exceptionally large because of the unusually strong (118)  $\langle 110 \rangle$  recrystallization texture. The major texture components of the

**Table 1.** Major texture components and their peak intensity (in multiples of random [mrd] units) of the three as-forged (FM) samples compared with those of the recrystallized (RM) samples. The (111) and (100) fiber-axes in the table are oriented perpendicularly to the liner surface. The pole density enclosed in parentheses indicates that the texture component is a part of the corresponding fiber texture. The pole densities marked with “-” correspond to intensity less than 2 mrd.

Texture	FM1	RM1	FM2	RM2	FM3	RM3
(111)-fiber	6	2	6	4	4	5
(111)<101>	8	(2)	(6)	(4)	(4)	(5)
(111)<257>	(6)	6	8	7	(4)	(5)
{001}-fiber	4	-	2	-	-	-
{001}<110>	20	13	(2)	-	-	-
{001}<100>	(4)	-	7	8	-	-
(118)<801>	-	-	4	7	-	-
(118)<110>	17	50	-	-	-	-
(013)<031>	-	-	-	-	5	5
Tex. strength	2.1	2.9	1.6	1.5	1.5	1.7

six samples are summarized in Table 1.

#### • Texture in SiC-Al Composites.

Textures of two SiC/Al composite specimens, one with 30 wt% SiC and other with 15 wt% SiC, were studied. Three pole figures of SiC whiskers in the composite, (004), (100), and (106), were measured based on the hexagonal cell with  $a=3.076 \text{ \AA}$  and  $c=15.12 \text{ \AA}$ . The ODFs were calculated from the three pole figures using the program popLA. All the experimental pole figures and the calculated inverse pole figures indicated that the SiC phase has a typical (001) fiber-texture with the fiber axis oriented parallel to the cylinder axis.

In an ideal fiber-texture, the (001) fiber-axes distribution may be represented by a 1-d distribution,  $P(x)$ , where  $x$  is the tilt angle measured from the fiber-axis direction. The 2-d distribution of the (004) pole figure was reduced to a 1-d distribution by circular averaging of the densities at a given tilt angle. The 1-d distribution was fitted to Pseudo-Voigt function,  $F(X)$ ,

**Table 2.** The results of the fiber-texture analysis of 30% and 15% SiC/Al composite samples, based on the Pseudo-Voigt function type distributions. The parameter eta is the Lorentzian fraction.

	30%SiC	15%SiC
eta	0.69	0.73
FWHM(0)	27.9	21.2
(001) %	91	90
(203) %	9	10

with double fiber texture with a strong (001)-fiber and a weak (203)-fiber (about 10% of the (001) in peak height) for the two samples. Similarly, the distribution of the ND direction (cylinder axis direction in the sample) in the crystal system was obtained from the ND inverse pole figure, in the form of a 1-d distribution. If the ODF is correct, the fiber-axes distributions in the sample system should be identical to the ND distribution in the crystal system. The two dis-

tributions were normalized to the random distribution (mrd unit) and compared in Table 2. The same result was obtained for the 15% sample.

## Neutron Autoradiography of Paintings

A number of paintings were studied in FY94. This included:

St. Sebastian Tended by Irene (Circle of Georges de La Tour), Kimbell Art Museum; Cheat with the Ace of Clubs by Georges de La Tour, Kimbell Art Museum; a test painting for a feasibility study, National Gallery of Art; Landscape, OCI collection.

The main effort, however, was in the area of instrumentation. One of the limitations to the traditional autoradiography method is that because of the low efficiency in using radiographic film as the radiation recording medium, only about a dozen working autoradiographs may be produced during the typical two month study period before the induced radioactivity in the painting is reduced to background levels again. Often, an accurate distribution of elements cannot be obtained in that there are too few data points available to distinguish the effects from different elements. Furthermore, the limited dynamic range and the non-linear nature of film response to radiation make quantitative analysis difficult.

Gamma ray spectroscopy is used instead to determine the quantity of elements present in the painting without knowing their exact locations. Elements such as phosphorus which emits no gamma rays cannot be determined by the gamma ray method at all. A sensitive linear responding radiation detector with high spatial resolution is needed as a film replacement if one is to attempt to examine the elemental composition at any location on the painting. The recently developed photostimulable storage phosphor imaging plate is such a detector that has been well-proven in biomedical research. The imaging plate has been shown to be 10 to 100 times more sensitive to radiation, particularly to charged particles, than the

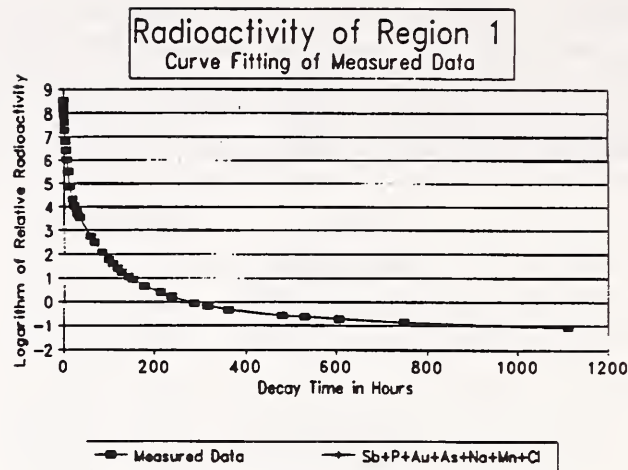


Figure 7. Radioactivity vs. time with new detectors.

fastest x-ray film/scintillation screen system. It exhibits a wide dynamic range ( $>10^5$ ) with excellent linearity. An experiment was conducted on a landscape painting (10" x 14", oil on masonite, private collection) to test the feasibility of autoradiographic study of paintings employing a storage phosphor imaging system. A Fuji Bio-Imager 2000 imaging system was kindly provided to us by Fuji Medical System, USA.

The landscape painting was placed in the NIST reactor thermal column painting activation port for 10 min at 15 MW, a reduction from the normal 20 min activation time. Following the activation, 55 time exposures were carried out on the painting with the storage phosphor imaging plates over a period of 2 months. Figure 7 shows the radioactivity decay history of a small dark brown area at the upper right hand corner of the painting. The decay history is a time plot of the measured radioactivity of the selected area as extracted from individual phosphor imager autoradiographs. Mathematically, the decay history can be expressed as

$$A(t) = a_1 e^{-\lambda_1 t} + a_2 e^{-\lambda_2 t} + \dots$$

where  $A(t)$  denotes the radioactivity of the selected area at time  $t$  after neutron activation. The letter " $i$ " is the number of different elements used in the painting that could be detected by the neutron activation method. Depending on

the complexity of the palette that the artist used "i" could be as high as 20 or 25. The values of  $\lambda_i$  represent the known characteristic decay constants for each type of element/isotope in the painting and 'a' is identified with the radioactivity of each element/isotope in the selected area at the end of painting activation when  $t=0$ . The amount of each different element in the selected area can be converted from the corresponding value of 'a' from a well-established data base. Assuming a library of 20 elements, one can select 20 different time values on the decay history curve to form 20 independent linear equations for the solving of  $\{a_1 \dots a_{20}\}$ . Values for  $\{a_1 \dots a_{20}\}$  can also be derived graphically on the decay history curve. The data from the selected small brown area has been analyzed graphically to consist of the following elements:

Element	Weight (...g)
Antimony	20
Phosphorus	32
Gold	2
Arsenic	6
Sodium	36
Manganese	42
Chlorine	87

The results of this experiment prove that the composition of a painting can be analyzed by neutron activation digital autoradiography, and if this analytical approach were expanded, it would enable the entire painting to be reconstructed by means of elemental distributions. This method overcomes the limitations of x-ray radiography or traditional film-based autoradiography, making possible the point-by-point analysis of any area of the painting wherein the location or distribution of any element can be mapped out. Computer software development for this program is continuing. An automated data analysis system is envisioned to generate elemental distribution profiles for the entire painting. We are also beginning to study the possibility of using the storage phosphor imaging plate for neutron detection for neutron scattering and diffraction experiments.

## References

- [1] A. D. Krawitz and R. A. Winholtz, *Mat. Sc. Eng. A*, **185**, 123 (1994).
- [2] P. C. Brand, H. J. Prask, J. Blackburn, R. J. Fields, and T. M. Proctor, *Proc. Matls. Res. Soc.* (Nov. 1994), in press.
- [3] T. Zacharia et al., unpublished.
- [4] O. Orringer, J. E. Gordon, Y. H. Tang and A. B. Periman, *Proceedings of the 1988 Applied Mechanics Rail Transportation Symposium, AMD-Vol. 96/RTD-Vol. 2*, pp. 87-94.
- [5] P. Prevey, (unpublished work).
- [6] J. W. Dally and W. F. Riley, *Experimental Stress Analysis*, (McGraw-Hill, New York), 1965, p 76.
- [7] J. S. Kallend, U. F. Kocks, A. D. Rollett, and H.-R. Wenk, *Operational texture analysis*, *Mat. Sci. Eng.*, **A132:1** (1991).

## Research Topics

### Evaluation of New Neutron Area-Detectors for NDE Applications

Y. T. Cheng<sup>18</sup>

### Design and Construction of a New Neutron Diffractometer for Single-Crystal Diffraction, Texture Determination, and Residual Stress Measurement

P. C. Brand<sup>23</sup>, C. S. Choi<sup>1,17</sup>, J. W. Lynn<sup>17</sup>, L. P. Robeson<sup>17</sup>, E. Prince<sup>17</sup>, and H. J. Prask<sup>17</sup>

### 'STRESS': A Comprehensive Code for Data Reduction in Neutron Diffraction Residual Stress Measurements

P. C. Brand<sup>23</sup>

### Determination of $d_0$ for Neutron Diffraction Residual Stress Measurements

P. C. Brand<sup>23</sup> and H. J. Prask<sup>17</sup>

### Evolution of Residual Stresses Around a V-notch Multipass Weld in a Steel Plate

J. Blackburn<sup>21</sup>, P. C. Brand<sup>23</sup>, R. J. Fields<sup>14</sup>, and H. J. Prask<sup>17</sup>

### Determination of Subsurface Residual Stresses in a 150 mm Steel Shell Base

P. C. Brand<sup>23</sup>, H. J. Prask<sup>17</sup>, W. Sharpe<sup>1</sup>, and C. S. Choi<sup>1,17</sup>

### Fabrication and Characterization of Standard Reference Specimens for Residual Stress Measurement Techniques

- H. J. Prask<sup>17</sup>, P. C. Brand<sup>23</sup>, T. M. Proctor<sup>19</sup>  
**The Effect of Texture and Sample Geometry on the r-Value of Heavy Gauge Tantalum Plate**  
 C. Michaluk<sup>4</sup>, C. S. Choi<sup>1,17</sup>, and J. Bingert<sup>12</sup>.
- Microstructure Study of Molybdenum Liners by Neutron Diffraction**  
 C. S. Choi<sup>1,17</sup>, E. L. Baker<sup>1</sup>, J. Orosz<sup>1</sup>, and D. H. Lassila<sup>25</sup>
- Application of O.D.F to the Rietveld Profile Refinement of Polycrystalline Solids**  
 C. S. Choi<sup>1,17</sup>, E. L. Baker<sup>1</sup>, and J. Orosz<sup>1</sup>
- ALIGN: A Comprehensive Code Facilitating the Alignment of a Spectrometer and Slits for Residual Stress Measurements by Means of Neutron Diffraction**  
 P. C. Brand<sup>23</sup>
- Residual Stress Analysis of Bent Steel Pipes**  
 P. C. Brand<sup>23</sup>, J. Goff<sup>9</sup>, M. T. Hutchings<sup>9</sup>, and H. J. Prask<sup>17</sup>
- Residual Stress Measurements on Spot Welded High-Strength Low Alloy Steel**  
 P. C. Brand<sup>23</sup>, J. Blackburn<sup>21</sup>, R. J. Fields<sup>14</sup>, and H. J. Prask<sup>17</sup>
- The Effect of the Total Neutron-Through-Specimen-Flight-Path on d-Spacing Determinations in Neutron Residual Stress Measurements by Means of k-scans**  
 P. C. Brand<sup>23</sup> and H. J. Prask<sup>17</sup>
- Characterization of a Kaowool-Reinforced Aluminum-Silicon Squeeze Casting Alloy for the Fabrication of Wear Resistant Automobile Pistons**  
 P. C. Brand<sup>23</sup>, C. G. Tibbetts<sup>7</sup>, and H. J. Prask<sup>17</sup>
- Residual Stress Measurements on Bead on Plate Repair Welds for Railroad Tank Cars**  
 P. C. Brand<sup>23</sup>, O. Orringer<sup>22</sup>, G. M. Hitcho<sup>14</sup>, and H. J. Prask<sup>17</sup>
- Residual Stress Measurement Feasibility Study of a Non-magnetized Nd<sub>2</sub>Fe<sub>14</sub>B Magnet Material**  
 P. C. Brand<sup>23</sup>, C. Fuerst<sup>7</sup>, and H. J. Prask<sup>17</sup>
- Residual Strain Measurements on a Compacted Iron Powder Specimen**  
 P. C. Brand<sup>23</sup>, S. Brown<sup>13</sup>, J. Wlassich<sup>13</sup>, and H. J. Prask<sup>17</sup>
- Strain Partitioning Feasibility Study for Titanium Matrix Composites**  
 B. Maruyama<sup>2,26</sup>, H. J. Prask<sup>17</sup>, and P. C. Brand<sup>23</sup>
- Orientation Distributions of SiC-Al Composites by Neutron Diffraction**  
 C.-S. Choi<sup>1,17</sup>
- Residual Stresses in Al-Metal-Matrix Composites**  
 H. J. Prask<sup>17</sup>, P. C. Brand<sup>23</sup>, and H. M. Ledbetter<sup>20</sup>
- Strains in (General Electric) Abrasive Disks**  
 P. C. Brand<sup>23</sup>, H. J. Prask<sup>17</sup>, and E. Drescher-Krasicka<sup>14</sup>
- An Evaluation of the Effect of Neutron Activation on Artists' Paints**  
 B. H. Berrie<sup>27</sup>, J. Cuttle<sup>27</sup>, S. Quillen Lomax<sup>27</sup>, E. R. de la Rie<sup>27</sup>, and Y.-T. Cheng<sup>18</sup>

### Affiliations

<sup>1</sup>Army Armament RD&E Ctr.

<sup>2</sup>MSEL, NIST

<sup>3</sup>Boeing Corp.

<sup>4</sup>Cabot Corp., PA

<sup>5</sup>Ceramics Division

<sup>6</sup>Detroit Institute of Art

<sup>7</sup>General Motors

<sup>8</sup>Hahn-Meitner Institut, Germany

<sup>9</sup>Oxford University

<sup>10</sup>Honeywell

<sup>11</sup>LA County Museum of Art

<sup>12</sup>Los Alamos National Laboratory

<sup>13</sup>M.I.T.

<sup>14</sup>Metallurgy Division

<sup>15</sup>National Museum of Art

<sup>16</sup>National Archives

<sup>17</sup>Reactor Radiation Division

<sup>18</sup>Smithsonian Institution

<sup>19</sup>T-Prosci Co.

<sup>20</sup>Materials Reliability Division, Boulder

<sup>21</sup>U.S. Navy David Taylor Research Center

<sup>22</sup>U.S. Department of Transportation

<sup>23</sup>University of Maryland

<sup>24</sup>University of Missouri

<sup>25</sup>LLNL, Livermore, CA

<sup>26</sup>Wright Laboratory

<sup>27</sup>National Gallery of Art



# Analytical Chemistry

## Nuclear Methods Group

The development and application of nuclear analytical techniques for elemental compositional analysis with greater accuracy, higher sensitivity and better selectivity are the goals of the Nuclear Methods Group. A high level of competence has been developed in both instrumental and radiochemical neutron activation analysis (INAA and RNAA). In addition, the group has pioneered the use of neutron beams as analytical probes with both prompt gamma activation analysis (PGAA) and neutron depth profiling (NDP). PGAA measures the total amount of an analyte present throughout a sample by the analysis of the prompt gamma-rays emitted during neutron capture. NDP, on the other hand, determines concentrations of several important elements (isotopes) as a function of depth within the first few micrometers of a surface by energy analysis of the prompt charged-particles emitted during neutron bombardment. These techniques (INAA, RNAA, PGAA, and NDP) provide a powerful combination of complementary tools to address a wide variety of analytical problems of great importance in science and technology. During the past few years, a large part of the group's efforts has been directed at the exploitation of the analytical applications of the guided cold-neutron beams available at the new Cold Neutron Research Facility (CNRF) at the NIST reactor. The group's involvement has been to design and construct state-of-the-art instruments for both PGAA and NDP using cold neutrons, while retaining and utilizing our existing expertise in INAA and RNAA.

### • SRM Analysis and Certification

The nuclear analytical methods have continued to contribute to the Standard Reference Material (SRM) certification effort. This year's efforts include measurements performed on a number of SRMs including: Typical (human) Diet, Petroleum Coke, Chlorine in Lubricating

Oils, Estuarine Sediment, Mussel Tissue, and Household Dust. Group members are serving as Technical Champions for a number of new SRMs, and as such are responsible for scientific decisions made throughout the production and certification process of these materials. Several highlights of the group's SRM work this year are described below.

Three nuclear analytical techniques (INAA, RNAA, and PGAA) have been used to determine a total of 23 different elements in the food reference material SRM 1548a, Typical Diet. This reference material was developed with the cooperation of the Department of Agriculture and the Food and Drug Administration, to provide a composite material containing all the components of a "typical" U.S. diet. Thirteen elements were determined by INAA, and seven elements each were determined by RNAA and PGAA. The results for four of the elements were obtained from two different nuclear analytical techniques. Of the 23 elements determined, seven elements were at the percent concentration level, eight elements at the mg/kg level, seven elements at the  $\mu\text{g}/\text{kg}$  level, and one element was below the detection limit of one  $\mu\text{g}/\text{kg}$ .

Another SRM that has been studied extensively this year is the Estuarine Sediment, SRM 1646a. Both the INAA and RNAA techniques have been used to analyze this material, with a total of 14 elements determined. Ten elements have been determined using INAA and five using RNAA, with one element determined by both techniques. One element, antimony, appears to be inhomogeneous in this matrix. Of the rest, the INAA data have average uncertainties of 2.3% (95% confidence interval). The RNAA results have average uncertainties of 5.5%, with three of the five elements determined at the ultratrace concentration level.

During the past year, cold neutron depth profiling has been used to complete the certification of the  $^{10}\text{B}$  concentration in the new

Boron Implant in Silicon (SRM 2137). This is the first SRM of its type available to semiconductor manufacturers and analytical laboratories. This SRM, consisting of 1 cm<sup>2</sup> silicon wafer pieces, is intended for the calibration of secondary ion mass spectrometry (SIMS) instruments, and is particularly important in semiconductor research and development applications. The SRM has been certified to contain  $1.018 \times 10^{15}$  atoms/cm<sup>2</sup> of <sup>10</sup>B with an uncertainty of  $0.035 \times 10^{15}$  atoms/cm<sup>2</sup>. The depth distribution of the boron implant has been measured by NDP and has also been studied by the Microanalysis Group of NIST using SIMS, and this information is also provided on the certificate. The improved neutron fluence rates of the CNRF, combined with the recent developments in neutron focusing, will enable the NDP instrument to be used to develop additional SRMs containing lower concentrations of dopants that are critical to quality assurance measurements in the semiconductor community.

#### • Neutron Activation Analysis Method Development

Although NAA has been in use for many years, new developments continue to provide improvements in detection sensitivities, elemental specificity, precision, and overall accuracy. Particularly in the last few years, the NAA technique has become one of the primary analytical techniques for the certification of elemental concentrations in biological SRMs. One important reason is that NAA has unique quality assurance characteristics that provide accurate analyses and which often allow the analytical values obtained to be internally evaluated and cross checked. In addition, the capability of INAA for nondestructive analyses (eliminating dissolution errors) and for homogeneity determinations at the  $\mu\text{g}/\text{kg}$  level for sample sizes as low as 100 mg has made this technique an integral component of trace element analyses at NIST. Furthermore, the relative matrix independence of NAA has resulted in applications to a wide variety of materials including high temperature supercon-

ductors, soils, fly ash, rocks and ores, and foods.

Optimizing the gamma-ray counting conditions for the various forms of NAA can generally improve precision, increase sample throughput, or both. This is especially important when counting the very small amount of radioactivity produced by ultratrace quantities of impurities, for example in semiconductor silicon or (after radiochemical separations) noble metals in human tissue. Sensitivity can be gained by using high-efficiency, low-background detectors; a subsidiary benefit is that less radioactive material needs to be generated, handled, and discarded. The sources of background in gamma-ray detectors have been reexamined at NIST and elsewhere in recent years, resulting in improved understanding. It is now clear that with care in the selection of the materials from which the detector and the shielding are constructed, the only important source of gamma-ray background is the interaction of cosmic ray particles with the shield and the detector itself. Experiments are underway to reduce this component by active, anti-cosmic ray shielding.

A new computer-controlled robotic sample changer (RSC) has been extensively evaluated and optimized, and is being effectively utilized in the certification of a variety of SRMs, as well as for other INAA and RNAA measurements. This system provides the capability for continuous utilization of a detector system, and is capable of precisely positioning eight different types of sample containers, ranging from a 100 ml polyethylene screw-top bottle (used for radiochemically separated samples) to a "2/5 dram" polyethylene snapcap vial, or a 54 mm diameter disposable plastic Petri dish. The system now provides a reliable and repeatable positioning uncertainty of  $\pm 0.51\%$  (1s; n=12) at 3 mm distance from the detector, and 0.25% (1s) for a 5 cm counting geometry. This system has been used this past year to provide data for the certification of including SRM 1548a, Typical Diet, and SRM 1646a, Estuarine Sediment.

A new pneumatic tube system has been designed and is currently being constructed for in-

sertion into the NIST nuclear reactor. This fast pneumatic tube will propel the sample out of the irradiation facility and into the counting location in 0.5 s or less, allowing the determination of nuclides with half-lives as low as one second. This facility will provide NIST with the capability for accurately determining fluorine through  $^{20}\text{F}$  ( $t_{1/2}=11.00$  s) at low levels. Another improvement will be to the determination of selenium through  $^{77\text{m}}\text{Se}$  ( $t_{1/2}=17.4$  s), along with the possibility of measuring lead (at elevated levels) using  $^{207\text{m}}\text{Pb}$  ( $t_{1/2}=0.8$  s). The irradiation facility will have two insertion locations, one with a highly thermalized neutron spectrum like our other, slower pneumatic tube systems, and the second will be in a location having a high epithermal component to the neutron spectrum. This second location offers the possibility of substantially improving sensitivity for the determination of iodine and other elements with high resonance integrals. It is hoped that the entire irradiation terminal (currently being constructed by an outside contractor) will be ready for insertion into the reactor before the end of the current shutdown period in the spring of 1995.

#### • Specimen Bank Research

The National Biomonitoring Specimen Bank Research Project (NBSB) was established at NIST/NBS more than a decade ago, and continues to support other government agencies' programs through banking and providing quality assurance (QA). These programs include the EPA Human Liver Project (HLP), the NOAA National Status and Trends (NS&T) program, the NCI Micronutrient Program, the IAEA/NIST/FDA/USDA Total Diet Study, the NOAA Alaska Marine Mammal Tissue Archival Project (AMMTAP), and the National Marine Mammal Tissue Bank (NMMTB). Research has centered on specimen banking protocols and improved analytical methodology. The group uses instrumental and radiochemical neutron activation analysis to determine element compositions of tissues included in the National Biomonitor-

ing Specimen Bank (NBSB). In addition, the NIST participation in intercalibration exercises with the project laboratories, and the development of QA materials for various marine analyses, has helped to enhance the quality of the analytical results used in the assessment of the environmental health of the nation.

During the past year liver samples from 24 marine mammals have been collected, processed, and archived in the NBSB for the NMMTB and AMMTAP. Instrumental neutron activation analysis (INAA) was chosen for the analysis of some of these banked specimens because of the relative ease with which a large number of elements can be determined in a small amount of material. Concentrations for up to 38 elements were measured in liver tissues from one pilot whale, four white-sided dolphins, four ringed seals, and two bearded seals. Mercury was determined in tissues from six ringed seals, two harbor porpoise, two bowhead whales, one bearded seal, and one spotted seal, and one belukha whale. Results of these analyses, in combination with results of previous analyses on additional animals and with information concerning the age of each animal, show that several trace elements bioaccumulate in liver tissue. Our data supports the concept that mercury and selenium accumulate with age in liver tissue, as has been reported by several researchers over the past two decades. Concentrations of both of these elements increase with age for the pilot whales, ringed seals, and belukha whales.

Because of the large number of elements that can be determined using INAA, we were able to discover that silver and vanadium also accumulate in liver tissues. These findings were not previously reported in the literature, probably because most researchers did not measure these elements. Hepatic silver concentrations increase with age for ringed seals, belukha whales, and pilot whales. For the Alaska marine mammals, hepatic vanadium increases with age. Vanadium levels in livers of marine mammals from the east coast are much lower than those measured in the Alaska mammals and show no correlation with

age. The presence of vanadium in the liver tissues of Alaskan mammals may indicate the presence of oil in the Alaskan environment, geochemical differences between Atlantic and Alaskan waters, or differences in the diets of animals from these two regions. Further research will include analyses of additional marine mammal tissues from both geographic regions and will include analysis of tissues from different species.

- **Neutron Activation—Mass Spectrometry**

The collaboration on neutron activation-mass spectrometry (NA-MS) with Brian Clarke and colleagues at McMaster University continues to provide valuable information on ultratrace levels of boron and lithium in a variety of materials. NA-MS uses neutron irradiation to generate  $^4\text{He}$  and  $^3\text{He}$  from  $^{10}\text{B}$  and  $^6\text{Li}$ , and high-precision He mass spectrometry to determine the concentration of each element. The thermal neutron irradiation facilities at NIST offer the best combination of a high thermal-neutron fluence and a very low level of fast neutrons to greatly reduce the interfering nuclear reactions produced by fast neutrons.

Many non-nuclear analytical techniques face a series of problems in measuring low-levels of boron and lithium including contamination control (blank), volatility and, in some cases, insufficiently low detection limits. NA-MS is, however, well suited to an investigation of the natural levels of boron and lithium at low levels, such as in biomaterials. Over the past few years we have determined B and Li concentrations in a wide variety of biological materials, including more than one hundred individual food items, as well as several different protein components of blood. Blood Li levels may be both genetically and environmentally regulated. An environmental contribution can be deduced from the relationship between the blood Li level and the amount of the element ingested. No such information is available for B, another element present in ultratrace amounts in human blood. Unusually high levels of Li and B in the surface

waters off northern Chile offer an opportunity to study the genetic and environmental regulation of these elements in the blood of healthy subjects.

Research is currently underway for the further optimization the NA-MS technique, and open new applications in the semiconductor industry, particularly in the area of low-level boron determination. Detection limits in the  $\mu\text{g}/\text{kg}$  range for boron and in the  $\text{ng}/\text{kg}$  range for lithium are expected in the near future.

- **Superconductivity Research**

The group has undertaken an active role in the NIST program on high-temperature superconductivity research. In cooperation with materials scientists at NIST and elsewhere, we are measuring impurities in superconductor starting materials and final products, as well as determining the stoichiometry of the major constituents. The needs of the superconductivity program have stimulated the development of methods for accurate, rapid analysis of these materials by both NAA and PGAA. In particular, an effort is underway to establish monitor-activation analysis techniques at NIST. Conventional NAA requires the irradiation and counting of a standard for each element to be determined in a given sample. Preparing numerous standard solutions requires much labor, and the accurate quantitation of unanticipated activities in the gamma spectrum is not possible. An elegant solution has been pioneered in Europe, which uses a dimensionless compound nuclear constant called  $k_0$ , which can be measured much more accurately than the cross sections and other constants that comprise it. We have begun to apply this approach to cold-neutron PGAA, which is especially subject to systematic errors from neutron scattering effects, and have found that the  $k_0$  approach for determining element ratios offers all the advantages that internal standards offer other methods. We intend to apply the  $k_0$  formalism to traditional NAA as well.

- **Neutron Depth Profiling**

Incremental improvements in the NDP instrument are continually being made. One of the requirements for the determination of the reaction depth in NDP is the ability to measure the residual energy of the charged particles accurately. Silicon surface barrier detectors used at room temperature are limited to about 10 keV FWHM resolution at the charged particle energies of interest. We are currently collaborating with Prof. Emile Schweikert and John Welsh, Jr. of Texas A&M University to improve the depth resolution by using time-of-flight (ToF) techniques. The residual energy of the heavy recoil particle is measured by ToF using microchannel plate detectors. Initial efforts are being focused towards profiling nitrogen distributions in semiconductor materials. Preliminary experiments have demonstrated that resolutions approaching a few nanometers are feasible, and the use of the ToF method for depth profiling of N has begun.

The characterization of a variety of diamond and diamond-like films continues to be of major interest to users of the NDP facility. Diamond-like substrates are used as precursors for electronic circuits that require efficient heat transfer, such as devices operated in a vacuum or with high-current components. Boron nitride is one diamond-like material ideally suited for analysis using NDP. NDP is currently being used to establish the stoichiometry of the nitrogen and boron in the matrix, and reveal non-uniformities in the film deposition profile. Collaborations with the Pennsylvania State University on vapor deposited diamond and boron nitride films are part of the Ph.D. thesis of Laurie Hackenberger.

Analyses have also been performed to determine the boron and nitrogen dopant distribution in a single layer, and in alternately doped multilayer deposits. Thin film analysis demands greater depth resolution be extracted from the data from NDP analysis. Kevin Coakley of the Statistical Engineering Division has developed mathematical approaches for interpreting the di-

amongst film data and furthermore has provided insights for optimizing the placement of the detectors and apertures to maximize the depth resolution.

Jeff Blackmon, a graduate student of the University of North Carolina working with us, has applied the NDP technique to the measurement of the  $^{17}\text{O}(p, \alpha)^{14}\text{N}$  cross section near  $E_p=70$  keV. He has been able to determine the concentration/depth distribution of the  $^{17}\text{O}$  using NDP, and the equally important boron concentration. Boron is involved in a competing nuclear reaction that interferes with analysis of the oxygen. The  $^{17}\text{O}$  cross section determination is important for the understanding of the life cycle of stars. Jeff received his Ph.D. in late 1994 and has submitted a paper for publication on this topic.

- **Prompt-Gamma Activation Analysis**

This has been a particularly productive year for prompt-gamma activation analysis (PGAA) at NIST. PGAA allows accurate, nondestructive measurements of a number of elements, including H,B,C,N,S, and Cd. Recent improvements to the cold neutron prompt gamma activation analysis (CNPGAA) instrument, constructed as part of the CNRF, have greatly improved its measurement capabilities. Furthermore, both the CNPGAA and University of Maryland-NIST thermal-neutron PGAA instruments have found research applications in many diverse areas within chemistry, physics, and materials sciences.

The additions of an atmosphere-controlled sample chamber and a bismuth germanate (BGO) Compton shielding detector to the CNPGAA instrument have had a significant impact on measurements. Installation of the sample chamber, a magnesium alloy box that may be flushed with helium or evacuated, has resulted in the elimination of gamma-ray background from atmospheric nitrogen and reduction of the hydrogen background by a factor of two. The addition of the BGO Compton shield has reduced the spectrum baseline by up to a factor of six, yield-

ing lower signal-to-noise ratios and improved detection limits.

Over the last few years, a major effort has been directed at improving our measurement capability for low levels of hydrogen using CNPGAA. This capability is of great value in numerous applications where quantitative, non-destructive analysis of small quantities of hydrogen in materials is necessary, such as in metallurgy. The recent modifications to the CNPGAA instrument have had a significant impact on these measurements. Detection limits of less than 10 micrograms for hydrogen have been achieved for some samples. These limits are often constrained by the background levels of this element in the materials surrounding the CNPGAA instrument. Further reduction of the hydrogen background to the submicrogram level should be possible in the near future.

CNPGAA has continually been used for measurements of H in a wide variety of materials. Analyses of two new titanium alloy jet engine turbine blades have yielded H concentrations of less than 50 mg/kg, demonstrating better than a factor of two improvement in detection limit for that material. The technique has also been used to calibrate titanium alloy hydrogen standards for use in neutron tomography experiments, to measure hydrogen concentrations of less than 10 mg/kg in new samples of Naval Research Laboratory quartz, to measure hydrogen concentrations in nanocrystalline metals, and to study uptake of hydrogen by Yb-doped SrCeO<sub>3</sub> for applications in fuel cells.

Much of the current research using the CNPGAA instrument has been dedicated to improving the quality of PGAA measurements. Elemental sensitivity ratios have been measured in a wide variety of pure compounds and mixtures of compounds in order to develop a  $k_0$  approach to PGAA. CNPGAA measurements indicate that systematic errors due to neutron scattering and self absorption in the sample matrix, variations in neutron flux, and sample positioning are largely eliminated when element ratios are measured. Therefore, the use of sensitivity

ratios in the determination of elemental concentrations is expected to give results superior to those using sensitivities measured from individual element standards. The method was recently applied to the analysis of the Allende meteorite.

In collaboration with the Reactor Radiation Division, PGAA and neutron reflectometry have been combined into a novel probe for studying layered structures. A standing neutron wave was set up in a multilayer polymer film and the capture gammas from a buried gadolinium layer were measured as a function of the grazing angle of the incident neutron beam. The PGAA and reflectometry data were interpreted by solving the Schrödinger equation for the system, which could be fit only by precise values of the parameters of the system. This combined PGAA and reflectometry technique offers promise as a new method to study interdiffusion of polymers, as well as other problems in materials science.

Other applications of PGAA have included measurement of boron in a suite of tourmalines as part of an interlaboratory study on the concentration of boron in minerals, and the analysis of trace elements (Mg, Al, Mn, Fe, Cu, Zn) in aluminum alloys to determine the feasibility of using PGAA as a technique for on-line sorting of scrap aluminum. The recent use of CNPGAA for determination of chlorine in terrestrial basalts has generated much interest among researchers in the field of cosmogenic nuclides, where accurate determination of total chlorine is needed to calculate production rates of <sup>36</sup>Cl from cosmic ray bombardment of terrestrial and extraterrestrial materials.

#### • Focused Neutron Research

A long-range program to explore and develop the analytical applications of focused beams of cold neutrons continues within the group. The goal of this research is to produce beams of neutrons which have intensities several orders of magnitude greater than previously available. Such beams will greatly enhance the capabilities of both PGAA and NDP, and may ultimately lead to a neutron probe for microanal-

ysis. Glancing-angle reflective optics is used to transport soft x-rays and thermal neutron beams through narrow channels, which act as miniature versions of neutron guides commonly used at research reactors. The advantage of the narrow ( $\approx 10 \mu\text{m}$ ) channels is that the neutron beam can be bent more sharply than for the wide ( $\approx 50 \text{ mm}$ ) guides. Recent developments in the manufacture of polycapillary fibers, with thousands of channels having sizes of a few micrometers, have enabled cold neutrons to be guided and focused on a scale suitable for laboratory needs. A high intensity beam on a small sample area can be useful for improving both the detection limits of individual elements and the spatial resolution of neutron absorption measurements in analytical research.

We are now one step closer towards the goals of the neutron focusing project, which include enhancing the detection limit of PGAA for decreasing sample sizes, and adding lateral spatial resolution for two dimensional compositional mapping. We have developed a polycapillary neutron lens, custom designed for the cold neutron PGAA facility at NIST. The lens, made with 1763 lead-silica glass polycapillary fibers, accepts a polychromatic cold neutron beam (wavelengths longer than 0.4 nm) from a neutron guide, 50 mm x 45 mm in cross section, and delivers a focused beam of 0.5 mm in diameter (full width at half maximum) at 52 mm from the exit of the capillaries. The average neutron current density at the focus is 80 times higher than that of the direct incident beam.

PGAA measurements using the lens have been performed on test samples of a 2% gadolinium glass particle (0.23 mm x 0.385 mm) and a cadmium metal particle (0.50 mm x 0.45 mm). The prompt gamma count rates for the Gd 182 keV and the Cd 558 keV peaks were compared to those obtained from the same samples without the lens. The gain in the prompt gamma signals is defined as the ratio of the count rate with the lens to that without the lens, representing the enhancement in the total absorption rate by using the lens. The gains obtained are  $58 \pm 10$  and

$67 \pm 1$  for the Gd and Cd samples, respectively.

Additional measurements have also been performed to demonstrate the spatial resolution in one dimension using a known boron distribution. In these experiments a 1 mm  $^6\text{LiF}$  aperture was placed at the focal plane to define the focused beam. Samples were glass polycapillary fibers, similar to those used in the focusing lens except differing in composition. A row of lead-silica and borosilicate (8 wt.% boron) fibers (five each, 0.4 mm in diameter), was arranged alternately (B-Pb-B-Pb...), side by side, behind the aperture. The prompt gamma count rate for the boron peak at 478 keV was monitored as the row of samples was scanned in the horizontal direction along the focal plane. The count rate was maximized when a borosilicate fiber centered on the focus, and was minimized when a lead-silica fiber did so, forming an oscillating prompt gamma response. At this submillimeter range, the peaks are partially resolved: (peak - valley)/(peak - background)  $\sim 38\%$  (100% represents complete resolution). The same experiment has also been performed on a row of fibers of the same composition and arrangement as above (three each), but of 1 mm diameter, for which a 97% resolution was obtained.

We are continuing efforts on reducing the neutron and gamma background and improving the neutron transmission efficiency of the lens. This research is being performed in collaboration with X-Ray Optical Systems, Inc. of Albany, New York, which has an Advanced Technology Program award to develop focusing systems for both x-rays and neutrons using capillary optics.

#### • Detector Imaging Research

The Nuclear Methods Group, working through a CRADA with CID Technologies Inc. and with the Surface and Microanalysis Science Division, have developed a video radiation detector (VRD) based upon a charged injection device (CID) camera and image processing system. The process is somewhat analogous to the nuclear track technique, and applications of the

two methods do overlap, however the VRD system allows real-time high resolution imaging of neutron and charged particle fields. The VRD system is essentially 100% efficient for the detection of alpha particles above a few MeV energy; emission rates as small as  $10^{-5}$ Bq have been localized. The system allows discrimination between tritons, alpha particles, and fission fragments. Spatial resolution of less than 11  $\mu\text{m}$  is achieved by interpolating between camera pixel elements. Because the charge injection device is sensitive to visible, X-ray and UV photons, charged-particle images can be correlated with optical images of the sample. As an example, it has been used for detecting spontaneous emission of naturally radioactive materials from minerals or contaminants in the analysis of environmental samples.

By adding a thin  $^6\text{Li}$  converter, we have adapted the VRD for the characterization of neutron focusing components for neutron intensity, determination of the focal plane, and analyzing individual elements in the focusing device. Neutron field maps obtained by using the VRD have been indispensable for the project. The location and size of the focus can be determined much more quickly with the VRD than by using a large series of photographic films. Thus the VRD system provides a faster image, a high resolution image in electronic format, and provides data of a greater dynamic range than that of photographic film.

#### • Group Interactions

The strong interaction with industrial scientists using NDP, PGAA, and NAA has continued during the year with a growing number of guest workers, research associates, and joint publications. For example, working this year with researchers from SEMATECH, we have used NDP to study various aspects of quality control using CVD (chemical vapor deposition) reactors. These measurements will be useful in optimizing process yield and reliability as well as establishing confidence for the industrial in-house analytical techniques.

#### Smithsonian Institution

The Conservation Analytical Laboratory of the Smithsonian Institution maintains an INAA research facility within the Nuclear Methods Group at NIST. This facility, which consists of two automated sample changers and four gamma detectors with associated electronics, provides high precision multi-element chemical data for use in a wide range of Smithsonian and Nuclear Methods Group research projects. In the past year over 2100 archaeological samples have been analyzed in support of eight Smithsonian research projects. The projects include studies of Classic Maya pottery, Bronze, and Iron age ceramics from Gordian in Turkey, Medieval Islamic ceramics and stone paste ware, Pre-Columbian Peruvian ceramics, and ceramics from the Indus Valley in Pakistan and the Oman Peninsula.

One highlight of this year's research involved a continuation of the study of the manufacture and exchange of ceramics between sites on the Oman Peninsula and sites located in modern Iran and Pakistan during the late third millennium B.C. This research, in collaboration, with Dr. Sophie Mery, CNRS, Art and Archéologie, has sought to combine mineralogical data from thin section analysis and chemical data from INAA to establish the area of manufacture and subsequent exchange across this broad region.

Earlier research had established indigenous Omani production of fine black painted red ware, originally believed by many archaeologists to be imports from across the Gulf. The current investigation concentrated on black slipped jars and other ceramic types, found in Oman. These ceramics are stylistically the same as the wares found in Harappan contexts in Pakistan and India. The combined mineralogical and chemical data demonstrated that the majority of these ceramics were in fact imports from across the Gulf of Oman and help to verify an active overwater trade network during the third millennium B.C. Further, comparison with chemical data for ceramics and bangles from another earlier study, established the source of the clay to be the Indus



River alluvium at or south of the ancient city of Mohenjo-Daro.

A single Indus style ceramic piece did not match the composition of the rest of the collection. This piece was, however, identical both chemically and mineralogically with ceramics found on the Oman Peninsula, but not of the Indus style. This finding leads to the possibility that Omani potters were producing sophisticated copies of Harappan ceramics thought, until now, to be beyond their technological ability. Further research will begin in 1995 to investigate this early example of technological transfer.

### Food and Drug Administration

(W. C. Cunningham, D. L. Anderson, C. R. Warner, and S. G. Capar)

The Food and Drug Administration (FDA) maintains a neutron activation analysis (NAA) facility in the reactor building of the National Institute of Standards and Technology (NIST). This facility is directed by FDA's Center for Food Safety and Applied Nutrition and provides agencywide analytical support for special investigations and applications research. NAA complements other analytical techniques used at FDA and serves as a reference technique and confirmatory quality assurance (QA) tool. Instrumental, neutron-capture prompt- $\gamma$ , and radiochemical NAA procedures (INAA, PGAA, and RNAA, respectively) continue as the prime nuclear analytical approaches. A radioisotope-induced X-ray emission (RIXE) spectrometer provides support for FDA programs which monitor toxic elements in housewares (especially Pb), and the low-level  $\gamma$ -ray counting facility developed by the Nuclear Methods Group of the NIST Inorganic Analytical Research Division is used to determine the radionuclide content of various matrices. This combination of analytical techniques enables diverse multielement and radiological information to be obtained for foods and related materials.

Day-to-day use of gram quantities of reference materials (RMs) during analyses of large numbers of food test samples is necessary for

quality assurance (QA) in FDA's Total Diet Study (TDS) Program. Because of the large quantities required, FDA's NAA Laboratory has examined two off-the-shelf foods, soy-based powdered infant formula (SPIF) and cocoa powder, as candidates for in-house RMs. SPIF has good RM characteristics because it is formulated to be a complete infant diet with proper fat content and is fortified with essential vitamins, minerals, and essential elements. Cocoa powder contains a number of elements of interest in concentrations suitable for quantitation (*e.g.*, Ca, Cd, Cu, Cr, Fe, K, Mg, Mn, Ni, Pb, and Zn) as well as enough fat to require (desirably) moderate effort for acid digestion. Both materials are relatively homogeneous in particle size and composition and have long shelf lives without refrigeration. Weight-stability characteristics and homogeneity for both materials were found to be excellent. After initial weight gains (following removal from bottles) of  $\sim 0.5\%/d$  for SPIF and  $\sim 0.5\%/h$  for cocoa powder, masses ( $\sim 0.5$  to 5 g) varied by  $<2\%$  for up to 1 year at laboratory relative humidities ranging up to 55%. Both within-unit and unit-to-unit nonhomogeneity was found to be  $<4\%$  for Al, Mg, Ca, Na, Cl, Mn, and K in nine units of SPIF (by INAA) and for H, B, C, N, Cl, and K in seven cocoa powder units (by PGAA).

FDA's NAA facility has begun an additional QA exercise under the TDS Program. NAA is being used to provide confirmatory multielement concentrations annually for 60 foods also analyzed at FDA's laboratory in Lenexa, Kansas. Low-level  $\gamma$ -ray counting will be used to provide confirmatory radionuclide activity concentrations for 15 foods analyzed at FDA's Winchester Engineering and Analytical Center in Massachusetts. The matrices will be varied to cover the entire range of foods included in the program.

To study the fate of bromates added during the manufacture of baked bread products, INAA was used in addition to high-pressure liquid chromatography to determine bromate and total bromine concentrations in several prod-

ucts. A relationship between added bromate and total bromine in baked bread was determined. This work will continue but has already resulted in inclusion of more labeling information for several products.

PGAA and low-level  $\gamma$ -ray counting were used to analyze 15 maple syrups for  $^{137}\text{Cs}$ , B, and K. K concentrations determined by the two techniques (using 2-g portions for PGAA) were in excellent agreement. The products were obtained in 1991, with one produced in Maryland, three in New York, four in Pennsylvania, two in New Hampshire, and five in Canada. All  $^{137}\text{Cs}$  activity concentrations were at least 100 times lower than those for which controls would be recommended according to Federal Radiation Council guidance, but the average  $^{137}\text{Cs}$  activity concentration for Canadian syrups (2.8 Bq/kg) was greater by nearly a factor of 20 than the average value (0.15 Bq/kg) for the other syrups. This distinction is apparently a result of fallout patterns from the era of atmospheric testing of nuclear weapons; no  $^{134}\text{Cs}$  was detected, which indicates that there was no influence from the Chernobyl accident. The data exhibited distinct regional groupings related to product source when the ratios of  $^{137}\text{Cs}$  activity to K content ( $\text{Bq}_{\text{Cs}}/\text{mg}_\text{K}$ ) were plotted vs. B concentrations.

Twenty-one ready-to-use hobby glazes, of which 18 were labeled "safe for food containers" (SFFC), were analyzed by PGAA for Al, B, Ba, Ca, Cd, Co, Cr, Cu, Fe, Gd, Hf, K, Mn, Na, Pb, Si, Sm, Sr, Ti, Zn, and Zr. (The SFFC glazes in this study were formulated by the manufacturer to leach  $<2 \mu\text{g Pb/mL}$  when applied to an 8-oz cup and fired to cone 06, or 980-990°C.) Pb was also accurately determined by X-ray fluorescence spectrometry (XRFS) using Pb K X-rays induced by the  $\gamma$ -ray component of the neutron beam. The XRFS limits of detection were 200-400  $\mu\text{g Pb/g}$  (dry weight), lower by a factor of 100 than those for PGAA (using the 7369-keV  $\gamma$ -ray). Pb concentrations (dry weight) were 0.16-27.2% in the SFFC glazes and 0.86-32% in the other glazes. The SFFC glazes contained from

$<0.6$  to 202  $\mu\text{g Cd/g}$ , and the concentrations of Co, Cr, and Cu (elements which may enhance Pb leaching from fired glazes) were as high as 1.2, 2.7, and 5.6%, respectively.

### Federal Bureau of Investigation

The Elemental and Metals Analysis Unit (EMAU) of the Federal Bureau of Investigation (FBI) Laboratory irradiates samples for neutron activation analysis (NAA) at the NIST reactor facility. These samples are evidence in criminal cases being investigated by the FBI, state, and local jurisdictions throughout the United States. The primary analysis is of lead projectiles (bullets and shotshell pellets). In a typical case bullets from a crime scene are compared with the bullets from cartridges found in the possession of a suspect. The samples are irradiated at NIST along with an appropriate standard (SRM 2416, or SRM 2417) and then transported to FBI Laboratory facilities for gamma-ray spectroscopy. By NAA, samples are quantitatively analyzed for trace amounts of copper, antimony, and arsenic. The quantities of these trace elements found thus characterizes each bullet and allows bullets to be compositionally compared within a specific case. Further, the lead data from approximately the last ten years has been stored in a database. With this database new samples can be compared to each other and to all samples the FBI has analyzed to give an idea of how common their composition is. When appropriate Special Agent Examiners provided expert court testimony in these cases.

The FBI also occasionally irradiates copper and steel samples at NIST. These analyses are also quantitative determinations for the trace elements present, and ultimately inter-sample comparison.

In addition to using NAA to analyze samples from criminal cases several projects of note are being worked on this year. Using NIST facilities EMAU has analyzed bullet lead which was used as a testing standard in a collaborative crime laboratory testing program. EMAU is also participating in a study of the effects of bullet frag-

ments on brain tissue by analyzing bullet lead before and after implantation in the brain tissue of mice. On-going research concerning the quantitative trace analysis of bullet and shot-shell pellet lead continues as questions arise in criminal cases.

### University of Maryland

The University of Maryland (at College Park, UMCP) aerosol chemistry group has used the NBSR reactor for instrumental neutron activation analysis to characterize atmospheric aerosol particles and gases for more than 20 years. Detailed and accurate multielement analyses are routinely achieved, nondestructively, for up to 40 elements in samples collected for periods of several hours to a few days on various types of filters and in cascade impactors which size fractionate the aerosol into as many as 10 size domains. Some of the elements measured, *e.g.*, As, Se, and Hg, are highly toxic and are, therefore, of epidemiological interest, especially in the Chesapeake Bay and Coastal Marine environments. Equally important is that information on elemental constituents remains a powerful, fundamental tool with which atmospheric sources, transport, and processes may be elucidated. Current work has focused on the characterization and deposition of submicrometer aerosol particles in the Chesapeake Bay Airshed.

Detailed investigations of the size-distribution and composition of urban aerosols are important to the scientific community because they contain information about the formation, sources, transport, and atmospheric behavior of particles containing toxic and nutrient substances, and respiratory irritants. This work extends measurement to very small (often  $<100 \mu\text{g}$ ) samples of submicrometer aerosol particles size-fractionated with low-pressure-drop Micro-Orifice Impactors (MOI). In a recently completed study, size-segregated aerosol samples were collected at three sites along the Chesapeake Bay to determine the size distributions and hygroscopic growth of

aerosol particles bearing elements of interest to Bay water quality. This information is sorely needed to improve predictions of dry-particle trace element fluxes to Bay surface waters.

Size-segregated particulate aerosol samples were collected with 9-stage micro-orifice impactors (MOIs). Twenty seven (243 stages) MOI samples were analyzed by instrumental neutron activation analysis (INAA) for up to 32 elements including Al, As, Br, Cd, Cr, Cu, Fe, Mn, S, Sb, Se, V, and Zn. Elemental deposition velocities ( $V'_d$ 's) as a function of particle size and frequency of meteorological conditions were estimated using an adaptation of Williams' (1982) model for dry deposition of particles to natural water surfaces. Specifically, size-dependent  $V_d$  curves for a series of discrete relative humidity (RH) and wind velocity intervals were weighted according to the frequency of occurrence of meteorological conditions in these intervals and combined to yield a single size-dependent  $V_d$  curve representative of annual conditions. Effective deposition velocities ( $V_{d,eff}$ ) for individual elements, were then calculated from the single size-dependent  $V_d$  curve and measured size spectra of the elements. The resulting  $V_{d,eff}$ 's were used with annual elemental concentrations determined in the Chesapeake Bay Atmospheric Deposition Study (CBADS) to estimate annual dry fluxes for 13 elements.

Highly resolved mass-size spectra for measured elements indicate that the crustal elements (Al, Fe, La, Sm) and key marker elements for seasalt (Na, Cl, Mg) were primarily associated with coarse particles with modal diameters ranging from 1.3 to 6.9  $\mu\text{m}$ . The anthropogenically-derived elements such as, Br, V, Sb, Se, and S were associated mostly with submicrometer particles with modal diameters ranging from 0.2 to 0.7  $\mu\text{m}$ .

Model calculations indicate that  $V'_d$ 's based on meteorological data averaged over long periods of time or collected at low temporal resolutions may be from 4 to 200% smaller than  $V'_d$ 's based on frequency distributions of hourly wind events. The inclusion of particle growth

effects in model calculations yielded  $V_d'$ s for the 0.1- to  $-1.0\mu\text{m}$  particle size range that were a factor of 2-3 larger than  $V_d$  estimates based on yearly averaged meteorological data or on the wind frequency spectrum without regard to fluctuations in relative humidity. Effective  $V_d$ 's predicted for the coarse-particle elements ranged from 0.3 to 0.6 cm/s, whereas those for the fine-particle elements ranged from 0.06 to 0.2 cm/s, and those for both were typically twofold smaller than deposition velocities used to calculate fluxes in CBADS. However, preliminary calculations suggest that consideration of RH gradients in the turbulent layer will bring model predictions closer to the values used previously in the Chesapeake Bay Atmospheric Deposition Study (CBADS).

Chemical Mass Balance (CMB) techniques were applied to the elemental size spectra to resolve the concentration versus particle size-distributions of aerosol containing the various elements into size-distributions by source. The resulting size spectra for each source were used to calculate deposition fluxes by size and source. The results indicate that soil is responsible for 96, 92, and 60% of the dry fluxes of Al, Fe, and Mn, respectively. Previous studies suggest that much of the soil dust in urban areas dispersed into the atmosphere by motor vehicle traffic. Regional sulfate, *i.e.*, predominately secondary aerosol imported into the State from distant coal- and oil-combustion sources, accounts for 96% of the sulfur flux and 67% of the Se. Previous studies at College Park, MD, suggest that, at the same RH, elements in regionally-transported aerosol are associated with larger particles than they are in aerosol from local sources (*i.e.*, 5 to 50 km away). Therefore, the former deposit more efficiently than the latter. The majority of the As flux (72%) is attributed to industrial steel sources. Marine aerosol accounted for 63% of the Br and motor vehicles, 31%. More importantly, emissions from incinerators accounted for most of the fluxes of Cd (77%), Sb (81%), Cr (93%), and Zn (97%). In each case, large (midpoint diameter,  $6.9\mu\text{m}$ )

particles accounted for the majority of the deposition, except for Se from local coal-fired power plants, for which predominately fine particles accounted for 19% of the flux. Despite the importance of large particles in determining dry fluxes of virtually all of the elements, it is not clear that these particles originate at the sources to which they have been assigned. Large-particle components for these elements may represent resuspended urban dust that was previously contaminated by (fine-particle) aerosol from these sources or, perhaps, the coarse particle components may result from kinematic coagulation, between coarse urban dust particles and fine-particle emissions as the former settle. This work provides the first estimates of  $V_d$  which take into account highly resolved concentration-vs-size distributions of particles as well as frequency of meteorological conditions typical of the Chesapeake Bay. These estimates should provide a framework for future studies (both field and laboratory) which are much needed to improve our understanding of processes governing dry atmospheric deposition to the Chesapeake Bay watershed.

## Research Topics

### Certification of Standard Reference Materials by Neutron Activation Analysis

R. R. Greenberg<sup>2</sup>, D. A. Becker<sup>2</sup>, R. Demiralp<sup>2</sup>, K. M. Garrity<sup>2</sup>, R. M. Lindstrom<sup>2</sup>, E. A. Mackey<sup>2</sup>, and B. R. Norman<sup>2</sup>.

### Improvements to INAA Methodology

M. Blaauw<sup>12</sup>, P. Bode<sup>12</sup>, R. R. Greenberg<sup>2</sup>, D. A. Becker<sup>2</sup>, R. Demiralp<sup>2</sup>, R. M. Lindstrom<sup>2</sup>, and E. A. Mackey<sup>2</sup>.

### Quality Assurance Improvements for NAA

R. R. Greenberg<sup>2</sup>, D. A. Becker<sup>2</sup>, R. Demiralp<sup>2</sup>, R. M. Lindstrom<sup>2</sup>, and E. A. Mackey<sup>2</sup>.

### Development of Radiochemical Separation for NAA

D. A. Becker<sup>2</sup>, K. M. Garrity<sup>2</sup>, R. R. Greenberg<sup>2</sup>, E. A. Mackey<sup>2</sup>, and B. R. Norman<sup>2</sup>.

### Evaluation of Errors and Interferences in NAA

D. A. Becker<sup>2</sup>, M. J. Blackman<sup>3</sup>, R. R.

Greenberg<sup>2</sup>, and R. M. Lindstrom<sup>2</sup>.

#### Trace Elemental Characterization of Silicon Semiconductor Materials

T. Z. Hossain<sup>14</sup>, R. G. Downing<sup>2</sup>, D. A. Becker<sup>2</sup> and R. M. Lindstrom<sup>2</sup>.

#### Improvements to PGAA Methodology

L. Robinson<sup>27</sup>, G. Molnár<sup>28</sup>, Z. Revay<sup>28</sup>, C. Yonezawa<sup>29</sup>, R. M. Lindstrom<sup>2</sup>, D. L. Anderson<sup>1</sup>, E. A. Mackey<sup>2</sup>, R. L. Paul<sup>2</sup>, and D. H. Vincent<sup>5</sup>.

#### Evaluation of Accuracy and Precision in INAA of Botanical Materials

D. A. Becker<sup>2</sup>.

#### Neutron Scattering Effects on PGAA

R. M. Lindstrom<sup>2</sup>, E. A. Mackey<sup>2</sup>, R. L. Paul<sup>2</sup>, and D. H. Vincent<sup>5</sup>.

#### New Developments in Monitor Activation Analysis

F. DeCorte<sup>13</sup>, R. F. Fleming<sup>5</sup>, G. P. Lamaze<sup>2</sup>, R. M. Lindstrom<sup>2</sup>, R. R. Greenberg<sup>2</sup>, E. A. Mackey<sup>2</sup>, and R. L. Paul<sup>2</sup>.

#### Neutron Activation — Mass Spectrometry

W. B. Clarke<sup>15</sup>, R. D. Barr<sup>16</sup>, R. G. Downing<sup>2</sup> and G. V. Iyengar<sup>2</sup>.

#### Bio Analytical and Specimen Bank Research

R. G. Downing<sup>2</sup>, K. A. Fitzpatrick<sup>2</sup>, K. M. Garrity<sup>2</sup>, R. R. Greenberg<sup>2</sup>, G. V. Iyengar<sup>2</sup>, B. J. Koster<sup>9</sup>, J. K. Langland<sup>2</sup>, and E. A. Mackey<sup>2</sup>.

#### Studies in Elemental Speciation

D. A. Becker<sup>2</sup> and K. M. Garrity<sup>2</sup>.

#### Multielement Analysis of Foods and Related Materials by NAA

D. L. Anderson<sup>1</sup>, W. C. Cunningham<sup>1</sup>, and T. R. Lindstrom<sup>1</sup>.

#### High Sensitivity Gamma-Ray Spectrometry

R. M. Lindstrom<sup>2</sup>.

#### Application of Radioisotope-Induced X-Ray Emission to the Identification of Lead and Other Elements in Ceramic Glazes and Housewares

D. L. Anderson<sup>1</sup>, W. C. Cunningham<sup>1</sup>, and T. R. Lindstrom<sup>1</sup>.

#### Hg and I Determination by INAA

B. R. Norman<sup>2</sup> and D. A. Becker<sup>2</sup>

#### Elemental Characterization of High Temperature Superconductors

D. A. Becker<sup>2</sup>, K. M. Garrity<sup>2</sup>, R. R. Greenberg<sup>2</sup>, R. M. Lindstrom<sup>2</sup>, E. A. Mackey<sup>2</sup>, R. L. Paul<sup>2</sup>, and D. H. Vincent<sup>5</sup>.

#### New Developments in NDP

E. A. Schweikert<sup>17</sup>, J. F. Welsh<sup>17</sup>, N. R. Parikh<sup>18</sup>, O. Mutis<sup>19</sup>, B. Wehring<sup>20</sup>, K. Ünlü<sup>20</sup>, V. Hnatowicz<sup>21</sup>, J. Vacik<sup>21</sup>, P. R. Davis<sup>22</sup>, R. G. Downing<sup>2</sup>, G. P. Lamaze<sup>2</sup>, and J. K. Langland<sup>2</sup>.

#### Neutron Depth Profiles of Boron and Nitrogen in Synthetic Diamond Films

L. Pilione<sup>23</sup>, R. Messier<sup>23</sup>, L. Hackenberger<sup>23</sup>, A. Badzian<sup>23</sup>, T. Badzian<sup>23</sup>, H. Hofsäss<sup>24</sup>, J. Biegel<sup>24</sup>, C. Ronning<sup>24</sup>, U. Griesmeier, M. Gross<sup>24</sup>, G. P. Lamaze<sup>2</sup>, and R. G. Downing<sup>2</sup>

#### Comparison of Nuclear Reactors for Analytical Chemistry

D. A. Becker<sup>2</sup>.

#### Determination of Hydrogen by PGAA

D. Meyn<sup>25</sup>, D. L. Anderson<sup>1</sup>, R. R. Greenberg<sup>2</sup>, R. M. Lindstrom<sup>2</sup>, E. A. Mackey<sup>2</sup>, R. L. Paul<sup>2</sup>, and D. H. Vincent<sup>5</sup>.

#### Analytical Applications of Cold Neutrons

H. Chen<sup>2,8</sup>, R. G. Downing<sup>2</sup>, R. R. Greenberg<sup>2</sup>, G. P. Lamaze<sup>2</sup>, J. K. Langland<sup>2</sup>, R. M. Lindstrom<sup>2</sup>, E. A. Mackey<sup>2</sup>, D. F. R. Mildner<sup>2</sup>, R. L. Paul<sup>2</sup>, V. A. Sharov<sup>7</sup>, and D. H. Vincent<sup>5</sup>.

#### Development of a Position-Sensitive Video Radiation Detector

J. Carbone<sup>30</sup>, R. Carta<sup>30</sup>, R. Wentink<sup>30</sup>, J. Zarnowski<sup>30</sup>, H. Chen<sup>2,8</sup>, R. G. Downing<sup>2</sup>, and C. J. Zeissler<sup>10</sup>

#### Chesapeake Bay Atmospheric Deposition Study

Z. C. Lin<sup>4</sup>, J. M. Ondov<sup>4</sup>, and Z. Y. Wu<sup>4</sup>.

#### Characterization of Submicrometer Aerosol Particles

F. Divita<sup>2</sup> and J. M. Ondov<sup>4</sup>.

#### Forensic Applications of NAA

E. R. Peele<sup>6</sup> and R. F. Rebbert<sup>6</sup>.

#### Archeological Applications of NAA

R. Bishop<sup>3</sup>, M. James Blackman<sup>3</sup>, and J. E. Myers<sup>3</sup>.

#### Ultra Low Level Radioactivity Measurement

A. Druckier<sup>31</sup>, R. G. Downing<sup>2</sup>, and G. P. Lamaze<sup>2</sup>

#### Self Diffusion at Isotopically-Pure <sup>10</sup>B/<sup>11</sup>B Boundaries

- S. M. Baker<sup>32</sup>, K. Wu<sup>32</sup>, G. Smith<sup>33</sup>, K. M. Hubbard<sup>33</sup>, M. Nastasi<sup>33</sup>, R. G. Downing<sup>2</sup>, and G. P. Lamaze<sup>2</sup>
- Profiling of Oxygen in Calibration Targets for Astrophysical Studies**  
J. C. Blackmon<sup>34,18</sup>, A. E. Champagne<sup>34,18</sup>, M. A. Hofstee<sup>34,18</sup>, M. S. Smith<sup>27</sup>, R. G. Downing<sup>2</sup>, and G. P. Lamaze<sup>2</sup>
- Use of Photostimuable Phosphorus Imaging Plate for Radiation Detection and Mapping**  
T. Cheng<sup>35</sup>, R. G. Downing<sup>2</sup>, H. Chen<sup>2,8</sup>, and D. F. R. Mildner<sup>2</sup>
- Compositional Analysis of Semiconductor Materials Using NDP**  
N. Cox<sup>36</sup>, B. Sun<sup>36</sup>, J. Gigante<sup>37</sup>, R. G. Downing<sup>2</sup>, and G. P. Lamaze<sup>2</sup>
- Study of Polycapillary Fibers for the Development Focusing Optics**  
D. Gibson<sup>38</sup>, Q.-F. Xiao<sup>38</sup>, V. A. Sharov<sup>38</sup>, W. Gibson<sup>39</sup>, C. A. MacDonald<sup>39</sup>, R. E. Benenson<sup>39</sup>, S. A. Werner<sup>8</sup>, V. V. Kvardakov<sup>7</sup>, V. A. Somenkov<sup>7</sup>, H. Chen<sup>2,8</sup>, D. F. R. Mildner<sup>2</sup>, and R. G. Downing<sup>2</sup>
- Neutron Transmission Techniques using Glass Capillary Optics**  
R. Shrack<sup>40</sup>, W. Siegmund<sup>40</sup>, H. Chen<sup>2,8</sup>, D.F.R. Mildner<sup>2</sup>, and R. G. Downing<sup>2</sup>
- Standards Development and Environmental Analysis Through the Use of Nuclear Techniques**  
N. Gras<sup>19</sup>, R. G. Downing<sup>2</sup>, and G. V. Iyengar<sup>2</sup>
- Tantalum Isotope Production**  
D. C. Hoffman<sup>41</sup>, K. Kacher<sup>41</sup>, and R. G. Downing<sup>2</sup>
- Neutron Tomography Technique Development**  
J. Brenhizer<sup>42</sup>, D. Raine<sup>42</sup>, R. Johnson<sup>42</sup>, H. Chen<sup>2,8</sup>, D. F. R. Mildner<sup>2</sup>, and R. G. Downing<sup>2</sup>
- Trace Bio-Active Elemental Analysis in Biological Materials**  
V. Iyengar<sup>43</sup>, D. Romn<sup>44</sup>, and R. G. Downing<sup>2</sup>
- Neutron Reflection Using Metal Coated Cones**  
D. B. O'Hara<sup>45</sup>, M. Espy<sup>45</sup>, J. M. Carpenter<sup>46</sup>, A. J. Schultz<sup>46</sup>, C. Fermon<sup>47</sup>, H. Chen<sup>2,8</sup>, D. F. R. Mildner<sup>2</sup>, and R. G. Downing<sup>2</sup>
- Applications of Neutron Beams for Advanced Material Investigations**  
G. Piderit<sup>19</sup>, E. Saravia<sup>19</sup>, R. G. Downing<sup>2</sup>, and G. P. Lamaze<sup>2</sup>
- Investigation of Neutron Transmission Through Metal Capillaries**  
P. L. Reeder<sup>48</sup>, R. A. Craig<sup>48</sup>, A. Magerl<sup>49</sup>, H. Chen<sup>2,8</sup>, D. F. R. Mildner<sup>2</sup>, and R. G. Downing<sup>2</sup>
- Cold-n PGAA and Neutron Focusing**  
J. Kern<sup>50</sup>, R. M. Lindstrom<sup>2</sup>, R. L. Paul<sup>2</sup>, H. Chen<sup>2,8</sup>, D. F. R. Mildner<sup>2</sup>, V. A. Sharov<sup>28</sup>, and C. J. Zeissler<sup>10</sup>
- Small-sample NAA**  
D. J. Lindstrom<sup>51</sup> and R. M. Lindstrom<sup>2</sup>
- Characterization of Derivatives of Y<sub>2</sub>BaNiO<sub>5</sub>**  
C. Broholm<sup>52</sup> and R. L. Paul<sup>2</sup>
- Characterization of Hydrofluorocarbons and Solid Acids**  
D. R. Corbin<sup>53</sup>, M. K. Crawford<sup>53</sup>, R. L. Paul<sup>2</sup>, and P. D. VerNooy<sup>53</sup>
- PGAA of Aluminum Alloys**  
C. L. Dobbs<sup>54</sup>, R. P. Gardner<sup>18</sup>, and R. L. Paul<sup>2</sup>
- Hydrogen in Cu<sub>80</sub>Co<sub>20</sub> by PGAA**  
A. Edelstein<sup>25</sup> and R. L. Paul<sup>2</sup>
- Chlorine in Basalts by PGAA**  
L. Harris<sup>56</sup>, R. L. Paul<sup>2</sup>, M. Caffee<sup>56</sup>, R. Finkel<sup>56</sup>, and H. Southon<sup>56</sup>
- Hydrogen by PGAA**  
G. Hubler<sup>25</sup>, R. L. Paul<sup>2</sup>, and R. M. Lindstrom<sup>2</sup>
- Grazing Incidence Prompt Gamma Emissions and Resonance-enhanced Neutron Standing Waves in a Thin Film**  
E. J. Kramer<sup>14</sup>, T. P. Russell<sup>57</sup>, P. Lambooy<sup>57</sup>, R. L. Paul<sup>2</sup>, R. M. Lindstrom<sup>2</sup>, H. Zhang<sup>4,65</sup>, P. D. Gallagher<sup>65</sup>, and S. K. Satija<sup>65</sup>
- Hydrogen in Titanium Alloys by PGAA**  
H. M. Privett<sup>58</sup>, W. J. Richards<sup>59</sup>, R. L. Paul<sup>2</sup>, and R. M. Lindstrom<sup>2</sup>
- Hydrogen in Nanocrystalline Metals by PGAA**  
P. G. Sanders<sup>60</sup>, R. L. Paul<sup>2</sup>, R. M. Lindstrom<sup>2</sup>, J. R. Weertman<sup>60</sup>, J. G. Barker<sup>65</sup>, and R. G. Siegel<sup>46</sup>
- Boron in Tourmalines by PGAA**  
J. D. Robertson<sup>61</sup>, M. D. Dyar<sup>62</sup>, and R. L. Paul<sup>2</sup>

**Hydrogen Uptake by Solid Proton Conductors by PGAA**F. Krug<sup>63</sup>, T. Schober<sup>63</sup>, T. Springer<sup>63</sup>, and R. L. Paul<sup>2</sup>**Gamma-ray Cascades in the Te- 128(n, $\gamma$ ) Reaction Observed in Coincidence Measurements**W. B. Walters<sup>4</sup>, R. L. Paul<sup>2</sup>, R. M. Lindstrom<sup>2</sup>, J. R. Swider<sup>4</sup>, and D. M. Mustillo<sup>4</sup>**Hydrogen in a  $\gamma$ -Fe<sub>2</sub> Thin Film**R. Ziolo<sup>64</sup> and R. L. Paul<sup>2</sup>**Affiliations**

- <sup>1</sup>Food and Drug Administration
- <sup>2</sup>Nuclear Methods Group
- <sup>3</sup>Smithsonian Institution
- <sup>4</sup>University of Maryland
- <sup>5</sup>University of Michigan
- <sup>6</sup>Federal Bureau of Investigation
- <sup>7</sup>Kurchatov Institute
- <sup>8</sup>University of Missouri
- <sup>9</sup>Separation Science Group
- <sup>10</sup>Surface & Microanalysis Science Division
- <sup>11</sup>CNRS, Art and Archaeologie
- <sup>12</sup>Delft University of Technology
- <sup>13</sup>University of Gent
- <sup>14</sup>Cornell University
- <sup>15</sup>McMaster University
- <sup>16</sup>McMaster University Health Sciences
- <sup>17</sup>Texas A&M University
- <sup>18</sup>University of North Carolina
- <sup>19</sup>Comision Chilena de Energia Nuclear
- <sup>20</sup>University of Texas at Austin
- <sup>21</sup>Czech Academy of Sciences
- <sup>22</sup>Lindfield College
- <sup>23</sup>The Pennsylvania State University
- <sup>24</sup>Universität Konstanz
- <sup>25</sup>U.S. Naval Research Laboratory
- <sup>27</sup>Oak Ridge National Laboratory
- <sup>28</sup>Hungarian Academy of Sciences
- <sup>29</sup>Japan Atomic Energy Research Institute
- <sup>30</sup>CID Technologies Inc.
- <sup>31</sup>Biotraces, Inc.
- <sup>32</sup>Harvey Mudd College
- <sup>33</sup>Los Alamos National Laboratory

<sup>34</sup>Triangle Universities Nuclear Laboratory<sup>35</sup>Industrial Quality, Inc.<sup>36</sup>Intel Corp.<sup>37</sup>Westinghouse<sup>38</sup>X-ray Optical Systems, Inc.<sup>39</sup>State University of New York<sup>40</sup>Schott Fiber Optics<sup>41</sup>Lawrence Berkeley Laboratory<sup>42</sup>University of Virginia<sup>43</sup>Biomaterial Sciences International, Inc.<sup>44</sup>Universidad de Antofagasta<sup>45</sup>Physitron, Inc.<sup>46</sup>Argonne National Laboratory<sup>47</sup>DRECAN/SPEC/CEA Saclay<sup>48</sup>Battelle Pacific Northwest Labs.<sup>49</sup>Institut Laue-Langevin<sup>50</sup>University of Fribourg<sup>51</sup>NASA Johnson Space Center<sup>52</sup>Johns Hopkins University<sup>53</sup>DuPont<sup>54</sup>Alcoa Tech Center<sup>56</sup>Lawrence Livermore National Laboratory<sup>57</sup>IBM Almaden Research Center<sup>58</sup>United Technologies, Pratt and Whitney<sup>59</sup>McClellan AFB<sup>60</sup>Northwestern University<sup>61</sup>University of Kentucky<sup>62</sup>West Chester University<sup>63</sup>IFF, KFA<sup>64</sup>Xerox Corporation<sup>65</sup>Reactor Radiation Division

# Neutron Interactions and Dosimetry

This group provides measurement services, standards, and fundamental research in support of NIST's mission as it relates to neutron technology and neutron physics. The industrial sectors served include materials development, scientific instrument calibration, electric power production, radiation protection, national defense, and radiation therapy. This project maintains, develops, and applies well-characterized neutron fields for detector development, methods evaluation, and standardization as needed for materials dosimetry in nuclear reactor applications and for personnel dosimetry in radiation protection. These neutron fields include thermal neutron beams, "white" and monochromatic cold neutron beams, a thermal-neutron-induced  $^{235}\text{U}$  fission neutron field, and  $^{252}\text{Cf}$  fission neutron fields, both moderated and unmoderated. The calibration of these neutron fields is derived from related artifacts, facilities, and capabilities maintained by the project: the national standard neutron source NBS-I, a manganous sulfate bath for neutron source comparisons, a collection of fissionable isotope mass standards (FIMS), a collection of boron and lithium isotopic standards, spectroscopy facilities for both gamma rays and alpha particles, and a capability to perform radiation transport calculations. The group also performs experimental tests of critical neutron transport data and computation methods.

The group carries out forefront research at the CNRF in neutron physics and tests of fundamental symmetry principles, develops advanced measurement techniques in neutron interferometry, and is developing neutron spin filters based on laser polarization of  $^3\text{He}$ .

Highlights of activities are given below.

## Fundamental Neutron Physics

### • Neutron Interferometry

The neutron interferometer station at the

NIST cold neutron facility has become operational. This station incorporates advanced vibration isolation and environmental control systems. Monoenergetic neutrons with energies in the range of 4 meV—20 meV are available for experiments. Initial measurements indicate vibrational isolation to be better than  $\pm 0.1 \mu\text{g}$  (as in the earth's gravitational acceleration). The positional stability of the setup is about  $\pm 2 \mu\text{m}$  in translation and about  $\pm 1 \mu$  radian in rotation. Interference patterns were obtained with two types of interferometers. Interference fringe visibility was greater than 70%, and phase stability as good as  $\pm 5$  milliradians/day was observed. These numbers suggest that NIST interferometer performance is on a par or better (in some cases by more than an order of magnitude) than other interferometer stations elsewhere. Steps are being implemented to enhance the beam intensity and improve the vibration isolation and the environmental control systems even further. A variety of fundamental physics experiments are expected to be carried out in the near future in collaboration with teams from universities in the United States and Europe. In addition, considerable efforts are being devoted to the development of neutron phase topography for the study of structural and phase transitional properties of materials.

### • Development of Neutron Spin Filters by Laser Polarization of $^3\text{He}$

The developmental program to produce polarized neutron beams using a  $^3\text{He}$  spin filter at NIST has seen major advances this year with the successful polarization of a sample of  $^3\text{He}$  in the guide hall. In addition, the polarization was measured using Nuclear Magnetic Resonance (NMR) and calibrated against the small NMR signal from a sample of pure water. The setup used to polarize the  $^3\text{He}$  could filter a beam of cold neutrons with sufficient  $^3\text{He}$  polarization.



The spin filter is based on the spin-dependent absorption of neutrons by polarized  $^3\text{He}$  in the reaction  $^3\text{He}(n,p)^3\text{H}$ . The polarized  $^3\text{He}$  is produced either by spin-exchange with laser optically pumped rubidium vapor or by direct optical pumping of metastable  $^3\text{He}$ . The polarization of the  $^3\text{He}$  is measured either using NMR, or by measuring the circular polarization of light emitted from an excited state of  $^3\text{He}$  (the second method only works for the metastable polarization technique). The polarization measured and calibrated this year was produced using the spin-exchange method.

In addition to the milestones mentioned above, significant progress has been made in determining whether the polarization of  $^3\text{He}$  produced using the spin-exchange technique could be improved by replacing the rubidium vapor with potassium vapor. Progress toward implementing the metastable apparatus includes construction of the vacuum system used to maintain the 1-2 torr  $^3\text{He}$  densities needed to sustain a metastable population, and construction and testing of the laser which will be used to polarize  $^3\text{He}$ .

Immediate plans are to complete the potassium/rubidium comparison, and then maximize the  $^3\text{He}$  polarization produced in the spin-exchange setup. When the reactor returns to operation in the spring, we will be able to test the spin filter on a neutron beam.

#### • Determination of the Neutron Lifetime

The program aimed at the determination of the neutron lifetime began observing useful neutron decay events on October 5, 1993. Data taking continued through May 23, 1994 when the reactor was shut down for upgrades and repairs. During that time, the proton detector was live for almost 124 days during which time some 10,500,000 decay events were logged. If the experiment were limited solely by statistics, this would give imply a result with better than 0.1% uncertainty. It is expected, however, that systematic effects will dominate our final uncertainty estimate. An important feature in this ef-

fort was a multiparametric data acquisition system that allows a detailed study of each event. This will be very useful in reducing systematic effects. Progress is currently underway to analyze the results.

## Neutron Fields and Standards

### • Fission Spectrum Standard Neutron Fields

Because the energy spectra are better known than in other neutron fields and because measured-to-calculated spectrum-averaged cross-section ratios of most dosimetry reactions agree in the  $^{252}\text{Cf}$  and  $^{235}\text{U}$  spectra to better than 6.5% (and in many case to  $\pm 3\%$ ), these two fission spectra are maintained and operated at NIST as standard neutron fields available for customer use. Although the  $^{252}\text{Cf}$  spectrum is the better known distribution, the fact that there are available fluence rates a factor of 1000 greater in the NIST  $^{235}\text{U}$  spectrum, results in it's more frequently use for reference irradiations. Furthermore, this utilization will increase in 1995-1996 in support of round robin dosimetry intercomparisons. Current needs are:

(1) Comparisons of methods and materials use to perform fast neutron dosimetry by neutron activation of select fission products in threshold fissionable isotopes, such as  $^{237}\text{Np}$  and  $^{238}\text{U}$ ;

(2) Comparison of fast neutron dosimetry accomplished with X-ray emitting  $^{93}\text{Nb}(n,n')^{93}\text{Nb}^m$  and  $^{103}\text{Rh}(n,n')^{103}\text{Rh}^m$  reactions to those of well accepted gamma-ray spectrometry methods;

(3) Benchmark calibrations of all spectrum characterization and fluence monitoring performed for industry support irradiations in the Materials Dosimetry Reference Field (MDRF), the NIST/University of Michigan engineering benchmark field. The test region in this facility is a cylindrical volume inside a cylindrical shell of iron in the pool adjacent to the Ford reactor core. The MDRF spectrum is similar to that inside a PWR reactor pressure vessel.

- **Cavity Fission Source: The NIST  $^{235}\text{U}$  Fission Spectrum Irradiation Facility**

This fission spectrum can normally be scheduled for availability in the graphite thermal column of the NIST Reactor with a few weeks notice. The spectrum above 1 MeV is a pure  $^{235}\text{U}$  fission spectrum and the fluence rate, at 20 Megawatts reactor power, is  $2.7\text{E}+10$  n/cm<sup>2</sup>s. Fluences for all irradiations are monitored using the  $^{58}\text{Ni}(n,p)^{58}\text{Co}$  reaction, to a nominal  $\pm 2.6\%$  uncertainty. This uncertainty is established by traceable records of the 70.8-day,  $^{58}\text{Co}$  gamma activity measured on a germanium counter whose efficiency is derived from a certified fluence irradiation in a  $^{252}\text{Cf}$  spectrum. This is accomplished for the 810.7 keV photopeak by relating counter response of  $^{58}\text{Co}$  to the  $^{252}\text{Cf}$  fluence based on the source  $4\pi$  emission rate (n/sec), measured by the  $\text{MnSO}_4$  Bath Technique, and half the accurately measured distance between two nickel foils positioned equidistant from, and on opposite sides of, the lightly encapsulated  $^{252}\text{Cf}$  source. The source strength is calibrated to nominally  $\pm 1.3\%$ , 0.85% of which has been established in an international round robin calibration. The distances measurement, uncertainties in the "point-source" sintered  $\text{Cf}_2\text{O}_3$  bead, and scattering corrections account for the rest of the reported uncertainty.

- **Benchmarking the Masses of Solid-State-Track-Recorder (SSTR) Dosimetry**

Previous annual reports and Ref. 1, 2 describe use of certified fluence irradiations in well characterized neutron fields (*e.g.*, a  $^{235}\text{U}$  fission spectrum) to assist industry in benchmarking fissionable deposit masses in the nanogram/cm<sup>2</sup> mass range. Current comparisons indicate that the masses, so deduced, agree with those determined with radioactive spiking techniques, employed during deposit fabrication, to within  $\pm 3.5\%$ , one standard deviation. This result is consistent with the reported 2.5% uncertainties for both types of measurement.

Since starting SSTR dosimetry in the ex-

vessel cavities of commercial-nuclear electric-power reactors, the Westinghouse Science & Technology Center (WSTC), Pittsburgh, PA., has deployed about 1500 SSTR neutron dosimeters in 17 different PWR reactors. The use of SSTR neutron dosimetry for reactor cavity vessel fluence monitoring is now considered a reliable technique capable of reasonably high accuracy. Additional benchmark referencing work is planned under NIST/WSTC cooperative industrial-research agreements for lighter mass deposits. All of this newly employed technology will be reviewed in a joint WSTC/NIST paper at the 7th SMORN Symposium on "Nuclear Reactor Surveillance and Diagnostics", Avignon, France, 19-23 June, 1995.

- **Microdosimetry of Gamma Rays**

As a first step in an effort to use microdosimetric methods to give a rough measurement of the photon energy in high intensity fields, we have measured the LET spectrum for  $^{137}\text{Cs}$  and  $^{60}\text{Co}$ , with results as shown. The two spectra are in good agreement with other measurements reported in the literature: in particular, the  $^{60}\text{Co}$  spectrum shows the characteristic peak at 0.3 keV/micrometer, corresponding to minimum ionization of the secondary electrons.

- **Response of Albedo Neutron Dosimeters as a Function of Angle of Incidence**

ICRU 39 and ICRU 47 suggest that neutron personnel dosimeters should have a particular, non-isotropic, response as a function of angle of incidence, although the detailed calculations are just starting to be produced. We have started a measurement program to determine the angular response for several different types of dosimeters, for both bare and  $\text{D}_2\text{O}$ -moderated californium.

- **Thermal Column Irradiations**

We have provided thermal column irradiations to superheated drop detectors mounted inside our environmental chamber, to test a theory of bubble production as a function of tempera-

ture. This work was part of a Master's thesis for a student at the U. S. Naval Academy.

We have used our measured thermal column fluence to calibrate BF<sub>3</sub> detectors for the DOE Environmental Measurements Laboratory and the Army Pulsed Reactor Facility.

## Research Topics

**Utilization of the Materials Dosimetry Reference Facility — Tests of New IRMM <sup>237</sup>Np and <sup>238</sup>U Fast Neutron Dosimeters**

E. D. McGarry<sup>8</sup>, J. A. Grundl<sup>8</sup>, C. M. Eisenhauer<sup>8</sup>, D. M. Gilliam<sup>8</sup>; A. I. Hawari<sup>16</sup>, P. A. Simpson<sup>16</sup>, and R. Venkatoraman<sup>16</sup>

**Calibration of a Thin-Window Counter for the <sup>103</sup>Rh(n,n')<sup>103m</sup>Rh Reaction in a Fission Spectrum Neutron Field**

E. D. McGarry<sup>8</sup> and M. Oliver<sup>2</sup>

**Benchmark Measurements and Calculations of Neutron Transport**

D. M. Gilliam<sup>8</sup>, M. S. Dewey<sup>8</sup>, J. S. Nico<sup>8</sup>, C. M. Eisenhauer<sup>8</sup>, and J. A. Grundl<sup>8</sup>

**Neutron Fluence Rate Measurements at the CNRF**

D. M. Gilliam<sup>8</sup> and J. S. Nico<sup>8</sup>

**Defined-Geometry Alpha Counting**

D. M. Gilliam<sup>8</sup> and J. S. Nico<sup>8</sup>

**Certified Neutron Fluence Standards from the Cavity Fission Source**

E. D. McGarry<sup>8</sup> and J. A. Grundl<sup>8</sup>

**Quality Assurance Checks on Masses and Impurities in Neutron Dosimeters for NRC Reactor Pressure Vessel Embrittlement Surveillance**

E. D. McGarry<sup>8</sup> and J. A. Grundl<sup>8</sup>

**Measurement of LET Spectra**

R. B. Schwartz<sup>8</sup>, H. Gerstenberg<sup>1</sup>, and P. Lamperti<sup>8</sup>

**Intercomparison of NIST and PNL Calibration Facilities**

R. B. Schwartz<sup>8</sup>, J. C. McDonald<sup>3</sup>, and M. K. Murphy<sup>3</sup>

**Response of Albedo Dosimeters Versus Distance from a Neutron Source**

R. B. Schwartz<sup>8</sup> and A. J. P. Ghilardi<sup>13</sup>

**Response of Albedo Neutron Dosimeters as a Function of Angle**

R. Schwartz<sup>8</sup>, B. A. Torres<sup>1</sup>, and E. Boswell<sup>8</sup>

**Determination of the Neutron Lifetime**

M.S. Dewey<sup>8</sup>, G.L. Greene<sup>8</sup>, D. M. Gilliam<sup>8</sup>, and W. M. Snow<sup>6</sup>

**Accurate Determination of Neutron Capture Flux**

M. S. Dewey<sup>8</sup>, M. Arif<sup>6</sup>, D. M. Gilliam<sup>8</sup>, G. L. Greene<sup>8</sup>, W. M. Snow<sup>6</sup>, J. Pauwels<sup>7</sup>, and R. D. Scott<sup>11</sup>

**Study of Time Reversal Invariance in Neutron Beta Decay**

J. F. Wilkerson<sup>18</sup>, E. Wasserman<sup>10</sup>, J. Nico<sup>8</sup>, R. G. H. Robertson<sup>10</sup>, S. Freedman<sup>10</sup>, A. Garcia<sup>10</sup>, T. Chupp<sup>16</sup>, K. Coulter<sup>16</sup>, M. S. Dewey<sup>8</sup>, G. L. Greene<sup>8</sup>, and A. Thompson<sup>8</sup>

**Observation of the Coriolus Acceleration of Neutrons in a Rotating Crystal**

A. Zeilinger<sup>15</sup>, M. Arif<sup>6</sup>, K. Raum<sup>17</sup>, M. Kollner<sup>17</sup>, and D. Brown<sup>8</sup>

**Parity Non-Conserving Neutron Spin Rotation**

B. Heckel<sup>18</sup>, D. Markoff<sup>18</sup>, E. Adelberger<sup>18</sup>, G. L. Greene<sup>8</sup>, and W. M. Snow<sup>6</sup>

**Highly Accurate Neutron Wavelength Measurements**

M. S. Dewey<sup>8</sup>, K. J. Coakley<sup>20</sup>, W. M. Snow<sup>6</sup>, M. Arif<sup>6</sup>, and G. L. Greene<sup>8</sup>

**LASER Polarization of <sup>3</sup>He for Neutron Spin Filters**

A. Thompson<sup>8</sup>, G. L. Greene<sup>8</sup>, T. Gentile<sup>8</sup>, and M. S. Dewey<sup>8</sup>

**Trapping of Ultra Cold Neutrons**

J. Doyle<sup>5</sup>, S. Lamoreaux<sup>18</sup>, R. Golub<sup>4</sup>, and G. L. Greene<sup>8</sup>

**Neutron Interferometry**

M. Arif<sup>6</sup>, D. Brown<sup>8</sup>, and G. L. Greene<sup>8</sup>.

## Affiliations

<sup>1</sup>Armed Forces Radiobiology Research Institute

<sup>2</sup>Army Pulsed Reactor Facility

<sup>3</sup>Battelle Pacific Northwest Laboratory (PNL)

<sup>4</sup>Hahn-Meitner Institute

<sup>5</sup>Harvard University

<sup>6</sup>Indiana University

<sup>7</sup>Inst for Ref Materials & Measurements (IRMM, CEC)

<sup>8</sup>Ionizing Radiation Division (or other NIST Divisions)

<sup>9</sup>Jackson State University

<sup>10</sup>Los Alamos National Laboratory

<sup>11</sup>Scottish Universities Research and Reactor Centre

<sup>12</sup>United States Naval Academy

<sup>13</sup>Universidade de São Paulo

<sup>14</sup>University of California, Berkeley

<sup>15</sup>University of Innsbruck

<sup>16</sup>University of Michigan

<sup>17</sup>University of Munich

<sup>18</sup>University of Washington

<sup>19</sup>Washington University, St. Louis

<sup>20</sup>Statistical Engineering Division

# Polymers Division Programs

## Block Copolymers, Blends and Networks in Bulk

- **SANS Studies of the Phase Behavior of Binary Polymer Blend/Diblock Copolymer Mixtures**

Small angle neutron scattering measurements have been conducted to investigate the effect of polystyrene- $d_8$ -polybutadiene diblock copolymer (PSD-PB) content on the phase behavior of a low-molecular-weight polystyrene- $d_8$ /polybutadiene (PSD/PB) mixture. SANS results of the general features of the scattering curves as a function of temperature and copolymer content has been obtained. For intermediate to high copolymer content (greater than 20 wt%), a pronounced peak of the scattering curve is observed at all temperatures. The peak intensity,  $S(q^*)$ , increases as temperature decreases for all samples, and no sharp change in the temperature dependence of  $S(q^*)$  is observed. The position,  $q^*$ , increases with increasing copolymer content and is weakly dependent on temperature. The analysis of the temperature and composition dependence of the peak intensity and peak position is being carried out at this time.

- **The Collapse of Free Polymer Chains in a Network**

Small angle neutron scattering has been used to measure the conformation of linear polymer chains at dilute concentration trapped in a matrix of crosslinked polymer. Three regimes are found depending on the length of the linear chain,  $N_l$ , with respect to the mesh size of the network,  $N_c$ . When  $N_l > N_c$  the radius of gyration of the linear chain, does not change from that observed in the uncrosslinked melt. When  $N_c < N_l$ , the size of the linear chains shrinks which has been predicted for isolated polymer chains trapped in a field of random obstacles. When  $N_c \ll N_l$  the linear chains are observed

to segregate. The collapse of polymer chains in a network has important implications for the distribution and transport of polymers in many heterogeneous environments.

- **Synthesis and Characterization of Organic-Inorganic Interpenetrating Polymer Networks**

Small angle neutron scattering has been used to characterize interpenetrating polymer networks synthesized by performing sol-gel chemistry and conventional organic polymerizations in mixtures of the monomers. The organic polymers were acrylates, methacrylates, or epoxies, and the inorganic phase was  $\text{SiO}_2$ . Polymerizations were conducted simultaneously or sequentially at a variety of relative rates, and the chemistry was designed to allow different amounts of grafting between the components. Wide variations in morphology were observed depending on the polymerization conditions, ranging from grossly phase separated to dendritic to finely divided structures (at a 100 Å size scale). The phases ranged from mixtures of the two components to relative pure phases. Transmission electron microscopy showed morphologies in agreement with the SANS results.

- **Structure Change and Alignment of Block Copolymers Under Shear**

The effect of shear flow on the morphology and order-disorder transition temperature,  $T_{ODT}$ , of a block copolymer of polystyrene- $d_8$ /polybutadiene/polystyrene- $d_8$  (SBS) with a block architecture of  $8 \times 10^3 / 54 \times 10^3 / 8 \times 10^3$  g/mole ( $M_w/M_n = 1.05$ ) was analyzed near the ODT using in-situ SANS, and on sheared and quenched specimens using SANS and TEM. The overall composition of the polymer was 23 wt.% polystyrene, and the ordered phase of this sample is a hexagonally packed cylindrical array, with unit cell parameter  $a = 25$  nm. The quiescent  $T_{ODT}$

of this material was  $116 \pm 5^\circ\text{C}$ , by dynamic mechanical measurements. The in-situ SANS showed that the cylinders quickly align in a shear field as observed previously by other workers. The TEM results on the sheared and quenched specimens indicated that a shear-induced change in the packing symmetry of the microphase separated cylinders occurred at sufficiently high shear rates. The transformation is akin to "martensitic transformations" observed in many different metals under deformation. This result implies that theories developed for atomic scale structural changes in metals may be more broadly applicable to the block copolymer class, on a meso-size scale. The  $T_{ODT}$  under shear by in-situ SANS was measured to shift upward by up to  $20^\circ\text{C}$ , as the shear rate was increased. Studies of this type are important to understand the effect of flow on the extrusion processing of these industrially important thermoplastic elastomer materials.

### Compatibilization of Polymer Blends by Strong Interactions and Reactions

We have examined several new approaches for the control of binary polymer blend phase behavior through means of either strong interactions or transesterification reactions. In our studies, we have characterized changes to both the phase diagram and the kinetics of phase separations for several different binary blends. Strong interactions may be introduced by chemically modifying segments to form sites for complexation or hydrogen bonding. We have shown that the introduction of a small number of interactive sites can dramatically change phase behavior in blends which are ordinarily incompatible. Another way to change the phase behavior is through transesterification reactions at high temperatures which result in either an exchange of segments between the different polymers or the grafting of one polymer onto the other. Transesterification induces compatibility in otherwise incompatible mixtures, leading to a homogeneous phase at high temperatures. At

intermediate temperatures, by contrast, a microdomain morphology with a broad interphase forms. A final aspect of this project examines compatibilization by the aforementioned mechanisms in ultra thin film polymer films cast on silicon substrates. We find that, due to the transesterification process, a copolymer layer gradually forms at the interface close to the substrate. For a bilayer of two polymers which interact through strong interactions, we observe mixing at the interface due to the complexation between the two components.

#### • Control of Phase Behavior Through Hydrogen Bonding

Hydrogen bonding in blends of polybutylmethacrylate (PBMA) and deuterated polystyrene (d-PS) was achieved by introducing a small amount perhexafluoro-2-hydroxyisopropyl- $\alpha$ -methylstyrene as a co-monomer in the d-PS polymerization. The resulting polystyrene, denoted d-PSOH, contains hydroxyl groups which have nearly the same acidity as phenol. In the d-PSOH/PBMA blend, Pearce et al. [1] have shown the presence of hydrogen bonding between the d-PSOH hydroxyl and the PBMA carbonyl groups. A small amount (1.2 mol %) of the perhexafluoro-2-hydroxyisopropyl groups dramatically affects the phase behavior. The d-PSOH/PBMA blend is miscible within a limited temperature range whereas the unmodified blend using identical molecular weights is immiscible. Small angle neutron scattering has been employed to study the kinetics of phase separation in the d-PSOH/PBMA blend. These experiments revealed an unusual growth behavior in hydrogen bonded blends. This might result in a domain structure which is different from the interconnected phases seen in classical spinodal decomposition, and there is a possibility that this might be useful for new materials.

#### • Control of Phase Behavior Through Complexation

Ionic complexes provide another means to

modify the interactions between immiscible polymers. In this study, we focus on how the nature and strength of complexation affects blend morphology and phase behavior. The blend consists of lightly sulfonated polystyrene ionomers with poly(*N,N'*-dimethylethylene sebacamide), a methylated Nylon. Because the polyamide exhibits no hydrogen bonding, as a result of substitution of the methyl group for the amide proton, it has a relatively low melting temperature ( $\sim 75^\circ\text{C}$ ) and is slow to crystallize. We have employed time resolved light scattering to examine the phase separation process in this blend, and have found that there is a temperature range where phase separation can occur but is limited by the complexation interactions. We believe that resulting morphology is influenced by the level of sulfonation and the type of counter cation; this will be a subject of investigation in the FY95.

- **Structural Stabilization of Through Transesterification Reactions**

Small angle neutron scattering was employed to how the morphology of two types of mixtures, polycarbonate (PC) with a noncrystallizable polyester copolymer and PC with polymethylmethacrylate (PMMA), can be controlled by choosing the appropriate thermal treatment. At high temperatures, transesterification results in the exchange of segments in the PC/Polyester blend, forming a random copolymer. By contrast, PC chains ends graft onto the PMMA backbone in the PC/PMMA blend. For both mixtures, annealing below  $170^\circ\text{C}$  results in large scale phase separation, just as for ordinary immiscible blends. However, for annealing above  $220^\circ\text{C}$ , transesterification reactions lead to the formation of a homogeneous phase. For the PC/Polyester blend, this phase consists of random copolymers. For the PC/PMMA blends, the details of the homogeneous phase are not yet clearly understood. One possibility is that a random network forms where PC chains provide links between PMMA backbones. At intermediate temperatures near  $200^\circ\text{C}$ , there is a

competition between the effects of immiscibility and transesterification. The resulting morphology contains domains with broad interfacial regions for both types of blends.

Continuing investigations have focussed on using dielectric spectroscopy as a characterizational tool for blends undergoing transesterification. For the PC/polyester case, we find that the glass transition temperatures and the dielectric amplitude increase dramatically upon annealing at  $220^\circ\text{C}$ . The data strongly suggest that, in the homogeneous, transesterified state, the dipoles of both components relax collectively. By contrast, only minimal changes are observed after annealing the initial untransesterified film at  $160^\circ\text{C}$ . The latter result, however, implies that some residual mixing is present even in the phase separated films. Dielectric measurements have been performed on a variety of compositions and thermal treatments. Overall, the data are consistent with the results of SANS and DSC.

- **Effects of Strong Interactions and Transesterification Reaction in Thin Films**

The behavior of polymer blends near surfaces and in thin film geometries is technologically important for applications in areas such as thin film adhesion and structural integrity of coatings. Surface analytical techniques such as x-ray and neutron reflectivity and atomic force microscopy were employed to measure the surfaces and interfaces of thin films of polymer blends with nanometer resolution. Here, we investigate the role of complexation and transesterification mechanisms as strategies to alter the phase behavior and control miscibility in such systems. These mechanisms may also serve to enhance thin film strength and adhesion.

The kinetics of interfacial mixing was examined in a thin bilayer of lightly sulfonated polystyrene and poly(*N,N'*-dimethylethylene sebacamide) Nylon. Neutron reflectivity was used to monitor the interface structure as a function of annealing time at a temperature above the Nylon melting point but below the glass transi-

tion for the sulfonated PS. The kinetics of the interfacial mixing was unique due to the strong interactions between styrene sulfonate and the amide group. Intermolecular complexes that act as physical crosslinks form upon mixing the two polymers, and this slows down the diffusion and interfacial mixing processes.

The structure of thin film blends of PC and deuterated PMMA was studied as a function of annealing time at 200°C. Initially, there is a rapid enrichment of PMMA at the silicon substrate surface. At longer times, this trend is reversed due to the transesterification reaction which tends to mix the chains near the interface. At later times, atomic force microscopy of the air/polymer interface shows a hole-pattern which evolves into droplets, similar to a roughening phenomena for immiscible blends reported separately. The late stage coalescence is inhibited by the block copolymer at the interface of the droplets as in the case of nonreactive blends stabilized by block copolymers.

### Polymer Blend Films

- **Phase Separation Induced Roughening In Thin Polymer Blend Films**

Phase separation in spun cast thin film blends (100-3000 Å) of deuterated polystyrene (dPS, 443k) and poly-vinylmethylether (PVME, 84k) was investigated by reflectivity and microscopy techniques. Using x-ray reflectivity, we have observed that phase separation in these thin films is accompanied by an abrupt macroscopic roughening of the air/polymer interface, that can be quantified by atomic force microscopy and reflectance optical microscopy. We interpret this roughening as a dewetting of the dPS rich phase from the PVME rich phase in order to minimize the unfavorable area of contact between the coexisting phases. Transition temperatures based on the roughening phenomena indicate a stabilization of the thin film phase boundary compared to the bulk. Depth profiles obtained by neutron reflection indicates capillary condensation of PVME at the air and sili-

con surface to be at least partly responsible for the stabilization of the phase boundary. Recent simulation results that model such a phenomena will be presented.

- **Kinetics of the Interfacial Mixing for a Polymer Blend Compatibilized by Complexation**

In this study, styrene sulfonate groups have been incorporated into polystyrene chains to compatibilize the blend with Poly(N,N'-dimethylethylene sebacamide), a nylon with a low melting temperature. Neutron reflectivity was used to characterize the interfacial structure for a bilayer film of the two polymers. The interfacial mixing was monitored as a function of annealing time at a temperature above the  $T_m$  of the nylon and below the  $T_g$  of the sulfonated PS. The kinetics of the interfacial mixing was unique due to a very strong interaction between the styrene sulfonate and the amide group. Intermolecular complexes that act as physical crosslinks form upon mixing the two polymers, and this slows down the diffusion and the interfacial mixing process.

- **Phase Separation in Thin Films of a Reactive Polymer Blend**

The competition between phase separation and transesterification was investigated in spun-cast thin film blends (~1000 Å) of polycarbonate (PC) and deuterated polymethylmethacrylate (dPMMA) by neutron and x-ray reflectivity and atomic force microscopy. Upon increasing the temperature to 200°C, we observe an initial rapid enrichment of dPMMA at the silicon surface due to phase separation. At longer times this trend is reversed due to the transesterification reaction of the blend in which the blend component chains connect and disconnect to form random copolymer chains. A unique feature of this reactive blend is that it self-generates its own block copolymer interfacial modifier which gradually leads to the formation of a copolymer layer between the surface segregated dPMMA layer and the bulk of the thin film. Atomic force



microscopy of the air/polymer interface shows an interesting hole-pattern to droplet evolution. The late stage coalescence is inhibited by the block copolymer at the interface of the droplets as in blends stabilized by diblock copolymers.

#### • Temperature of Ultrathin Polymer Films on Silicon

The glass transition temperature,  $T_g$ , of polymer thin films on silicon wafers was determined in order to explore the effect of the presence of a silicon surface on local polymer chain dynamics. To mimic the interface behavior, the film thickness included in this work was as low as 50 Å. Three polymers, polystyrene (PS), polymethylmethacrylate (PMMA) and poly-2-vinylpyridine (P2VP) were chosen for this work; their interaction energy or the work of adhesion with silicon can be ranked as P2VP>PMMA>PS.  $T_g$  of thin films was determined by monitoring the film thickness as a function of temperature, and  $T_g$  was identified as the temperature where the thermal expansion coefficient underwent a sudden change. X-ray and neutron reflectivities were used to determine film thickness with a precision of a few angstroms.

For PS with its initial thickness below 100 Å, a decrease in film thickness with temperature was noticed. This contraction in thickness took place as low as 30 °C and was found for all the PS molecular weights studied so far. If one regards  $T_g$  as the temperature where chains exhibit significant mobility, this result can be interpreted as  $T_g$  starts at 30 °C in thin PS films. For PMMA with thickness between 75 to 600 Å, no change in  $T_g$  from its bulk value was observed. However, the thermal expansion coefficient of thin films was found to be lower than that of the bulk one. The P2VP results suggested that  $T_g$  of thin films below 100 Å was greater than 160 °C which was the instrument limit. An elevation in  $T_g$  was also observed for PS on hydrogen passivated silicon surfaces.

An in-depth understanding of polymer chain dynamics near surfaces or interfaces is a prereq-

uisite for one to predict and to control the performances of polymer thin films adhered to metals or silicon substrate. Molecular dynamics calculations suggested that the chain packing density at a polymer/solid interface depended on the interaction energy between these two materials in contact. Therefore one expects that the local chain dynamics at interfaces also depends on the interaction energy. As an initial attempt to probe the influence of the interaction energy on local chain dynamics, ultrathin films of polymers with different adhesion energy to silicon single crystal wafer were prepared and their  $T_g$  were determined.

Due to its susceptibility of radiation damage by x-ray neutron reflectivity (NR) was used in all the PMMA measurements, while x-ray reflectivity (XR) was used for PS and P2VP. Deuterated poly methylmethacrylate (d-PMMA) with a polydispersity of 1.10 and a number-average molecular weight of 135,000 g/mol was synthesized via a group transfer polymerization method. The polymer is 57% syndiotactic, 37% atactic and 6% isotactic. The d-PMMA was spin-cast from redistilled o-xylene onto clean Si (111) wafers (Semiconductor Processing Co.; Boston, MA) [1] which had been pretreated with a sulfuric acid-NoChromix[1] solution for a least 12 hours, followed by a thorough distilled water rinse. Initial d-PMMA film thicknesses of 75 to 570 Å (at 30-60 °C) were prepared in this work. Samples were annealed under vacuum at 110 °C for more than an hour to ensure that films were of uniform density and then allowed to cool under vacuum to approximately 30-60 °C. Following this annealing procedure ultrathin d-PMMA films were characterized under vacuum by neutron reflectometry (BT-7 and NG-7 Reflectometers, Research Reactor and Cold Neutron Research Facility, NIST) at various temperatures using either thermal neutrons with a wavelength of 2.35 Å on BT-7 or cold neutrons with a wavelength of 4.1 Å on NG-7. The temperature was electronically controlled within 0.2 °C of the desired setpoint and the d-PMMA films were maintained at the desired temperature for approxi-

mately one hour before the neutron reflectometry measurements were performed. Modeling and fitting of the neutron reflectivity data was by non-linear least squares fitting of profiles generated using a recursive multilayer method [2].

For PS and P2VP all the measurements were taken using x-ray reflectivity (XR). Polystyrene (Aldrich Chemical; Milwaukee, WI) [1] of molecular weights 184,000, 573,000 and 1,447,000 were spin-coated from toluene onto silicon wafers cleaned in an identical way as described above. Initial film thicknesses were varied from 45 to 835 Å. A broad molecular weight ( $M_w=200,000$ ) P2VP was used in this study. The data deduction used in XR measurements was the same as that for the NR.

Typical neutron reflectivity scans of a d-PMMA film taken at several temperatures are shown in figure 1. The increase in film thickness with increasing temperature is readily apparent in figure 1 where one can observe a decrease in distance between the interference fringes (*i.e.* the maxima and minima). with the increase in temperature. Above the bulk glass transition temperature (which is 115 °C as determined by differential scanning calorimetry), there is an increase in the rate of expansion. The calculated thickness expansion for all the d-PMMA ultrathin films considered here are listed in Table 1. Clearly there is a trend of decreasing expansion with decreasing film thickness, both below and above 120 °C. These values of thickness thermal expansion coefficient listed in Table 1 for PMMA thin films are generally less than the (3-d) bulk value reported in the literature.

A clear indication of the efficacy of this measurement procedure is that the mass is conserved during the expansion of the d-PMMA ultrathin films. To illustrate this, the products of the film thickness and the density, determined by fitting the reflectivity data, were calculated for films with thicknesses of 76, 106, 212, and 581 Å at 120 °C. These products are essentially independent of temperature; mass conservation holds for all of the film thicknesses studied. This is also indicative of negligible in-plane expansion (*i.e.*

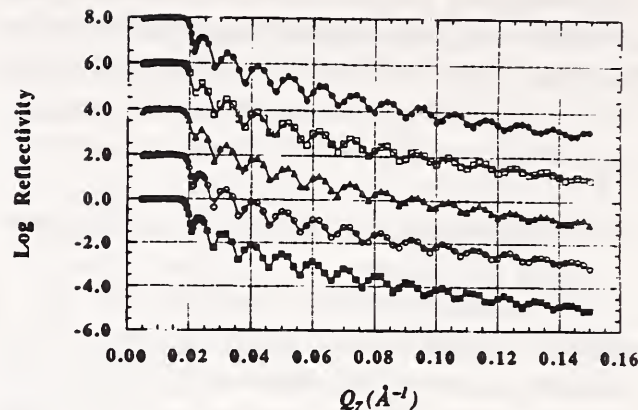


**Figure 1.** Specular reflectivity profiles and their corresponding modeled fits (solid lines) measured for an ultrathin deuterated poly methylmethacrylate (d-PMMA) film at various temperatures. The thickness changes are readily apparent here. The temperatures and measured thicknesses are denoted as follows: (l) 30°C and 571.5 Å, (o) 90 °C and 577.5 Å, (s) 120 °C and 580.5 Å, (m) 145 °C and 589.6 Å and (n) 170 °C and 596.8 Å.

parallel to the solid substrate).

The measured thicknesses of polystyrene ultrathin films with varying temperature are strongly dependent on the initial polystyrene film thickness. Over the temperature range 25-150 °C, the polystyrene thin films show different behaviors, depending on their initial thicknesses. One should note that the radius of gyration,  $R_G$ , for polystyrene ( $M_V=573,000$ ) in melt is 212 Å. Very thin films, (*i.e.* 100 Å or less), display film contraction at temperatures which are less than the glass transition temperature measured for polystyrene in the bulk, 104 °C [3]. Samples with thicker initial thicknesses display little change with temperature until approximately 60 °C, where they begin to expand. Once again this is well below the bulk glass transition temperature of 104 °C. The contraction and expansion of the ultrathin polystyrene films is both thermally reversible and independent of the molecular weights tested herein. In this work, density variations of the ultrathin polystyrene films have not been determined, since the density changes of thin films are best observed as variations in

the critical angle. In our x-ray reflectivity data, however, there are no readily observable changes in the data at low  $Q_z$  near the critical edge. This behavior is not surprising since the x-ray scattering length density of Si,  $Q_c^2 = 10.4 \times 10^{-4} \text{ \AA}^{-2}$ , is significantly larger than that of polystyrene,  $Q_c^2 = 4.8 \times 10^{-4} \text{ \AA}^{-2}$ , and therefore dominate.

**Table 1.** The calculated thermal expansion values below and above the glass transition temperature ( $120 \text{ }^\circ\text{C}$ ) are given for four ultrathin d-PMMA films of varying thickness on silicon substrates. Note the trend of decreasing thermal expansion with decreasing film thickness, both below and above the glass transition temperature.

75.7 Å	$1.09 \times 10^{-4}$	$4.44 \times 10^{-4}$
105.9 Å	$1.33 \times 10^{-4}$	$4.58 \times 10^{-4}$
212.4 Å	$1.26 \times 10^{-4}$	$5.21 \times 10^{-4}$
580.5 Å	$1.73 \times 10^{-4}$	$5.40 \times 10^{-4}$
bulk PMMA	$2.25\text{-}2.70 \times 10^{-4}$	$5.6\text{-}5.8 \times 10^{-4}$

The same PS thin films were also prepared on silicon wafers with hydrogen passivated surface. It is well known that PS adheres stronger on hydrogen passivated surface than on oxide covered one. Grossly different thermal behavior was observed; no  $T_g$  was detected up to  $160 \text{ }^\circ\text{C}$  for PS film up to  $400 \text{ \AA}$  thick. Within the temperature range of  $23 \text{ }^\circ\text{C}$  to  $160 \text{ }^\circ\text{C}$ , the thermal expansion coefficient was close to that of PS in glassy state; this strongly suggests that the  $T_g$  of thin PS film on the passivated silicon is highly elevated. The same phenomenon was also observed from P2VP films on silicon with oxide covered surfaces.

## References

- [1] J. F. Ankner and C. J. Majkrzak, in *Neutron Optical Devices and Applications*, SPIE Proc. Vol. 1738 (SPIE, Bellingham, WA, 1992), p. 260.
- [2] *Polymer Handbook 2nd Edition*, J. Brandrup and E. H. Immergut, eds., Wiley-Interscience (1975).

## Research Topics

### Thermodynamic Interactions in Model Polyolefin Blends

D. J. Lohse<sup>1</sup>, W. W. Graessley<sup>2</sup>, and G. Reichart<sup>2</sup>

### Thermodynamic Interactions and Correlations in Mixtures of Homopolymers and Block Copolymers of Polyolefins

N. P. Balsara<sup>3</sup> and C. C. Han<sup>4</sup>

### Ordering of Triblock Copolymers

Y. Matsushita<sup>5</sup>, H. Torikai<sup>5</sup>, I. Noda<sup>5</sup>, A. Karim<sup>4</sup>, and C. C. Han<sup>4</sup>

### Compatibilization Effects of Block Copolymers on Polymer Blends

A. I. Nakatani<sup>4</sup>, L. P. Sung<sup>4</sup>, and C. C. Han<sup>4</sup>

### SANS from Dilute Blends of Deuterated Polystyrene in Poly(vinylmethylether) and Protonated Polystyrene

R. M. Briber<sup>6</sup>, B. J. Bauer<sup>4</sup>, and B. Hammouda<sup>7</sup>

### SANS Study of Independently Crosslinked Blends of Deuterated Polystyrene and Poly(vinylmethylether)

R. M. Briber<sup>6</sup> and B. J. Bauer<sup>4</sup>

### Shear-Induced Morphological Structures in Triblock Copolymers

F. A. Morrison<sup>8</sup>, J. A. Mays<sup>9</sup>, M. Muthukumar<sup>10</sup>, A. I. Nakatani<sup>4</sup>, C. L. Jackson<sup>4</sup>, and C. C. Han<sup>4</sup>

### Anisotropic Response of a Liquid Crystalline Polymer to Shear as Studied by SANS

M. D. Dadmun<sup>11</sup> and C. C. Han<sup>4</sup>

### Structural Stabilization of Phase-Separating PC/Polyester Blends Through Interfacial Modification by Transesterification Reactions

H. Yoon<sup>8</sup>, Y. Feng<sup>12</sup>, and C. C. Han<sup>4</sup>

### Phase Behavior of Polymer Blends with Hydrogen Bonding

G. Merkle<sup>4</sup> and C. C. Han<sup>4</sup>

### Phase Separation and Surface Segregation in Binary Polymer Thin Film Blends

A. Karim<sup>4</sup>, S. K. Kumar<sup>13</sup>, and C. C. Han<sup>4</sup>

### Silica Filled In-Situ Composites

B. J. Bauer<sup>4</sup>, C. L. Jackson<sup>4</sup>, A. I. Nakatani<sup>4</sup>, and C. C. Han<sup>4</sup>

### Volume Phase Transition of Polymer Gel

F. Ikkii<sup>4</sup>, M. Shibayama<sup>14</sup>, and C. C. Han<sup>4</sup>

### Low Temperature Behavior of Polydimethylsiloxane Rubber

M. Kent<sup>15</sup>, G. Beaucage<sup>15</sup>, and C. C. Han<sup>4</sup>

### Phase Separation and Crystallization Behavior of Polydimethylsiloxane/Polyethylene Blends

D. Marr<sup>16</sup> and C. C. Han<sup>4</sup>

**Gelation of Polyvinylchloride in Methacrylate**M. Fair<sup>17</sup>, A. I. Nakatani<sup>4</sup>, and C. C. Han<sup>4</sup>**Hydrophobic Interactions in Polymer Solutions**E. J. Amis<sup>18</sup> and C. C. Han<sup>4</sup>**Phase Separation Kinetics in Polycarbonate/Polymethylmethacrylate Blends**M. Miyake<sup>19</sup>, T. Hashimoto<sup>19</sup>, and C. C. Han<sup>4</sup>**Polymers at Solid Surfaces**W.-L. Wu<sup>4</sup>**Polymer Blend Consortium**G. S. Allen<sup>20</sup>, R. Domgy<sup>21</sup>, A. Yang<sup>21</sup>, R. Thudium<sup>22</sup>, and S. Pearson<sup>23</sup>**Affiliations**<sup>1</sup>Exxon Research and Engineering Co.<sup>2</sup>Princeton University<sup>3</sup>Polytechnical University of New York<sup>4</sup>Polymers Division<sup>5</sup>Nagoya University, Japan<sup>6</sup>University of Maryland<sup>7</sup>Reactor Radiation Division<sup>8</sup>Michigan Technical University<sup>9</sup>University of Alabama<sup>10</sup>University of Massachusetts<sup>11</sup>University of Tennessee<sup>12</sup>University of Connecticut<sup>13</sup>Penn State University<sup>14</sup>Kyoto Institute of Technology<sup>15</sup>Sandia National Laboratories<sup>16</sup>Kaychem Company<sup>17</sup>Aristech Chemical Corp.<sup>18</sup>University of Southern California<sup>19</sup>Kyoto University<sup>20</sup>Rohm and Haas<sup>21</sup>Armstrong World, Ind., Inc.<sup>22</sup>Goodyear Tire and Rubber Corp.<sup>23</sup>3M Company

## Exxon Research at the CNRF

Exxon Research and Engineering Company is a member of the CNRF's participating research teams in small angle neutron scattering (with NIST and University of Minnesota). We also participate in other type of research activities at CNRF, for example, neutron reflectivity, neutron radiography and neutron tomography. The short reports in this chapter reflect only part of the experiments Exxon scientists and their collaborators performed during the last year, while a more complete list of these experiments can be found at the end of this section in Research Topics.

### • Thermodynamics of Polyolefin Blends

Over the last several years we have been engaged in a study of the basic thermodynamics of mixtures of polyolefins which has relied heavily on SANS experiments at NIST. Polyolefins are saturated hydrocarbon polymers which are among the most common plastics (polyethylene, polypropylene) and elastomers (ethylene-propylene copolymer, polyisobutylene). These are often used as blends, and their phase behavior has an important effect on the properties and so utility of such materials. It is difficult to obtain data on polyolefin blend thermodynamics in the liquid state by conventional means because of the great similarity of these polymer to one another in such properties as density and refractive index. Deuterium labeling and SANS has allowed the direct determination of the interactions in these blends, and this technique has now been used on over 50 blends involving some 30 different polyolefins.

From such a wealth of data we have begun to extract some general conclusions about the thermodynamics of mixing that can apply not only to the polyolefins but to other polymers as well. A major portion of this work has involved random copolymers of ethylene and butene, covering the whole range from polyethylene to polybutene. The interactions between a

pair of copolymers, as measured by the Flory interaction parameter,  $\chi$ , depends not only on the relative difference in butene content between the copolymers but also on the absolute level of branching; the  $\chi$  values are larger the greater the butene content. This means that the commonly used mean field theory for copolymer mixing which relies on a single parameter to describe the interaction between ethylene and butene groups cannot explain these data. Rather, we have found that the simplest explanation is to assign a value to each copolymer (at each temperature) which can be used as a solubility parameter in the Hildebrand regular solution scheme to describe the  $\chi$  parameters seen.

More recently we have measured blends of these ethylene-butene copolymers with many other polyolefins, as well as mixtures of these other polymers with each other. These are all saturated hydrocarbon polymers with empirical formula  $\text{CH}_2$ , but that vary in the lengths, types, and frequency of branching. In the majority of cases, the regular solution, solubility parameter formulation can be used to explain the  $\chi$ 's and phase behavior seen. Moreover, these solubility parameters as determined from the blends by SANS are essentially equal to the square root of the internal pressures (cohesive energy densities) of the pure components from PVT measurements. (It should be emphasized that these solubility parameters cannot be derived from any sort of a group contribution scheme.) Thus, the majority of these polyolefin blends act as regular mixtures for which the interaction energies of the blends can be directly calculated from the cohesive energies of the components. The next step is to see how these cohesive energies can be related back to the detailed structures of the chains.

For a small fraction of the blends, these regular solution ideas do not work, and so we have designated these mixtures as "irregular". Several of them have a somewhat greater interaction

energy density than would be expected (that is, a destabilization of the single phase), which can be explained by equation-of-state effects. However, most of the irregular blends have a much *lower* interaction energy density than predicted by the regular solution ideas, and in fact some of them even have negative  $\chi$  values. Also, several of these irregular blends display LCST phase behavior; that is, they are single phase at room temperature and phase separate upon heating. Such behavior is not uncommon for polymer blends, but is generally attributed to the presence of strong, specific interactions between the components, such as from hydrogen bonding. In our case only dispersive, van der Waals forces can be expected between these polyolefins. As a result of this surprising discovery, we are now attempting to determine the origins of these strong interactions in the irregular blends.

#### • Aggregating Block Copolymers as Model Systems to Study Polymer Brush Dynamics

A-B block copolymers in a selective solvent — good for the B species and bad for the A species form micellar aggregates with a compact A-core and a corona (brush) of B “hairs” reaching into the solvent. Whereas polystyrene (PS)-polyisoprene (PI) in decane forms special micelles with a PS core of about 10 nm radius, polyethylene (PE)-polyethylene-propylene (PEP) forms micellar platelets, the shape of which is governed by the habitus of PE crystallites forming the core. These planar aggregates have large (several hundred nanometers) lateral extension and a core thickness in the range of 10 nm. Both systems are model systems for polymer brushes, either on a spherical surface or planar. Both small angle neutron scattering (SANS) and neutron spin-echo (NSE) experiments were performed on these systems. Especially, NSE experiments allow for the investigation of the dynamics of the brushes which reflects their viscoelastic properties. The brush dynamics is explained using a model based on an idea of deGennes describing the brush prop-

erties in terms of scaling relations for osmotic pressure and viscosity of a semidilute solution with inhomogeneous density.

#### • Polymers in Microemulsion

We have measured the dimension of the microemulsion droplets containing polymer whose radius of gyration in water without the microemulsion is several times larger than the droplet radius, in order to test the validity of a microemulsion model based on interfacial rigidity. The system of interest is a standard water in oil microemulsion and a series of water soluble polyacryamide at different molecular weights. Both SANS and dynamic light scattering have been employed to study the size and the distribution of sizes of the droplets containing polymers. The high molecular weight polymers (in the range of 1 to 2 million daltons) were polymerized in-situ using a strong Gamma source. The lower molecular weight systems were polymer standards incorporated into the droplet system by prolonged stirring of the polymer containing water phase into the oil continuous microemulsion. We have found that at the lower polymer concentrations, the microemulsion splits into a bimodal distribution, with the larger droplet radius depending on the molecular weight of the polymer. We have derived a preliminary theory based on Safran's model on the minimization of the free energy containing an extra term which takes into account of the elastic energy of the compressed polymer. Our data showed very good agreement with the theory. Figure 1 shows a plot of the measured radius of the larger droplets of the bimodal distribution normalized by the radius of the unperturbed microemulsion as a function of the normalized radius of gyration of the polymers it contained. The theoretical curves represent predictions with different bending elastic constant  $k$  in units of  $k_B T$ .

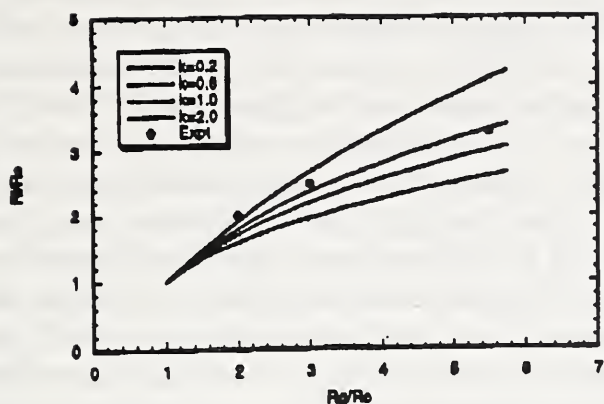


**Figure 1.** The radius of microemulsion droplets containing polyacryamide as a function of the radius of gyration of the polymers. Both radii are normalized by  $R_o$ , the radius of droplets without polymer. Solid curves are calculations with various bending elastic constant  $k$ .

#### • Binary Mixtures in Silica Gels

We have performed SANS experiments designed to probe structure in a binary mixture water ( $D_2O$ )/lutidine system confined in silica gels over the wavelength range 60 Å to 2000 Å. The fractal dimension of the gels made in  $D_2O$  as determined by fits to the SANS data is  $D_f = 2.1 \pm 0.1$ , and is consistent with previous light scattering results.

Studies of the gel-mixture samples in the one-phase region show several interesting features. Even well away from  $T_c$ , the critical temperature, the scattering shows a strong static response of the mixture to the fluctuations in silica concentration, over the entire range of length scales studied here. As the temperature approaches  $T_c$ , the response saturates on small length scales. The length scale associated with this behavior is not distinguishable from that associated with the critical fluctuations to within the present accuracy. However, the amplitude of the response is clearly not proportional to the susceptibility of the mixture, as it would be for linear response. The scattering can be fit very well to the sum of three contributions: critical

fluctuations of the mixture, preferentially adsorbed fluid, and the silica gel itself. The critical parameters found in this manner are comparable to those of the pure system. This treatment of the data is similar to that used to analyze neutron scattering data for field-cooled random-field magnets in the paramagnetic phase, however the correlated nature of the gel structure results in a more complicated expression.

Studies of the gel-mixture samples in the two-phase region reveal qualitative evidence for the existence of domains corresponding to lutidine-rich and water-rich phases. This is reminiscent of the domains observed in field-cooled antiferromagnets doped with non-magnetic impurities. For the gel-mixture system the domains coarsen noticeably with time, and their size is considerably larger than the distance over which fluctuations in silica concentration are correlated. The time scale of the coarsening process changes dramatically with concentration, which is intriguing but unexplained.

#### • A Scattering Evaluation of Diethyl-lithium Association States

A subject of controversy in living anionic polymerizations has been centered on the association state exhibited by the diethyl-lithium chain ends in hydrocarbon solvents. Both dimers and tetramers have been proposed as the aggregation state of these allylic active centers. The latter value has been favored by many as a consequence of the perceived direct connection between the kinetic order of the propagation event and the inverse of chain-end association state. A recent evaluation of these kinetic orders has shown, though, that they range from 0.11 to 0.25 with the majority of the values residing in the vicinity of 0.18 to 0.21.

We have utilized a combination of scattering techniques, including SANS and both static and dynamic light scattering, to measure these aggregation states. The protocols for sample preparation involved the usual high vacuum procedures. Hydrogenous polystyryllithium was prepared in  $d_6$ -benzene. A portion of that

solution was exposed to d6-1,3-butadiene or d8-isoprene. Termination was done using d4-methanol.

The SANS measurements were done using two different systems having base polymers of different molecular weights. It can be seen from the data that the terminated, the styryllithium (PSLi) and butadiene capped chains exhibit typical linear chain behavior. The 4-arm material, the tetramer, was made by linking the active butadiene chains with  $\text{SiCl}_4$ . Its molecular weight, via SANS, is  $3.5 \times 10^4$ . Thus, this star serves as an adequate model for the associated tetramer structure. It is clear from the data that little, if any, associated tetrameric structures exist in this system and that dimers are present. Parallel results were obtained for the other system examined by SANS where both butadiene and isoprene capped chains were examined. Furthermore, the radius of gyration values for the linear PS (27 Å) and 4-armed star (48 Å) are compatible with the predicted values. Also, the SANS profile of the 4-armed star has been reproduced by a simulation approach.

It can be noted from the SANS data that the butadiene capped chain shows a higher intensity at low  $q$  values relative to the parent polystyryllithium. This is apparently caused by the presence of associates with large aggregation states. Both static and dynamic light scattering confirm the presence of large aggregates, with aggregation numbers much larger than 2 or even 4. The static scattered intensity from the living solution is an order of magnitude larger than that obtained from the terminated solution. For the dynamic light scattering, the data from the terminated solution were consistent with a single relaxation mode, while two modes are required to fit the data from the living solution. The hydrodynamic radius, measured in the terminated solution, is  $R_h = 32$  Å, which is in reasonable agreement with the expected value for polystyrene chains in a good solvent. The  $R_h$  values obtained from the two modes in the living solutions are 1200 Å and 45 Å. The smaller of the two is in reasonable agreement with that

expected from a dimer. The larger aggregate is much larger than twice the fully stretched length of the polymer chains. This rules out compact micellar star-shaped aggregates with Li at the core. A possible conjecture for the structure of these aggregates are cylindrical structures with a "spine" of Li. Such a structure has been found for polyisoprene capped with a zwitterion. Since the scattering power of the large aggregates must be much larger than that of the dimers (due to its apparent size), we conclude that relatively few chains are associated in the large aggregates because of our ability to pick up the diffusion of the dimers at all angles. To quantify these remarks, we need an exact model for the aggregate, and this requires further experimentation.

#### • Worm-like Micelles Under Shear

Worm-like surfactant micelles are initially spherical at low surfactant concentrations, just above the critical micellar concentration (CMC). They transform and undergo uniaxial growth to become cylindrical aggregates as the concentration is increased to become cylindrical aggregates with a length that can be extremely long compared to their lateral dimensions. The bonding of these aggregates is not permanent, and they break and reform continuously; hence, they are sometimes called 'living polymers'. Since, however, the interaction between the 'segments' of the micelle is quite different from that of a polymer chain, it is unclear what aspects of polymer conformation apply to them. In addition, because of their 'living' nature, the structure and dynamics can change dramatically with concentration, or by the influence of a shear flow.

Here we report scattering studies of an ionic type of worm-like micelles, in dilute and semi-dilute solutions, with and without shear. The micellar solution, vinyl alkyl quaternary ammonium bromide, was made up by mixing a surfactant solution with an equimolar amount of sodium salicylate in  $\text{D}_2\text{O}$ . The CMC was determined by surface tension measurements to be 0.002 wt%, and viscosity data suggest an over-



lap concentration  $c^*$  near 0.15 wt%. For the dilute solution, the concentration was 0.1 wt%; for the semi-dilute solution it was 1.0 wt%.

If the solution is dilute and shear is absent, the scattering patterns are consistent with rod-like molecules with a rather large length. We combined both SANS and static light scattering results, and determined a radius of 23 Å and a length of 3400 Å for the average micelle size. Under an applied shear flow, the dilute solution scatters anisotropically, indicating shear-induced alignment, as expected, and the length of the micelles grows to at least twice of its value at rest while the lateral dimension remains the same. However, the anisotropy is found to occur only when the shear rate is above a 'threshold' value of about 40 Hz. Furthermore, at that threshold shear rate, there exists an initial time period during which the scattering pattern is still isotropic. By contrast, no such threshold shear is observed for the semi-dilute solutions.

#### • Asphaltene Aggregates in Solution

Asphaltenes are one of the basic constituents of bitumen from which "heavy" crude oil is extracted from reservoirs such as tar sands in Alberta, Canada. One of the fundamental research issues in heavy oil recovery programs is what gives bitumen its extremely high viscosity. In order to understand this, we have undertaken a program to study the structure and association of the asphaltene components in various solvents, *e.g.*, toluene or 1-methyl-naphthalene by SANS, and to correlate the results with rheological measurements of the same solutions under same conditions. Another component of bitumen is the so-called "maltene" or resins, which are thought to associate with the asphaltenes in the bitumen and to give rise to high viscosity. Our SANS results can be summarized as follows: In dilute solutions (1% - 5%) at room temperature and in both solvents, the asphaltenes are aggregated into large non-monodisperse clusters, but at temperatures  $>70$  °C, they disaggregate and form a solution of fairly monodisperse particles of radius of gyration 42 Å. There

appears to be, in 1-methyl-naphthalene, no evidence of any association of the asphaltene and maltenes (the latter being determined to have a radius of gyration of about 17 Å). SANS data of asphaltenes in solution up to concentration of  $\sim 30\%$  have been recorded and are currently being analyzed to model the interactions between the basic colloidal asphaltene particles.

#### • Colloidal Dispersions in Non-aqueous Solvent

Dispersions of inorganic colloids in non-aqueous media are widely used in industrial application, for example, as additives to lubricating oils for neutralizing acids formed during the combustion in engines. The one being studied here consists of a Magnesium Carbonate core surrounded by a surfactant shell, dispersed in an organic solvent (oil). There is also considerable interest in the science communities, in the structure of these core-shell type of particles, the origin of their colloid stability and their behavior in concentrated dispersions. SANS is a particularly powerful technique because we can change the solvent contrast to easily match the scattering length density of either core, shell, or neither, and compare the results of each experiment.

We dilute the sample using octane/ deuterated octane to 1wt% so interactions between colloidal particles are negligible. According to the chemical components of the colloid/surfactant and the oil (See Table 1), we designed three different matching conditions for the solvent: O3S: 11.1% d-decane (rest is the original oil and decane), matches the surfactant. In this case, the data can be fitted with a spherical model with Shultz distribution of the radius:  $R=18.1$  Å ( $\Delta R/R=0.49$ ).

O2S: 55.5% d-decane, matches the core particles. In this case, we fitted the data with a shell structure with an inner radius of 18.0 Å ( $\Delta R/R=0.41$ ), in excellent agreement with the above O3S matching, and an outer radius of 59.2 Å.

O1S: does not match any part of the colloidal structure, but contains the maximum amount of

Table 1. Mass and Neutron Scattering Length Densities for the Colloid and Solvents.

	Formula	Density /g cm <sup>-3</sup>	$\rho \times 10^{-10}$ (n.s.l.d.) /cm <sup>-2</sup>
Colloid core	3MgCO <sub>3</sub> Mg(OH) <sub>2</sub> 3H <sub>2</sub> O	2.16	3.34
Surfactant	C <sub>30</sub> H <sub>53</sub> SO <sub>3</sub> <sup>-1</sup>	1.0†	0.25
Octane	C <sub>8</sub> H <sub>18</sub>	0.704	-0.524
Octane-d18	C <sub>8</sub> D <sub>18</sub>	0.815	6.44

†Estimate

d-octane and therefore least amount of hydrogen content. It also provides the best contrast to both the core and shell parts of the colloidal structure. The data are being fitted with a form containing both core and shell structure.

#### • Neutron Waveguides

Total reflection of neutrons from smooth interfaces has a wide range of applications in neutron optics. Neutron guide tubes have been successfully constructed for transporting neutrons. Hollow glass capillaries of micrometer diameters have been used to form a neutron focusing lens. In both cases, the propagation of neutrons is described by geometrical optics. If the transverse size of the guiding device is sufficiently small, the wave nature of neutrons becomes essential, such as in a planar waveguide composed of a thin film sandwiched between media of lower refractive indices. Similar to guides for visible light and x-rays, a neutron guide can sustain only a discrete set of guided modes, each corresponding to two coherent neutron waves with well-defined momenta that are equal in amplitude but opposite in sign. Since the physics of a thin-film waveguide is equivalent to that of a one-dimensional potential well, coupling of neutrons can be achieved from a thin boundary layers, corresponding to the resonant tunneling of particles through a thin barrier. If the coupling efficiency is high, the flux of neutron inside the waveguide can be substantially increased as has been achieved in both the op-

tical and x-ray waveguides. We have fabricated and tested a TiO<sub>2</sub>/Ti/Si thin-film guide structure composed of a coupling, guiding, and decoupling sections. The guiding layer was a 1200 Å thick Ti film evaporated on a Si wafer. A roughly 150 Å thick TiO<sub>2</sub> film was then formed electro-chemically from this Ti film. By masking off the coupling and decoupling regions, a 6000 Å thick SiO<sub>2</sub> layer was evaporated onto the center of the TiO<sub>2</sub> film, completing the main body of the guide. In our measurements, a monochromatic neutron beam was used. The guided neutron waves were directly observed by systematically varying the incident angle of the incident beam (on the coupling side) and then detecting the neutrons exiting the decoupling region. The resonant nature of the coupling was also confirmed since only for a small limited range of incident angles, did we observe the guided neutron waves. Detailed analysis of the measured intensity indicated that the neutron flux inside the waveguide was enhanced by a factor of two. The enhancement factor can be readily increased by optimizing the parameters of the waveguide structure and further measurements are in progress.

#### • Neutron Microtomography

The 3-d study of fluid transport in porous media with about 20 micron spatial resolution is the goal of this exploratory effort. Last May, prior to the cold source upgrade, our CCD based 2-d position sensitive detector demonstrated the

feasibility of 60 micron tomographic scanning at NG7-30 M SANS station in a maximum flux configuration. We also demonstrated the utility of the instrument for imaging changes in hydrocarbon and water saturations in a sintered bead pack during drainage. The initial estimate that the statistical accuracy of the detector is neutron flux limited was confirmed by applying a cascade model and calculating the detective quantum efficiency (DQE) for a variety of detector configurations. Spatial resolution was evaluated by measuring the modulation transfer function (MTF) of the detector from an image of a Cadmium edge. The MTF and DQE were measured for NE-426(ZnS,LiF), GS-20 (Li glass) and LiI(Eu) scintillator materials. In all cases the maximum resolution of the detector is scintillator limited. The Li glass gave the best result when both MTF and DQE are considered. Although the light output of this material is low compared to NE-426 and LiI(Eu) it is a better match to the CCD full well depth and yields an acceptable DQE of 57% . This scintillator has the potential for better than 400:1 signal to noise ratio in a single full well CCD image given adequate integration time. MTF measurements indicate a spatial resolution of 8 lp/mm at 10% modulation 13 lp/mm at 1% . We estimate the maximum useful spatial resolution of this material to be 75 microns which is close to our previous qualitative estimate. MTF results for NE-426 and LiI(Eu) show that the spatial resolution of these materials is unacceptable for our purposes. Further improvements in resolution will require a scintillator material with shorter range for both internally scattered neutrons and generated charged particles. Given these results, we expect that the cold neutron facility upgrade will permit significant improvement in data acquisition speed and signal to noise for both tomographic imaging and time dependent radiography.

## Research Topics

### Diblock Copolymer Aggregates in Solution

J. S. Huang<sup>3</sup>, L. J. Fetters<sup>3</sup>, D. Perahia<sup>3</sup>, M. Y.

Lin<sup>3</sup>, A. P. Gast<sup>11</sup>, G. McConnell<sup>11</sup>, E. Lin<sup>11</sup>, D. Richter<sup>4</sup>, L. Willner<sup>4</sup>, and D. Schneiders<sup>4</sup>.

### Graft Copolymers

D. G. Peiffer<sup>3</sup>, W. Dozier<sup>1</sup>, M. Y. Lin<sup>3</sup>, and M. Rabeony<sup>3</sup>

### Polymers in Microemulsion

J. S. Huang<sup>3</sup>, D. Perahia<sup>3</sup>, M. Y. Lin<sup>3</sup>, R. G. Wilk<sup>2</sup>, R. E. Stefandl<sup>2</sup>, and C. Gryte<sup>2</sup>

### Emulsion Interfacial Structure

A. Bailey<sup>3</sup>, M. Y. Lin<sup>3</sup>, D. A. Weitz<sup>3</sup>, and S. K. Sinha<sup>3</sup>

### Worm-like Micelles Under Shear

M. Y. Lin<sup>3</sup>, M. W. Kim<sup>3</sup>, S. K. Sinha<sup>3</sup>, D. G. Peiffer<sup>3</sup>, H.J.M. Hanley<sup>6</sup>, and G. C. Straty<sup>6</sup>

### Asphaltene Solutions

M. Y. Lin<sup>3</sup>, S. K. Sinha<sup>3</sup>, and E. Herbolzheimer<sup>3</sup>

### Binary Fluids in Silica Gel

B. J. Frisken<sup>10</sup>, M. Y. Lin<sup>3</sup>, D. S. Cannell<sup>13</sup>, and S. K. Sinha<sup>3</sup>

### Thermodynamics of Polyolefin Blends

D. J. Lohse<sup>3</sup>, W. W. Graessley<sup>8</sup>, R. Krishnamoorti<sup>8</sup> and G. C. Reichart<sup>8</sup>

### Proprietary Polymer Research

A. Hanyu<sup>3</sup>, and F. Stehling<sup>3</sup>

### Neutron Tomography/Radiography

J. H. Dunsmuir<sup>3</sup>, M. Y. Lin<sup>3</sup>, and S. K. Sinha<sup>3</sup>

### Polymer/Surfactant Layers Near a Liquid Surface

S. K. Sinha<sup>3</sup>, K. Chari<sup>5</sup>, S. K. Satija<sup>9</sup>, M. Y. Lin<sup>3</sup>, P. D. Gallagher<sup>9</sup>, and A. Karim<sup>9</sup>

### Neutron Reflectivity From Polymer on Surfaces

D. Perahia<sup>3</sup>, L. J. Fetters<sup>3</sup>, S. K. Sinha<sup>3</sup>, S. K. Satija<sup>9</sup>, and D. G. Wiesler<sup>9</sup>

### Neutron Waveguides

Y.-P. Feng<sup>3</sup>, S. K. Sinha<sup>3</sup>, H. Zhang<sup>12</sup>, C. F. Majkrzak<sup>9</sup>, and H. W. Deckman<sup>3</sup>

### Colloids in Non-aqueous Solvent

M. Y. Lin<sup>3</sup>, S. K. Sinha<sup>3</sup>, D. A. Weitz<sup>3</sup>, and J. P. Stokes<sup>3</sup>

### A Study of Dienyllithium Association States

L. J. Fetters<sup>3</sup>, N. P. Balsara<sup>7</sup>, J. S. Huang<sup>3</sup>, and M. Y. Lin<sup>3</sup>

### Fenofluid in Non-aqueous Solvent

W. Luo<sup>14</sup>, M. Y. Lin<sup>3</sup>, and J. W. Lynn<sup>9</sup>

**Affiliations**

- <sup>1</sup>Argonne National Laboratory
- <sup>2</sup>Columbia University
- <sup>3</sup>Exxon Research & Engineering Co.  
and other Exxon affiliates
- <sup>4</sup>KFA, Germany
- <sup>5</sup>Kodak
- <sup>6</sup>Thermophysics Division, NIST Boulder
- <sup>7</sup>Polytechnic University
- <sup>8</sup>Princeton University
- <sup>9</sup>Reactor Radiation Division
- <sup>10</sup>Simon Fraser University
- <sup>11</sup>Stanford University
- <sup>12</sup>University of Maryland
- <sup>13</sup>University of California, Santa Barbara
- <sup>14</sup>University of Central Florida

# University of Minnesota Programs

The University of Minnesota, through its Center for Interfacial Engineering, is a member of the CNRF's participating research teams (PRT) in small angle neutron scattering (SANS) (with NIST and the Exxon Research and Engineering Co.) and reflectometry (with NIST and IBM).

## SANS

### • Block Copolymer Phase Behavior

This program includes several research projects aimed at establishing the molecular factors responsible for the complex phase behavior exhibited by block copolymers. Numerous materials have been prepared by anionic polymerization, followed in certain instances by catalytic hydrogenation. Rheological testing is employed to establish phase transition temperatures. Small angle neutron scattering provides the principal means of determining the ordered state symmetry, and is also used to characterize fluctuation effects in the disordered state. Nearly 100 model block copolymers have been synthesized and examined in this way during the last several years. In the past year this effort has resulted in the identification of a new bicontinuous cubic phase (Ia3d space group symmetry), in PEP-PEE, PE-PEE, PI-PS, and PS-PVP diblock copolymers. In addition, an empirical correlation has been established between the renormalized degree of polymerization  $\bar{N} = a^6 N / v^2$  ( $a$  and  $v$  are the statistical segment length and volume, respectively, and  $N$  is the degree of polymerization) and phase complexity. As  $\bar{N} \rightarrow \infty$ , we find that the bicontinuous phase disappears while decreasing  $\bar{N}$  increases the temperature range over which it occurs. The associated composition dependence of this phase behavior has been linked to that displayed by low molecular weight solvated surfactants and lipids. Along with these experiments on single component block copolymer melts we have been inves-

tigating binary mixtures of diblock copolymers. This aspect of our work has shown that block polydispersity does not appreciably change the temperature window over which the complex bicontinuous and perforated phases are observed. However, the composition range where these phases are observed is quite sensitive to the relative component molecular weights and compositions. SANS experiments with PE-PEE, PS-P2VP and PE-PEP have confirmed that the detailed block copolymer phase diagram can be efficiently mapped using binary mixtures.

### • Influence of Shear on Block Copolymers

Block copolymers melt microstructures are susceptible to orientation and transformation during deformation. We have developed a dynamic shearing device that is ideally suited for probing these effects while conducting SANS measurements. One of these devices is now located at the PRT SANS instrument for use with high molecular weight polymers or other viscoelastic materials. During the past year we have examined the influence of shear on a variety of ordered and disordered block copolymer melts. Extensive measurement on materials containing a lamellar morphology have revealed shearing conditions that lead to two distinct orientations: perpendicular (lamellar normals perpendicular to both the shear direction and shear gradient) and parallel (lamellar normals coincident with the shear gradient). When the two blocks in a diblock have similar frictional properties (*e.g.*, entanglement molecular weights) a perpendicular arrangement is always obtained near the order-disorder transition above a critical shear rate. Asymmetric frictional properties tend to favor the parallel orientation. The response of hexagonally packed cylinders is also dependent on the ratio of frictional properties. However, with this morphology the composition also plays a significant role. We have found

that a more entangled matrix block favors full orientation (*i.e.*, cylinders aligned with respect to shear direction and shear plane). Certain morphologies also display a tendency to transform when deformed. For example, the bicontinuous  $I\bar{a}3d$  phase can be induced to change into cylinders under certain conditions. Surprisingly below a critical shear rate this interconnected morphology appears to survive large strains (100-500%). Another example of a shear induced phase transition occurs with the bcc sphere state, which can be driven into hexagonally packed cylinders.

- **Epitaxial Relationships in Block Copolymer Order-Order Phase Transitions**

During the past year we discovered a remarkable feature associated with the hexagonal-to- $I\bar{a}3d$  bicontinuous phase transition in block copolymer melts. Although these microstructures are composed of nearly random walk chains, the phase transition occurs in a highly cooperative fashion that converts the cylinder axis into a (111) direction of the cubic unit cell. This behavior is essentially identical to what is known to occur in certain lyotropic liquid crystalline systems. However, owing to the mechanical integrity of these polymer specimens the nature of the epitaxy, and its effects on phase transition kinetics, can be a study in great detail. We have exploited the phase behavior documented in a number of our block copolymers along with the dynamic shearing device in conducting these experiments. Several phase transitions, including hex cylinders-to-bcc spheres, hexagonally perforated layers-to-hex cylinders, and hex cylinders-to- $I\bar{a}3d$  bicontinuous have been investigated.

- **Binary Polymer Mixture Phase Behavior**

One of the most effective methods of characterizing the phase diagram of a polymer-polymer mixture is by neutron scattering. The segment-segment interaction parameter ( $\chi$ ) can be determined in the one-phase region. Extrapolation

of the inverse zero-angle intensity provides an estimate of the stability temperature while the equilibrium (binodal) point can be associated with a discontinuous change in the scattering profile. Fluctuation effects can also be characterized near the critical point. We have examined these features in two classes of polymers: model polyolefin mixtures and isotopic mixtures. Perdeuterated poly(ethylene) (PE), obtained by deuterating perdeuterated poly(1,4 butadiene), was mixed with poly(ethylenepropylene) (PEP). These components were carefully synthesized so that the critical temperature for demixing was at an experimentally tractable 132 °C. SANS measurements were performed on several mixture compositions, from which  $\chi(T)$  was determined. This has been compared with the corresponding block copolymer result. The isotopic system dPEP and hPEP was evaluated in the one-phase region at several compositions, revealing a nearly composition independent  $\chi$  parameter. Because this system is slow to nucleate phase separation in the metastable region, the mixtures could be cooled right down to the stability limit thereby providing an excellent characterization of the phase diagram. Both the PE/PEP and dPEP/hPEP mixtures are being used in collaborative investigations of phase separation dynamics (nucleation and growth and spinodal decomposition).

## Reflectometry

- **Confined Block Copolymers**

Morphology and surface wetting behavior of block copolymer thin films have been investigated in confinement. Model diblock copolymer of nearly synmetric poly(ethylene-propylene)-poly(ethylethylene) (PEP-PEE) was studied in confinement between hard walls of poly(styrene), and poly(styrene) and silicon. A homopolymer of a higher glass transition temperature than the copolymer was found to be effective in suppressing the formation of islands and holes that would otherwise form at the copolymer/air interface. From neutron reflectometry

tivity measurements, we infer that the domain period of the diblock copolymer in confinement is a function of the film thickness. The chains adopt an expanded or a contracted conformation (wrt unconfined situation) such that the free energy is minimized. A lamellar morphology parallel to the confining surfaces is observed at all degrees of frustration. In addition, model fitting of reflectivity profiles reveal that the PEE block always preferentially segregates to the confining surfaces. The strong wetting tendency of PEE block is reasoned to be due to the conformational asymmetry and is well documented in literature. We hypothesize an effective interfacial energy for each block with the confining surfaces that includes non-local entropic contributions, and interpret the results in confinement (consistent with the recent theoretical and numerical calculations) due to the reduction in the effective interfacial energy of the PEE block. These results also provide a new approach towards probing the influence of chain stretching on the stability of block copolymer structures.

- **Selective Solvent Effects on Block Copolymer Films**

Ordered films of symmetric,  $f=0.5$ , poly(styrene -*b*-2-vinyl pyridine) (PS-PVP) block copolymer on silicon substrates have been exposed to methanol and examined using neutron reflectivity. In the dry state, these films form alternating lamellar PS and PVP domains aligned parallel to the substrate surface. Methanol is a preferential solvent for PVP; consequently, it tends to segregate more to the PVP domains in the film. When the dry film is exposed to methanol, considerable swelling of the film occurs and the reflectivity curve for the swollen film shows dramatic differences from that for the dry film. Above about 40 K molecular weight of the diblock, the swelling (at ambient temperatures) is reversible in that the initial dry reflectivity profile of the film is recovered after the solvent is allowed to evaporate from the film. The films achieve equilibrium swelling relatively rapidly (on the

time scale of several minutes for a film that is about 1000 Å thick), where equilibrium is defined in the sense that no further noticeable changes occur in the swollen film reflectivity profile over a period of about 5 hrs. Furthermore, after initial exposure to solvent and subsequent drying, the films shrink slightly (a few percent) compared to the initial dry thickness. This decrease in film thickness has been attributed to a solvent-induced annealing of the film when the presence of solvent releases some of the degrees of freedom associated with chain motion. Preliminary results indicate that the local degree of swelling of the film increases with the distance from the substrate, at least for the first several microstructure periods. The overall structure remains approximately lamellar.

- **Block Copolymer Thin Films**

The bulk phase behavior of block copolymers can be modified when these materials are confined within thin films. Certain morphologies do not easily conform to the flat symmetry of a hard wall, or the boundary conditions imposed by selective wetting of one block component at the film surfaces. We have been exploring how these factors influence phase behavior using block copolymers that have been well-characterized in the bulk state. Of particular interest are the newly discovered HPL (hexagonally perforated layers) and bicontinuous  $I_{\bar{a}3d}$  morphologies. To date we have shown that a reduction in film thickness reduces the number of phases observed while increasing the order-disorder transition temperature. Because specular reflectivity does not probe in-plane order, the neutron reflection experiments must be complemented with other, more direct techniques, such as electron microscopy. Measurements have been conducted on a wide variety of diblock copolymers and block copolymer mixtures. Selective deuteration has allowed us to identify the chain packing characteristics in mixtures that contain a bimodal distribution of block lengths.

**Research Topics****Phase Behavior of PE-PEE Diblock Copolymer Mixtures**

J. Zhao<sup>1</sup>, D. Majumdar<sup>1</sup>, F. S. Bates<sup>1</sup>, K. Almdal<sup>2</sup>, K. Mortensen<sup>2</sup>

**Phase Diagram of PE-PEP Diblock Copolymers**

J. H. Rosedale<sup>1,6</sup>, J. Zhao<sup>2</sup>, A. Khandpur<sup>1</sup>, F. S. Bates<sup>1</sup>, K. Almdal<sup>2</sup>, and K. Mortensen<sup>2</sup>

**Order and Disorder in PS-PVP Block Copolymers and Block Copolymer Mixtures**

M. F. Schulz<sup>1</sup>, A. Khandpur<sup>1</sup>, F. S. Bates<sup>2</sup>, K. Almdal<sup>2</sup>, K. Mortensen<sup>2</sup>

**Influence of Shear on the Lamellar Phase in Diblock Copolymers**

T. Tepe<sup>1</sup>, M. Tirrell<sup>1</sup>, and F. S. Bates<sup>2</sup>

**Shear Induced Order-Order Transitions in Block Copolymer Melts**

K. Koppi<sup>1,7</sup>, T. Tepe<sup>1</sup>, F. S. Bates<sup>1</sup>, and M. Tirrell<sup>1</sup>

**Fluctuation Effects in Asymmetric Diblock Copolymers**

K. Almdal<sup>2</sup>, K. Mortensen<sup>2</sup>, F. S. Bates<sup>1</sup>, and T. Tepe<sup>1</sup>

**Epitaxial Order-Order Phase Transitions in Block Copolymers**

M. F. Schulz<sup>1</sup>, J. Zhao<sup>1</sup>, F. S. Bates<sup>1</sup>, K. Almdal<sup>2</sup>, K. Mortensen<sup>2</sup>

**Spinodal Decomposition and Nucleation and Growth in Model Polymer Mixtures**

P. Wiltzius<sup>3</sup>, W. Maurer<sup>1</sup>, F. S. Bates<sup>1</sup>, and T. P. Lodge<sup>1</sup>,

**Polymer-Polymer Thermodynamics: Binary Mixtures versus Block Copolymer**

N. Singh<sup>1,8</sup>, W. Maurer<sup>1</sup>, F. S. Bates<sup>1</sup>, T. P. Lodge<sup>1</sup>

**Entropy Driven Surface Segregation in Block Copolymers**

N. Singh<sup>1,8</sup>, A. Karim<sup>4</sup>, M. Sikka<sup>1,9</sup>, N. Konneripalli<sup>1</sup>, S. K. Satija<sup>5</sup>, and C. F. Majkrzak<sup>5</sup>

**Confined Block Copolymers**

N. Konneripalli<sup>1</sup>, N. Singh<sup>1,8</sup>, F. S. Bates<sup>1</sup>, and S. K. Satija<sup>5</sup>

**Selective Solvation in Lamellar Block Copolymer Thin Films**

R. Levicki<sup>1</sup>, N. Konneripalli<sup>1</sup>, M. Tirrell<sup>1</sup>, F. S. Bates<sup>1</sup>, and S. K. Satija<sup>5</sup>

**Block Copolymer Thin Film Phase Behavior**

N. Singh<sup>1,8</sup>, M. Sikka<sup>1,9</sup>, F. S. Bates<sup>1</sup>, S. K. Satija<sup>5</sup>, C. F. Majkrzak<sup>5</sup>, and A. Karim<sup>4</sup>

**Affiliations**

<sup>1</sup> University of Minnesota

<sup>2</sup> Risø National Laboratory, Denmark

<sup>3</sup> AT&T Bell Laboratories

<sup>4</sup> Polymers Division NIST

<sup>5</sup> Reactor Division NIST

<sup>6</sup> current address: Rohm and Haas

<sup>7</sup> current address: Dow Chemical

<sup>8</sup> current address: General Electric

<sup>9</sup> current address: U. Pennsylvania



# CNRF Instrumentation Development

FY94 saw very significant progress made in a broad spectrum of CNRF instrumentation. This includes the near-completion of the neutron interferometer, continued installation and testing of parts of the disk chopper TOF spectrometer, completion of parts of the back-scattering spectrometer, progress with the spin-echo spectrometer, and improvements in the two Center for High Resolution Neutron Scattering (CHRNS) instruments: the CHRNS 30-m SANS and the SPINS spectrometers. Significant achievements in the development of neutron capillary guides have continued along with important developments in a number of other areas.

Instrumentation related to Fundamental Neutron Physics and to prompt-gamma activation analysis and cold neutron depth profiling is described elsewhere in this report.

## New Instruments

### • Disk Chopper Time-of-Flight Spectrometer (DCS)

This instrument, shown schematically in figure 1, will be used for a variety of experiments, such as investigating quasielastic scattering and low energy inelastic scattering spectra in materials that exhibit diffusional and vibrational phenomena [1]. It will use a set of chopper disks, and a partitioned guide, to produce pulses of neutrons of a single wavelength at the sample position. The first and last chopper pairs determine the incident wavelength and the three intermediate choppers remove contaminant wavelengths and unwanted pulses. There are three slots in each of the disks belonging to the first and last counter-rotating chopper pairs. By appropriately phasing these disks the resolution of the instrument can be changed, without having to change the incident wavelength or the speed of the choppers. The sample chamber will accept a variety of cryostats or furnaces, providing the capability to locate the sample at the correct

position and in the desired orientation. A total of 840 detectors will be placed 4 meters from the sample, in three parallel banks. Their total active area will be almost 11 m<sup>2</sup>. The anticipated energy resolution of the instrument in its high resolution (low resolution) mode of operation, with the choppers spinning at 20,000 rpm, is  $\approx 250$  ( $\approx 1250$ )  $\mu\text{eV}$  at 2 Å and  $\approx 6$  ( $\approx 25$ )  $\mu\text{eV}$  at 8 Å incident wavelength [1].

During the past year we have continued to test the choppers extensively. On the whole they have performed remarkably well, but on several occasions we have had problems with the magnetic bearing control modules and with the VME-based chopper control modules. We are developing methods of monitoring chopper performance that are largely independent of the chopper control electronics. For example we routinely use a commercial PC-based multichannel scaler (with 16,384 channels and a minimum dwell time of 5 ns) to measure the long-term phase stability of the choppers.

The guide, which incorporates an optical filter to remove high energy radiation [2], was delivered in late 1994 and will be installed in 1995. There has been considerable progress in the design of the sample chamber (Fig. 2).

A major effort has been devoted to developing the data acquisition and chopper control software that runs on the VAX 4000. Recognizing the need to prevent the possibility of conflicts in user actions, and the desire to implement code that is virtually platform-independent, all hardware control is concentrated in a single interface program which has unique access to hardware peripherals. This program talks to user-friendly programs that determine all aspects of instrument operation. Software for the Fermi chopper spectrometer and for the backscattering spectrometer will be developed in similar fashion.

As of mid-December 1994 we had received 669 detectors and 662 amplifiers from the manu-

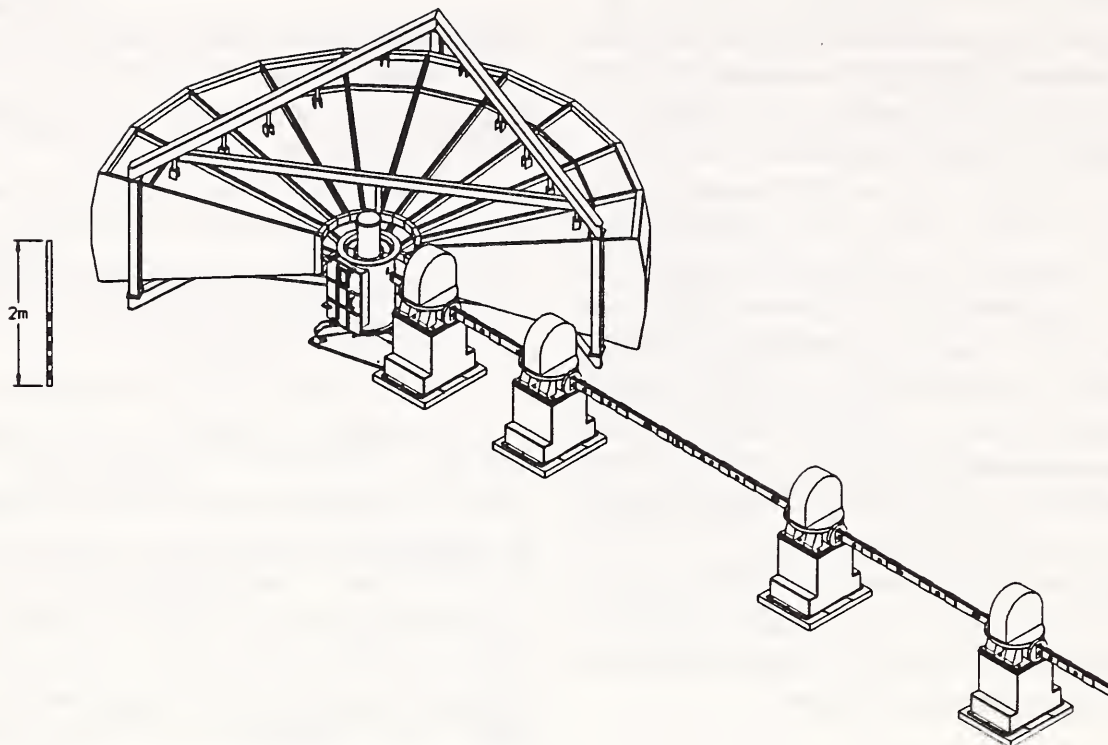


**Figure 1.** 3-d view of the disk chopper spectrometer (DCS) showing the neutron guide, four chopper housings, the sample chamber, and the flight chamber.

facturer. All detectors and amplifiers are tested for compliance with contract specifications and defective units are returned for repair or replacement. At an early stage these tests revealed an oversight in the method of fabrication of the amplifier cases, and modified procedures were immediately adopted by the manufacturer. Two detectors have so far been returned.

In its final form the data acquisition system will comprise a PC-controlled digital input/output board that will interrogate and store data from approximately 27 data input boards, each of which treats the signals from 32 detector amplifiers. A data input board has been designed, with extensive simulation tests to ensure proper signal timing, and a prototype board has been constructed and is being tested. The present design uses standard TTL components

but a version using field-programmable gate arrays is also planned.

- “SPINS” Spectrometer

The Spin Polarized Inelastic Neutron Scattering (SPINS) spectrometer is an innovative hybrid of that mainstay of inelastic neutron scattering, the triple-axis spectrometer, designed to provide high energy resolution, full polarization analysis, and higher intensity than conventional triple-axis spectrometers. The basic spectrometer, initially configured as a triple-axis instrument with a vertically focusing pyrolytic graphite monochromator and analyzer, was installed on its neutron guide in the spring of 1993. A higher than desirable general background level and problems with the drive mechanism for the instrument’s monochromator shield, how-

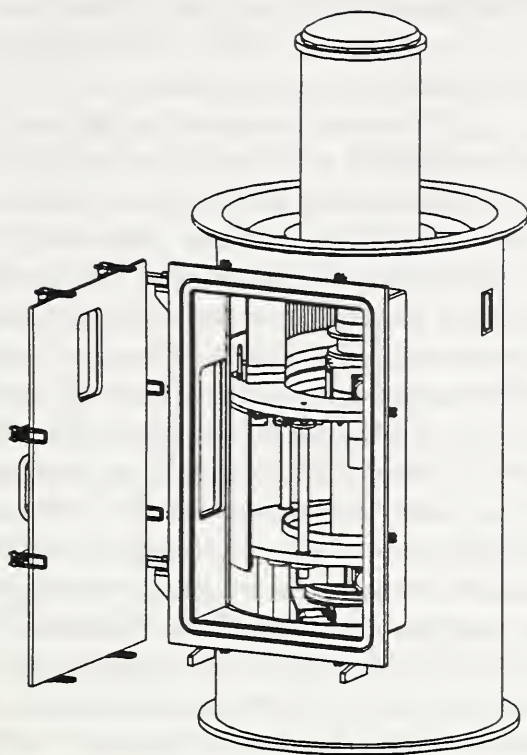


**Figure 2.** The proposed design for the sample chamber of the Disk Chopper Spectrometer, showing the oscillating radial collimator (ORC), and a cryostat bolted to the sample table. The inside diameter of the chamber is  $\approx 73$  cm and its height is  $\approx 138$  cm. The ORC can be lowered  $\approx 30$  cm in order to accommodate ancillary equipment, such as a neutron camera, at beam height. The large door simplifies access to the sample position and to sample and collimator positioning equipment.

ever, necessitated modifications to the instrument that were undertaken in the fall of 1993 and successfully completed by the early spring of 1994. As a result, the background radiation at the instrument has been reduced to an acceptable level and the instrument now operates smoothly and reliably under computer control over its entire design range of incident neutron energies from 2 to 17 meV and delivers the expected flux at the sample position.

Development of the advanced instrumenta-

tion that will give the SPINS instrument its unique capabilities has proceeded in parallel with the construction of the basic spectrometer and is now substantially complete. The design goal of 95% polarizing efficiency (with 70% transmission of neutrons of the selected spin state) has been met in extensive in-beam tests of a full scale prototype transmission polarizer, consisting of a stack of 100 mechanically curved thin plates of silicon, each with an iron-silicon supermirror coating. The mechanical construction of the Drabkin-type, energy-dependent spin flipper, that in conjunction with the polarizers partially decouples the energy and momentum resolution of the spectrometer, has also been completed and work on the electronics to provide easy programmable control of the currents in the device is well underway. In addition, through a collaboration with Collin Broholm's group in the Physics Department of Johns Hopkins University, a focusing multi-crystal energy analyzer, designed to be interchangeable with the Drabkin flipper, has been constructed for high energy resolution measurements with unpolarized neutrons. A 12.5 cm thick polyethylene shield, lined with boron impregnated rubber, to house the energy analyzer and detector bank has also been constructed. This shield has been designed to accommodate either the Drabkin flipper or the horizontally focusing crystal analyzer. The SPINS spectrometer is expected to become fully operational soon after the CNRF resumes operation in early 1995.

The SPINS spectrometer, along with the 30 m SANS instrument on guide NG-3, are partially supported by the NSF through its Center for High Resolution Neutron Scattering at the CNRF.

#### • SANS Instrument Improvements

During the shutdown to install the new liquid hydrogen cold source, a number of improvements were made to the NG-7 30-meter SANS instrument. Chief among these were modifications to the sample chamber and post-sample flight path to allow the instrument's area detec-

tor to be positioned as close as 1.2 m from the sample thus increasing the maximum Q limit to  $6 \text{ nm}^{-1}$ . The total Q-range now accessible extends from  $0.015$  to  $6 \text{ nm}^{-1}$  and matches that available on the newer CHRNS 30 m SANS instrument on guide NG-3. The manual system for inserting and removing sections of neutron guides to vary the beam collimation in the pre-sample flight path was also replaced by the same type of computer-controlled, stepper-motor-driven system that has proven reliable in nearly two years of operation at the NG-3 SANS. The neutron shielding at the instrument was also improved through the use of  $^6\text{LiF}$ -based materials in an effort to eliminate potential sources of parasitic scattering and to reduce ambient capture gamma radiation. These improvements were made possible, in part, through support from Texaco Inc. which has recently joined NIST, the Exxon Research and Engineering Co., and the University of Minnesota as members of the Participating Research Team that uses and supports the operation of the NG-7 SANS instrument.

- **Neutron-Backscattering Spectrometer**

The CNRF High-Flux Backscattering Spectrometer (HFBS) is currently under development and will occupy the end position on guide NG-2. The purpose of the instrument is to provide the neutron user community with an energy resolution of less than  $1 \mu\text{eV}$  with as high a flux as possible using state-of-the-art neutron optics. To this end, the instrument design incorporates several flux-enhancing elements including a 4 m long converging guide, a spherically-focussing monochromator and analyzer, and a novel device known as a phase space transform (PST) chopper. The HFBS will operate in a fixed-final-energy mode of  $E_f=2.08 \text{ meV}$ . This energy is set by the d-spacing between the (111) lattice planes of silicon which covers the analyzer. The incident neutron energy will be varied using a Si(111) monochromator attached to a Doppler drive which, when running at full speed, will permit users access to a maximum

neutron energy transfer of  $\Delta E=\pm 50 \mu\text{eV}$ . The target energy resolution for the HFBS is  $\approx 0.75 \mu\text{eV}$  FWHM with a Q-range of  $0.15$  to  $1.8 \text{ \AA}^{-1}$ .

It is hoped that the HFBS, at the expense of some degradation in energy resolution, will provide a significant increase in flux beyond that presently available at other backscattering facilities. The converging guide will focus the neutron beam down from a cross-section of  $15 \text{ cm} \times 6 \text{ cm}$  to  $2.8 \text{ cm} \times 2.8 \text{ cm}$ . The guide will be coated with  $2\theta_c(\text{Ni})$  supermirrors on all interior sides, and should increase the flux incident on the PST chopper by a factor of 3, while increasing the beam divergence. The effect of the PST chopper is then to Doppler-shift neutron energies up or down depending on whether they are less than or greater than  $2.08 \text{ meV}$ , respectively. Monte Carlo simulations suggest that the phase-space transformation process should enhance the flux of  $2.08 \text{ meV}$  neutrons on the monochromator by a factor of 3 to 6 over that from a stationary deflecting crystal. This factor will depend critically on the reflectivity of the pyrolytic graphite (PG) crystals that are to be used in the construction of the chopper. Extensive measurements of the neutron reflectivity and intrinsic mosaic width of hundreds of PG crystals are being carried out at Brookhaven National Laboratory to select the best PG crystals possible.

All of the major components of the HFBS have been ordered and should arrive by June of 1995 with the exception of the analyzer. This includes the neutron velocity selector, neutron guide, converging guide, Doppler drive, monochromator, and phase space transform chopper. Delivery of the analyzer has been delayed pending the completion of a series of tests at the ILL on three analyzer sections using IN16. The results of these tests will be used to determine the Si(111) wafer thickness necessary to reach the target energy resolution with maximal neutron reflectivity. The HFBS analyzer will stand 2 m tall, span  $165^\circ$  in scattering angle, and cover an area of  $\approx 12 \text{ m}^2$  nearly 70% more than that of IN16. The analyzer is scheduled for completion by September of 1995 assuming the

ILL reactor restarts in November of 1994. If this schedule holds, then the HFBS, which will operate as a user instrument, should come on line in early 1996.

#### • Spin Echo Spectrometer

The Neutron Spin Echo (NSE) Spectrometer is being built and will be operated as a PRT facility involving NIST, KFA-Jülich, and Exxon Research and Engineering Co. The KFA-Jülich has recently finished construction of a similar spectrometer. The CNRF NSE spectrometer will be installed in the end position on guide NG-5. The instrument is optimized to maximize the neutron flux on the sample (by keeping the length as short as possible), while achieving as high a resolution as practicable. The maximum Fourier time is expected to be at least  $9.2 \times 10^{19} \lambda^3 s/m^3$  (*i.e.* 47 ns for 8 Å neutrons, which corresponds to an energy resolution of 14 neV). The design attempts to reduce the magnetic field coupling between the two main coils in order to allow access to large momentum transfers (up to  $2 \text{ \AA}^{-1}$ ).

The incident beam will be monochromatized to  $\approx 10\%$  by a mechanical velocity selector (delivered this year by Dornier), and polarized by a transmission cavity similar to that developed for SANS use. Provisions have been made for the possible use of a reflection polarizer at longer wavelengths or a Drabkin flipper for better monochromatization of the beam. An optical filter, similar to that designed for the NG-4 Disk Chopper Spectrometer, is being considered. This would allow an increase in the neutron flux on the sample of 40% as a Bi/Be filter will not be required. The planned optical filter will allow 75% flux transmission at 6 Å, and 100% above 8 Å.

The main coils, along with their power supplies are to be delivered in November 1994. The remaining electronics and carriers for the coils will be delivered in fall of 1995.

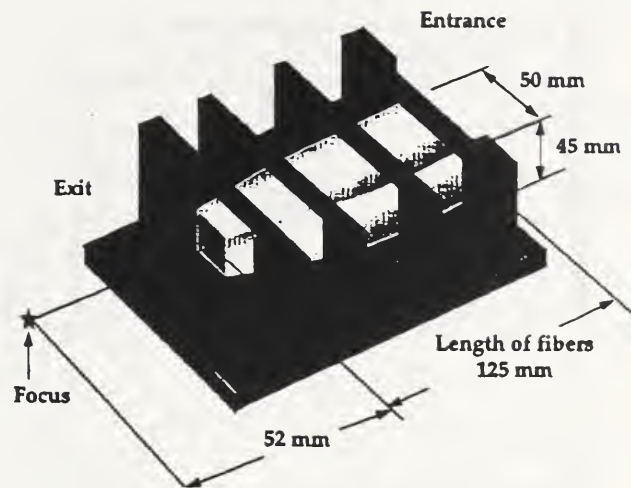


Figure 3. A sketch of the neutron lens.

#### Other Instrumentation

##### • Capillary Neutron Optics

A new neutron lens [3] has been constructed to focus neutrons from the exit of guide NG-7 (at the PGAA station). The design of the new lens is based on earlier neutron transmission and divergence measurements of individual capillary fibers and prototype lenses [4-7]. The lens is made with polycapillary fibers drawn from lead silicate glass with a critical angle of  $11.0 \text{ mrad nm}^{-1}$ . A sketch of the lens is shown in figure 3. The fractional filled area of the lens, defined by the ratio of the area occupied by fibers to that of the entire entrance, is 0.175. The outermost fibers (along the x-direction, *i.e.* horizontal, transverse) have the maximum bending angle (or half-convergence angle),  $\Omega$ , of 0.22 rad (about  $13^\circ$ ).

The lens is placed at the NG-7/PGAA location, where no collimation is used between the exit of the guide and the lens, so that the lens is fully illuminated. The size and intensity of the transmitted neutron beam is determined using a video radiation detector (VRD) [8]. The average intensity is evaluated by integrating the number of counts on the pixels within the area

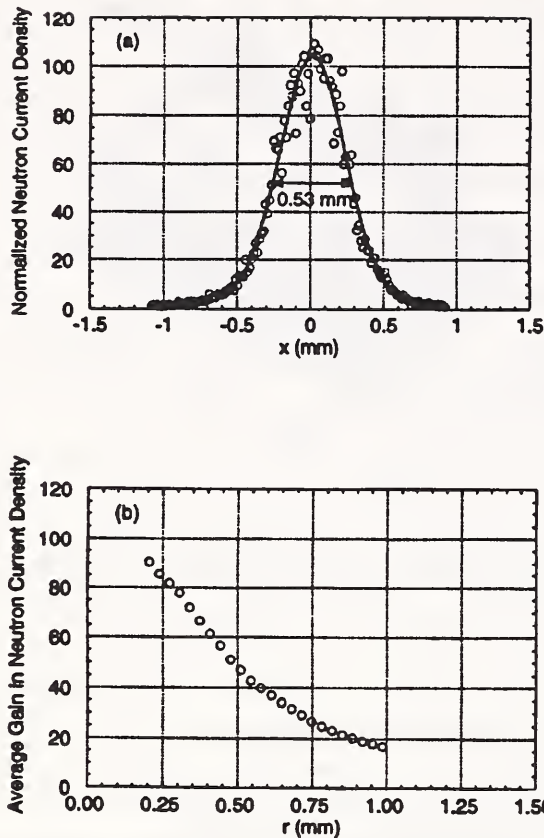


**Figure 4.** (a) The neutron beam distribution obtained by a line profiling across the center of the focus. (b) The average current density gain as a function of the radius  $r$  of the concentric sampling area centered on the focus.

of interest. A line profile obtained by sampling across the center of the image at the focal point, normalized to the incident beam current density, is shown in figure 4 (a) which gives a FWHM of 0.53 mm. Shown in figure 4 (b) is the average current density gain as a function of sampling radius, which is obtained by measuring neutron intensity over areas with various radii at the focus normalized to the intensity of the incident beam. The peak gain is 105, and an average gain over the area of diameter 0.53 mm is 80. PGAA measurements have been performed [9] to demonstrate the enhanced detection sensitivity and spatial resolution in one dimension. In these experiments the 1 mm  $^6\text{LiF}$  aperture is placed at the focal plane to define the fo-

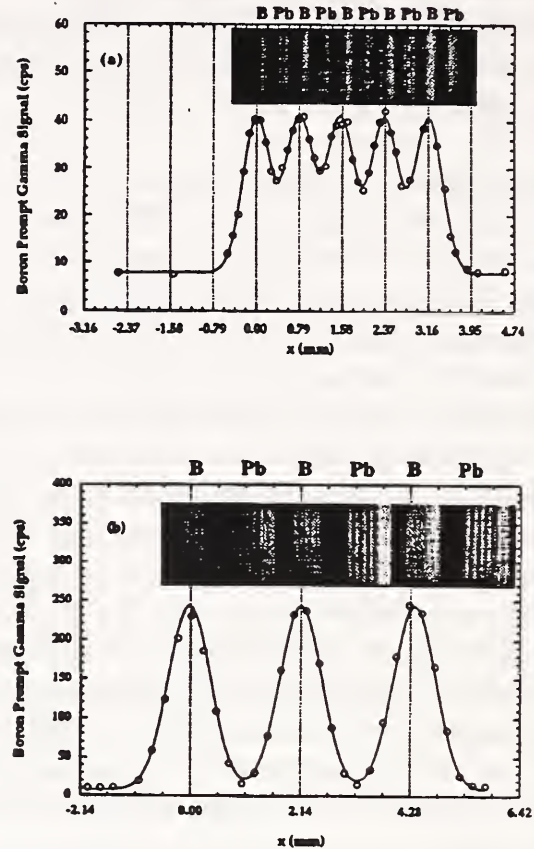


**Figure 5.** Scanning fiber samples across the focus for PGAA measurement. (a) 0.4 mm fibers, (b) 1 mm fibers.

cused beam. A glass bead containing 2 wt.% Gd (0.23 mm x 0.385 mm in cross section) and a Cd metal particle (0.5 mm x 0.45 mm in cross section) have been measured with and without the lens. The gain in the gamma count rate in both cases, *i.e.*, for the gadolinium 182 keV peak and cadmium 558 keV peak, is a factor of 60. In the resolution measurement, the samples are glass polycapillary fibers, similar to those used in the focusing lens except differing in composition. A row of lead-silica and borosilicate fibers, is arranged alternately (B-Pb-B-Pb...), side by side, behind the aperture. Two sets of fibers have been measured: one with diameter 0.4 mm, the other 1 mm. The count rate of the boron peak at 478 keV is monitored as the row of samples is scanned in the  $x$  direction along the focal plane. Figure 5 shows an overlay of an

optical microscope image of the fibers and the PGAA count rate at the corresponding fiber positions. The peaks are partially resolved: (peak-valley)/(peak-background)  $\sim 38\%$  (100% represents complete resolution) for the smaller fibers, and are almost completely resolved (97%) for the larger ones.

### The Hydrogen Cold Source

A major part of the current reactor shutdown, which began May 26, 1994, is the replacement of the  $D_2O$  cold source with a liquid hydrogen source [10]. It is expected the new source will increase the yield of long wavelength neutrons ( $\lambda > 0.4$  nm) by a factor of four. As of December 31, most of the work on the hydrogen source was complete. The  $D_2O$  cryostat was pulled from the reactor along with the Bi tip on July 5. After installation of new shutters for the beam port, the cryostat assembly was inserted October 26. The condenser was mounted on the north face of the reactor in December, and both the liquid hydrogen supply line to the moderator chamber, and the hydrogen recirculation line to the ballast tank, are complete.

All components of the hydrogen system have been carefully constructed, subject to rigorous quality control. Prototypes of the moderator chamber and the helium containment vessel have been hydraulically tested to failure at 450 psig and 1300 psig, respectively, far beyond any credible pressure expected in these components in the event of an accident. All welds have been either radiographed or pneumatically tested according to ASME code. Each component was also helium leak tested, and no leaks have been found at the detection limit of  $10^{-9}$  stp cc/sec.

Construction and testing of the cold source will be complete in the spring of 1995. Procedures for startup tests are being prepared for review by the Safety Evaluation Committee. These tests will determine operating limits under abnormal conditions, such as loss of  $D_2O$  cooling or refrigerator outage, and further tests will establish optimum performance conditions for routine operation. The refrigerator will be

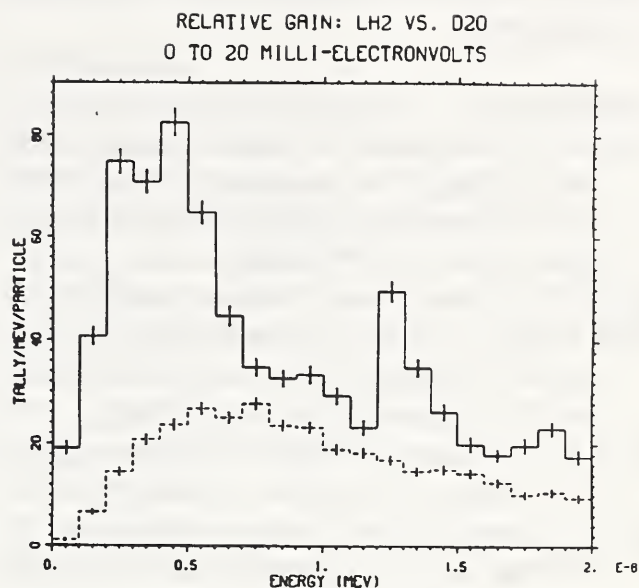


Figure 6. Relative cold neutron currents from the liquid hydrogen source vs. the  $D_2O$  source. For neutrons with energies less than 5 meV, the calculated gain is 4.3.

programmed to maintain a nearly constant hydrogen pressure in the event of a reactor scram, thus keeping constant the inventory of liquid hydrogen in the moderator chamber.

In addition to the installation of the cold source, there has been a continuous effort to benchmark the computational model of the NBSR core. The model, using the Monte Carlo code, MCNP, has been used extensively for reactor calculations as well as cold source performance calculations. A comparison between early measurements of the cold neutron flux from the  $D_2O$  source, and the MCNP results, led us to conclude that the scattering kernel initially used for  $D_2O$  ice was under-predicting the production of cold neutrons. A new kernel was generated, which has much better agreement with the measurements. Recent gain calculations using the new kernel, shown in figure 6, predict a gain in cold neutron production of at least a factor of four, integrated over wavelengths greater than 0.4 nm. Coupled with the gains associated with the return to 20 MW (factor of 1.3), and other factors, the flux of cold neutrons is ex-

pected to be six times higher than it was before the shutdown.

## References

- [1] J. R. D. Copley and T. J. Udovic, *J. Res. NIST* **98**, 71 (1993); F. B. Altorfer, J. C. Cook and J. R. D. Copley, to be published in *Mat. Res. Soc. Symp. Proc.*, Vol. **376** (1995).
- [2] J. R. D. Copley, *J. Neut. Research* **2**, 95 (1994).
- [3] Q. F. Xiao, H. Chen, V. A. Sharov, D. F. R. Mildner, R. G. Downing, N. Gao, and D. M. Gibson, *Rev. Sci. Instrum.*, **65** 3399-3402 (1994).
- [4] D. F. R. Mildner, H. Chen, R. G. Downing, and V. A. Sharov, *J. Neut. Res.* **1**, 1-11 (1993).
- [5] Q. F. Xiao, H. Chen, D. F. R. Mildner, R. G. Downing, and R. E. Benenson, *Rev. Sci. Instrum.* **64**, 3252-3257 (1993).
- [6] H. Chen, D. F. R. Mildner, R. G. Downing, R. E. Benenson, Q. F. Xiao, and V. A. Sharov, *Nucl. Instrum. & Meth.* **B89**, 401-411 (1994).
- [7] H. Chen, D. F. Mildner, and Q. F. Xiao, *Appl. Phys. Lett.* **64**, 2068-2070 (1994).
- [8] R. G. Downing, C. J. Zeissler, and H. Chen, *SPIE Conf. Proc.* **1737**, 308-321 (1993).
- [9] H. Chen, V. A. Sharov, D. F. R. Mildner, R. G. Downing, R. L. Paul, R. M. Lindstrom, C. J. Zeissler, and Q. F. Xiao, *Nucl. Instrum. Meth.*, **B95**, 107-114 (1995).
- [10] "NIST Reactor: Summary of Activities July 1991 through September 1992", *NISTIR* 5120 (February 1993), p. 92.

## Research Topics

### Cold Neutron Focusing Using Capillary Optics

H. Chen<sup>4,6</sup>, R. G. Downing<sup>4</sup>, D. F. R. Mildner<sup>4</sup>, V. A. Sharov<sup>14</sup>, R. E. Benenson<sup>11</sup>, and Q. F. Xiao<sup>14</sup>

### The Medium-Resolution Time-of-Flight Spectrometer

T. J. Udovic<sup>10</sup>

### The NSF/NIST (CHRNS) Triple-Axis Spectrometer

V. Nunez<sup>12</sup>, C. F. Majkrzak<sup>10</sup>, S. F. Trevino<sup>1,10</sup>, and C. L. Broholm<sup>7</sup>

### The NIST/IBM/U. of Minn. Cold Neutron Reflectometer

S. K. Satija<sup>10</sup> and P. D. Gallagher<sup>10</sup>

### Performance of the Liquid Hydrogen Cold Neutron Source

R. E. Williams<sup>10</sup>, J. M. Rowe<sup>10</sup>, and P. A. Kopetka<sup>10</sup>

### Fe-Si Supermirror Polarizers

C. F. Majkrzak<sup>10</sup>, J. F. Ankner<sup>15</sup>, and V. Nunez<sup>12</sup>

### Ni-C-TiMn Supermirror Reflectivity Measurements

C. F. Majkrzak<sup>10</sup> and J. F. Ankner<sup>15</sup>

### Drabkin Energy-Dependent Spin Flipper Fabrication

C. F. Majkrzak<sup>10</sup>, L. Passell<sup>2</sup>, V. Nunez<sup>12</sup>, H. P. Layer<sup>10</sup>, W. E. Dickerson<sup>10</sup>

### Analysis and Simulation of the Performance of Oscillating Radial Collimators

J. R. D. Copley<sup>10</sup> and J. C. Cook<sup>5,12</sup>

### Resolution Properties of Counter-rotating Chopper Monochromators for Neutron Spectroscopy

J. C. Cook<sup>5,12</sup>

### A Transmission Polarizing Cavity for SANS

W. J. Orts<sup>10</sup>, J. G. Barker<sup>10</sup>, C. F. Majkrzak<sup>10</sup>, and C. J. Glinka<sup>10</sup>

### The Cold Neutron High-Flux Backscattering Spectrometer

P. M. Gehring<sup>10</sup>, C. W. Brocker<sup>12</sup>, R. Christman<sup>16</sup>, and D. A. Neumann<sup>10</sup>

### Test of Si(111) Analyzer Crystals for the Backscattering Spectrometer

B. Frick<sup>5</sup>, P. M. Gehring<sup>10</sup>, D. A. Neumann<sup>10</sup>, C. Appel<sup>18</sup> and C. W. Brocker<sup>12</sup>

### Pyrolytic Graphite Mosaic Measurements for the Phase Space Transform Chopper

P. M. Gehring<sup>10</sup>, D. A. Neumann<sup>10</sup>, A. Moore<sup>17</sup>, and C. W. Brocker<sup>12</sup>

### Modeling of Neutron Focusing Lenses

D. F. R. Mildner<sup>4</sup>, H. Chen<sup>4,6</sup>, R. G. Downing<sup>4</sup>, Q. F. Xiao<sup>14</sup>, and J. W. Swider<sup>12</sup>

### Neutron Transmission of Polycapillary Fibers

H. Chen<sup>4,6</sup>, D. F. R. Mildner<sup>4</sup>, R. E. Benenson<sup>11</sup>, Q. F. Xiao<sup>14</sup>, and V. A. Sharov<sup>6,14</sup>

### The Neutron Spin Echo Spectrometer

N. Rosov<sup>10</sup>, J. M. Rowe<sup>10</sup>, and M. Monkenbusch<sup>8</sup>



**A High Pressure Cell for SANS Measurements**B. Hammouda<sup>10</sup> and J. Moyer<sup>16</sup>**The NIST Cold Neutron Depth Profiling Instrument**G. P. Lamaze<sup>4</sup> and R. G. Downing<sup>4</sup>**30-m SANS Instrument (NG-7) Improvements**C. J. Glinka<sup>10</sup>, J. G. Barker<sup>10</sup>, S. Krueger<sup>10</sup>, E. Sheu<sup>19</sup>, J. Moyer<sup>16</sup>, M. Rinehart<sup>10</sup>, W. Clow<sup>10</sup>, and G. Baltic<sup>10</sup>**Cold-Neutron Prompt-Gamma Activation Analysis**R. M. Lindstrom<sup>4</sup>, R. L. Paul<sup>4</sup>, and E. A. Mackey<sup>4</sup>**Preliminary Evaluations of a New Neutron Focusing Lens for Materials Characterization**H. Chen<sup>4,6</sup>, V. A. Sharov<sup>14</sup>, D. F. R. Mildner<sup>4</sup>, R. G. Downing<sup>4</sup>, R. L. Paul<sup>4</sup>, R. M. Lindstrom<sup>4</sup>, C. J. Zeissler<sup>20</sup>, and Q. F. Xiao<sup>14</sup>**The Disk Chopper Time-of-Flight Spectrometer**J. R. D. Copley<sup>10</sup>, J. C. Cook<sup>5,12</sup>, D. J. Pierce<sup>10</sup>, F. Altorfer<sup>12</sup>, and C. W. Brocker<sup>12</sup>**Performance Tests of the Choppers for the Disk Chopper Time-of-Flight Spectrometer**F. Altorfer<sup>12</sup>, J. C. Cook<sup>5,12</sup>, J. R. D. Copley<sup>10</sup>, and D. Kulp<sup>10</sup>**Acceptance Tests of the Detectors and Amplifiers for the Disk Chopper Time-of-Flight Spectrometer**W. Gorman<sup>10</sup> and H.P. Layer<sup>10</sup>**Data Acquisition Hardware and Software for the Disk Chopper Time-of-Flight Spectrometer**H. P. Layer<sup>10</sup>, G. C. Greene<sup>10</sup>, P. Klosowski<sup>12</sup>, and J. R. D. Copley<sup>10</sup>**Transmission Properties of Short Curved Neutron Guides**J. R. D. Copley<sup>10</sup>**Ray-tracing Calculations of Neutron Focussing Properties of Toroidal Mirrors**J. R. D. Copley<sup>10</sup> and C. Lartigue<sup>5</sup>**Tests of Candidate Gd<sub>2</sub>O<sub>3</sub> Coatings for Collimator Blades**J. C. Cook<sup>5,12</sup>, E. A. Mackey<sup>4</sup>, and J. R. D. Copley<sup>10</sup>**Affiliations**<sup>1</sup>Army Armament RD&E Center<sup>2</sup>Brookhaven National Lab<sup>3</sup>CSTL, NIST Boulder<sup>4</sup>Inorganic Analytical Research Division<sup>5</sup>Institut Laue-Langevin<sup>6</sup>University of Missouri<sup>7</sup>Johns Hopkins University<sup>8</sup>KFA Jülich<sup>9</sup>Polymers Division<sup>10</sup>Reactor Radiation Division<sup>11</sup>SUNY (Albany)<sup>12</sup>University of Maryland<sup>13</sup>University of Minnesota<sup>14</sup>X-Ray Optical Systems, Inc.<sup>15</sup>MURR, University of Missouri at Columbia<sup>16</sup>NESCO Service Company<sup>17</sup>Advanced Ceramics Corp.<sup>18</sup>SFA, Inc.<sup>19</sup>Texaco Research and Development<sup>20</sup>Surface and Microanalysis Sci. Div.

## Guest Researchers and Collaborations

Scientists from other institutions and other divisions of NIST play a most important part in the research activity at the NBSR. They insure that the industrial and academic research communities obtain a maximal benefit from the operation of the NBSR and its instrumentation. The participation of guest researchers is most evident in the Cold Neutron Research Facility (CNRF), which is a national facility dedicated to providing all U.S. researchers with access to the most modern cold neutron beam instrumentation. However, guest researchers also play an indispensable role in the research carried out on the thermal beam instruments in the NBSR reactor hall, and in a variety of programs, such as activation analysis and radiation standards research, which do not involve neutron scattering instrumentation.

The number of research participants is plotted against time in figure 1. It is evident that external user participation has shown strong and steady growth for a number of years. RRD staff are a fairly small, although essential, component of the total number of scientists and engineers who have contributed to research and development activities at the NBSR. External participants are often involved in more than one experiment in any one year, but are counted only once per year in the data of figure 1. The rightmost column of the figure represents participants from 52 U.S. industrial laboratories, 90 universities, 40 other government institutions, and 114 foreign institutions.

Guest researchers obtain access to NBSR instrumentation in several different ways. For the cold neutron beam instruments, the most straightforward procedure is through the formal proposal system of the CNRF. In the case of the thermal neutron beam instruments, which are not offered through the proposal system, the usual mode of access is through direct collaboration with NIST scientists on specific experiments or limited research projects. Another very im-

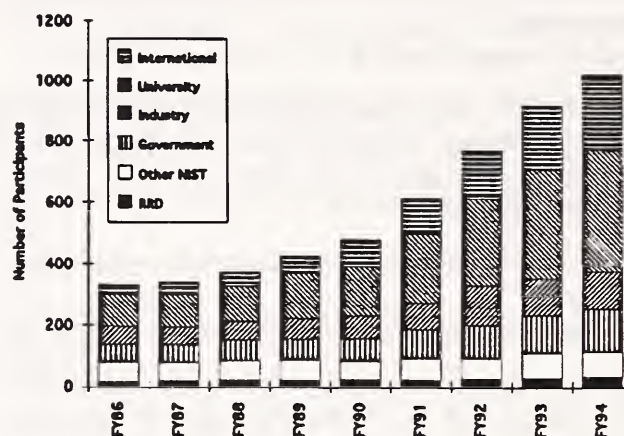


Figure 1. Research participants at the NBSR.

portant mode of access involves more formal collaborations, usually of longer duration and with larger groups rather than with individual scientists.

During the period October 1993 through September 1994 (FY94), the NBSR operated for approximately eight months on its regular schedule. On May 26, 1994, the reactor was shut down and entered its current extended period of work on major improvements to its operating capabilities. Prior to this date, there were 183 days of operation at power during FY94. Since the shutdown will extend well into FY95, it is to be expected that guest researcher participation will be somewhat reduced for these two reporting periods. However, when the reactor resumes full operation in March or April of 1995, we anticipate that more guest researchers than ever will come to take advantage of the improved research capabilities that will then become available.

The CNRF proposal system has now been operating for more than two years. Four calls for proposals have been issued, the last in May 1994, with a deadline of July 23, 1993, during the past fiscal year. The experiments approved from the last proposal round were mainly carried out in FY94, in the period from August 1993 to the

start of the extended shutdown. The number of proposals received in response to the four successive calls has steadily increased, from 37 in the first round to 76 in the fourth. The number of instrument-days allocated increased from 60 to 218, reflecting both the larger number of proposals and the coming on line of more instruments. These data exclude the experiments for the analytical chemistry and fundamental physics stations, which are considered separately. The fraction of the total beam time reserved for general users is 75% on the CHRNS 30-m SANS, and 67% for the other scattering instruments, except for participating research team (PRT) instruments (see below), on which 25% of the time is set aside for general users.

When the reactor is operating under normal scheduling conditions, calls for proposals are issued twice yearly to a mailing list of more than 1700 scientists. Soon after the proposal deadline, the proposals received in response to a call are mailed out for external peer review. The final decisions for beam time allocations are made by a Program Advisory Committee (PAC), which compares the proposals received on the basis of the written reviews. The PAC members, who are appointed by NIST management, represent a wide range of expertise in neutron beam research, and advise NIST on all relevant aspects of CNRF operation.

The part of the CNRF which accommodates the most users is the Center for High resolution Neutron Scattering (CHRNS), which is funded by the National Science Foundation. The primary CHRNS instrument is one of the 30-m SANS diffractometers, but 50% of the cold-neutron triple-axis spectrometer is also supported in the CHRNS operation. The latter is being developed into a novel spin-polarized instrument which will simultaneously allow polarization analysis and high signal intensity. Before the current shutdown, the CHRNS was already approaching its full capacity to serve users in terms of the number of available instrument-days, but the major upgrades currently in progress will mean a qualitative improvement in

performance when the NBSR resumes operation in the spring of 1995.

Two of the CNRF instruments—the cold neutron reflectometer and one of the 30-m SANS diffractometers—were built by participating research teams (PRTs), consortia of several institutions which shared the cost of instrument development and construction. On these instruments, 75% of the beam time is reserved for PRT members, and 25% for general users through the CNRF proposal system. The PRT research programs are discussed in other sections of this annual report.

Several of the newest instruments are worthy of discussion with regard to their recent effect on guest researcher participation at the NBSR. The high-resolution powder diffractometer at BT-1 in the reactor hall has performed extremely well in its first year of operation, from the start of routine operation in June 1993 to the beginning of the long shutdown in May 1994. More than 700 data sets were collected in that period, with the great majority of experiments involving collaborations with guest researchers. The latter came from over 50 institutions. Although the powder diffractometer is not part of the formal proposal system, scientists from other institutions may communicate directly with NIST personnel to arrange their experiments, and many take the opportunity to do so. More formal collaborative programs have been established with groups at MIT and the University of California, Santa Barbara. There is a possibility that some fraction of the instrument time on BT-1 may be offered through the formal proposal system in the near future.

The cold neutron reflectometer on neutron guide NG-7 is another new instrument that has been in great demand from users since it began operation in 1993. Although it is a PRT instrument, with only 25% of the time available through the CNRF proposal system, experiments on the reflectometer usually involve not only the PRT members (NIST, IBM, Univ. of Minnesota), but also scientists from other institutions. The success of this instrument, and the

rapid rise of the technique of neutron reflectometry in general, have prompted NIST management to plan for the relocation of the polarized beam reflectometer from its present position on BT-7 in the reactor hall to neutron guide NG-7 in the guide hall, where its effectiveness will be enhanced severalfold because of greater useful intensity due to the new cold source.

The Fermi-chopper spectrometer (FCS) is another instrument that has recently received much increased user demand. It is currently the only cold-neutron time-of-flight spectrometer at a U.S. research reactor. It has attracted users from universities, government laboratories and industry, representing a diverse range of applications, from polymers and liquid crystals to glasses and superconductors. The demand for the FCS is indicative of the need for more cold neutron spectrometers in the United States. The three major spectrometers which are currently under construction in the CNRF guide hall will greatly enhance U.S. capabilities in cold neutron spectroscopy, bringing them up to a world-class standard. They will permit experiments with much higher energy resolution and sensitivity. The Disk Chopper Spectrometer (DCS) will permit resolution down to  $6 \mu\text{eV}$ , compared with  $60 \mu\text{eV}$  for the FCS. The DCS will be very versatile, allowing wavelength and resolution to be changed across a wide range simply by changing the phases of its seven choppers. The DCS will be completed in calendar year 1996. The backscattering spectrometer, also to be completed in 1996, will have an energy resolution of  $0.75 \mu\text{eV}$ , and a dynamic range of  $\pm 50 \mu\text{eV}$ . The phase space transformer device which it will employ to increase the monochromatic beam intensity will make this instrument competitive with the world's best. Finally, the spin-echo spectrometer will allow effective energy resolution in the neV range. Some major components (coils for incident and scattered beam paths) have been constructed, but much design and development is needed before operation can begin, possibly in 1996 or 1997. The addition of these three spectrometers to the CNRF will enable

guest researchers to pursue many new opportunities in polymer science and in biological applications, as well as in the traditional areas of physics, chemistry, and materials science.

Yet another class of users will be attracted by the new residual stress, texture, and single crystal diffractometer being constructed at BT-8 in the reactor hall. It should be operational in mid-1995. Residual stress and texture are of primary interest to engineering and materials science applications in industrial and government laboratories, as detailed in another section of this annual report. It is expected that the new instrument will have a throughput for residual stress problems at least five times greater than the existing setup at BT-6, making feasible measurements that have been previously considered too time-consuming to undertake.

A project to modernize all of the thermal neutron instruments in the reactor hall has been initiated, which will, over the next few years, greatly improve the safety and ease of operation. In most cases, the data-taking capabilities of the instruments will also be enhanced. The filter-analyzer option on one of the instruments will be replaced by a dedicated filter-analyzer instrument, with a factor of forty greater acceptance in the solid angle subtended by the analyzers. Horizontally-focussing monochromators and analyzers will be available, permitting a substantial gain in intensity for many triple-axis experiments. New monochromator drums will give a lower background, improved safety, and greater ease of operation. All of these improvements will aid guest researchers to carry out their experiments.

Access to the analytical chemistry stations, *i.e.* cold neutron depth profiling (CNDP) and prompt-gamma activation analysis (PGAA), is handled somewhat differently from the CNRF neutron scattering instruments, because the duration of experiments can vary from a few hours to several weeks, depending on the nature of the proposed project. Proposals can be submitted on the standard CNRF proposal form, but use of the forms is not required, and less formal propos-

als submitted directly to the instrument scientists (contacts) are considered immediately and are not sent out for external peer review. For both the CNDP and PGAA stations, up to 67% of the time is available to guest researchers on this basis.

The fundamental neutron physics stations in the guide hall operate under yet another process of review. The experiments at these two stations, a dedicated cold neutron beam at the end of the NG-6 guide, and the neutron interferometry station on NG-7, are typically of much longer duration than for other CNRF instruments, and involve highly specialized equipment. The purpose of these stations is to measure fundamental properties of the neutron and neutron interactions, and to explore basic propositions of quantum mechanics. External participation in such experiments requires long-term and costly commitments and a more thorough and inevitably slower review than offered by the formal user proposal system becomes necessary. An advisory committee separate from the PAC has been established to review the use of the fundamental physics stations, in order to ensure that they properly serve the needs of their research community.

The division makes a special effort to accommodate experimenters who can make a case for immediate access based on clear scientific urgency. If the planned experiment is to be carried out on a CNRF instrument, a short proposal can be submitted which is quickly reviewed and assigned beam time if approved by the PAC. Alternatively, NIST staff members can be contacted to arrange collaboration for use of a non-CNRF instrument, or for employing NIST beam time on a CNRF instrument.

Several non-NIST programs are also served by the NBSR through the provision of services such as irradiation, radiography, and materials characterization. Examples include a program with the Smithsonian Institution for autoradiography of paintings, a program with the FDA for characterization of food and drugs, and activation analysis services for the FBI. Shorter-

term projects receive use of NBSR facilities on an as-needed, case-by-case basis. Depending its nature, a project may be arranged as a collaboration with NIST or as an independent study by the outside agency. In some cases, non-NIST researchers perform proprietary research using NBSR facilities. In such cases, the researchers' institutions are assessed charges on a full-cost recovery basis.

Guest researcher activity will undoubtedly continue to increase in its level and its diversity for a number of years. The improvements being made during the current shutdown will have a major effect on future prospects. The operation of the NBSR at 20 MW, and the installation of the new cold source and the last three neutron guides, means that the NBSR will come back on line in 1995 with markedly enhanced capabilities for neutron beam experiments, and a greater number and variety of user experiments will become practicable. Encouraging use of the NBSR and the CNRF by the broadest possible community, and fostering the development of new applications for neutron beams, will remain primary missions of the division.

For further information on the use of the instrumentation at the NBSR, contact Bill Kamitakahara at (301) 975-6878, or any RRD staff member.

# Reactor Operations and Engineering

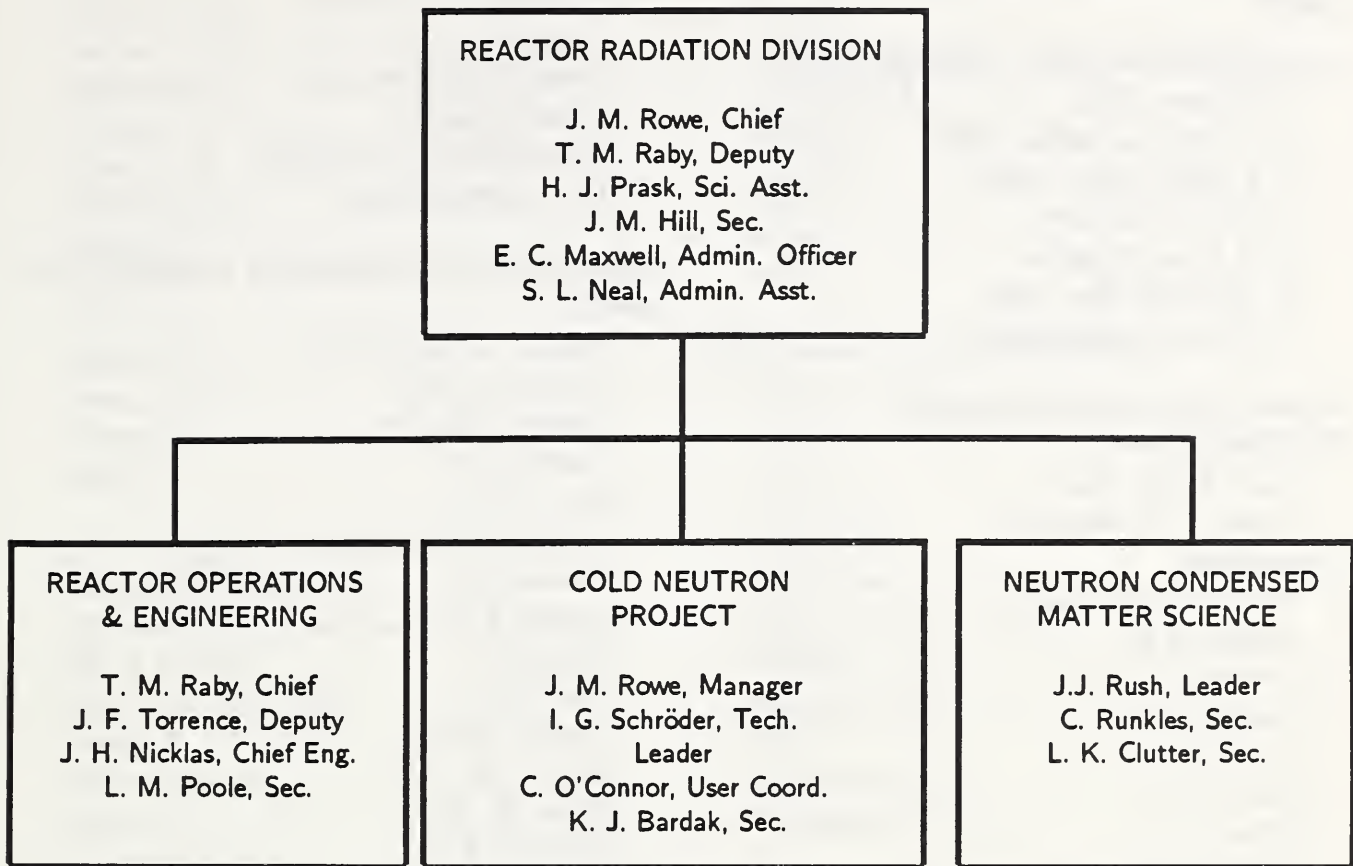
From October 1993 through May 1994 the reactor operated virtually continuously with perhaps the most extensive utilization in the history of the facility. At the end of May 1994, the reactor was shut down to begin major upgrade of reactor systems and installation of the new liquid hydrogen cold source. This is a wide ranging and ambitious in-house program that involves redesign and replacement of major segments of the reactor facility. The outage is expected to last to the spring of 1995. Projects that are ongoing or completed include:

1. Complete dismantling and disposal of most of the primary, secondary and auxiliary cooling systems including removal of four heat exchangers.
2. Disposal of large quantities of radioactive waste including fuel element cuttings and primary IX-resins.
3. Installation of five new heat exchangers.
4. Installation of new secondary cooling water filtration system.
5. Repiping of primary, secondary and auxiliary cooling systems.
6. Redesign and installation of process instrumentation.
7. Redesign of primary ion-exchange systems.
8. Custom shielding for all ion-exchangers and the purification heat exchanger.
9. Replacement of the control rods.
10. Reactor control room upgrade.
11. Major items of maintenance including among others, replacement of all valve diaphragms, overhaul of the emergency diesel generators, refurbishing of the confinement building, overhaul of the cooling tower and maintenance of thermal shield cooling coils.
12. On-line examination and inspection of reactor internals.

During maintenance and inspection of the top refueling plug, it was discovered that the boron plate underneath had deteriorated and was interfering with the operation of the transfer arms. This necessitated removal and complete rebuilding of the entire top plug fuel transfer system. This is another and unexpected major project that requires significant effort. However, the work will be done simultaneously with the other projects and should not extend the shutdown. New heavy water is scheduled to arrive at the beginning of 1995 and will be put in the reactor just prior to startup at which time the old tritiated water will be shipped back to the Department of Energy.

Overall, outage projects have moved so well and so expeditiously as to surpass expectations.

# Personnel Roster



The Division staff is organized formally into three groups, as shown in Table 1; however, staff are utilized where necessary, irrespective of group. Below the group level of organization, personnel are grouped into research teams according to their predominant interest. Once again, these groupings are not hard and fast—there are many overlapping interests. These teams, including long-term guest researchers, are shown in Table 2. A number of “non-resident” Ph.D. students and continuing collaborators from universities and industry are not listed. It should be noted that members of the Cold Neutron Project are included in the teams by scientific interest, even though in most cases, their predominant responsibility is for CNRF instrument building and/or operation. In fact, they have only 30% of their time given to the conduct of research, while 70% is dedicated to the facility. Likewise, many members of

the Neutron Condensed Matter Science Group have sizable CNRF responsibilities, which may amount for as much as 1/2 time when needed.

**Table 1. NBSR and CNRF Resident Staff****ADMINISTRATIVE - DIVISION 856**

J. M. Rowe, Chief  
 E. C. Maxwell, Admin. Off.  
 S. L. Neal, Admin. Asst.  
 J. M. Hill, Secretary  
 H. J. Prask, Physicist  
 D. E. Brady, Elect. Eng.  
 J. M. Nicol, Res. Chemist

**REACTOR OPERATIONS & ENGINEERING**

Raby, T. M., Chief  
 Poole, L. M., Secretary

**Operations**

Torrence, J. F., Deputy  
 Beasley, R. D.  
 Bickford, N. A.  
 Cassells, M. G.  
 Clark, F. C.  
 Dilks, H. W.  
 Flynn, D. J.  
 Guarin, E. L.  
 Lindstrom, L. T.  
 McDonald, M. J.  
 Mueller, M. W.  
 Myers, T. J.  
 Ring, J. H.  
 Sprow, R. P.  
 Stiber, R. F.  
 Thompson, R. G.  
 Toth, A. L.  
 Wilkison, D. P.  
 Wright, K. D.

**Engineering**

Nicklas, J. H., Chief  
 Beatty, J. A.  
 Hall, K.  
 Heine, C. J.  
 Liposky, P. J.  
 Shuman, L.  
 Suthar, M. A.

**Research Associates**

Anderson, D. A. (FDA)  
 Billos, J.  
 Cheng, T. (Smithsonian)  
 Cunningham, R.  
 Cunningham, W. C. (FDA)  
 Olin, J. (Smithsonian)

**NEUTRON CONDENSED MATTER SCIENCE**

Rush, J. J., Group Ldr.  
 Runkles, C., Sec.  
 Clutter, L. K., Sec.  
 Baltic, G. M.  
 Berk, N. F.  
 Borchers, J. A.  
 Bostian, D.  
 Casella, R. C.  
 Clem, D.  
 Clow, W.  
 Copley, J. R. D.  
 Dura, J. A.  
 Erwin, R. W.  
 Fravel, D. H.  
 Glinka, C. J.  
 Green, T. A.  
 Karen, V. L.  
 Knill, W. C.  
 Lynn, J. W.  
 Majkrzak, C. F.  
 Mighell, A. D.  
 Neumann, D. A.  
 Orts, W. J.  
 Prince, E.  
 Reznik, D.  
 Rinehart, M. J.  
 Rymes, W. H.  
 Santodonato, L.  
 Santoro, A.  
 Satija, S. K.  
 Stalick, J. K.  
 Udovic, T. J.  
 Wiesler, D. G.  
 Williams, R. H.



**Guest Scientists**

Altorfer, F. B.  
 Choi, C. S.  
 Clinton, T. W.  
 Fischer, J. E.  
 Giebultowicz, T.  
 Grigereit, T.  
 Huang, Q. Z.  
 Klosowski, P.  
 Morris, R.  
 Mrose, M.  
 Nunez, V.  
 Trevino, S. F.  
 Watanabe, T.  
 Yildirim, T.  
 Zhang, H.

**COLD NEUTRON PROJECT**

Rowe, J. M., Ldr.  
 O'Connor, C. L., User Coord.  
 Hill, J. M., Sec.  
 Bardak, K., Clk. Typ.  
 Barker, J.  
 Dickerson, W. E.  
 Fulford, D.  
 Gallagher, P. D.  
 Gehring, P. M.  
 Gorman, W.  
 Greene, G. C.  
 Hammouda, B.  
 Heald, A. E.  
 Kamitakahara W. A.  
 Klosowski, P.  
 Kopetka, P. H.  
 Krueger, S.  
 Kulp, D.  
 LaRock, J. G.  
 Layer, H. P.  
 Pierce, D. J.  
 Robeson, L.  
 Rosov, N.  
 Schroder, I. G.  
 Thai, T. T.  
 Tobin, P. L.  
 Williams, R. E.

**Guest Scientists**

Allen, A.  
 Brand, P.  
 Brocker, C.  
 Christman, R.  
 Desrosier, F. L.  
 Lin, M. Y.  
 Moyer, J. J.  
 Nunes, A.  
 Wrenn, C.

**NEUTRON INTERACTIONS**

Gilliam, D., Ldr.  
 Mattiello, R., Sec.  
 Arif, M.  
 Boswell, E.  
 Dewey, M. S.  
 Eisenhauer, C. M.  
 Greene, G. L.  
 Grundl, J.  
 McGarry, E. D.  
 Nico, J.  
 Schwartz, R. B.  
 Thompson, A.

**HEALTH PHYSICS - DIVISION 354**

Slaback, L., Ldr.  
 Thomas, C. L., Sec.  
 Brown, D.  
 Campbell, C.  
 Cassells, L.  
 Clark, J.  
 Deardorff, G.  
 Fink, L.  
 Mengers, T.  
 Shubiak, J.

**NUCLEAR METHODS GROUP - DIVISION 834**

Greenberg, R. R., Ldr.  
 Wilson, J., Sec.  
 Becker, D.  
 Benenson, R. E.  
 Bishop, R. L.  
 Blackman, M. J.  
 Chen, H.

Demiralp, R.  
Downing, R. G.  
Fitzpatrick, K.  
Garrity, K. M.  
Iyengar, G. V.  
Koster, B.  
Lamaze, G. P.  
Langland, J. K.  
Lindstrom, R. M.  
Mackey, E. A.  
Mildner, D.F.R.  
Norman, B. R.  
Paul, R. L.  
Sharov, V. A.  
Swider, J.  
Welsh, J. F.

## Research and Engineering Staff

- J. G. Barker           SANS instrumentation and research  
Microstructure of materials
- N. F. Berk             Condensed matter theory  
Scattering theory for microstructure analysis  
Computer software for graphics and data analysis
- N. A. Bickford        Reactor operations  
Reactor irradiations  
Reactor utilization
- J. A. Borchers        Thin-film analysis  
Artificially modulated materials  
Magnetism
- D. E. Brady           Electrical/electronic engineering  
Nuclear reactor instrumentation
- R. C. Casella         Condensed matter theory, including high  $T_c$   
Group theory analyses of neutron scattering from condensed matter  
Fundamental physics, especially as related to reactor experiments
- J. R. D. Copley       Time-of-flight spectrometer development  
Neutron instrumentation conceptual design  
Condensed matter physics
- W. E. Dickerson      Neutron scattering instrumentation  
Microcomputer interfacing  
Nuclear and engineering physics
- J. A. Dura            Combined molecular beam epitaxy and neutron reflectivity/  
                          diffraction instrumentation  
Surface, interfacial, and epitaxial physics  
Metastable phases in artificial materials
- R. W. Erwin           Magnetic materials  
Phase transformations  
Cryogenics
- D. B. Fulford         SANS equipment development and maintenance  
Mechanical engineering
- P. D. Gallagher      Neutron reflectometry instrumentation  
Interfacial phenomena in polymer systems and complex fluids  
Phase transitions and critical phenomena

- P. M. Gehring  
Neutron backscattering instrumentation  
Magnetic and structural phase transitions in disordered systems  
Dynamics of high  $T_c$  materials
- C. J. Glinka  
SANS microstructure of metals and porous media  
Magnetic materials  
Cold neutron instrument development
- G. C. Greene  
System and user software for cold neutron instrumentation  
Spectrometer and data acquisition systems interfaces
- B. Hammouda  
SANS from polymers, liquid crystals, and colloids  
Dynamics of polymers in solution  
Scattering from sheared fluids
- A. E. Heald  
Design engineering  
Neutron instrumentation  
Shielding
- W. A. Kamitakahara  
The CNRF guest researcher program  
Dynamics of disordered solids  
Condensed matter physics
- V. L. Karen  
Crystallographic database development  
Theory of lattices and symmetry  
Neutron and x-ray diffraction
- P. Klosowski  
Scientific data visualization  
Numerical computer modeling  
Data acquisition software and hardware
- P. A. Kopetka  
Mechanical engineering  
Cold source design  
Electro-mechanical systems
- S. Krueger  
SANS instrumentation  
Microstructure of materials  
Biological problems
- J. G. LaRock  
Mechanical engineering  
Neutron instrumentation design
- H. P. Layer  
Electronics and data processing  
Advanced instrumentation  
Fundamental physics
- P. J. Liposky  
Design engineering  
Nuclear systems and components

J. W. Lynn	Condensed matter physics Magnetic and superconducting materials Neutron scattering methods
C. F. Majkrzak	Condensed matter physics Polarized neutron scattering and instrumentation development Neutron reflectivity measurements
A. D. Mighell	Crystallographic database development Single crystal and powder diffraction Theory of lattices
D. A. Neumann	Molecular and layered materials Condensed matter physics Neutron and x-ray scattering instrumentation
J. M. Nicol	Properties of catalysts and adsorbates Molecular materials Division safety
J. H. Nicklas	Mechanical engineering Reactor fuel design Reactor engineering support
W. J. Orts	SANS instrumentation Neutron scattering and reflectivity from polymers Polarized neutron small angle scattering
D. J. Pierce	Mechanical engineering Neutron instrumentation design
H. J. Prask	Residual stress measurement methodology Neutron NDE applications Neutron NDE instrumentation
E. Prince	Structural properties of alloys, catalysts, and minerals Advanced crystallographic refinement methods Software for materials structure analyses
T. M. Raby	Reactor operations Nuclear engineering Reactor standards
G. Reilly	Design engineering Nuclear systems and components
D. Reznik	Condensed matter physics Dynamics of High $T_c$ materials Dynamics of fullerenes

- N. Rosov  
Spin echo techniques  
Phase transformations  
Magnetic materials
- J. M. Rowe  
Orientationally disordered solids  
Hydrogen in metals  
Cold neutron research and instrumentation
- J. J. Rush  
Catalysts and molecular materials  
Hydrogen in metals  
Inelastic scattering methods
- L. Santodonato  
Condensed matter physics  
Cryogenics
- A. Santoro  
Structure of electronic and structured ceramics  
Theory of crystal lattices  
Powder diffraction methods
- S. K. Satija  
Low-dimensional molecular systems  
Fractal aspects of microporous media  
Neutron reflectometry
- I. G. Schröder  
Cold neutron instrumentation development  
Nuclear and engineering physics  
Optical devices for neutron transport
- J. K. Stalick  
Neutron and x-ray diffraction  
Inorganic chemistry  
Crystal database development
- M. A. Suthar  
Design engineering  
Nuclear systems and components
- J. F. Torrence  
Reactor supervision  
Reactor maintenance  
Nuclear engineering
- T. J. Udovic  
Neutron time-of-flight instrumentation  
Properties of catalysts and adsorbates  
Hydrogen in metals
- D. G. Wiesler  
Neutron and x-ray reflectometry  
Condensed matter physics  
Electrochemistry
- R. E. Williams  
Cold neutron source development  
Nuclear engineering

**Technical Staff**

**Reactor Operations**

Richard D. Beasley  
Mark G. Cassells  
Forrest C. Clark  
Howard W. Dilks  
Daniel J. Flynn  
Enrique L. Guarin  
Larry T. Lindstrom  
Michael J. McDonald

William W. Mueller  
Thomas J. Myers  
John H. Ring  
Ricky P. Sprow  
Robert F. Stiber  
Attila L. Toth  
Daniel P. Wilkison  
Kevin D. Wright

**Reactor Engineering**

James A. Beatty  
Keith Hall  
Lynn A. Shuman

**Neutron Condensed Matter Research**

George M. Baltic  
C. Douglas Bostian  
David Clem  
William R. Clow, Jr.  
Francis L. Desrosier  
Donald H. Fravel  
William T. Gorman  
Thomas A. Green

Wayne C. Knill  
Doris Kulp  
Michael J. Rinehart  
Lewis P. Robeson  
William H. Rymes  
Thuan T. Thai  
Patrick J. Tobin  
Robert H. Williams (Leader)

## Publications

- Adler, S., Russek, S., Reimer, J., Fendorf, M., Stacy, A., Huang, Q., Santoro, A., Lynn, J. W., Baltisberger, J., Werner, U., "Local Structure, Vacancy Ordering, and Oxide-ion Motion in Defective Perovskites," *Solid State Ionics* **68**, 193 (1994).
- Allen, A. J., Berk, N. F., "Analysis of SAS Data Dominated by Multiple Scattering for Systems Containing Eccentrically-Shaped Particles or Pores," *J. Appl. Cryst.*, in press.
- Allen, A. J., Jemian, P.R., Black, D.R., Burdette, H.E., Spal, R.D., Krueger, S., Long, G.G., "Ultra Small Angle X-ray Scattering to Bridge the Gap Between Visible Light Scattering and Standard SAXS Cameras", *Nucl. Instr. & Meth. in Phys. Res. A*, **347**, 487 (1994).
- Allen, A. J., Long, G.G., Kerch, H.M., Krueger, S., Skandan, G., Hahn, H., Parker, J.C., "Sintering Studies of Nanophase Ceramic Oxides Using Small-angle Scattering", in *Prococeedings CIMTEC World Ceramics Congress and Forum on New Materials*, (Florence, Italy, Jun. 27 - Jul. 4, 1994) in press.
- Anastasiadis, S. H., Menelle, A., Russell, T. P., Satija, S. K., Majkrzak, C. F., "Very Thin Films of Symmetric Diblock Copolymers," *Progr. Colloid. Polym. Sci.* **91**, 88 (1993).
- Antipov, E. V., Capponi, J. J., Chaillout, C., Chmaissem, O., Loureiro, S. M., Mare, M., Putilin, S. N., Santoro, A., Tholence, J. L., "Synthesis and Neutron Powder Diffraction Study of Superconductor  $\text{HgBa}_2\text{CaCu}_2\text{O}_{6+\delta}$  Before and After Heat Treatment," *Physica C*, in press.
- Aronson, M. C., Osborn, R., Robinson, R. A., Lynn, J. W., Chau, R., Seaman, C. L., Maple, M. B., "Non-Fermi Liquid Scaling in  $\text{UPd}_x\text{Cu}_{b-x}$  ( $x=1,1.5$ )," *Physica B* in press.
- Axe, J. D., Moss, S. C., Neumann, D. A., "Structure and Dynamics of Crystalline  $\text{C}_{60}$ ", in *Solid State Physics*, Vol. 48, edited by H. Ehrenreich and F. Spaepen (Academic Press, 1994), p. 150.
- Bao, W., Broholm, C., Aeppli, G., Honig, J. M., Metcalf, P., "Spin Dynamics in Metallic and Insulating  $\text{V}_2\text{O}_3$ ," *Phys. Rev. Lett.*, in press.
- Berk, N. F., Majkrzak, C. F., "Using Parametric B- Splines to Fit Specular Reflectivities", *Phys. Rev. B*, in press.
- Balsara, N. P., Dai, H. J., Kesani, P. A., Garetz, B. A., Hammouda, B., "Influence of Imperfections on the Disordering of Block Copolymer Cylinders," *Macromolecules* **27**, 7406 (1994).
- Balsara, N., Hammouda, B., "Shear Effects on Solvated Block Copolymer Lamellae: PS-PI in DOP," *Phys. Rev. Lett.* **72**, 360 (1994).
- Balsara, N. P., Hammouda, B., Kesani, P. K., Jonnalagadda, S. V., Straty, G. C., "In-Situ Small Angle Neutron Scattering from a Block Copolymer Solution Under Shear," *Macromolecules* **27**, 2566 (1994).
- Barker, J.G., Pedersen, J.S., "Instrumental Smearing Effects in Circularly Symmetric Small- Angle Neutron Scattering by Numerical and Analytical Methods," *J. Appl. Cryst.*, in press.



- Bendersky, L. A., Stalick, J. K., Waterstrat, R. M., "Crystal Structure of the  $Zr_3Pd_4$  Phase," *J. Alloys Compounds* **201**, 121 (1993).
- Bennett, K., Wenk, H.-R., Choi, C. S., Trevino, S. F., Durham, W. B., Stern, L. A., "Texture Measurement at 77 K of Deformed  $D_2O$  Ice II polycrystals: A Study by Neutron Diffraction," in *Textures of Geological Materials*, edited by Bunge, H. J., Siegesmund, S., Skrotzki, W. and Weber, K., (1994), p. 251.
- Birch, W. R., Knewton, M. A., Garoff, S., Suter, R. M., Satija, S., "The Structure of Precursing Thin Films of an Anionic Surfactant on a Silicon Oxide/Silicon Surface," *Langmuir*, in press.
- Borchers, J. A., Ankner, J. F., Majkrzak, C. F., Engel, B. N., Wiedmann, M. H., Van Leeuwen, R. A., Falco, C. M., "Spatial Modulation of the Magnetic Moment in Co/Pd Superlattices Observed by Polarized Neutron Reflectivity," *J. Appl. Phys.* **75**, 6498 (1994).
- Borchers, J. A., Erwin, R.W., Berry, S. D., Lind, D. M., Lochner, E., Shaw, K. A., "Magnetic Structure Determination for  $Fe_3O_4/NiO$  Superlattices," *Appl. Phys. Lett.* **64**, 381 (1994).
- Borchers, J. A., Erwin, R.W., Berry, S. D., Lind, D. M., Ankner, J. F., Lochner, E., Shaw, K. A., Hilton, D., "Long-Range Magnetic Order in  $Fe_3O_4/NiO$  Superlattices," *Phys. Rev. B.*, in press.
- Brand, P. C., Prask, H. J., "The Neutron Residual Stress Measurement Research Program at the National Institute of Standards and Technology (NIST)," in *Proceedings Fourth International Conference on Residual Stresses* (Baltimore, MD, June, 1994), p. 230.
- Brand, P. C., Prask, H. J., "New Methods for the Alignment of Instrumentation for Residual Stress Measurements by Means of Neutron Diffraction," *J. Appl. Cryst.* **27**, 164 (1994).
- Briber, R., Bauer, B., Hammouda, B., "SANS from Dilute Blends of dPS in PVME and in HPS," *J. Chem. Phys.* **102**, 2592 (1994).
- Casella, R. C., "On the Roles of Local Classical Acceleration and Spatial Separation in the Neutral Particle Analogs of the Aharonov-Bohm Phases," *Phys. Rev. Lett.*, in press.
- Chang, K. J., Hsieh, W. T., Li, W.-H., Lee, K. C., Lynn, J. W., Lai, C. C., Ku, H. C., "Magnetic Ordering of Pr and Cu in  $TlBa_2PrCu_2O_{7-y}$ ," *Phys. Rev. B* **49**, 12200 (1994).
- Chattopadhyay, T., Lynn, J. W., Rosov, N., Grigereit, T. E., Barilo, S. N., Zhigunov, D. I., "Magnetic Ordering in  $Eu_2CuO_4$ ," *Phys. Rev. B* **49**, 9944 (1994).
- Choi, C. S., "Application of ODF to the Rietveld Profile Refinement of Polycrystalline Solid," in *Adv. X-ray Anal.* Vol. 37, edited by J. V. Gilfrich et al, (Plenum Press, New York, 1994), p. 49.
- Choi, C. S., Baker, E. L., Orosz, J., "Microstructure Study of Molybdenum Liners by Neutron Diffraction," in *Non-Destructive Characterization in Materials VI*, edited by R. E. Green, Jr., et al. (Plenum Press, New York, 1994), p. 637.
- Christides, C., Dennis, T. J. S., Prassides, K., Cappelletti, R. L., Neumann, D. A., Copley, J. R. D., "Rotational Dynamics of Solid  $C_{70}$ : A Neutron Scattering Study," *Phys. Rev. B* **49**, 2897 (1994).

- Christides, C., Prassides, K., Neumann, D. A., Copley, J. R. D., Mizuki, J., Tanigaki, K., Hirose, I., Ebbesen, T. W., "Rotational Dynamics of  $C_{60}$  in  $Na_2RbC_{60}$ ," *Europhys. Lett.* **24**, 755 (1993).
- Clinton, T. W., Lynn, J. W., Liu, J. Z., Jia, Y. X., Shelton, R. N., "Two- and Three-Dimensional Magnetic Order of Er in Superconducting  $ErBa_2Cu_3O_7$ ," *Physica C* **217**, 53 (1993).
- Clinton, T. W., Lynn, J. W., Liu, J. Z., Jia, Y. X., Goodwin, T. J., Shelton, R. N., "Magnetic Order of  $DyBa_2Cu_3O_{6+x}$ ,  $0 < x < 1$ ," *Phys. Rev. B*, in press.
- Clinton, T. W., Lynn, J. W., Lee, B. W., Buchgeister, M., Maple, M. B., "Effects of the Chain Layer Oxygen on the Magnetic Order of Nd in  $NdBa_2Cu_3O_{6+x}$ ," *Phys. Rev. B*, in press.
- Clinton, T. W., Lynn, J. W., Peng, J. L., "Influence of Chain-Site Oxygen on the Magnetic Order of Er in  $ErBa_2Cu_3O_{6+x}$ ," *Phys. Rev. B*, in press.
- Composto, R. J., Mansfield, T., Beaucage, G., Stein, R. S., Iyengar, D. R., McCarthy, T. J., Satija, S. K., Ankner, J. F., Majkrzak, C. F., "The Volume Fraction Profile of Terminally Adsorbed Polymers," in *Complex Fluids*, (MRS, Pittsburgh, PA, 1994).
- Copley, J. R. D., David, W. I. F., Neumann, D. A., "Structure and Dynamics of Buckyballs," *Neutron News* **4**, 20 (1993).
- Copley, J. R. D., Cook, J. C., "An Analysis of the Effectiveness of Oscillating Radial Collimators in Neutron Scattering Applications," *Nucl. Instrum. & Methods, Phys. Res. A* **345**, 313 (1994).
- Copley, J. R. D., "Transmission Properties of Short Curved Neutron Guides: I. Acceptance Diagram Analysis and Calculations," *Nucl. Instrum. & Methods, Phys. Res. A*, in press.
- Copley, J. R. D., "Transmission Properties of Neutron Optical Filters," *J. Neut. Res.* **2**, 95 (1994)
- del Moral, A., Arnundas, J. I., Gehring, P. M., "Spin-Glass Behavior in a Weak Random-Anisotropy Magnet  $Dy_xY_{1-x}Al_2$ ," *J. Phys. C* **6**, 4779 (1994).
- Dender, D., Lefmann, K., Reich, D., Broholm, C., Aeppli, G., "Neutron Scattering Study of the  $S = 1/2$  1D Heisenberg Antiferromagnet Copper Benzoate," *Phys. Rev. B*, in press.
- Ditusa, J. F., Cheong, S-W., Park, J.-H., Aeppli, G., Broholm, C., Chen, C. T., "Magnetic and Charge Dynamics in a Doped One-Dimensional Transition Metal Oxide," *Phys. Rev. Lett* **73**, 1857 (1994).
- Dura, J. A., Pippenger, P. M., Halas, N. J., Xiong, X. Z., Chow, P. C., Moss, S. C., "Epitaxial Integration of Single Crystal  $C_{60}$ ," *Appl. Phys. Lett.* **63**, 3443 (1993).
- Dura, J. A., Vigliante, A., Golding, T. D., Moss, S. C., "Epitaxial Growth of Sb/GaSb Structures: An Example of V/III-V Heteroepitaxy," *J. Appl. Phys.*, in press.
- Eastman, J. A., Fitzsimmons, M. R., Robinson, R. A., Lynn, J. W., "The Neel Temperatures of Nanocrystalline Chromium," *Appl. Phys. Lett.*, in press.

- Everitt, B. A., Borchers, J. A., Salamon, M. B., Rhyne, J. J., Erwin, R.W., Park, B. J., Flynn, C.P., "Magnetic Ordering of Nd in Nd/Y Superlattices," *J. Mag. Magn. Matls.*, in press.
- Everitt, B. A., Salamon, M. B., Flynn, C. P., Park, B. J., Borchers, J. A. Erwin, R. W., Tsui, F., "Magnetic Properties of Dy-Lu Alloys," *J. Appl. Phys.* **75**, 6592 (1994).
- Feng, Y. P., Majkrzak, C. F., Sinha, S. K., Wiesler, D. G., Zhang, H., Deckman, H. W., "Direct Observation of Neutron Guided Waves in a Thin-Film Waveguide," *Phys. Rev. B* **49**, 10814 (1994).
- Gehring, P. M., Neumann, D. A., Kamitakahara, W. A., Rush, J. J., Eaton, P. E., VanMeurs, D. P., "Neutron-Scattering Study of the Lattice Modes of Solid Cubane," *J. Phys. Chem.*, in press.
- Gehring, P. M. Chou, H., Shapiro, S. M., Hriljac, J. A., Chen, D. H., Toulouse, J., Rytz, D., Boatner, "Anomalous Dispersion and Thermal Expansion in Lightly-Doped  $\text{KTa}_{1-x}\text{Nb}_x\text{O}_3$ ," *Ferroelectrics* **150**, 47 (1993).
- Gehring, P. M., Hirota, K., Majkrzak, C. F., Shirane, G., "Absence of the Anomalous Second Length Scale in the Bulk of a Terbium Single Crystal," *Phys. Rev. B*, in press.
- Giebultowicz, T. M., Nunez, V., Springholz, G., Bauer, G., Chen, J., Dresselhaus, M. S., Furdyna, J. K., "Interlayer Coupling in (111) EuTe/PbTe AFM Multilayers," *J. Mag. Magn. Matls.*, in press.
- Giebultowicz, T. M., Luo, H., Samarth, N., Furdyna, J. K., Nunez, V., Rhyne, J. J., Faschinger, W., Springholtz, G., Bauer, G., Sitter, H., "Strain-induced Helimagnetism, Finite Thickness Effects and Interlayer Coupling in Magnetic Semiconductor Multilayers," *Physica B* **198**, 163 (1994).
- Giebultowicz, T. M., Faschinger, W., Nunez, V., P. Klosowski, P., Bauer, G., Sitter, H., Furdyna, J. K., "Antiferromagnetic Spin Ordering and Interlayer Magnetic Correlations in MnTe/CdTe Superlattices," *J. Cryst. Growth* **138**, 877 (1994).
- Green, M., Kurmoo, M., Stalick, J., Day, P., "The Crystal Structure and Magnetic Properties of  $\text{CuGeO}_3$  a Possible Spins-Peierls Compound," *Chem. Commun.*, 1995 (1994)
- Grigereit, T. E., Lynn, J. W., Huang, Q., Santoro, A., Cava, R. J., Krajewski, J. J., Peck Jr., W. F., "Observation of Oscillatory Magnetic Order in the Antiferromagnetic Superconductor  $\text{HoNi}_2\text{B}_2\text{C}$ ," *Phys. Rev. Lett.*, in press.
- Gygax, F. N., Amato, A., Anderson, I. S. Rush, J. J., Schenck, A., Solt, G., " $\mu^+$  Localization and Tunneling in Sc," *Hyperfine Interactions* **85**, 73 (1994).
- Gygax, F. N., Amato, A., Anderson, I. S., Rush, J. J., Schenck, A., "Study of  $\mu^+$  Localization and Diffusion in Sc and  $\text{ScH}_{0.05}$ ," *Z. Phys. Chem.* **181**, 119 (1993).
- Gygax, F. N., Amato, A., Feyerherm, R., Schenck, A., Anderson, I. S., Udovic, T. J., Solt, G., "Dynamics of  $\mu^+$  in Sc and  $\text{ScH}_x$ ," *J. Alloys and Compounds*, in press.

- Hammouda, B., "Random Phase Approximations for Compressible Polymer Blends," *J. Non-Crystalline Solids* **172**, 927 (1994).
- Hammouda, B., Bauer, B. J., Russell, T. P., "SANS From Deuterated Polystyrene/Polybutylmethacrylate Homopolymer Blend Mixtures," *Macromolecules* **27**, 2357 (1994).
- Hammouda, B., Bauer, B., "Compressibility of Two Polymer Blend Mixtures," *Macromolecules*, in press.
- Harrison, W. T. A., Gier, T. E., Nicol, J. M., Stucky, G. D., "Tetrahedral-Framework Lithium Zinc Phosphate Phases: Location of Light-Atom Positions in  $\text{LiZnPO}_3 \cdot \text{H}_2\text{O}$  by Powder Neutron Diffraction; Structure Determination of  $\text{LiZnPO}_4$  by Ab Initio Methods," *J. Solid State Chem.*, in press.
- Harrison, W. T. A., Liang, C. S., Nicol, J. M., Stucky, G. D., "Microporous, Noncentrosymmetric, Octahedral/Tetrahedral-Framework Phases:  $\text{K}_{2/3}\text{Li}_{1/3}\text{Nb}_2\text{PO}_8$ ,  $\text{K}_{2/3}\text{Li}_{1/3}\text{Ta}_2\text{PO}_8$  and  $\text{K}_{2/3}\text{Ag}_{1/3}\text{Nb}_2\text{PO}_8$ ," *Inorg. Chem.*, in press.
- Harrison, W. T. A., Nenoff, T. M., Newsam, J. M., Nicol, J. M., Stucky, G. D., "The Crystal Structure of a New Sodium Zinc Arsenate Phase Solved by Simulated Annealing," *Zeolites*, **506** (1993).
- Hirota, K., Shirane, G., Gehring, P. M., Majkrzak, C. F., "Neutron-Scattering Studies of the Two Magnetic Correlation Lengths in Terbium," *Phys. Rev. B* **49**, 11967 (1994).
- Hsieh, W. T., Li, W-H, Lee, K. C., Lynn, J. W. Shieh, J. H., Ku, H. C., "Magnetic Ordering of Pr in  $\text{Pb}_2\text{Sr}_2\text{PrCu}_3\text{O}_8$ ," *J. Appl. Phys.*, in press.
- Huang, Q., Lynn, J. W., Meng, R. L., Chu, C. W., "Crystal Structure of Annealed and As-prepared  $\text{HgBa}_2\text{CaCu}_2\text{O}_{6+}$ ," *Physica C* **218**, 356 (1994).
- Huang, Q., Soubeyroux, J. L., Chmaissem, O., Natali-Sora, I., Santoro, A., Cava, R. J., Krajewski, J. J., Peck, Jr., W. F., "Neutron Powder Diffraction Study of the Crystal Structures of  $\text{Sr}_2\text{RuO}_4$  and  $\text{SrIrO}_4$  at Room Temperature and at 10 K," *J. Solid State Chem.* **112**, 355 (1994).
- Huang, Q., Chaissem, O., Capponi, J. J., Chaillout, C., Marezio, M., Tholence, J. L. Santoro, A., "Neutron Powder Diffraction Study of the Crystal Structure of  $\text{HgBa}_2\text{Ca}_4\text{Cu}_5\text{O}_{12+\delta}$  at Room Temperature and at 10 K," *Physica C* **227**, 1 (1994).
- Huang, Q., Karen, P., Karen, V. L., Kjekshus, A., Lynn, J. W., Mighell, A. D., Natali Sora, I., Rosov, N., Santoro, A., "Neutron Powder Diffraction Study of the Nuclear and Magnetic Structures of the Oxygen-Deficient Perovskite  $\text{YBaCuCoO}_5$ ," *J. Solid State Chem.* **108**, 80 (1994).
- Huang, Q., Udovic, T. J., Rush, J. J., Schefer, J., Anderson, I.S., "Characterization of the Structure of  $\text{TbD}_{2.25}$  at 70 K by Neutron Powder Diffraction," *J. Alloys and Compounds*, in press.

- Huang, Q., Santoro, A., Grigereit, T. E., Lynn, J. W., Cava, R. J., Krajewski, J. J., Peck, Jr., W. F., "Neutron Powder Diffraction Study of the Nuclear and Magnetic Structure of the Antiferromagnetic Superconductor  $\text{HoNi}_2\text{B}_2\text{C}$ ," *Phys. Rev. B*, in press.
- Ilavsky, J., Herman, H., Berndt, C.C., Goland, A.N., Long, G.G., Krueger, S., Allen, A.J., "Porosity in Plasma-sprayed Alumina Deposits" in '1994 Thermal Spray Industrial Applications', Ed. C.C. Berndt and S. Sampath, ASM International, Materials Park, OH, 709-714, (1994).
- Isaacs, E. D., Zschack, P., Broholm, C., Burnes, C., Aeppli, G., Ramirez, A. P., Oglesby, C. S., Bucher, E., Erwin, R. W., "Suppression of the Antiferromagnetic Moment in the Superconducting Phase of  $\text{UPt}_3$ ," *Phys. Rev. Lett.*, in press.
- Joubran, R., Parris, N., Lu, S., Trevino, S., "Synergetic Effect of Sucrose and Ethanol on Formation of Triglyceride Micromulsions," *J. Dispersion Sci. & Tech.* **15**, 687 (1994).
- Karim, A., Satija, S. K., Han, C. C., Slaweki, T. M., Kumar, S. K., Russell, T. P., "Phase Behavior of Thin Polymer Blend Film," *ACS PMSE* **71**, 280 (1994).
- Karim, A., Satija, S. K., Orts, W., Ankner, J. F., Majkrzak, C. F., Fetters, L. J., "Chemical Grafting of Silane End-Functionalized Polymer on Silicon Surfaces," in *MRS Symposium Proceedings*, Vol. 304, 149 (1993).
- Karim, A., Slaweki, T., Kumar, S., Russell, T. P., Satija, S., Han, C. C., Rafailovich, M., Sokolov, J. "Phase Separation Induced Roughening Transition in Thin Polymer Blend Films," *Phys. Rev. Lett.*, in press.
- Keimer, B., Aksay, I., Dogan, F., Erwin, R. W., Lynn, J. W., Sarikaya, M., "Inclined-Field Structure, Morphology and Pinning of the Vortex Lattice in Microtwined  $\text{YBa}_2\text{Cu}_3\text{O}_7$ ," *Science* **262**, 83 (1993).
- Keimer, B., Shih, W.Y., Erwin, R.W., Lynn, J. W., Dogan, F., Aksay, I. A., "Vortex Lattice Symmetry and Electronic Structure in  $\text{YBa}_2\text{Cu}_3\text{O}_7$ ," *Phys. Rev. Lett.*, in press.
- Keimer, B., Lynn, J. W., Erwin, R. W., Dogan, F., Shih, W. Y., Aksay, I. A., "Vortex Structures  $\text{YBa}_2\text{Cu}_3\text{O}_7$ ," *J. Appl. Phys.*, in press.
- Kerch, H. M., Burdette, H. E., Gerhardt, R., Krueger, S., Allen, A. J., Long, G. G., "In-Situ Microstructure Characterization of Sintering of Controlled Porosity Materials," in *Better Ceramics Through Chemistry VI*, Vol. 346, edited by A. Cheetham (MRS, Pittsburgh, PA, 1994), p. 177.
- Kim, K. D., Sperling, L. H., Klein, A., Hammouda, B., "Reputation Time, Temperature, and Co-Surfactant Effects on the Molecular Interdiffusion Rate During Polystyrene Latex Film Formation," *Macromolecules* **27**, 6841 (1994).
- Knell, U., Heid, C., Wipf, H., Udovic, T. J., Rush, J. J., Lauter, H. J., "Hydrogen in  $\text{YBa}_2\text{Cu}_3\text{O}_x$ : A Neutron Spectroscopy and a Nuclear Magnetic Resonance Study," *Z. Phys. Chem.* **179**, 397 (1993).

- Koneripalli, N., Singh, N., Levicky, R., Bates, F. S., Gallagher, P. D., Satija, S. K., "Confined Block Copolymers Thin Films," *Macromolecules*, in press.
- Krueger, S., Olson, G. J., Johnsonbaugh, D., Beveridge, T. J., "Characterization of the Binding of Gallium, Platinum and Uranium to *Pseudomonas fluorescens* using Small Angle X-ray Scattering and Transmission Electron Microscopy," *Applied and Environmental Microbiology* **59**, 4056 (1993).
- Krueger, S., Andrews, A. P., Nossal, R., "Small Angle Neutron Scattering Studies of Structural Characteristics of Agarose Gels," *Biophys. Chem.*, in press.
- Lambooy, P., Russell, T. P., Kellog, G. J., Mayes, A. M., Gallagher, P. D., Satija, S.K., "Observed Frustration in Confined Block Copolymers," *Phys. Rev. Lett.* **72**, 2899 (1994).
- Lee, D. D., Barker, J., Chen, S. H., "Absolute Calibration of Small Angle Neutron Scattering Data Using Strong Coherent Scattering," *J. de Physique IV*, Vol. 3, in *IX International Conference on Small Angle Scattering*, edited by A Brûlet, J. P. Cotton, and J. Teixeira (les editions de physique, Cedex, France, 1993), p. C8-431.
- Lee, E. M., Elmiger, M., Passell, L., Majkrzak, C. F. "The Brookhaven Neutron Reflection Spectrometer," *Nucl. Instrum & Methods, Phys. Res. B* **93**, 75 (1994).
- Lee, D. D., Chen, S. H., Satija, S. K., Majkrzak, "Investigation of Surface Ordering in a Microemulsion Near the Lamellar Transition by Neutron Reflectivity," in *Proceedings of 2nd Liquid State Conference (EPS, Florence, Italy, 1993)*.
- Lee, W. T., Kaiser, H., Rhyne, J. J., Dumesnil, K., Dufour, C., Mangin, Ph., Marchal, G., Erwin, R.W., Borchers, J. A., "Exchange Coupling in Dy/Er Metallic Superlattices," *J. Appl. Phys.* **75**, 6477 (1994).
- Li, W-H., Jou, C. J., Shyr, S. T., Lee, K. C., Lynn, J. W., Tsay, H. L., Yang, H. D., "Effects of Ga-Doping on the Magnetic Ordering of Pr in  $\text{PrBa}_2\text{Cu}_3\text{O}_7$ ," *J. Appl. Phys.*, in press.
- Lieb, R. J., Trevino, S.F., Barnes, J. D., "Onset and Nature of Fracture of Uniaxially Compressed Gun Propellants A Small Angle Neutron and X-Ray Scattering Study," *J. Mat. Res. Soc.*, in press.
- Lieb, R. J., Trevino, S. F., "A Small Angle Neutron and X-Ray Scattering Study of the Onset and Nature of Fracture of Uniaxially Compressed Gun Propellants," *Proceedings of U.S. Army Science Conference*, in press.
- Lin, D., Nunes, A. C., Majkrzak, C. F., Berkowitz, A. E., "Polarized Neutron Study of the Magnetization Density Distribution within a  $\text{CoFe}_2\text{O}_4$  Colloidal Particle II," *JMMM*, in press
- Lind, D. M., Berry, S. D., Borchers, J. A., Erwin, R. W., Lochner, E., Stoyonov, P., Shaw, K. A., "Magnetic Order in Layered Oxide Structures:  $\text{Fe}_3\text{O}_4$  Thin Films and  $\text{Fe}_3\text{O}_4/\text{NiO}$  Superlattices," *J. Mag. Magn. Matls.*, in press.

- Lind, D M., Borchers, J. A., Erwin, R. W., Ankner, J. F., Lochner, E., Shaw, K. A., DiBari, R. C., Portwine, W., Stoyonov, P., Berry, S. D., "Investigations of the Interplay Between Crystalline and Magnetic Ordering in  $\text{Fe}_3\text{O}_4/\text{NiO}$  Superlattice," *J. Appl. Phys.* **76**, 6284 (1994).
- Liu, Y., Rafailovich, M. H., Sokolov, J. Schwarz, S. A., Zhong, X., Eisenber, A., Kramer, E. J., Sauer, B. B., Satija, S., "Wetting Behavior of Homopolymer Films on Chemically Similar Block Copolymer Surfaces," *Phys. Rev. Lett.* **73**, 440 (1994).
- Long, G.G., Allen, A.J., Krueger, S., Thomas, J., Johnson, D.L., Hwang, C.J., "Small-angle Scattering Studies of the Microstructure of Silicon Nitride During Processing", in Volume I: High Performance Materials in Engine Technology, Proceedings CIMTEC World Ceramics Congress and Forum on New Materials, Florence, ( Italy, Jun. 27-Jul. 4, 1994), in press.
- Lynn, J. W., Rosov, N., Grigereit, T. E., "Vortex Dynamics and Melting in Niobium," *J. Mag. Mater.*, in press.
- Lynn, J. W., Rosov, N., Grigereit, T., Zhang, H., Clinton, T. W., "Reply to "Comment on Vortex Dynamics and Melting in Niobium," *Phys. Rev. Lett.* **74**, in press.
- Lynn, J. W., Rosov, N., Acet, M., Bach, H., "Polarization Analysis of the Magnetic Excitations in  $\text{Fe}_{65}\text{Ni}_{35}$  Invar," *J. Appl. Phys.* **75**, 6069 (1994).
- Lynn, J. W., Rosov, N., Grigeret, T. E., Zhang, H., Clinton, T. W., "Vortex Dynamics and Melting in Niobium," *Phys. Rev. Lett.* **72**, 3413 (1994).
- Lynn, J. W., "Magnetic Neutron Scattering," *J. Appl. Phys.* **75**, 6806 (1994).
- Majkrzak, C. F., "Chapter XIII: Polarized Neutrons," in *Handbook of Neutron Scattering*, edited by W. Glaser (Springer-Verlag), in press.
- Majkrzak, C. F., Ankner, J. F., Berk, N. F., Gibbs, D., "Neutron and X-ray Diffraction Studies of Magnetic Multilayers," in *Magnetic Multilayers*, edited by Watson, R., and Bennett, L., (World Scientific Publishers), in press.
- Majkrzak, C. F., "Advances in Polarized Neutron Reflectometry," *Physica B*, in press.
- Mang, J., Hammouda, B., Kumar, S., "Discotic Micellar Nematic and Lamellar Phases under Shear Flow," *Europhys. Lett.* **28**, 489 (1994).
- Mayes, A. M., Barker, J. G., Russell, T. P., "Swelling Effects in Semidilute Block Copolymer Solutions," *J. Chem. Phys.* **101**, 5213 (1994).
- Mayes, A. M., Johnson, R. D. Russell, T. P., Smith, S. D., Satija, S. D., Majkrzak, C. F., "Distributions of Chain Ends and Junction Points in Ordered Block Copolymers," *Macromolecules* **26**, 1047 (1993).
- Mayes, A. M., Russell, T. P., Deline, V. R., Satija, S. K., Majkrzak, C. F., "Block Copolymer Mixtures as Revealed by Neutron Reflectivity," *Macromolecules* **27**, 7447 (1994).

- McGhie, A. R., Fischer, J. E., Stephens, P. W., Cappelletti, R. L., Neumann, D. A., Mueller, W. H., Mohn, H., ter Meer, H.-U., "Phase Transitions in Solid C<sub>70</sub> Supercooling, Metastable Phases and Impurity Effect," *Phys. Rev. B* **49**, 12614 (1994).
- Metoki, N., Zeidler, Th., Schreyer, A., Moraive, Ch., Romahn, U., Brohl, K., Zabel, H., Ankner, J. F., Majkrzak, C. F., "Exchange Coupling in (111)-Oriented Co/Cu Superlattices: No Evidence for Antiferromagnetic Alignment," *Phys. Rev. B*, in press.
- Morris, R. E., Owen, J. J., Stalick, J. K., Cheetham, A. K., "Determination of Complex Structures from Powder Diffraction Data; the Crystal Structure of La<sub>3</sub>Ti<sub>5</sub>Al<sub>15</sub>O<sub>37</sub>," *J. Solid State Chem.* **111**, 52 (1994).
- Moudden, A. H., Gehring, P. M., Shirane, G., Matsuda, M., Hennion, B., Endoh, Y., Tanaka, I., Kojima, H., "High Energy Phonon Dispersion in La<sub>1.85</sub>Sr<sub>1.15</sub>CuO<sub>4</sub>," *Physica B*, in press.
- Murthy, N. S., Orts, W. J., "Hydration in Semicrystalline Polymers: Small Angle Neutron Scattering Studies of the Effect of Drawing in Nylon 6 Fibers," *J. Polym. Sci B* **32**, 2695 (1994).
- Nakotte, H., Bruck, E., Brabers, J. H. V. J., Prokes, K., de Boer, F. R., Sechovsky, V., Buschow, K. H. J., Andreev, A. V., Lynn, J. W., "Magnetic Properties of Single-Crystalline UCu<sub>3</sub>Al<sub>2</sub>," *IEEE Transactions on Magnetics* **30**, 1217 (1994).
- Natali Sora, I., Wong-Ng, W., Huang, Q., Roth, R. S., Rawn, C. J., Burton, B. P., Santoro, A., "X-Ray and Neutron Diffraction Study of CaBi<sub>2</sub>O<sub>4</sub>," *J. Solid State Chem.* **109**, 251 (1994).
- Natali Sora, I., Huang, Q., Lynn, J. W., Rosov, N., Karen, P., Kjekshus, A., Karen, V. L., Mighell, A. D., Santoro, A., "Neutron Powder Diffraction Study of the Nuclear and Magnetic Structures of the Substitution Compound (Y<sub>1-x</sub>Ca<sub>x</sub>)Ba<sub>2</sub>Fe<sub>3</sub>O<sub>8+x</sub> (x = 0.05, 0.10 and 0.20)," *Phys. Rev. B* **49**, 3465 (1994).
- Nenoff, T. M., Harrison, W. T. A., Gier, T. E., Keder, N. L., Zaremba, C. M., Srdanov, V. I., Nicol, J. M., Stucky, G. D., "Structural and Chemical Investigations of Na<sub>3</sub>(ABO<sub>4</sub>)<sub>3</sub>•4H<sub>2</sub>O-Type Sodalite Phases," *Inorg. Chem.* **33**, 2472 (1994).
- Neumann, D. A., Copley, J. R. D., Reznik, D., Kamitakahara, W. A., Rush, J. J., Paul, R. L., Lindstrom, R. M., "Inelastic Neutron Scattering Studies of Rotational Excitations and the Orientational Potential in C<sub>60</sub> and A<sub>3</sub>C<sub>60</sub> Compounds," *J. Phys. Chem. Solids* **54**, 1699 (1993).
- Nicol, J. M., Udovic, T. J., Cavanagh, R. R., Xu, Z., Kawi, S., Mure, T., Gates, B. C., "Characterization of the Interaction of Hydrogen with Iridium Clusters, in Zeolites by Inelastic Neutron Scattering Spectroscopy," in *Molecularly Designed Ultrafine/Nanostructured Materials*, Mat. Res. Soc. Symp. Proceedings, Vol. 351 edited by K.E. Gonsalves, G.-M. Chow, T.D. Xiao, and R. C. Cammarata, (MRS, Pittsburgh, PA, 1994), p. 189.
- Nunez, V., Giebultowicz, T. M., Faschinger, W., Bauer, G., Sitter, H., Furdyna, J. K., "Helical Spin Ordering and Interlayer Correlations in MnTe/CdTe," *J. Mag. & Magn. Matls.*, in press.



- Nunez, V., Giebultowicz, T. M. Faschinger, W., Bauer, G., Sitter, H., Furdyna, J. K., "Helical Spin Ordering and Interlayer Correlations in Strained-Layer MnTe/CdTe Superlattices," Proceedings of International Congress on Physics of Semiconductors (Vancouver, 1994), in press.
- Nunez, V., Giebultowicz, T. M. Faschinger, W., Bauer, G., Sitter, H., Furdyna, J. K., "Investigation of Magnetic Structure of MnTe/CdTe Multilayers by Neutron Diffraction," in *MRS Proceedings Fall Meeting* (Boston, MA, 1994), in press.
- O'Connor, C., editor "Materials Science and Engineering Laboratory-Reactor Radiation, Technical Activities 1993," NISTIR 5317 (1993)
- Orts, W. J., "SANS Study of Chirality and Order in Cellulose Liquid Crystals," *Polymer Preprints*, in press.
- Orts, W. J., Godbout, L., Marchessault, R.H., Reveol, J.-F., "Shear Alignment of Cellulose Microfibrils in Aqueous Suspension," in *Shear Induced Ordering of Polymer Systems*, edited by A. I. Nakatani and M. Dadmun (Am. Chem. Soc. ,Washington, DC), in press.
- Orts, W. J. Godbout, L., Marchessault, R. H., Revol, J.-F., "A Small Angle Neutron Scattering (SANS) Study of the Chiral Nematic Ordering of Cellulose Microfibrils in Aqueous Suspension," *Proc. ACS, PMSE 70, 334* (1994).
- Pechan, M. J., Ankner, J. F., Kelly, D. M., Majkrzak, Schuller, I. K., "Magnetic Profile as a function of Structural Disorder in Fe/Cr Superlattices," in *Proceedings of the 38th MMM Conference* (Minneapolis, MN), Nov. 1993.
- Perahia, D., Wiesler, D. G., Satija, S. K., Fetters, L. J, Sinha, S. K., Milner, S. T., "Neutron Reflectivity of End Grafted Polymers: Concentration and Solvent Quality Dependence in Equilibrium Conditions," *Phys. Rev. Lett.* **72**, 100 (1994).
- Prask, H. J., "The Reactor and Cold Neutron Research Facility at NIST," *Neutron News* **5**, 10 (1994).
- Prask, H. J., "Materials Characterization with Cold Neutron," in *Proceedings of Nondestruction Characterization of Materials VI*, edited by R.E. Green and C.O. Ruud, (Plenum Press, New York, June 1994), p. 773.
- Prask, H. J., Fields, R. J., Brand, P. C. Blackburn, J. M., "Evolution of Residual Stresses Around a V-Notch Weldment," edited by M. R. James (Soc. for Exper. Mechs., Bethel, CT) in *Proceedings Fourth International Conference on Residual Stresses*, (Baltimore, MD, June, 1994), p. 1198.
- Radaelli, P. G., Marezio, M., Perroux, M., de Brion, S., Tholence, J. L., Huang, Q., Santoro, A., "Synthesis and Properties of a Cuprate Superconductor Containing Double Mercury-Oxygen Layers," *Science*, **265**, 380 (1994).
- Reis, K. P., Jacobson, A. J., Nicol, J. M., "A Powder Neutron Diffraction Investigation of Structure and Cation Ordering in  $Ba_{2+x}Bi_{2-x}O_{6-x}$ ," *J. Solid State Chem.* **107**, 428 (1993).

- Reznik, D., Kamitakahara, W. A., Neumann, D. A., Copley, J. R. D., Fischer, J. E., Strongin, R. M., Cichy, M. A., Smith III, A. B., "Neutron Scattering Study of Librations and Intramolecular Phonons in  $\text{Rb}_{2.6}\text{K}_{0.4}\text{C}_{60}$ ," *Phys. Rev. B* **49**, 1005 (1994).
- Reznik, D., Keimer, B., Dogan, F., Aksay, I. A., "High Resolution Inelastic Neutron Scattering Study of Phonon Self-Energy Effects in YBCO," *Physica C*, in press.
- Reznik, D., Olk, C. M., Neumann, D. A., Copley, J. R. D., "X-ray Powder Diffraction from Carbon Nanotubes and Nanoparticles", *Phys. Rev. B*, in press.
- Rhyne, J. J., Salamon, M. B., Flynn, C. P., Erwin, R. W., Borchers, J. A., "Magnetic Structures of Superlattices," *J. Mag. Magn. Matls.* **129**, 39 (1994).
- Robinson, R. A., Purwanto, A., Kohgi, M., Canfield, P. C., Kamilyama, T., Ishigaki, T., Lynn, J. W., Erwin, R., "On the Crystallography and Magnetism of the Heavy-Fermion Compound  $\text{YbBiPt}$ ," *Phys. Rev. B*, in press.
- Robinson, R. A., Lynn, J. W., Lawson, A. C., Nakotte, H., "Temperature Dependence of Magnetic Order in Single-Crystalline  $\text{UPdSn}$ ," *J. Appl. Phys.* **75**, 6589 (1994).
- Rosov, N., Lynn, J. W., Grigereit, T. E., "Neutron Scattering Studies of the Vortex Lattice in Niobium and  $\text{R}_{123}$  Superconductors," *J. Appl. Phys.*, in press.
- Rosov, N., Lynn, J. W., Kästner, J., Wassermann, E. F., Chattopadhyay, T., Bach, H., "Temperature Dependence of the Magnetic Excitations in Ordered and Disordered  $\text{Fe}_{72}\text{Pt}_{28}$ ," *J. Appl. Phys.* **75**, 6072 (1994).
- Rosov, N., Lynn, J. W., Kastner, J., Wassermann, E. F., Chattopadhyay, T., Bach, H., "Polarization Analysis of the Magnetic Excitations in  $\text{Fe}_{72}\text{Pt}_{28}$  Alloys," *J. Mag. Magn. Matls.*, in press.
- Rowe, J. M., Prask, H. J., "Neutron Techniques in Materials Science and Related Disciplines," 4th International Conference on Application of Nuclear Techniques: Neutron and their Applications (June 12-18, 1994, Crete, Greece), in press.
- Sanders, P. G., Wertmann, J. R., Barker, J. G., Siegel, R. W., "Small Angle Neutron Scattering from Nanocrystalline Pd and Cu Compacted at Elevated Temperatures," in *Nonastructured Materials: Molecularly Designed Ultrafine/Nanostructured Materials* edited by E. K. Gansalves, G. Chow, T. D. Xiao, R. C. Cammarata, *Mat. Res. Soc. Symp. Proceedings*, 351 (1994), p. 319.
- Sanders, P. G., Weertman, J. R., Barker, J. G., Siegel, R.W., "Small Angle Neutron Scattering from Nanocrystalline Palladium as a Function of Annealing," *Scripta Metallurgica et Materialia* **29**, 91 (1993).
- Satija, S. K., Karim, A., Douglas, J. F., "Concentration Profiles of End Anchored Polymer Brushes under Variable Solvent," *Polymers Preprint*, in press.

- Schreyer, A., Ankner, J. F., Schäfer, M., Zeidler, Th., Zabel, H., Majkrzak, C. F., Grünberg, P., "Direct Observation of a Non-Collinear 50-Coupled Magnetization Profile in a Fe/Cr (001) Superlattice," Proceedings of ICM '94, in press.
- Schreyer, A., Ankner, Zabel, H., Schäfer, M., Majkrzak, C. F., Grünberg, P., "Direct Observation of Non Collinear Spin Structures in Fe/Cr (100) Superlattices Using Spin Polarized Neutron Reflectometry," *Physica B* 198, 173 (1994).
- Schreyer, A., Metoki, N., Zeidler, Th., Bödeker, P., Abromeit, A., Morawe, Ch., Romahn, U., Sonntag, P., Bröhl, K., Zabel, H., Ankner, J.F., Majkrzak, C.F., "Exchange Coupling in Single Crystalline Co/Cu(III) Superlattices," *J. Mag. Magn. Matls.*, in press.
- Schober, T., Hempelmann, R., Udovic, T.J., "Hydrogen Sites in ZrCoH<sub>3</sub> by Neutron Vibrational Spectroscopy," *Z. Phys. Chem.* 179, 211 (1993).
- Schönfeld, C., Hempelmann, R., Richter, D., Springer, T., Dianoux, A. J., Rush, J. J., Udovic, T. J., Bennington, S. M., "Dynamics of Hydrogen in  $\alpha$ -LaNi<sub>5</sub> Hydride Investigated by Neutron Scattering," *Phys. Rev. B* 50, 853 (1994).
- Schröder, A., Lynn, J. W., Erwin, R. W., Loewenhaupt, M., Lohneysen, H. V., "Magnetic Structure of the Heavy Fermion Alloy CeCu<sub>5.5</sub>Au<sub>0.5</sub>," *Physica B* 199&200, 47 (1994).
- Schwarzenbach, D., Abrahams, S. C., Flack, H. D., Prince, E., Wilson, A. J. C., "Statistical Descriptors in Crystallography, II. Report of a Working Group on Expression of Uncertainty in Measurement," *Acta Crystallgr. A*, in press.
- Sikka, M., Singh, N., Bates, F. S., Karim, A., Satija, S., Majkrzak, C. F., "Surface Segregation in Model Symmetric Polyolefin Diblock Copolymer Melts," *Macromolecules, J de Phys. II (France)* 4, 2231 (1994).
- Sinha, S. K., Lynn, J. W., Grigereit, T. E., Hossain, Z., Gupta, L. C., Nagarajan, R., Godart, C., "Neutron Diffraction Study of Antiferromagnetic Order in the Magnetic Superconductor ErNi<sub>2</sub>B<sub>2</sub>C," *Phys. Rev. B*, in press.
- Sinha, S. K., Sanyal, M. K., Satija, S. K., Majkrzak, C. F., Neumann, D. A., Homma, H., Szpala, S., Gibaud, A., Morkoç, H., "X-ray Scattering Studies of Surface Roughness of GaAs/AlAs Multilayers," *Physica B* 198, 72 (1994).
- Skanthakumar, S., Lynn, J. W., Sumarlin, I. W., "Comment on "Spin Structures of Tetragonal Lamellar Copper Oxides," *Phys. Rev. Lett.*, in press.
- Slade, R. C. T., Hall, G. P., Ramanan, A., Nicol, J. M., "Neutron Scattering Study of Protonic Species in Ammonium Pentamolybdate, (NH<sub>4</sub>)Mo<sub>5.33</sub>H<sub>3</sub>O<sub>18</sub>," *J. Chem. Soc. Faraday Trans.* 90, 3579 (1994).
- Slade, R. C. T., Hall, G. P., Ramanan, A., Nicol, J. M., "A Neutron Scattering Study of Protonic Species in Ammonium Decamolybdate (NH<sub>4</sub>)Mo<sub>5</sub>O<sub>15</sub>(OH)·2H<sub>2</sub>O," *J. Mater. Chem.*, in press.

- Smith, P. A., Kerch, H., Krueger, S., Long, G. G., Keller, J., Haber, R. A., "Pore Sizes and Filtration Rates from Two Alumina Slips," *J. Amer. Ceram. Soc.* **77**, 1777 (1994).
- Stalick, J. K., Santoro, A., "Crystal Chemistry of the Substitution Compounds of  $\text{YBa}_2\text{Cu}_3\text{O}_7$ ," in *Current Status and Future Directions in Condensed Matter Physics*, edited by S.K. Maikl (Plenum, New York), in press.
- Stuhr, U., Wipf, H., Udovic, T. J., Weissmüller, J., Glieter, H., "Inelastic Neutron Scattering Study," *J. Phys: Condensed Matter.*, in press.
- Stuhr, U., Wipf, H., Udovic, T. J., Weissmüller, J., Gleiter, H., "The Vibrational Excitations and the Position of Hydrogen in Nanocrystalline Pd," *J. Phys.: Condens. Matter*, in press.
- Sumarlin, I. W., Lynn, J. W., Chattopadhyay, T., "Dispersion of Magnetic Excitations of the Pr ions in  $\text{Pr}_2\text{CuO}_4$ ," *Physica C* **219**, 195 (1994).
- Sumarlin, I. W., Lynn, J. W., Chattopadhyay, T., Barilo, S.N., Zhigunov, D.K., Peng, J.L., "Magnetic Structure and Spin Dynamics of the Pr and Cu in  $\text{Pr}_2\text{CuO}_4$ ," *Phys. Rev. B*, in press.
- Suzuki, M., Suzuki, I. S., Burr, C. R., Wiesler, D. G., Rosov, N., Koga, K., "Structural and Magnetic Properties of  $\text{CuCl}_2$  Graphite Intercalation Compounds," *Phys. Rev. B*, in press.
- Toney, M. F., Howard, J. N., Richer, J., Borges, G. L., Gordon, J. G., McIroy, O. R., Wiesler, D. G., Yee, D., Sorensen, L. B., "Distribution of Water Molecules at the Silver (III)-Electrolyte Interface," *Nature* **368**, 444 (1994).
- Trevino, S. F., Joubran, R., Parris, N., Berk, N. F., "The Structure of a Triglyceride Microemulsion: A Small Angle Neutron Scattering Study", *Langmuir* **10**, 2547 (1994).
- Udovic, T. J., Rush, J. J., Anderson, I. S., "Neutron Spectroscopic Evidence of Concentration-Dependent Hydrogen Ordering in the Octahedral Sublattice of  $\beta\text{-TbH}_{2+x}$ ," *Phys. Rev. B* **50**, 7144.
- Udovic, T. J., Huang, Q., Rush, J. J., Schefer, J., Anderson, I. S., "Neutron-Powder-Diffraction Study of the Long-Range Order in the Octahedral Sublattice of  $\text{LaD}_{2.25}$ ," *Phys. Rev. B*, in press.
- Udovic, T. J., Rush, J. J., Anderson, I. S., "Neutron Spectroscopic Comparison of  $\beta$ -Phase Rare-Earth Hydrides," *J. Alloys & Comp.*, in press.
- Udovic, T. J., Rush, J. J., Anderson, I. S., Daou, J. N., Vajda, P., Blaschko, O., "The Vibrations of Hydrogen and Deuterium in Solid Solution with Lutetium," *Phys. Rev. B* **50**, 3696 (1994).
- Udovic, T. J., Rush, J. J., Hempelmann, R., Richter, D., "Low-energy Vibrations and Octahedral-Site Occupation in  $\text{Nb}_{95}\text{V}_5\text{H(D)}_y$ ," *J. Alloys & Comp.*, in press.
- Udovic, T. J., Rush, J. J., Anderson, I. S., "Local-Mode Dynamics in  $\text{YH}_2$  and  $\text{YD}_2$  by Isotope Dilution Neutron Spectroscopy," *Phys. Rev. B* **50**, 15739 (1994).

- VanderHart, D. L., Orts, W. J., "A  $^{13}\text{C}$  Determination of the Degree of Cocrystallization in random Copolymers of Poly( $\beta$ -Hydroxybutyrate-co- $\beta$ -Hydroxyvalerate)," *Macromolecules*, in press.
- Vierheller, T. R., Foster, M. D., Schmidt, A., Mathauer, K., Knoll, W., Wegner, G., Satija, S., Majkrzak, C. F., "Structure and Thermal Stability of Langmuir-Blodgett-Kuhn Layers of Hairy-Rod Polymers Probed with Neutron and X-ray Reflectometry," *Macromolecules* **27**, 6893 (1994).
- Wiesler, D. G., Zabel, H., Shapiro, S. M., "Two Dimensional XY Type Magnetism in Intercalated Graphite: an Elastic and Inelastic Neutron Scattering Study," *Z. Phys.B* **93**, 277 (1994).
- Wiesler, D. G., Toney, M. F., Melroy, O. R., McMillan, C. S., Smyrl, W. H., "X-ray Diffraction from Anodic  $\text{TiO}_2$  Films: In Situ and Ex Situ Comparison of the  $\text{Ti}(0001)$  Face," *Surf. Sci.* **302**, 341 (1993).
- Wiesler, D. G., Majkrzak, C. F., "In-Situ Neutron Reflectivity Study of Titanium Anodization," *Electrochemical Soc.*, in press.
- Wiesler, D. G., Majkrzak, C. F., "Neutron Reflectometry Studies of Surface Oxidation," *Physica B* **198**, 181 (1994).
- Wu, S. Y., Hsieh, W. T., Li, W-H, Lee, K. C., Lynn, J. W., Yang, H. D., "Two-Dimensional Magnetic Order in  $\text{Pb}_2\text{Sr}_2\text{TbCu}_3\text{O}_8$ ," *J. Appl. Phys.* **75**, 6598 (1994).
- Wu, W., J. H., Orts, W. J., Majkrzak, C.F., Hunston, D.L., "Water Absorption at a Polyimide/Silicon Wafer Interface", *Polym. Eng., & Sci.*, in press.
- Wu, W., Orts, W. J., Van Zanten, J. H., Fanconi, B. M., "Density Profile of Spin Cast Polymethylmethacrylate Thin Films," *J. Polymer Sci . B, Polym. Phys. Ed.*, in press.
- Wu, W., Van Zanten, J. H., Orts, W. J., "Film Thickness Dependent Thermal Expansion in Ultrathin Polymethylmethacrylate Films on Silicon," *Macromolecules*, in press.
- Zhang, H., Gallagher, P. D., Satija, S. K., Lindstrom, R. M. Paul, R. L., Russell, T. P., Lambooy, P., Kramer, E. J., Bates, F. S., "Grazing Incidence Prompt Gamma Emissions and Resonance-Enhanced Neutron Standing Waves in a Thin Film," *Phys. Rev. Lett.* **72**, 3044 (1994).

### Independent Publications

- Allen, A.J., Gavillet, D., Weertman, J.R., "SANS and TEM Studies of Isothermal  $\text{M}_2\text{C}$  Carbide Precipitation in Ultrahigh Strength AF1410 Steels", *Acta Metall. Mater.* **41**, 1869-1884 (1993).
- Anderson, D. L., Cunningham, W. C., "In-House Reference Material Characterization Using Nuclear Methods, ANS Transactions, in press.
- Anderson, D. L., Cunningham, W. C., Lindstrom, T. R., "Concentrations and Intakes of H, B, S, K, Na, Cl, and NaCl in Foods," *J. Food Comp. and Anal.* **7**, 59 (1994).
- Anderson, D. L., Cunningham, W. C., Lindstrom, T. R., Olmez, I., Identification of Lead and Other Elements in Ceramic Glases and Housewares Using  $^{109}\text{Cd}$ -Induced X-Ray Emission, *J. AOAC Int.*, in press.

- Anderson, D. L., Downing, R. G., and Iyengar, G. V., "Trace Elements in Food Reference Materials: Compositional and Analytical Perspectives," *Fres. J. Anal. Chem.*, in press.
- Anderson, D. L., Kitto, M. E., McCarthy, L., Zoller, W. H., "Sources and Atmospheric Distribution of Particulate and Gas-Phase Boron," *Atmospheric Environment* **28**, 1401 (1994).
- Arif, M., Dewey, S., Greene, G. L., Jacobson, D., Werner, S., "X-Ray Determination of the Elastic Deformation of a Perfect Crystal Neutron Interferometer: Implications for Gravitational Phase Shift Experiment," *Phys. Lett. A* **184**, 154 (1994).
- Balsara, N. P., Fetters, L. J., Huang, J. S., Jeon, H. S., Lin, M. Y., "A Scattering Evaluation of Dienyllithium Association States," *ACS PMSE*, in press.
- Balsara, N. P., Jonnalagadda, S. V., Lin, C. C., Han, C. C., Krishnamoorti, R., "Thermodynamics Interactions and Correlations in Mixtures of Two Homopolymers and a Block Copolymer by Small Angle Neutron Scattering", *J. Chem. Phys.* **99**, 10011 (1993).
- Balsara, N. P., Lin, C. C., Dai, H. J., Krishnamoorti, R., "Effect of Saturation on Thermodynamics of Polystyrene-Polyisoprene Block Copolymers", *Macromolecules* **27**, 1216 (1994).
- Balsara, N. P., Lohse, D. J. Graessley, W. W., Krishnamoorti, R., "Small Angle Neutron Scattering by Partially Deuterated Polymers and Their Blends," *J. Chem. Phys.* **100**, 3905 (1994).
- Bates, F. S., Schulz, M. F., Khandpur, A. K., Förster, S., Rosendale, J. H., Almdal, K., Mortensen, K., "Fluctuations, Conformational Asymmetry and Block Copolymer Phase Behavior," *Faraday Discuss. Chem. Soc.*, in press.
- Becker, D. A., "Resolution of Discrepant Analytical Data in the Certification of Platinum in Two Automobile Catalyst SRMs," *Fres. J. Anal. Chem.*, in press.
- Becker, D. A., "Determination of 21 Elements by INAA for Certification of SRM 1570a, Spinach," *J. of Radioanal. and Nucl. Chem.*, in press.
- Becker, D. A., Gills, T. E., "Recent Developments in NIST Botanical SRMs," *Fres. J. Anal. Chem.*, in press.
- Becker, P. R. Mackey, E. A., Demiralp, R., Suydam, R., Wise, S. A., Koster, B. J., Early, G., "Relationship of Silver to Selenium and Mercury in the Liver Tissue of Two Species of Toothed Whales (Odontocetes)," *Marine Pollution Bulletin*, in press.
- Becker, D. A., Anderson, D. L., Lindstrom, R. M., Greenberg, R. R., Garrity, K. M., Mackey, E. A., "Use of INAA, PGAA, and RNAA to Determine 30 Elements for Certification of an SRM: Tomato leaves, 1573a," *J. Radioanal. and Nucl. Chem. Articles* **179**, 149 (1994).
- Bender, J. W., Wagner, N. J., "Structure and Rheology Relations in Colloidal Suspensions: Shear Thinning and Shear Thickening Properties of Dense Suspensions," *Proceedings of the AIChE International Forum on Fine Particle Technology, Denver, 1994*, in press.

- Blaauw, M., Lindstrom, R. M., "Local Area Networks in Neutron Activation Analysis: Advantages and Pitfall," *J. Radioanal. and Nucl. Chem.* **169**, 443 (1993).
- Bobyak, L., Pilione, L. J., Messier, R., Lamaze, G. P., "Effect of Stoichiometry on the Phases Present in Boron Nitride Thin Films," *J. Vac. Sci. Technol.* **12**, 1569 (1994).
- Chen, S. H., Ku, C. Y., Rouch, J., Tartaghia, P., "Structure and Dynamics of Water-in-Oil Microemulsions Near the Critical and Percolation Points," *Proceedings of the 12th Symposium on Thermophysical Properties International J. of Thermophysics*, in press.
- Chen, H., Sharov, V. A., Mildner, D. F. R., Downing, R. G., Paul, R. M., Lindstrom, R. L., Zeissler, C. J., and Xiao, Q. F., "Prompt Gamma Activation Analysis Enhanced by a Neutron Focusing Capillary Lens," *Nucl. Instrum. and Meth. B*, in press.
- Chen, H., Mildner, D. F. R., Xiao, Q. F., "Neutron Focusing Lens Using Polycapillary Fibers," *Appl. Phys. Lett.* **64**, 2068 (1994).
- Chen, H., Mildner, D. F. R., Downing, R. G., Benenson, R. E., Xiao, Q. F., and Sharov, V. A., "Neutron Focusing Using Capillary Optics," *Proceedings Third European Conference on Accelerators in Applied Research and Technology*, *Nucl. Instrum. and Meth. B* **89**, 401 (1994).
- Chiba, M., Iyengar, G. V., Greenberg, R. R., Gills, T. E., "Determination of Tin in Biological Materials by Atomic Absorption Spectrophotometry and Neutron Activation Analysis," *Sci. Total Environ.* **148**, 39 (1994).
- Cheung, Y. W., Stein, R. S., "Critical Analysis of the Phase Behavior of Poly( $\epsilon$ -aprolactone) (PCL)/polycarbonate(PC) Blends," *Macromolecules* **27**, 2512 (1994).
- Clarke, S. M., Melrose, J., Rennie, A. R., Ottewill, R. H., Heyes, D., Mitchell, P. J., Hanley, H. J. M., Straty, G. C., "The Structure and Rheology of Hard Sphere Systems," *J. Phys.: Condens. Matter.* **6** A333 (1994).
- Crawford, M. K., Corbin, D. R., Vernooy, P. D., "Prompt  $\gamma$ -Activation Analysis of Solid Acid Catalysts," *Trans. Am. Nuc. Soc.*, in press.
- Cunningham, W. C., Anderson, D. L., Baratta, E. J., "Radionuclides in Domestic and Imported Foods in the United States 1987-1992," *J. AOAC International* **77**, in press.
- Dadmun, M., Han, Charles, "A Neutron Scattering Study of the Orientation of a Liquid Crystalline Polymer by Shear Flow," *Macromolecules* **27**, 7522 (1994).
- Divita, F., Ondov, J. M. "Size Spectra and Hygroscopic Growth of V Aerosol in Washington, D.C., Air and Waste Management Assoc., in press.
- Divita, F., Suarez, A., Ondov, J. M., "Size Spectra and Hygroscopic Growth of Particles Bearing As, Se, Sb, and Zn in College Park Aerosol," *J. Radionaly. Nuc. Chem.*, in press.
- Douglas, C. B., Kaler, E. W., "Bilayer Phases in Aqueous Mixtures of *n*-Dodecylpentaoxyethylene Glycol Monoether (C<sub>12</sub>D<sub>5</sub>) and Sodium Decyl Sulfonate (C<sub>10</sub>SO<sub>3</sub>Na)," *J. Chem. Soc., Faraday Trans.* **90**, 471 (1994).

- Douglas, C. B., Kaler, E. W., "A Scattering Study of Mixed Micelles of *n*-Dodecylhexaoxyethylene Glycol Monoether (C<sub>12</sub>E<sub>6</sub>) and Sodium Dodecyl Sulfonate (C<sub>12</sub>SO<sub>3</sub>Na) in D<sub>2</sub>O," *Langmuir* **10**, 1075 (1994).
- Downing, R. G., Iyengar, G. V., "Methodological Issues in the Analytical Determination of Boron," *Environ. Health Perspect*, in press.
- Fetters, L. J., Huang, J. S., Young, R. N., Hadjichristidis, N., "More Light on the Concept of Unreactivity Arising from Active Center Association in Anionic Polymerizations," *Macromolecules*, in press.
- Fetters, L. J., Lohse, D. J., Richter, D., Witten, T. A., Zirkel, A., "Connection between Polymer Molecular Weight, Density, Chain Dimensions and Melt Viscosity Properties," *Macromol.* **27**, 4639 (1994).
- Fujiwara, S., Mendelson, R. A., "The Statistical Labeling Method and In Situ Neutron Scattering and Diffraction Measurements on Ordered Systems," *J. Appl. Cryst.*, in press.
- Full, A. P., Kaler, E. W., "Structure and Dynamics of Polymerizable Microemulsions," *Langmuir*, in press.
- Graessley, W. W., Krishnamoorti, R., Balsara, N. P., Butera, R. J., Fetters, L. J., Lohse, D. J., Schultz, D. N., Sissano, J. A., "Thermodynamics of Mixing for Blends of Model Ethylene-Butene Copolymers," *Macromol.* **27**, 3896 (1994).
- Greene, G. L., *Neutron Nuclei and Matter* by J. Byrne, *Physics Today* **47**, 65 (1994).
- Greene, G. L., "The Neutron", to appear in *The Macmillan Encyclopedia of Physics*, John Rigden, Editor-in Chief, (1994).
- Greene, G. L., Bowles, T., Schmiedmayer, J., Seestrom, S., Snow, W. M., "Fundamental Physics" in *Technology and Science at a High-Power Spallation Source*, Proceedings of a workshop held at Argonne National Laboratory, eds. G. Aeppli and B. Brown, U.S. Government Printing Office Publication 1994-547-499 (1994).
- Greene, G. L., Kloor, H., Fischbach, E., and Talmadge, C., "Limits on New Forces Co-existing with Electromagnetism," *Phy. Rev. B* **50**, 2900, (1994).
- Greene, G. L., Thompson, A., Dewey, M. S., "A New Method for the Accurate Determination of the Polarization of a Neutron Beam Using a Polarized <sup>3</sup>He Spin Filter," in press.
- Greenberg, R. R., "Accuracy in Standards Preparation for Neutron Activation Analysis," *J. Radioanal. and Nucl. Chem. Articles* **179**, 149 (1994).
- Greenberg, R. R., Kane, J. S., Gills, T. E., "Certification of New NIST Fly Ash Standard Reference Material," *Fres. J. Anal. Chem.*, in press.
- Greenberg, R. R., Mackey, E. A., Becker, D. A., "The Application of Instrumental Neutron Activation Analysis for the Certification of the New NIST Fly Ash SRM," *J. Radioanal. and Nucl. Chem.*, in press.



- Han, Charles C., Yoom, Hichang, "Statics and Kinetics of Phase Behavior in Polymer Blends", *NATAS (North American Thermal Analysis Society) Polymer Blends and Copolymers Symposium*, (1993), p. 22.
- Hanley, I. W., Gehlsen, M. D., Khandpur, A. K., Koppi, K. A., Rosedale, J. H., Schulz, M. F., Bates, F. S., Almdal, K., Mortensen, K., "Complex Layered Phases in Asymmetric Diblock Copolymers," *J. Phys. II (France)*, in press.
- Hanley, I. W., Koppi, K. A., Rosedale, J. H., Bates F. S., Almdal, K., Mortensen, K., "Hexagonal Mesophases Between Lamellae and Cylinders in a Diblock Copolymer Melt," *Macromolecules*, **26**, 5959 (1993).
- Hanley, H. J. M., Straty, G. C., Lindner, P., "Partial Scattered Intensities from a Binary Suspension of Polystyrene and Silica," *Langmuir* **10**, 72 (1994).
- Hawari, A., Venkataraman, R., Fleming, R., Eisenhauer, C., Grundl, J., McGarry, E.D., "The Materials Dosimetry Reference Facility, Eighth ASTM-Euratom Symposium on Reactor Dosimetry," (Vail, Colorado), in press.
- He, M., Hill, R. M., Lin, Z., Scriven, L. E., Davis, H. T., "Phase Behavior and Microstructure of Polyoxyethylene Trisiloxane Surfactants in Aqueous Solution," *J. Phys. Chem.* **97**, 8820 (1993).
- Heuser, B. J., "Small-Angle Neutron Scattering Study of Dislocations in Deformed Single Crystal Cu," *J. Appl. Cryst.*, in press.
- Hight, S. C., Anderson, D. L., Cunningham, W. C., Capar, S. G., Lamont, W. H., Sinex, S. A., "Analysis of Dietary Supplements for Nutritional, Toxic, and Other Elements, *J. Food Composition and Analysis* **6**, 121 (1993).
- Hobbie, E., Bauer, B., Han, C., "Fractal Growth During Early-Stage Spinodal Decomposition in a Hydrogen-Bonded Polymer Blend", *Physical Review Letters*, **12**, 1830 (1994).
- Hobbie, E., Nakatani, A. I., Han, C., "Shear-induced Mixing in Polymer Blends", *Modern Physics, Letters B* **19**, 1143, (1994).
- Hofsass, H. C. Biegel, J., Ronning, C., Downing, R. G., and Lamaze, G. P., "Characterization of Doped Diamondlike Carbon Films and Multilayers," *Proceedings Materials Research Society*, in press.
- Huang, J. S., Fetters, L. J., Richter, D., Hadjichristidis, Farago, B., Gast, A. P., "Structure and Dynamics of the Diblock Cp-polymer Aggregates in Solution," in *Physics of Complex Fluids and Biological Systems*, edited by Sung, W., Jeong, Y.H., Choi, S.I., (Min Eum Sa Press 1993), p. 75.
- Iyengar, G. V., Wolf, W. R., Demiralp, R., and Greenberg, R. R., "Mixed Total Diet Slurry as a Prospective Reference Material," *Fresenius J. Anal. Chem.* **348**, 426 (1994).
- Jackson, C. L., Barnes, K. A., Morrison, F. A., Mays, J. W., Nakatani, A. I., Han, C. C., "A Shear-induced Martensitic-like Transformation in a Block Copolymer Melt", *Macromolecules*, in press.

- Jackson, C. L., Mathukumar, M., Barnes, K. A., Morrison, F. A., May, J. W., Nakatani, A. I., Han, C. C., "Shear-Excited Morphological States in a Triblock Copolymer American Chemical Society", Am. Chem. Soc., Polymer Preprints **35**, 624, (1994).
- Jackson, C. L., Morrison, F., Mays, J., Mathukumar, M., Nakatani, A., Han, C. C., "Shear-induced Changes in the Order-disorder Transition Temperature and the Morphology of a Triblock Copolymer. ACS Symposium Series, *Flow-Induced Structures in Polymers*, in press.
- Jemian, P. R., Allen, A. J., "The Effect of the Shape-Function on Small-Angle Scattering Data Analysis by the Maximum Entropy Method", J. Appl. Cryst. **27**, 693 (1994).
- Jinnai, H., Hasegawa, H., Hashimoto, T., Han, C. C., "Time-Resolved Small-Angle Neutron Scattering Study of Spinodal Decomposition in Polybutadiene Blends: 1. Effect of Initial Thermal Fluctuations", J. Chem. Phys. **99**, 4545 (1993).
- Kessler, E. G., Henins, A., Deslattes, R. D., Nielsen, L. Arif, M., "Precision Comparison of the Lattice Parameters of Silicon Monocrystals," J. Res. Natl. Inst. Stand. Technol. **9**, (1994).
- Klein, J., Jumacheva, E. Mahalu, D., Perahia, D., Fetters, L. J., "Reduction of Frictional Forces between Solid Surfaces Bearing Polymer Brushes," Nature **370**, 634 (1994).
- Kline, S. R., Kaler, E. W., "Colloidal Interactions in Water/ 2-Butoxyethanol Solvents," Langmuir **10**, 412 (1994).
- Koehler, R. D., Kaler, E. W., "Structure of Sheared Cetyl Trimethylammonium Tosylate/Sodium Dodecyl Benzene Sulfonate Rodlike Micellar Solutions," in *Rheology of Surfactant Solutions*, edited by C. A. Herb and R. Prud'homme, (ACS), in press.
- Koehler, R. D., Schubert, K.-V., Strey, R., Kaler, E. W., "The Lifshitz Line in Binary Systems: Structures in Water/C<sub>4</sub>E<sub>1</sub> Mixtures," J. Chem. Phys., in press.
- Koppi, K. A., Tirrell, M., Bates, F. S., Almdal, K., Mortensen, K., "Epitaxial Growth and Shearing of the Body Centered Cubic Phase in Diblock Copolymer Melts," J. Rheology **38**, 999 (1994).
- Krishnamoorti, R., Graessley, W. W., Balsara, N. P., Lohse, D. J., "The Compositional Dependence of Thermodynamic Interactions in Blends of Model Polyolefins," J. Chem. Phys. **100**, 3894 (1994).
- Krishnamoorti, R., Graessley, W. W., Balsara, N. P., Lohse, D. J., "The Structural Origin of Thermodynamic Interactions in Blends of Saturated Hydrocarbon Polymers," Macromol. **27**, 3037 (1994).
- Krishnamoorti, R., Graessley, W. W., Balsara, N. P., Lohse, D. J., "The Compositional Dependence of Thermodynamic Interactions in Blends of Model Polyolefins," J. Chem. Phys. **100**, 3894 (1994).
- Kuznetsov, I. A., Serebrov, A. P., Stepanenko, I. V., Alduschenkov, A. V., Lasakov, M. S., Kokin, A. A., Mostovoi, Yu. A., Yerozolimsky, B. G., Dewey, M. S., "Measurements of the Antineutrino

- Spin Asymmetry in Beta Decay of the Neutron and Restrictions on the Mass of a Right-handed Gauge Boson," *Phys. Rev. Lett.*, in press.
- Lamaze, G. P., Downing, R. G., Hackenberger, L. B., Piliore, L. J., Messier, R., "Analysis of Cubic Boron Nitride Thin Films by Neutron Depth Profiling," *Diamond and Related Materials* **3**, 728 (1994).
- Lamaze, G. P., Badzian, A., Badzian, T., Downing, R. G., Piliore, L. J., "Boron and Nitrogen Analysis of CVD Diamond Films Using Cold Neutron Depth Profiling," *Advances in New Diamond Science and Technology*, in press.
- Landsberger, S., Peshev, S., Becker, D.A., "Determination of Silicon in Biological and Botanical Reference Materials by Epithermal INAA and Compton Suppression," *Nucl. Inst. and Meth. in Phys Res.*, in press.
- Lee, D. D., Chen, S. H., "Local Geometry of Surfactant Monolayers in a Ternary Microemulsion System," *Phys. Rev. Lett.* **73**, 106 (1994).
- Lin, C. C., Jonnalagadda, S. V., Kesani, P. K., Dai, H. J., Balsara, N. P., "Effect of Molecular Structure on the Thermodynamics of Block Copolymer Melts", *Macromolecules*, **27**, 7769 (1994).
- Lin, M. Y., Sinha, S. K., Chari, K., "Polymer-surfactant Assemblies in Water: A SANS Study," *J. Physique IV (Paris)* **3**, 153 (1993).
- Lin, M. Y., Sinha, S. K., Drake, J. M., Wu, X-L., Thiyagarajan, P., Stanley, H. B., "Study of Phase Separation of a Binary Mixture in Confined Geometry," *Phys. Rev. Lett.* **72**, 2207 (1994).
- Lin, M. Y., Sinha, S. K., Drake, J. M., Thiyagarajan, P., Wu, X.-L., Stanley, H. B., "SANS Studies of Fluid Phase Transitions in Porous Media," *J. Physique IV (Paris)* **3**, 109 (1993).
- Lindstrom, R. M., "SUM and MEAN: Standard Programs for Activation Analysis," *Biol. Trace Element Res.*, in press.
- Lindstrom, R. M., Paul, R. L., Walters, W. B., Molnar, G., "Analytical Applications of Cold Neutron Capture and Opportunities for Nuclear Physics, *Proceedings 8th International Symposium Capture Gamma-Ray Spectroscopy and Related Topics*, edited by J. Ker World Scientific, (Singapore, 1994), p. 955.
- Lindstrom, R. M., Fleming, R. F., "Dead Time, Pileup, and Accurate Gamma-Ray Spectrometry," *Radioact and Radiochem.*, in press.
- Lindstrom, R. M., Mackey, E. A., Paul, R. L., "Analytical Applications of Guided Neutron Beams," *Biol. Trace Elem. Res.*, in press.
- Lindstrom, R. M., Paul, R. L., Vincent, D. H., Greenberg, R. R., "Measuring Hydrogen by Cold-Neutron Prompt-Gamma Activation Analysis," *J. Radioanal. & Nucle. Chem.* **180**, 271 (1994).
- Lindstrom, R. M., Yonezawa, C., "Prompt-Gamma Activation Analysis with Guided Neutron Beams," in *Prompt Gamma Neutron Activation Analysis*, edited by Z. B. Alfassi, C. Chung (CRC Press, Boca Raton), in press.

- Lindstrom, R. M., "Prompt-Gamma Activation Analysis and Applications in Industry, Environment, and Medicine," *Acta Physica Hungarica*, in press.
- Livingston, R. A., Allen, A. J., "Application of Small-Angle Neutron Scattering Method to the Study of the Durability of Historic New Materials, (Florence, Italy, Jun. 27 - Jul. 4, 1994), in press.
- Lohse, D. J. Balsara, N. P., Fetters, L. J., Schultz, D. N., Sissano, J. A., Graessley, W. W., Krishnamoorti, R., "Thermodynamics of Random Copolymer Mixtures by SANS," in *New Advances in Polyolefins*, edited by T. C. Chung, (Plenum Press, New York, 1993), p. 175.
- MacConnell, G. A., Lin, E. K., Gast, A. P., Huang, J. S., Lin, M. Y., Smith, S. D., "Structure and Interactions in Tethered Chain Systems," Royal Society of Chemistry, Faraday Discussion No. 98, Sept. 1994.
- Mackey, E. A., "Effects of Target Temperature on Analytical Sensitivities of Cold Neutron Prompt Gamma-Ray Activation Analysis," *Biol. Trace Element Res.*, in press.
- Mass, J. L., Burlitch, J. M., McGuire, S. C., Hossain, T. Z., Demiralp, R., "Neutron Activation Analysis of Al in  $Mg_2SiO_4$ ," *Nucl. Instrum. Meth. in Phys. Res.*, in press.
- Matsushita, Y., Torikai, N., Mogi, Y., Noda, I., Han, C. C., "Chain Conformations of Homopolymers Dissolved in a Microdomain of Diblock Copolymer", *Macromolecules*, in press.
- McConnell, G. A., Gast, A. P., Huang, J. S., Smith, S. D., "Disorder-Order Transitions in Soft Sphere Polymer Micelles," *Phys. Rev. Lett.* **71**, 2102 (1993).
- Mildner, D. F. R., "Neutron Focusing Optics for Low-Resolution Small-Angle Scattering," *J. Appl. Cryst.* **27**, 521 (1994).
- Mildner, D. F. R., "The Focal Length of Neutron Lenses Using Capillary Optics", *J. Cryst.* **26**, 721 (1993).
- Mildner, D. F. R., Arif, M., Stone, C. A., Crawford, R. K., "The Neutron Transmission of Single Crystal Sapphire Filters," *J. Appl. Cryst.* **26**, 438 (1993).
- Mildner, D. F. R., Chen, H., "The Neutron Transmission Through a Cylindrical Guide Tube," *J. Appl. Cryst.* **27**, 316 (1994).
- Mildner, D. F. R., Chen, H., Downing, R. G., Sharov, V. A., Xiao, Q. F., "Cold Neutron Guiding and Focusing," *Acta Phys. Hungarica* **75**, 183 (1994).
- Mildner, D. F. R., Chen, H., "The Characterization of a Polycapillary Neutron Lens," *J. Appl. Cryst.* **27**, 943 (1994).
- Mildner, D. F. R., Chen, H., Downing, R. G., Benenson, R. E., and Glinka, C. G., "Low-Resolution Small-Angle Scattering Using Neutron Focusing Optics," *J. de Phys. Coll. C* **8**, 3435 (1993).

- Mildner, D. F. R., Sharov, V. A., Chen, H., "The Number of Reflections of a Neutron Beam Transmitted by a Capillary Fiber," *J. Appl. Cryst.*, in press.
- Muzny, C. D., Straty, G. C., Hanley, H. J. M., "A SANS Study of Dense Sheared Silica Gels," *Phys. Rev. B.*, in press.
- Muzny, C. D., Hansen, D., Straty, G. C., Evans, D. J., Hanley, H. J. M., "Simulation and SANS Studies of Gelation under Shear," *Int. J. Thermophysics*, in press.
- Norman, B.R., Iyengar, G.V., "Determination of Iodine in Diverse Botanical and Dietary Matrices by Preirradiation Combustion Followed by Neutron Activation Analysis," *Fresenius J. Anal. Chem.* **348**, 430 (1994).
- Olah, G. A., Rokop, S. E., Wang, C.-L. A., Blechner, S. L., Trehwella, J., "Troponin I Encompasses an Extended TroponinC in the  $\text{Ca}^{2+}$  Bound Complex: A Small-Angle X-ray and Neutron Scattering Study," *Biochemistry* **33**, 8233 (1994).
- Olah, G. A., Trehwella, J., "A Model Structure of the Muscle Protein Complex  $4\text{Ca}^{2+} \bullet \text{Troponin C} \bullet \text{Troponin I}$  Derived from Small-Angle Scattering Data: Implications for Regulation," *Biochemistry* **33**, 12800 (1994).
- Paul, R. L., Englert, P. A. J., Lindstrom, R. M., "Mapping of Neutron Flux Gradient at NIST Reactor to Optimize Neutron Activation Analysis of  $^{53}\text{Mn}$ ," *J. Radionanal. and Nucl. Chem. Letters* in press.
- Paul, R. L., Lindstrom, R. M., Vincent, D. H., "Cold Neutron Prompt Gamma Activation Analysis at NIST: A Progress Report," *J. Radionanal. and Nucl. Chem.* **180**, 263 (1994).
- Paul, R. L., Lindstrom, R. M., "Determination of Hydrogen in Titanium Alloy Jet Engine Compressor Blades by Cold Neutron Capture Prompt Gamma-Ray Activation Analysis," *Diagnostic Techniques for Semiconductor Proceeding*, in *Proceedings Materials Research Society Symposium*, edited by O. J. Glembocki, S. W. Pang, F. H. Pollak, G. M. Crean, and G. Larrabee, Vol. 403 (1994), p. 324.
- Paul, R. L., Lindstrom, R. M., "Determination of Hydrogen in Titanium Alloy Jet Engine Compressor Blades by Cold Neutron Capture Prompt Gamma-Ray Activation Analysis," *Review of Progress in Quantitative Nondestructive Evaluation*, edited by D. O. Thompson and D. E. Chimenti Vol. 13 (1994), p. 1619.
- Paul, R. L., Mackey, E. A., "Neutron Scattering by Hydrogen in Cold Neutron Prompt Gamma-Activation Analysis," *Radioanal. and Nucl. Chem.*, **181**, 321 (1994).
- Quinn, T. L., "Size Distribution and Dry Deposition of Elemental Constituents of Aerosols on the Chesapeake Bay, Ph.D. Thesis, University of Maryland, College Park, MD (1994).
- Richter, D., Jucknischke, Willner, L., Fetters, L. J., Lin, M. Y., Huang, J. S., Roovers, J., Toporovski, C., Zhou, L. L., "Structure of Star Polymers in Solution by Small Angle Neutron Scattering," *Macromol.* **27**, 3821 (1994).

- Richter, D., Jucknischke, O., Willner, L., Fetters, L. J., Lin, M. Y., Huang, J. S., Roovers, J., Toporowski, C., Zhou, L. L. "Scaling Properties and Ordering Phenomena of Star Polymers in Solution, *J. de Phys. IV, Coloque C8 3, 3* (1993).
- Richter, D., Willner, L., Zirkel, A., Farago, B., Fetters, L. J., Huang, J. S., "Onset of Topological Constraints in Polymer Melts," *Phys. Rev. Lett.* **71**, 4158 (1993).
- Sanders, P. G., Weertman, J. R., Barker, J. G., Siegel, R. W., "Small Angle Neutron Scattering from Nanocrystalline Pd and Cu Compacted at Elevated Temperatures," in *MRS Symp.*, (Spring, 1994), in press.
- Schantz, M., Benner, B., Hays, M., Kelly, R., Vocke, R., Demiralp, R., Greenberg, R. R., Schiller, S., Lauertier, G., Wise, S., Welch, M., May, W. E., "Certification of Standard Reference Material (SRM) 1941a, Organics in Marine Sediment," *Fresenius J. of Anal. Chem.* in press.
- Schubert, K.-V., Strey, R., Kline, S. R., Kaler, E. W., "Small Angle Neutron Scattering Near Lifshitz Lines: Transition from Weakly Structured Mixtures to Microemulsions," *J. Chem. Phys.* **101**, 5343 (1994).
- Schul, M. F., Bates, F. S., Almdal, K., Mortensen, K., "Epitaxial Relationship for Hexagonal-to-Cubic Phase Transition in a Block Copolymer Mixture," *Phys. Rev. Lett.* **73**, 86 (1994).
- Schulz, M. F., Bates, F. S., Almdal, K., Mortensen, K., "Epitaxial Hexagonal-to Cubic Phase Transition in a Block Copolymer Mixture," *Phys. Rev. Lett.*, **73**, 86 (1994).
- Schwartz, R. B., and Eisenhauer, C. M., "Test of a Neutron Spectrometer in NIST Standard Fields, "Radiation Protection Dosimetry," **55**, 99 (1994).
- Singh, N., Kudrie, A., Sikka, M., Bates, F. S., "Surface Topography of Symmetric and Asymmetric Polyolefin Block Copolymer Films", *J. Phys II (France)*, in press.
- Small, J. A., Zeissler, C. J., Sharov, V. A., Chen, H., Paul, R. L., Rivay, Zs., Mildner, D. F. R., Downing, R. G., Lindstrom, R. M., "The Prompt-Gamma Activation Analysis of particles Excited by a Focused-Neutron Probe," in *Proceedings 28th Annual Meeting of the Microbeam Analysis Society*, (1994), p. 137..
- Sung, L., Nakatani, A., Fauvarque, P., Douglas, J., Han, C., "SANS Studies of the Phase Behavior of Binary Polymer Blend/Diblock Copolymer Mixtures", *ACS PMSE Preprints*, **71**, 370, (1994).
- Swider, J. R., Mustillo, D. M., Conticchio, L. F., Walters, W. B., Paul, R. L., Lindstrom, R. M., "Gamma-Ray Cascades in the Te-128(n,T)Reaction Observed in Coincidence Measurements," *Proceedings 8th International Symposium Capture Gamma-Ray Spectroscopy and Related Topics*, edited by J. Kern, World Scientific, (Singapore,1994), p. 335.
- Wagner, N. J., Walker, L. M., "The Determination of the Texture Viscosity and Elasticity of a Nematic PBLG/d-DMF Solution through Magnetic Field Alignment," *Macromolecules*, in press.
- Willner, L., Jucknischke, O., Richter, D., Roovers, J., Zhou, L. L., Toporowski, P. M., Fetters, Huang, J. S., Lin, M. Y., Hadjichristidis, N., "Structure of Star Polymers in Solution by Small Angle Neutron Scattering," *Macromolecules* **27**, 3821 (1994).

- Wu, W., Kent, M., "Moisture Absorption at Polymer/Silicon Wafer Interface", Proceedings of 1994 MRS Meeting 338, 565, (1994).
- Wu, W., Van Zanten, J. H., Orts, W. J., "Glass Transition Temperature of Ultrathin Polymer Films on Silicon", in *Proceedings of 1994 ISHM Meeting*, (Boston), in press.
- Wu, W., Van Zanten, J. H., Orts, W. J., "Thermal Expansion Measurements of Thin PMMA Films", in press.
- Wu, Z. Y., Han, M., Lin, Z. C., Ondov, J. M., "Chesapeake Bay Atmospheric Deposition Study, Year 1: Sources and Dry Deposition of Selected Elements in Aerosol Particles," *Atmos. Environ.* 28, 1471 (1994).
- Xiao, Q. F., Chen, H., Mildner, D. F. R., Downing, R. G., Benenson, R. E., "A Comparison of Experiment and Simulation for Neutron Guidance through Glass Polycapillary Fibers," *Review of Sci. Instrum.* 64, 3252 (1993).
- Yoon, H., Feng, Y., Qiu, Y., Han, C. C., "Structural Stabilization of Phase Separating PC/Polyester Blends through Interfacial Modification by Transesterification Reaction", *J. of Polymer Science*, in press.
- Yoon, H., Han, C. C., "Interfacial Structure in Reacting PMMA/PC Polymer Blends", *Poly. Eng. Sci.*, in press.
- Young, R. N., Fetters, L. J., Huang, J. S., Krishamoorti, R., "Some Light on the Concept of Unreactivity Arising from Active Center Association in Anionic Polymerization," *Polymer International* 33, 217 (1994).
- Zeisler, R., Becker, D. A., "Certifying the Chemical Composition of a Biological Material — A Case Study," *J. of Radioanal. and Nucl. Chem.*, in press.
- Zeisler, R., Demiralp, R., Koster, B. J., Becker, P. R., Ostapczuk, P., Burow, M., and Wise, S. A., "Determination of Inorganic Constituents in Marine Mammal Tissues," *Science of the Total Environment*, 139/140, 365 (1993).
- Zeisler, R., Demiralp, R., Makarewicz, M., "High Count Rate Gamma Spectrometry: A Recent Experiment in High Accuracy NAA Applications," *J. Radioanal. and Nucl. Chem. Articles* 179, 61 (1994).







